Interpretation of the data of geothermal investigations
at the Karkar Site

Independent interpretation
of the results of the 3D MT, gravity and
CO₂ surveys conducted
at the Karkar Site

Project GEF-CS-4/2008

Final Report

Yerevan – 2012

Table of Content

Introduction

This work has been carried out in the framework of the ARMENIA GEOTHERMAL PROJECT GEF Grant # TF: 092563. The following two tasks were provided for in the Terms of Reference under this phase of the Project.

Task 1: To perform the interpretation, the Consultant will have to analyze the results of Phase 2 investigations at the Karkar site, including data of the 3D MT geophysical, gravimetric and CO_2 surveys. The analysis shall be based on a database organized in homogeneous digital layers of standard GIS format, enabling easy superposition of diverse types of information – topography, geology, hydrochemistry and geophysics.

Task 2: Based on the results of the analysis, the Consultant will have to identify and substantiate in detail the suggested presence (or absence) of potential geothermal strata and isolating layers within the site of Karkar, estimate their thickness and depth of occurrence.

Based on the interpretation results, the Consultant will identify the site for further detailed investigations within the Karkar geothermal field, up to, and inclusive of, determining the drilling location, or providing substantiated justification for considering the field not promising for further investigation.

Despite the TOR had limited the assigned interpretation to Project Phase 2, namely, to the 3D magneto-telluric, gravimetric and CO_2 soil gas surveys conducted by WesternGeco in 2011, the Contractor decided to extend the list of interpreted data considerably, willing to provide as much detailed and impartial interpretation for the Karkar Site as possible and to offer most substantiated arguments in support of the "*drill/not drill*" decision it would propose with respect to an exploratory well. Considering this, the interpreted data included the following in addition to the findings of the 2011 surveys as mentioned above:

1. **Data of geological and geophysical studies conducted in 1988 – 1989;**
2. **Data of the 2D MT survey, gravimetric, magnetometric and geological investigations conducted in 2004;**
3. **Data of the 2D MT survey and geological studies conducted for Project Phase 1 under the ARMENIA GEOTHERMAL PROJECT GEF Grant # TF: 092563 in 2009;**
4. **Data of petrographic, geochemical and isotope studies conducted by the IGS of the NAS of RA in 2007–2009.**

The presented Final Report consists of 2 parts: Part 1 – "Creation of Databases and Critical Analysis" and Part 2 – "Interpretation of Data, Structural and Conceptual Modeling".

This Final Report and the performed interpretation were carried out by two groups – one from the Republic of Armenia and one from the USA. The group of the University of South Florida (USA) prepared the following sections of the Final Report: Chapter 4.1.2 – *Comparing locations of MT Data Collection from the 2004, 2009, and 2011 MT Surv*eys; Chapter 3 – *Gravity Model: Data Interpretation and Modeling*; and Chapter 4 – Hydrothermal Model: Data Interpretation and Modeling. The rest of the sections were prepared by GEORISK Scientific Research CJS (RA) with contributions from experts and consultants from the Institute of Geological Sciences of the NAS of RA: Dr. R. A. Mirijanyan, Prof. R. L. Melkonyan, Corresponding member to the Academy of Sciences of Armenia, and Prof. R. T. Jrbashyan, Academician of the Academy of Sciences of Armenia.

Acknowledgements

Part I.

CONSTRUCTION OF DATABASES AND CRITICAL ANALYSIS

Part 1. CONSTRUCTION OF DATABASES AND CRITICAL ANALYSIS

INTRODUCTION

The Karkar Site and the Jermaghbyur Site are situated one near the other and encompass a single geological structure with common geothermal potential (Fig. 1.1).

Considering this, to interpret data for Karkar Site it was necessary also to apply the data collected in the past, during geothermal investigations at the Jermaghbyur site.

The process of database construction and critical analysis of the data included the following steps:

- Construction of an interpretation database in 2D and 3D GIS formats to incorporate earlier studies conducted at the Jermaghbyur/Karkar sites.
- Construction of an interpretation database in 2D and 3D GIS formats to incorporate the studies implemented in 2009-2011 in the framework of the *ARMENIA GEOTHERMAL PROJECT GEF Grant # TF: 092563*.
- Correlation and critical analysis of the information provided by the earlier studies and the investigations of 2009 in 2D and 3D GIS format.

1. CONSTRUCTION OF AN INTERPRETATION DATABASE IN 2D AND 3D GIS FORMATS TO INCORPORATE EARLIER STUDIES CONDUCTED AT THE JERMAGHBYUR/KARKAR SITES IN 1988-89 AND 2004.

To perform data interpretation and assess the geothermal potential of the Karkar site, it is extremely important to select the most meaningful and credible data from the earlier studies and construct a GIS database. The following data were selected from the entire bulk of evidence provided by the earlier studies (listed in the order of their importance for further interpretation):

- Results of the magneto-telluric (MT), gravimetric and magnetometric investigations conducted in 2004;
- Results of the seismic and gravimetric investigations conducted in 1988-1989.
- Results provided by the drilling and documentation of Borehole no. 4;
- Results of the structural-geological investigations of 1988-1989 and 2004.

Data from all above-listed studies were digitized and introduced into the GIS database. Considering that the reports with the data of geothermal investigations of 1988-89 and 2004 were prepared in Russian, below we provide the main evidence extracted from them and used to interpret the data from the surveys accomplished in 2009-2011 under individual projects within the *ARMENIA GEOTHERMAL PROJECT GEF Grant # TF: 092563.*

1.1 Results of the MT, gravimetric and magnetometric investigations of 2004

The magneto-telluric sounding at the site of Jermaghbyur was realized in 2004 by «Nord-West», a Moscow-based company, in the framework of the sub-contract signed with the Institute of Geophysics and Engineering Seismology of the NAS of RA (*hereinafter*, IGES). The MT sounding was performed with MTU–5 and MTU-5A equipment («Phoenix Geophysics

Ltd», Canada). The Company surveyed 2 longer and 2 shorter profiles with the total length of 17.7 km, with station spacing ranging from 100 to 400 m. The total number of stations (points) amounted to 172. The geometry of the Jermaghbyur site and disposition of the profiles are shown in Fig. 1.2. Detailed gravimetric and magnetometric measurements were carried out along MT survey Profiles 1 and 2. The data of MT sounding collected along those profiles are of greatest interest and will be used in this interpretation. Fig. 1.3 shows the numbers of MT sounding points, and Figs. 1.4 and 1.5 demonstrate the geo-electrical section along Profiles 1 and 2 for the depths of 2 km and 3-4 km[1]. Fig. 1.6 presents the geo-electrical sections along Profiles 1 and 2 for the depths of 20 km and 10 km.[2]

Five (5) zones are identified according to the results of the MT sounding interpretation presented in the IGES Report (2004).

- **Layer 1 – bedding depth of 0-400 m**. The profile is represented by high-resistance volcanic rocks with resistance values within the first thousands of Ohm-meters (Figs. 1.4 and 1.5). The zone was interpreted as a thermo-insulating shield facilitating accumulation of heat and heat carrier in the geothermal reservoir.

- **Layer 2 –bedding depth of 400-1,200 m.** This is a horizon of abnormally low resistance (40-60 Ohm-m) (Figs. 1.4 and 1.5): the lowest resistance values (up to the first Ohm-meters) and the greatest thickness of Layer 2 are characteristic of the southern part of Profile 1 (points NN 50-58) and the easternmost part of Profile 2 (points NN 28-30). The IGES report (2004) interpreted the low resistance values in these horizons as a presumed effect of saturation of rock fractures and pores with high-temperature, mineralized waters. It was suggested that the water was heated by gas and ascended from great depths.

- **Layer 3 – roof bedding depth of 2,000 – 3,000 m.** Rock resistance increases gradually starting from the absolute elevation of 2,000 m above sea level. The depth of 3 km is marked by a bright geo-electrical boundary representing the roof of the high-resistance base horizon (Figs. 1.4 and 1.5). Two zones of lower resistance are recorded on Profile 1 at depths of 1.5 to 2 km, within sections of Points 21 to 35, and 46 to 56.

It is difficult to determine the boundaries of these anomalies accurately as they are strongly shielded with the higher conductive horizon. These anomalous zones could be spatially coincident with the seismic inhomogeneities identified in 1988.

Layer 4 – bedding depth of 10,000 – 20,000 m. Based on the results of MTS data interpretation, geo-electrical sections were plotted down to the depths of 20 km and 10 km on Profile 1 and Profile 2, respectively (Fig. 1.6). The lower conductive layer located beneath the high-resistance basement is detected at depths of about 20 km. The roof of this layer is raised in the southeast and northeast of the studied area. In the IGES report (2004), the presence of the lower resistance zone within the high-resistance basement at points NN 28-30 of Profile 2 and at points NN 53-58 of Profile 1is interpreted as a sub-vertical conduit for fluids flowing from the upper conductor, and the zone, where the magneto-telluric field is normalized.

The following conclusion was made in the IGES Report (2004):

---

[1]For Profile 2 in Fig. 5, orientation by cardinal points is changed from W-E to E-W. To ensure compatibility of patterns further, Profile N 2 of 2004 and the Profile of 2009 are always oriented so that to give a view from the north to the south.

1. The MT survey data of 2004 detected a zone of spreading of anomalous, low-resistance (40-60 Ohm-meter) horizon around the Jermaghbyur spring. The high conductivity of this zone was presumably related to the presence of mineralized, high-temperature waters. The low-resistance zone has small size (~ 400-500 m in diameter) and is not detected from the depth of ~ 800 m downward.

2. The MT data of 2004 identify two zones of lower resistance at the depths of 1,000 and 1,500 m (Figs. 1.4, 1.5 and 1.7):

   - Zone 1 is sub-latitudinal and intersects with Profile 1 in the region of MTS Points 25-35.
   - Zone 2 is located in the region of MTS Points 47-55 on Profile 1.

3. As per the map included in the IGES report (2004), the greatest dimensions of Zone 1 and Zone 2 might be 2 x 1.2 km and 2 x 1 km, respectively. The IGES report says that resistance values characteristic of those anomaly zones are not as low as in the zone located in the region of the Jermaghbyur Spring (100-1,200 Ohm-m) and are strongly shielded by the upper layer, having higher total conductivity and occurring above.

4. Three-dimensional inhomogeneities of high resistance are identified on Profile 1(Points 37-47) and Profile 2 (points 11-19), which can be interpreted to be intrusive rocks (Fig. 1.8).

5. The lowest resistance values and the greatest thickness of Layer 2 (up to the first ohm-meters) are typical for the southern part of Profile 1 (№№50-58) and the north-eastern part of Profile 2 (NN 28-30). The low rock resistances in these horizons could be presumably related to the saturation of rock pores and fissures with high-temperature saline waters. Apparently, this gas-heated water ascends from great depths (Figs. 1.4, 1.5 and 1.9).

6. At these sites, a sub-vertical conductive zone is detected at depths of 7 to 8 km. In the interval of MT points 27-30 on Profile 2, this zone joins the conductive horizon occurring higher (Figs. 1.6 and 1.10). According to the IGES Report (2004), further research is required to understand the geological nature of the detected anomaly zone better. However, the regular arrangement of volcanic centers of the Karkar group within this zone suggests that it could be related to a magma-conductive channel (fluid conduit) linking the lower (base) geo-electrical horizon (h = 10-25 km) with the volcanogenic sedimentary layer that occurs higher (h = 3 km).

1.2. Results of the seismic and gravimetric studies conducted in 1988-1989

Seismic investigations in the Upper Vorotan area were conducted in 1984-85 along four profiles. Profile locations are shown in Fig. 1.11. However, the disposition of the profiles seems to be questionable. The southeastern flank of Profile PR85/16 traverses Holocene lava flows over a distance of 6 km. In general, terrains of Holocene lava flow are hardly passable, even for a skilled alpinist, and it is difficult to imagine how seismic profile could have been surveyed and a seismic array with sensors arranged across such area. The same comment applies to the southeastern flanks of Profiles PR85/15 and PR85/14. Apparently, like in the case of MT profile geometry in 2004, the actual profile locations in the terrain were generalized and showed in the report as ideally straight lines, without coordinate referencing (Fig. 1.11).

The data of seismic translucence enabled detection of two areas of low-velocity inhomegeneities: one was located in the region of the Jermaghbyur thermal spring, and the other was located in the region of the Karkar volcanic group (Fig. 1.11). These

inhomogeneities occur above the refraction boundary that was identified at the depth of 2.0-2.5 km.

The Jermaghbyur inhomogeneity extends also toward the northwestern flank of the Karkar site and represents an elliptic body located at the depth of about 1,500 m. Horizontally, it measures 2,500-3,500 m across in the southwestern direction and not less than 6,000 m across in the northeastern direction (Figs. 1.11 and 1.12).

The second inhomogeneity is located on the southern flank of the Karkar site and represents a province elongated in the northeastern direction and located at the depth of about 1,800 m (Figs. 1.11 and 1.12). Lateral horizontal dimensions of this body are 3,000-4,000 m in the northwestern and at least 5,000-5,500 m in the northeastern directions.

The identified seismic inhomogeneities both represent bodies, in which velocities are much lower compared to the host medium and their filling matter has higher attenuation factor. The studies of 1989-2004 suggested that according to the seismic characteristics those bodies might represent near-surface magma chambers filled with some substance that had not cooled yet.

Over the sites of Jermaghbyur, Karkar and in neighboring areas, Yanikyan et al. (1988) conducted a detailed gravimetric survey at the scale of 1:50,000. The results of that work are important for the interpretation and development of a conceptual model for the regional geothermal potential.

1.3. Results provided by the drilling and documentation of Borehole no. 4

Borehole N 4 was drilled to a depth of 1 km in the northwestern corner of the Karkar Site in 1988 (Fig. 1.13). The borehole log is shown in Table 1 (IGES Report 2004).
.

Table 1.1

Interval, m	Rock Type
< 17	Alluvium and diluvium, boulder and pebble sediments
17 – 70	Late-Quaternary (Holocene) basaltic andesite, dense and massive, with colors ranging from dark-grey to black
70 – 78	Alluvium and diluvium sediments with debris of different rocks
78 – 123	Middle-Pleistocene basaltic andesite, dark-grey, massive, rarely cavernous
123 – 1000	Quartz monzonite, grey and massive granosyenite

The quartz monzonite and granosyenite rocks cut by the borehole in the interval of 123-1,000 m are of greatest interest for the interpretation. These intrusive rocks have prismatic-grain, hypidiamorphic structure. The mineralogical composition includes plagioclase, common potash feldspar, quartz; the dark-colored minerals are represented by clinopyroxene and biotite. In the leucocratic mineral composition, plagioclase is predominant, and quartz counts for 10-12% of the total mass.

The recovered core (interval from 620 to 865 m) was used to determine the thermal-physical parameters (thermal conductivity, thermal diffusivity, and heat capacity) and the density of the rocks.

The borehole thermal tests were conducted in three cycles at various depths. The results are listed below:
- 99°C at the depth of 920 m measured 2 days later;
- 91.5°C at the depth of 840 m measured 10 days later;

- 58°C at the depth of 550 m measured 4 months later.

According to the data of the IGES report (2004), temperature in the borehole remained the same (about 3°C) downward to the depth of 125 m. Further to the depth of 200 m, the temperature was increasing. As typical for intervals with descending vertical flow of fluids, like in the annular space of the borehole in the considered case, the temperature curve had concave shape (Fig. 1.14).

From the depth of 340-345 m, an inverse pattern was observed downhole, attesting to the presence of an ascending vertical movement of the fluid in the open hole. The thermogram had convex shape typical for such cases (Fig. 1.14).

At the depth of about 200 m, the ascending and descending flows actually mix, bearing evidence of the complex and unique hydro-geological settings of the site. At the depth of 340 m, the borehole cut a water-bearing horizon that was about 20 m thick. Borehole temperature at the level of this horizon was similar to the temperature of Jermaghbyur spring water on the surface.

The log of the borehole interval at depths of 350-840 m is characterized by linear increase of temperature with constant slope of the curve (Fig. 1.14), suggesting that rocks in this interval can be considered as a heat-insulating stratum.

1.4. The results of the structural-geological investigations conducted in 1988-89 and 2004

The Karkar-Jermaghbyur Fault (KJF), striking to the NW, appeared the basic structural unit identified by the investigations conducted at the site in 1988-1989 (Fig. 1.18). The structural and geological investigations of 2004 resulted in the preparation of a fault map for the Jermaghbyur Site (1:25,000), which served the basis for developing "*The Conceptual Model of the Jermaghbyur Geothermal Deposit*" (Report by IGES, 2004) (Figs. 1.15, 1.16, and 1.17). In structural aspect, the conceptual model of the Jermaghbyur site was based on the identification of a "*graben-shaped depression filled with rocks of the Neogene-Paleogene, Cretaceous and possibly Jurassic periods*". The graben-shaped depression was bounded with two pairs of faults striking to the northeast, as shown on the geology map and on the cross-section presented in Figs. 1.15, 1.16 and 1.17.

The faults identified in 1988-89 and 2004 were digitized and entered into the GIS database (Fig. 1.18).

2. CONSTRUCTION OF AN INTERPRETATION DATABASE IN GIS FORMAT BASED ON THE STUDIES REALIZED BY ASSIGNMENTS UNDERTAKEN FOR THE ARMENIA GEOTHERMAL PROJECT GEF Grant # TF: 09256..

To interpret the available information and estimate geothermal potential of the Karkar Site, the Contractor constructed a database, incorporating data collected by the series of projects under Phases 1 and 2 of the ARMENIA GEOTHERMAL PROJECT GEF Grant # TF: 09256 in 2009 and 2011.

The results of the studies listed below were introduced into the GIS database in 2D and 3D formats:

1. Structural-geological and volcanological studies carried out jointly by GEORISK Scientific Research CJS and the South Florida University in 2009.

2. Geochemical investigations carried out by GEORISK Scientific Research CJS and the South Florida University in 2009.
3. 2D MT and TEM surveys carried out by GEORISK Scientific Research CJS and the South Florida University in 2009.
4. Interpretations of the 2D MT and TEM surveys of 2009 года conducted independently by the "Nord-West" Company (Russian Federation), and jointly by GEORISK CJS and the University of South Florida.
5. 3D MT and gravimetry surveys, as well as CO_2 gas surveys conducted by Western Geco (Italy) in 2011.
6. Interpretations of the 3D MT and gravimetry surveys of 2011, realized independently by the Western Geco Company (Italy), and by GEORISK CJS in cooperation with the University of South Florida.

2.1. Results of the structural-geological and volcanological investigations conducted in 2009

Identification of a large structure of *pull-apart basin* type appeared the main outcome of the structural-geological and volcanological investigations conducted by GEORISK CJS in 2009. It bounds the flanks of an aligned system, including Middle-to-Late Pleistocene volcanoes of the Karkar group and many Holocene volcanoes (Fig. 1.19). The *pull-apart* basin originated on the southern flank of the 280 km-long Pambak-Sevan Fault, the most active structure of Armenia. The report of "GEORISK" Scientific Research Company prepared in 2009 provides detailed description of the geometry, kinematics, morphostructural and geological manifestations of this fault, as well as of the features of volcanism at the Karkar site. There is no need to reproduce description of its characteristics here, but it is important to emphasize the details critical for further interpretation of the results and to incorporate them in the database.

By the order of importance for the consequent interpretation, the following findings are selected from the outcome of the study conducted in 2009:

- The Pleistocene and Holocene volcanic activity at the site developed under the settings of intense tension inside the structure of the *pull-apart* basin.
- The faults forming the Karkar *pull-apart* basin, like all other similar structures worldwide, can create a *flower-type structure* at depth. Examples of such structure are shown in Fig. 1.20.
- On the western and eastern flanks of the Karkar *pull-apart* basin, the faults form systems consisting of 8 to 10 juxtaposed sub-parallel branches with helicoidal bends of planes, dipping inside the structure of the *pull-apart* basin (Figs. 1.21 and 1.22). On the surface, areas of the closely-spaced faults and helicoidal bends show up as depressions that could have had volcano-tectonic origin. The bottom of the western Depression D1 (and partly of D2) accommodates small lakes and a swamp (Fig. 1.21), and the eastern depression D3 is filled with water of Lake Sevlich (Fig. 1.22).
- A dome of quartz-rhyolite extrusion is embedded on the western flank of Depression D1, within the zone of the main fault branch (Fig. 1.23). A body of olivine trachybasalts is located to the south and elongates along the main fault scarp. A dome of the same olivine trachybasalts is located inside Depression D1 (Fig. 1.23).

2.2. The results of the 2D MT and TEM surveys conducted in 2009

The MT/TEM investigations of 2009 were conducted with consideration of the evidence collected by the structural-geological scouting and volcanological studies.

The MT/TEM survey was implemented by the staff of the University of South Florida (USA) with participation of GEORISK Scientific Research Company.

The ARMENIA GEOTHERMAL PROJECT intentionally separated the stages of processing and interpretation of the MT survey data. To ensure credibility, the results were interpreted independently by two groups: University of South Florida (USA) and the "Nord-West" Company (Moscow, RF). The Russian company was the same one that carried out the MT survey over the Jermaghbyur site in 2004.

The findings of the interpretations performed by both groups are shown in Fig. 1.24. Despite the scales they used are different, the general patterns derived show good rate of correlation. Further we use the materials of both interpretations jointly for the assessment of the geothermal potential. The evidence of the MT/TEM surveys and their interpretations are included in the reports prepared by GEORISK CJS and "Nord-West" Company.

Our interpretation of all available MT data will be presented in the next sections.

2.3. The results of 3D MT, gravimetric and CO_2 gas surveys of 2011.

The 3D MT, gravimetric as well as CO_2 gas surveys conducted in 2011 were realized with consideration of the findings of the structural-geological studies and 2D MT surveys of 2009, as well as based on the results of their interpretation.

The 3D MT, gravimetric and CO_2 gas surveys were implemented by Western Geco Company (Italy), and the outcome of this study was presented in their report for 2011. The report by Western Geco provided also a brief interpretation of the 3D MT data.

The 3D MT and gravimetry surveys produced important results, and we discuss and interpret them in the following sections of this report. The results of the CO_2 survey have not revealed any anomalies of CO_2 emission, which is consistent with the data collected by GEORISK CJS in 2009, when the methane emission survey also did not detect any anomalies.

3. CORRELATION AND CRITICAL ANALYSIS IN 2D AND 3D GIS FORMATS OF THE STUDIES CONDUCTED IN 1988-89, 2004, 2009 AND 2011

The purpose of this correlation and critical analysis is to determine whether it is possible to apply the available evidence for continued joint interpretation. For this purpose, all data were digitized and entered into the database constructed in GIS format. Four (4) GIS software packages were used, including: *ArcGIS* 9.3, *ArcScene* 9.3, *ArcGlobe* 3D and *Global Mapper* v.10.02. The last three programs permitted presentation and integrated analysis of data in 3D (three-dimensional) format.

The principal bulk of correlated and analyzed data was composed of the results of MT surveys realized in 2004 and 2009, and 2011, and of the information collected by the structural-geological studies of 1988-89, 2004 and 2009.

3.1. Correlation and critical analysis of the MT data collected in 2004, 2009 and 2011.

The compatibility of the MT data from the surveys of 2004, 2009 and 2011, and the feasibility of their combined interpretation to result in a single MT model are extremely important. 2D MT survey profiles in 2004 and 2009 passed through areas of geothermal activity manifestations within the studied terrain, such as the Jermaghbyur spring and Borehole N4. Areas of 3D MT surveys of 2011 encompassed Borehole N4, but did not reach the Jermaghbyur spring. The compatibility of data from all these three MT surveys would render it possible to conduct a complex interpretation and reliability assessment of the derived model for the purposes of evaluation of the geothermal potential at the Karkar site.

Considering this, two independent assessments of the compatibility of the MT surveys of different years have been organized. GEORISK CJS performed one of these assessments applying 2D and 3D GIS software, and the second one was accomplished by Prof. Stewart Sandberg, a renowned geophysicist from the University of South Florida. Both assessments are presented below.

3.1.1. Compatibility assessment for the MT surveys of 2004, 2009 and 2011, applying 2D and 3D GIS software (implemented by GEORISK CJS)

Apart from the factors of structural geology and terrain accessibility, the choice of MT profiles for the survey of 2009 was dictated also by an attempt to make the 2009 MT survey compatible with the 2004 MT data so that to enable consequent integrated interpretation of the two data sets (see Report of GEORISK CJS, 2009). With this purpose, the western flank of the 2009 MT survey profile was laid so that it could fully coincide with Profile 2, surveyed in 2004, over the distance of at least 4 km (Fig. 1.25 or 1.24). Within the section starting from Points 18 (2009) and 08 (2004) and stretching up to Points 7 (2009) and 30 (2004), both profiles run parallel one to another (Fig. 1.24). In our view, the geometry of 2004 MT profiles shown in the IGES Report (2004) was idealized and this can explain the observed slight inconsistency between the profiles of 2009 and 2004. Unfortunately, the IGES report (2004) does not include the coordinates of the MT sounding points, which precludes correlation of the data with higher accuracy.

To improve the quality of integrated interpretation of the 2004 and 2009 MT survey data, in 2009 the profile was oriented across the main geological structures present at the site, including: the Karkar-Jermaghbyur Fault identified in 1988, faults shown on the 2004 map (Figs. 1.18), and faults bounding the *pull-apart* basin and shown in the study of 2009 (Fig. 1.25). With the same purpose of improved interpretative efficiency, the 2009 profile was laid through the area of the Jermaghbyur thermal spring and Borehole no. 4 (Fig. 1.25). The areas covered by the 3D MT survey of 2011 also encompassed the MT profiles of 2004 and 2009, and the location of Borehole N4 (Fig. 1.25).

This approach enabled involvement of the information about the borehole and the Jermaghbyur spring during the interpretation; moreover, this approach created additional capabilities for correlating the datasets of 2004, 2009 and 2011.

Difficulties encountered in the correlation of the MT data of 2004, 2009 and 2011 were caused by the inconsistency of the scales of 2D finite models produced by those studies. However, even with inconsistent scales, the comparison between Profile 2 of 2004 and the 2009 Profile surveyed along the same route demonstrated their full similarity along the entire distance of 3 km from Points 18 (2009) and 08 (2004) to Points 7 (2009) and 30 (2004) (Fig. 1.26). Ii is noteworthy that the 2004 MT data are consistent with both interpretation options –

the one made by the University of South Florida (USA), and the one proposed by the Nord-West group.

At the same depths (of about 500-1,200 m), both profiles distinctly identify the Low Resistance Layer 2 in Fig. 1.26. Besides, the correlation of 3D MT survey data from 2011 with the data collected in 2004 and 2009 also clearly records low-resistance Layer 2 at the depths of 500 – 1000 m in the area of Depression D1 and near Lake Sevlich (Fig. 1.27).

Therefore, the critical analysis of the MT survey data of 2004, 2009 and 2011 indicates their complete compatibility and the possibility of integrated application of these data sets in the joint interpretation as performed in the following sections of this report.

3.1.2. Comparing locations of MT Data Collection from the 2004, 2009, and 2011 MT Surveys (implemented by S. Sandberg)

WesternGeco MT data were collected in 2011. This is the third MT survey in the region that we are aware of, each conducted for the purpose of exploration of potential geothermal resources. MT and audio-magnetotelluric (AMT) data were acquired previously by the Institute of Geophysics and Engineering Seismology (IGES) of the National Academy of Sciences o Armenia, in cooperation with the "Nord-West" Company (Moscow State University). That survey took place in 2004, and their data acquisition was mostly west of the WesternGeco survey area, focusing at the Jermaghbyur hot springs site. A second survey was conducted in 2009 jointly by the GEORISK Scientific Research CJS (Armenia) and University of South Florida (USF). This survey included a traverse from the hot spring area east, through the area surveyed by WesternGeco, a region inferred to be a fault-bounded basin based on geological mapping and structural analysis by staff of the GEORISK. The WesternGeco MT survey, the most detailed to date, consisted of a grid of MT data acquisition across the fault-bounded basin.

The locations of the 2004 MT (and AMT) sites are shown in Figure 1.24. The 2009 GEORISK/ USF MT survey station locations (along with TEM soundings) are shown in Figure 1.29. In order to compare the 2004 and 2009 geophysical surveys, Figure 1.30 shows a map with the positions of sites from both surveys. As can be seen in Figure 1.30, the 2009 geophysical survey overlap the northern portion of the 2004 geophysical survey, and the 2009 data extended much further east.

The geophysical data acquisition positions from the 2011 WesternGeco report are shown co-located with the 2009 MT sites in Figure 1.31.

We note that Dr. Piotr Dlugosz, in his review dated January 4, 2012, emphasized the need to collect data west of the WesternGeco survey area, encompassing the Jermaghbyur hot springs site. We agree that correlation between the WesternGeco survey and the existing hot springs is important. We also add that the data acquired in 2009 by the GEORISK and University of South Florida (USF) does extend to the hot springs, as shown in Figure 1.29. We address the consistency and repeatability of the data from these two surveys in a following section of this report. Nevertheless, it is clear that utility of the 3D modeling performed by WesternGeco would have been greatly enhanced by jointly modeling the 2009 GEORISK/USF data with the data collected by WesternGeco in 2011.

3.1.2.1. Numerical Modeling Used in the MT Survey Interpretations

The 2004 MT survey was modeled and interpreted using 1D models of individual sites, stitched together to form 2D models. The GEORISK/USF 2009 data were modeled using 2D inverse modeling, and the 2011 WesternGeco data were modeled using a full 3D inversion modeling code. This 3D inversion modeling code is state-of the-art, and considered to be perhaps

the best MT modeling code available. The WesternGeco 3D model should provide a more reliable view of the resistivity distribution in the subsurface than was possible using 1D and 2D inverse models. However, the MT data themselves, which are exemplary, indicate that in some parts of the field area 1D and/or 2D modeling may be sufficient. With regard to interpretation of the 2009 survey results, it was noted that in the data pseudosections the TM and TE modes have a lot of similarities, indicating that the profile is largely 1D, which was also indicated by the semi-layering of resistivity in the 2D model. Also, the 10 Hz polar diagrams for the 2009 data become quite circular, also indicating 1D tendency, at least in the shallow subsurface. Although not discussed in the 2009 report, the 10 second polar diagrams (Figure 18 of that report) indicate similarity of orientation for most sites, with the principal axis approximately in the west-northwest direction, supporting the N90E rotation prior to 2D modeling.

In addition, Figure 1.32 shows induction arrows calculated from the 2004 MT data. Note the consistent directions of arrows in the northeastern portion of the map, where the 2009 MT data were collected, and where some of the 2011 WesternGeco data were collected. This indicator of dimensionality also suggests that a 2D modeling approach could be applied in that area with good results. Therefore, MT results suggest that it is reasonable to compare 2D and 3D inversion models based on 2009 and 2011 surveys, respectively, with the caveat that more detailed and very high quality of data collection in 2011 should improve model resolution.

3.1.2.2. Comparison of 3D (WesternGeco, 2011) and 2D (GEORISK/USF, 2009). Inverse Models.

WesternGeco resistivity/depth from the 3D model are presented in two formats in their report. First, a series of 10 cross-sections are presented, as indexed in Figure 1.24 of their report, and reproduced as part of Figure 1.31 above. Figure 1.33 shows these cross-sections in relation to the 2009 MT survey positions. Second, the WesternGeco 3D model is illustrated by depth slices, showing resistivity in map view versus elevation for horizontal slices at 1000, 1500, 2000, 2250, 2500, 2750, and 3000 masl. We begin by comparing cross-sections for the 2D (USF, 2009) and 3D (WesternGeco, 2011) models.

The 2D GEORISK/USF 2009 model is compared with sections WE 1 and WE 3 of the 3D WesternGeco 2011 model. Only these two sections can be readily compared, due to the geometry of the station positions and the orientation of the 2009 2D profile.

3.1.2 3. Section WE 1

Figure 1.34 shows the western portion of 2D Model 3 from the 2009 GEORISK/ USF interpretation. Borehole 4 is also shown, as well as the position of a water bearing interval in that borehole, interpreted from the model. Note the spatial correlation of this water-bearing zone with the low-resistivity zone extending east of the well (the blue/purple region in the model). However, there is a gap between the borehole and that lowest resistivities at this stratigraphic level, of approximately 1500 m.

WesternGeco section WE 1 is shown in Figure 1.35, co-located over the western portion of the 2009 GEORISK/USF model from Figure 1.34. It is important to recognize that the resistivity color scales are opposite; low resistivity on the 2009 model is represented by blue and green, whereas low resistivity on the WesternGeco section is represented by red and yellow. Without obtaining the proprietary software used by WesternGeco to generate these figures, the resistivity anomalies could to be rendered on an equivalent color scale.

In order to compare these two resistivity distributions, Figure 1.36 shows a relatively shallow region of low-resistivity in the 3D model enclosed by a heavy dashed line. In addition,

another heavy dashed line deeper in the section marks where the resistivity of the 3D model increases with depth. Figure 1.37 shows these two interpreted features (heavy dashed lines) transferred onto the 2009 2D model from Figure 1.34. It is evident by comparing Figure 1.36 and Figure 1.37 that the two features are present in both the 2D model and the 3D model. This suggests consistency in location and depth of resistivity anomalies between the two models.

We note there is a discrepancy between the 2D and 3D models involving the lower resistivity contact between stratigraphically higher low resistivity and stratigraphically deeper high resistivity units. This contact is shown by the heavy dashed line on Figures 1.36 and 1.37. In the 3D model, this resistivity contrast is depicted as a linear, east-dipping contact. On the 2D model, this feature is shown as a basement (?) resistivity high, reaching approximately 1500 masl at its shallowest point, but dipping west and east from this point along the profile. By comparison with borehole 4 stratigraphic logs, discussed in detail later in this report, it appears likely that this high resistivity zone correlates with unfractured igneous intrusion, lying beneath fractured igneous intrusion (quartz monzonite). The discrepancy between the 2D and 3D models in this area is caused by extrapolation of the 3D model toward the west, away from the data control of the 2011 survey grid. This results in a shallowing of that interface toward the west as depicted in the 3D model (Figure 1.36). However, the 2D model is based upon 2009 data that extends further west, namely to stations KK01, KK18, KK19, and KK20, thus avoiding the need to extrapolate the model. This result indicates it would have been preferable for WesternGeco to include the 2009 profile data in their 3D model.

3.1.2.4. Section WE 3

The 2009 GEORISK/USF 2D model, including the eastern portion, is shown in Figure 1.38. Shown in Figure 1.39 is the WesternGeco section WE 1 co-located on this 2D model from Figure 10. Again, note the opposite color scales between the 2D and 3D models. Also, Figure 1.39 shows three interpreted features, which are resistivity boundaries in the model, shown by the heavy dashed lines. These three interpreted features are shown directly on the 2D model in Figure 1.40 for comparison. As can be seen in these figures, there is reasonable correspondence between the 2D and 3D models.

We have shown that there is considerable agreement between the 2009 GEORISK/USF 2D MT model, and the 2011 WesternGeco 3D MT model, based upon our cross-sectional analysis. It has already been shown that the 2009 model is in agreement with models derived from the 2004 survey and subsequent 1D modeling. Therefore, we conclude that the WesternGeco model is valid, and in addition, due to the 3D nature of the modeling, which is state-of-the-art, the 3D model of subsurface resistivity more accurately depicts the resistivity distribution than previous works.

3.1.2.5. Other Comments and Analysis Regarding the 3D Model

Referring back to Figure 1.32, and correlating locations of the 2004 MT survey with the 2009 MT survey positions shown in Figure 1.29, and locations of the 2011 MT survey positions shown in Figures 1.30 and 1.33, with relation to the 2009 survey, we can analyze the induction arrows from both 2004 and 2011.

Figure 1.41 shows tipper strike and induction arrows from the WesternGeco report. The region outlined by the red circle from their report is stated as anomalous, and is discussed briefly as an example of multi-dimensionality in the western portion of their survey. However, note that most of these arrows point toward the northeast, indicative of a conductive body toward the southwest. These arrows are computed from 100s data, which has a skin-depth of at

least 15 km for the resistivities in this area. This is consistent with the low-resistivity at depth at the western portion of the 2D model, Figure 1.40. This is another indication that the 2D model may be more accurate in the west, toward the hot springs area.

Figure 1.42 shows resistivity of the 3D model at an elevation of 2000 masl. In addition, the figure shows a low-resistivity zone, labeled Zone B. It appears that this low-resistivity zone has some correlation with a topographic low. Many of the induction arrows shown in Figure 1.32, southwest of Zone B, are pointing away, toward the southwest also providing confirmation that the conductive region, Zone B, is present. The 2004 data were computed at a period of 10s, yielding a skin depth of approximately 10 km, which is consistent with these analyses.

Therefore, we conclude this analysis of the 3D WesternGeco model and its relationship to the 2D GEORISK/ USF model from 2009. As previously stated, the 2004 modeling was shown to be consistent with the 2D GEORISK/ USF model.

3.2. Correlation and critical analysis of the structural-geological investigations of 1988-1989, 2004 and 2009

There have been three structural models proposed for the Karkar Site that can be further interpreted during the assessment of geothermal potential and development of a conceptual model.

The 1988 Model assumes that the Karkar-Jermaghbyur Fault could provide for structural and fluidal links between the Karkar Volcano and the thermal spring of Jermaghbyur (Fig. 1.43). On the left-bank area of the Vorotan River, the Karkar-Jermaghbyur Fault, along with the parallel Vorotan Fault and Sandoukht-Bougour Fault, bounds a NW-striking Neogene-Quaternary depression, which overlies an older Meso-Cenozoic basement (Gabriyelyan et al., 1981, Azizbekyan, 1987).

The IGES 2004 Model assumes that paired NE-striking lineaments L1, L2, L3 and L4 bound a graben-shaped depression striking to the E-NE (Fig. 1.44). Further, it suggests that the NW-striking Karkar-Jermaghbyur Fault traversed the graben-shaped depression obliquely and thus developed a "*regional nodal localization structure of the abyssal heat: the Jermaghbyur and the Karkar anomalies of abyssal heat located along the Karkar-Jermaghbyur Fault striking to the NW-SE and stretching, respectively, along the Bougour and Moukhourtaryan lineament zones of the NE-SW strike*" (end of citation from page 27 of the IGES Report 2004; Fig. 1.44). The conceptual model of the Jermaghbyur site proposed in the IGES Report 2004 was based on this structural model.

The GEORISK-2009 Model implies presence of a large structure of *pull-apart* basin, bounded by the system of active strike-slip faults on the flanks (Fig. 1.45). It suggests that intense tensile stresses appearing inside the structure of the *pull-apart* basin may help to explain development of the Pleistocene and intense Holocene volcanism and could have facilitated establishment of structural settings favorable for origination of a geothermal reservoir (Fig. 1.45).

The comparison of these three models indicates that their basic concepts are conflicting in terms of structure and kinematics, since the faults they are incorporating could not have co-existed within the single stress field (Fig. 1.46). Hence it is not possible to interpret and assess the geothermal potential of the Karkar site using the three structural models concurrently.

Therefore, it is first necessary to estimate the credibility of geological structures identified in each of the three models, then evaluate all structural models as a whole, and, eventually, judge about the credibility of the conceptual models of geothermal reservoir chosen on their basis.

We correlated the credibility of the geological structures identified in the structural models by applying the criteria of manifestation of an identified geological feature:

- in the morphological structure and relief, based on the remote sensing data and DEM analysis;
- in the morphological structure and surface geology, as established by the field work data;
- in deep geological structure, as established by the geophysical studies conducted in 1988-89 and 2004.

3.2.1. Manifestation of the faults in the morphological structure and in the relief based on remote sensing data and analysis of DEM

The following data were applied when analyzing the rate of manifestation of the faults suggested in all three models.

1. Remote sensing materials:
- Satellite images from the systems of Landsat TM and Landsat ET (USA), of various spectral ranges and resolution capacity of 30 m;
- Satellite images from the SPOT system (EU), of various spectral ranges and resolution capacity of 5-10 m;
- *Corona* (USA) satellite images with resolution capacity of 1 m;
- *Quick Bird* (USA) satellite images with resolution capacity of 0.6 m;
- Air photos at the scale of 1:100,000;
- Air photos at the scale of 1: 20,000;
- Air photos at the scale of 1:10,000.

2. Digital elevation models (DEM) with the vertical resolution capacity of:
- 45 m,
- 10 m,
- 5 m.

The listed materials were all (except of the *Corona* images) introduced into GIS and analyzed in 2D and 3D format. The results of the analysis are described below:

The 1988 Model: The Karkar-Jermaghbyur Fault is identified at the Karkar Volcano site only.
The IGES 2004 Model: Lineaments L1, L2, L3 and L4 are identified neither on the satellite imagery, nor on the air photos or digital elevation models.
The GEORISK 2009 Model: All faults of this model are clearly identifiable on the remote sensing materials and many of them are discernible on the digital elevation models with resolution capacity of 10 m and 5 m.

Fig. 1.47 shows the 3D relief model with superposition of an air photo, where red arrows indicate fault routes on the western margin of the *pull-apart* basin structure (GEORISK 2009 Model), and black arrows point to the routes of Lineaments L1 and L2, which, as inferred in the IGES 2004 Model, represent the northwestern boundary of the graben-shaped structure. As one can see in Fig.1.47, Lineaments L1 and L2 in no way manifest themselves on the air photo, in the relief or in morphological structure.

3.2.2. Manifestation of the faults in the morphological structure and surface geology as established by the field work data

The 1988 Model: The Karkar-Jermaghbyur Fault is identified at the site of cinder volcano Karkar. The western half of the Karkar volcano is dislocated by 500-570 m by the right-lateral strike-slip fault (d-e). A flow of basaltic andesite (An) erupted from this zone of dislocation (Figs. 1.47 and 1.48).

The IGES 2004 Model: The field works of 2009 did not identify any signs enabling one to distinguish Lineaments L1, L2, L3 and L4 (Fig. 1.37).

The GEORISK 2009 Model: The field works identified the bounding faults on the western and eastern sides of the *pull-apart* basin with high rate of confidence. The report prepared by GEORISK (2009) provides many examples of morphological structures and geological units dislocated by the faults.

The faults of the western sides of the *pull-apart* basin, demonstrated in Fig. 1.49, displaced the cinder cone by 128 m right-laterally, and threw its eastern half vertically down by 10-15 m. A small basaltic andesite flow was erupted from a lateral fracture that broke through on the northern flank of the lowered eastern side (a in Fig. 1.49). South of this volcano, the system consisting of 8 to 10 juxtaposed sub-parallel fault branches displaced a river and a watershed range with horizontal and vertical offsets amounting to 230-240 m and 24-28 m, respectively (Figs. 1.21, 1.22, and 1.50). Three fault branches are clearly manifested to the south of Depression D1, near the Karkar Volcano. The central branch (Fc) shown in Figs. 1.47, 1.48, and 1.51 displaces flanks *a*, *b* and *c* of an erosion gully by 320 m right-laterally. The *a-b* offset by 220 m is older, while the *b-c* offset by 100 m is younger. The eastern fault branch dislocated the flank of the Karkar Volcano by 130 m, and the western one – by 500-570 m (Figs. 1.47, 1.48, and 1.51). Therefore, the cumulative horizontal offset of the Karkar volcano ranges up to 950-1,000 m.

The faults of the eastern sides of the *pull-apart* basin are also well pronounced in the morphological structure and are easily identified during field inspection. Fig. 1.22 shows Depression D3, which was formed by the system of 8 to 10 faults and filled with Lake Sevlich waters. A large river that flowed across the depression before was dislocated by these faults by 267 m right-laterally. The main fault scarp developed a tectonic dam, dammed the river and formed a dead valley east of the dam (Figs. 1.22 and 1.52).

3.2.3. Manifestation of the faults in deep geological structure as established by the data of geophysical studies of 1988-89, 2004 and 2009

The following data sets were applied to analyze the rate of expression of the faults in the deep geological structure:
- Regional gravimetry map (1:200,000);
- Detailed gravimetry map (1:50,000);
- Profiles of gravimetry and magnetometry surveys carried out by the IGES in 2004;
- 2D MT surveys of 2004 and 2009, and 3D MT survey of 2011.

The regional gravimetry map at the scale of 1:200,000 shows a well-manifested relative minimum of gravity, the southwestern side of which accommodates the Karkar and Jermaghbyur sites (Fig. 1.53). The comparison of the **1988 Model** with this map indicates that the Karkar-Jermaghbyur Fault has the same orientation as the south-western flank of the gravity anomaly (Fig. 1.53).

The **GEORISK 2009 Model** is also well proved by the geometry of the negative gravity anomaly. The configuration of the gravity anomaly elongates southward, similarly to the geometry of the southern flank of the *pull-apart* basin structure (Fig. 1.54).

The **IGES 2004 Model** does not have any confirmation in the pattern of the regional gravity field. Lineaments L1, L2, L3 and L4 all strike to the northeast and are oriented perpendicularly to the northwestern direction of the gravity field isolines (Fig. 1.55).

The **detailed gravity map (scale of 1:50,000)** was prepared by Yanikyan et al. (1988) and is very precise. The locations of measurement points (Fig. 1.56) indicate density of the data and high resolution capability of the map. The correlation of the regional map (1:200,000) and the detailed map (1:50,000) demonstrates high rate of compatibility (Fig. 1.57). The detailed map also bears evidence of a clearly manifested relative minimum of gravity anomaly, stretched in the north-northwestern direction, with the Karkar and Jermaghbyur sites located on its western flank (Fig. 1.57).

Like in the case of the regional map, the **1988 Model** demonstrates that the Karkar-Jermaghbyur Fault fits quite well into the pattern of the detailed gravimetry map (Fig. 1.58).

The **GEORISK 2009 Model** shows good coherence of geometries of the western and eastern branches of the faults bounding the *pull-apart* basin, and the geometry of the gravity anomaly. The most distinct feature is that the *pull-apart* basin structure and the gravity anomaly both are closing up in the south (Fig. 1.59)

Like the regional data, the 1:50 000 gravity survey does not support **IGES 2004 Model** in any way (Fig. 1.60). Lineaments L1, L2, L3 and L4 are oriented perpendicularly to the isolines of the gravity field.

3.2.4. Profile gravimetry and magnetometry surveys carried out by the IGES in 2004

In 2004, the IGES implemented the gravimetry and magnetometry surveys along Profiles 1 and 2 of the MT survey (Figs. 1.2, 1.3, and 1.18). Profile 1 run across the Karkar-Jermaghbyur Fault and Lineaments L1, L2 and L3; Profile 2 cut through Lineaments L1 and L2, the Karkar-Jermaghbyur Fault and the active faults traversing Depression D1 (Figs. 1.18, and 1.25). Therefore, as these profiles cross the main faults included in all of the three structural models, it should be possible to analyze whether the faults are reflected in any gravity or magnetic field anomalies. Fig. 1,61a, b shows data for Profiles 1 and 2, where arrows indicate faults identified in the three models.

The analysis of the curves depicting changes of the gravity and magnetic fields indicates single anomaly of the gravity field at the site of 6.5-8.5 km on Profile 1 and the coincidence of this anomaly with Lineament L3 at the point of 8.5 km. In the meantime, the section of 6.5-8.5 km corresponds to the area, where Profile 1 runs at the distance of 150-200 m from, and parallel to, the displaced part of the Karkar Volcano, which produced eruption of the basaltic andesite lava flow. Therefore, it is very difficult to judge whether the gravity anomaly reflects Lineament L3 or the Karkar-Jermaghbyur Fault or it must be related to the ejection vent of basaltic andesite lava.

Gravity and magnetic field anomalies are distinguished clearly within the section of 3 – 4.5 km of Profile 2, where the latter traverses depression D1, which accommodates the system of active strike-slip faults shown in the GEORISK 2009 Model.

Therefore, the analysis of geophysical profiles surveyed by the IGES in 2004 indicates that the gravity and magnetic anomalies are highly coherent with the faults considered in the GEORISK 2009 Model. With certain reservation, one case of coincidence is established for Lineament L3 from the IGES Model.

The layout of faults provided in the IGES Report (2004) includes also the ten faults identified during the profile gravimetric survey (1-10 in Figs. 1.18, and 1.25) and the two faults identified by geological evidence (1.11 and 1.12 in Figs. 1.18 and 1.25). As far as these faults are not described in the text of the IGES Report (2004) and were not used for the development of the structural and conceptual models, we will not consider them during our analysis.

3.2.5. Data of the 2D MT survey of 2004

The 2D finite models based on the MT survey of Profile 1 in 2004 show two faults – one at measurement point 22 (depth of 4 km) or point 26 (depth of 2 km), and one at the site of measurement point 35 for both of these depths (Fig. 1.4). The first fault shown on the section of the MT profile between Points 22 and 26 might correspond to Lineament L2, and the second one (Point 35) does not match any of the faults considered by the three models.

The sub-vertical conduit zone identified within Profile 2 (Points 27 to 30) and Profile 1 (points 55 to 58) may be the most important anomaly detected by the MT survey in 2004. The IGES Report (2004) interpreted this zone as magma (fluid) conduit. It corresponds exactly to the area of active faults bounding the *pull-apart* basin in the west, as considered by the GEORISK 2009 Model (Fig. 1.62).

The following section presents correlation with the MT survey data of 2009 and the 3D MT survey of 2011.

The analysis of fault manifestations in geophysical fields leads us to the following conclusions:
- The faults considered by the **GEORISK 2009 Model** are quite well manifested on both the regional (1:200,000), and detailed (1:50,000) gravimetric maps. Within Depression D1, these faults are clearly expressed in the data of the gravimetric and magnetometric surveys of 2004 and the MT survey (2004).
- Although to a considerably lesser extent, the Karkar-Jermaghbyur fault (**1988 Model**) has manifested itself in all types of data mentioned above.
- Lineaments shown in **Model IGES 2004** are almost not reflected in the geophysical fields.

Based on these observations, we suggest that the faults included in the GEORISK 2009 Model could reflect elements of deep geological structure. The interpretation of the deep structure will be provided in the following sections of this report.

Table 1 demonstrates the comparison and estimated credibility weights assigned to the faults that served the framework for the structural models developed in 1988, 2004, and 2009. This correlation applies the same three criteria that were used to assess the credibility of the faults considered by the models, namely, rates of fault manifestation:
- in the morphological structure and relief (based on the remote sensing data and DEM);
- in the morphological structure and surface geology (based on field work evidence);
- in the deep geological structure (based on the data of geophysical studies of 1988-89 and 2004).

The integrity of evidence presented in paragraphs 4.2.1–4.2.5 and summarized in Table 1 indicates that the identification of faults according to the structural model IGES 2004 is of

low confidence. The same evidence supports the model of GEORISK 2009 and the Karkar-Jermaghbyur Fault considered in the 1988 Model.

3.2.6. Correlation and critical analysis of the structural models of 1988 and 2004

The Model of 1988 assumed that the Karkar-Jermaghbyur Fault could provide for the structural link and fluid conductivity between the Karkar Volcano and the thermal spring of Jermaghbyur. At present, there is neither any evidence that such link exists, nor any explanation of the structural control and specific layout of geothermal reservoirs or fluid channels in the zone of the Karkar-Jermaghbyur Fault. On the other hand, such possibility is not in contradiction with the geophysical evidence available today. Meanwhile the existing geological data inspire with less optimism in case of the 1988 Model. The Karkar-Jermaghbyur Fault has a length of just 9–10 km: this is too short a length for a fault, providing structural and fluid control of a geothermal resource. According to the 1988 Model, the Karkar-Jermaghbyur and other faults are bounding a NW-striking depression of Neogene-Quaternary age located on the left-bank of the Vorotan River. However, the model does not interpret how this depression would control a geothermal resource.

Table 1: Credibility weights assigned to the faults identified within the Karkar Site in the Models of 1988, IGES 2004 and GEORISK 2009

Model	Fault name	Data Used to Identify a Fault and Estimated Rate of Credibility:						Final Estimated Weight
		DEM and RS	Surface geological manifestation	1:50,000 gravimetric data (Yanikyan, 1988)	MT data of 2004	Magnetometric data of 2004 (Figs. 5.1 and 5.2)	Gravimetric data of 2004 (Figs 4.5 and 6.4)	
Model 1988	KJF Karkar-Jermaghbyur Fault	At the Karkar Volcano site only	At the Karkar Volcano site only	Not credibly, but probably **less than 50%**	MT Points 2.07 and 1.17 -1.14	Not credibly, less than 20%	Segment of 6.5– 8.5 km on Profile 1	**70%** / **Less than 50%**
IGES 2004	L1 Lineament 1	Not credibly, less than 20%	Not credibly, less than 20%	Not credibly, less than 20%	MT Points 2.02; 1.17, 3.03, 4.01	Segment of 2.3 km on Profile 1 / Segment of 0.3 km on Profile 2	Segment of 2.3 km on Profile 1 / Segment of 3 km on Profile 2	**Not credibly, less than 20%**
	L2 Lineament 2	Not credibly, less than 20%	Not credibly, less than 20%	Not credibly, less than 20%	MT Points 2.09, 1.26, 3.07, 4.03	Segment of 3.1 km on Profile 1 / Segment of 1.5 km on Profile 2	Segment of 3.1 km on Profile 1 / Segment of 1.5 km on Profile.2	**Not credibly, less than 20%**
	L3 Lineament 3	Not credibly, less than 20%	Not credibly, less than 20%	Not credibly, less than 20%	MT Points 21.57	Segment of 8.5 km on Profile 1	Segment of 8.5 km on Profile 1	**Not credibly, less than 20%**
	L4 Lineament 4	Not credibly, less than 20%	Not credibly, less than 20%	Not credibly, less than20%	NO DATA	NO DATA	NO DATA	**Not credibly, less than 20%**
GEORISK 2009	Western branch of the Karkar *pull-apart* basin	With high credibility - 100%	With high credibility - 100%	With high credibility - 100%	With high credibility - 100%	With high credibility - 100%	With high credibility - 100%	**With high credibility - 100%**
	Eastern branch of the Karkar *pull-apart* basin	With high credibility - 100%	With high credibility - 100%	With high credibility - 100%	NO DATA	NO DATA	NO DATA	**With high credibility - 100%**

Weight Estimates

A	Highly credible (identified with high confidence)	100%
B	Credible (identified with confidence)	70%
C	Low credible, but still possible (identified with little confidence, but not to be ruled out)	Less than 50%
D	Not credible (unconfident)	Less than 20%

The IGES 2004 Model. The structural concept of this model was based on the identification of "*the regional nodal localization structure of abyssal heat: the Jermaghbyur and Karkar abyssal heat anomalies located along the NW-SE-striking Karkar-Jermaghbyur Fault and stretched, respectively, along the Bougour and Moukhourtaryan lineament zones striking to the NE-SW, which bear evidence of a potential graben-shaped block bounded by the mentioned lineament zones and by the fault, and also by an inferred fault on the NE, presumably developed in the watershed part of the Vorotan-Akera River, on the strip of crustal basement uplift*" (end of citation from pages 27 and 28 , IGES Report, 2004).

The wording of the statement cited above seems to be poor in geological sense and difficult to apprehend. Hence we will try to construe its meaning in more clear form and to analyze how credible it could be.

The structural concept proposed by the IGES 2004 Model could be described by a few inter-related statements.

1. The Jermaghbyur and Karkar anomalies of abyssal heat are located along the Karkar-Jermaghbyur Fault striking to the northwest.
2. The Jermaghbyur and Karkar anomalies of abyssal heat are stretching along the NE-striking Bougour and Moukhourtaryan lineament zones.
3. The lineament zones, striking to the NE, border the graben, which accommodates the mentioned abyssal heat anomalies of Jermaghbyur and Karkar, being linked together with the Karkar-Jermaghbyur Fault oriented transversely to the graben.
4. The intersection of the NE-striking graben with the Karkar-Jermaghbyur Fault striking to the NW is interpreted as *"the regional nodal localization structure."*

Below we consider and analyze the 4 principal statements laid in the framework of the structural concept proposed in IGES Model 2004.

Statement 1 - The Jermaghbyur and Karkar anomalies of abyssal heat are located along the Karkar-Jermaghbyur Fault striking to the northwest.

This statement seems to be a replica of the 1988 Model**.** The only, although vague, difference from the Model of 1988 is recognition of the Jermaghbyur and Karkar abyssal heat anomalies. The text of the IGES Report (2004) does not contain any description of data used to support the identification, or understand the nature of these anomalies. We may just suppose that "*abyssal heat anomalies*" were meant to understand the two seismic anomalies identified in 1988 and, possibly, the two highly conductive zones identified based on the MT survey in 2004. Whatever was actually meant, there is no evidence to prove that the identified seismic or magneto-telluric anomalies could represent anomalies of abyssal heat. Hence, this inference is nothing but a hypothesis.

Statement 2 - The Jermaghbyur and Karkar anomalies of abyssal heat are stretching along the NE-striking Bougour and Moukhourtaryan lineament zones (L1, L2, L3 and L4).

The IGES Report (2004) neither explains, nor documents the identification of the NE-striking Lineaments L1, L2, L3 and L4, but refers to the study [51] that should have described this. The mentioned reference [51] is the study by Hamlet Toumanian published in the *Investigation of the Earth from Space* journal in 1983. Unfortunately, the study had regional context and lacked any specific description of the identified lineaments likewise. Fig. 1.63 reproduces the map from Toumanyan (1983), which clearly shows just three of the four

lineaments (highlighted by us as L1, L2 and L3). Two important circumstances must be mentioned before we proceed to analyzing Statement 2 from the IGES 2004 Model.

1. After remote sensing information became available in the 1970-s, lineaments have been identified and discussed in many scientific works. Since then, the evolution of the term *lineament,* suggested by Hobbs as early as in 1915, gained a new impetus. *Lineament* has been always meant to understand a linear anomaly identified on satellite images, which does not necessarily correspond to a fault or any other unit of geological structure. Lineaments identified on satellite images could be ranked geological structures only after being mapped in field.

2. Toumanyan (1983) indicates that he identified the lineaments by analyzing images taken from *Meteor* and *ERTS* satellites and *SOYUZ* spacecrafts. The photos made by the mentioned space objects late in the 1970's and early in the 1980's have resolution capacity ranging from 1 km (*Meteor*) to a few hundreds of meters (*ERTS, SOYUZ*). Therefore, analysis of those satellite images could help to identify structures that were more than 1 km wide only. In the IGES Report of 2004 (pp. 27-28), Toumanyan comments: *"The mentioned lineaments correspond to fault zones that developed over a width of 0.7-1.3 km, concealed under the lava flow (N2-Q)."* Apparently this means that the lineaments represent surface reflection of faults concealed beneath the Neogene-Quaternary lavas.

In Sections 4.2.1 and 4.2.2 and Table 1 of this report, we demonstrate that presence of the lineaments (L1, L2, L3, L4) striking to the northeast is not confirmed even by the most advanced satellite images, providing resolution in the range from 30 m to 1 m and 0.6 m, or modern analytical tools offered by GIS technology. Any manifestation of the lineaments in the surface morphological structure and geology is not confirmed either.

Therefore, the lineaments identified on the meteorological satellite images with resolution of 0.7-1 km by the regional-context studies as early as 25 years ago cannot be considered a sufficient and justified basis to construct a 1:25,000 structural model intended for the practical goal of geothermal resource assessment.

Statement 3 - The lineament zones, striking to the NE, bound the graben, which accommodates the mentioned abyssal heat anomalies of Jermaghbyur and Karkar, linked together with the Karkar-Jermaghbyur Fault that is oriented transversely to the graben.

This is the fundamental statement of the structural Model IGES 2004. It was incorporated in the conclusion and recommendations of the IGES Report (2004) and became the framework for development of the conceptual model of the Jermaghbyur geothermal deposit (Fig. 1.15).

The statement can be construed as follows. The NE-striking lineaments correspond to normal faults that caused offsets of the Paleogene, Cretaceous, and Jurassic rocks and even of the crystalline basement, and shaped a graben at a depth of 5 to 6 km beneath the Karkar-Jermaghbyur sites. This is mentioned in the text of the report, and demonstrated on the geological section prepared by Toumanyan (see Fig. 1.17).

This strange and abrupt change from the lineaments to the 6 km-deep graben ought to be explained and proved. However, the IGES Report (2004) does not offer any proof. Moreover, the only 1 km-deep borehole drilled in the region of the Karkar-Jermaghbyur cut nothing but an intrusion, therefore geological section reproduced in Fig. 1.17 looks strange. The source of the detailed classification shown in this section with indications of sedimentary rocks of the Jurassic and Cretaceous ages, as well as of the stratigraphy units, their stages and thicknesses, remains unknown as this is not commented in the text of the report. The only comment is

found in the legend accompanying the section in Fig. 1.17, saying that the layers and their thicknesses were identified based on the general density characteristics and also by the MT and RWCM [Refracted Wave Correlation] data. No more details are provided. Such explanation lacks justification required for the preparation of a geological section like the one presented in Fig. 1.17.

However, this is not the main problem with the section shown in Fig. 1.17 and with the entire structure of the northeastern graben suggested in the IGES Model 2004.

According to the section in Fig. 1.17, the two pairs of lineaments - L1 and L2 in the north and L3 and L4 in the south - shape the graben that dislocated the crystalline basement by 5 km (Fig. 1.17). Along with this, the crystalline basement occurs about 1 km deep on both sides of the graben and 6 km deep in its center (Fig. 1.17).

The maps of gravity field anomalies of both the regional (1:200,000) and detailed (1:50,000) scales should have necessarily reflected a graben structure with crystalline basement displacements of this size. Meanwhile, the mentioned maps contain nothing that could suggest the presence of such graben; below we will bring forward the three main arguments to support our statement.

1. The crystalline basement is composed of rocks that reflect in a strong contrast of the gravity field. In Armenia, these rocks are always reflected as relative positive anomalies of gravity. In the meantime, areas around the sites of Jermaghbyur and Karkar are characterized by well-pronounced regional anomaly of negative gravity (Figs. 1.53-1.60).

2. The NE-oriented graben with 5 km large-displacements of the crystalline basement on both sides should have been reflected in the configuration and in the values of gravity field anomaly isolines on both the regional and detailed maps. Meanwhile, both gravimetric maps demonstrate that the isolines are oriented to the north-northwest, transverse to the orientation of the supposed graben, and do not suggest 5 km large vertical displacements on its sides (Figs. 1.53-1.60).

3. Even assuming that contrasting rocks of the crystalline basement do not exist in the base of the graben, such deep structure should have anyway expressed itself in the regional and detailed maps of the gravity fields, and on the profile gravimetric, magnetometric and MT surveys conducted by the IGES in 2004. Evidence presented in paragraphs 4.2.3, 4.2.4 and 4.2.5 and Table 1 of this report demonstrates that the listed research materials do not indicate any signs of presence of a NE-striking graben.

Statement 4 - **The intersection of the NE-striking graben with the Karkar-Jermaghbyur Fault striking to the NW is interpreted as *"the regional nodal localization structure."***

There is little to comment on such statement. It represents a combination of the *lineament nodes* theory suggested by Hobbs in 1915 and the presumed, yet not proved presence of the graben.

Therefore, the structural Model IGES 2004, as well as the faults it was based on, are not confirmed by the evidence of:
- Remote sensing;
- Morphology and surface geology structure;
- Geophysics and deep geological structure.

Hence, such structural model can not be considered a sound basis for the conceptual model of the geothermal deposit of Jermaghbyur developed by the IGES. The conceptual model suggested by the IGES raises many other questions. Fig. 1.64 reproduces the gravity model (a) and the density model (b) built along Profile 1 and shown together in Fig. 4.6 of the IGES

Report (2004). Fig. 1.64c reproduces Fig. 4.7 from the IGES Report (2004), also named as "density model on Profile 1," while Fig. 1.64d demonstrates the final conceptual model built again along Profile 1 and based on all preceding data.

The observed inconsistency between the gravity model (Fig. 1.64a) and the density model created on its basis (Fig. 1.64b) on one hand, and the density model shown in Fig. 1.64c along with the conceptual model (1.64d), on the other hand, is unexplainable. It determines internal conflict and does not allow us to consider the conceptual model of IGES credible.

Fig. 1.1: The Karkar-1 Site and Jermaghbyur-2 Site
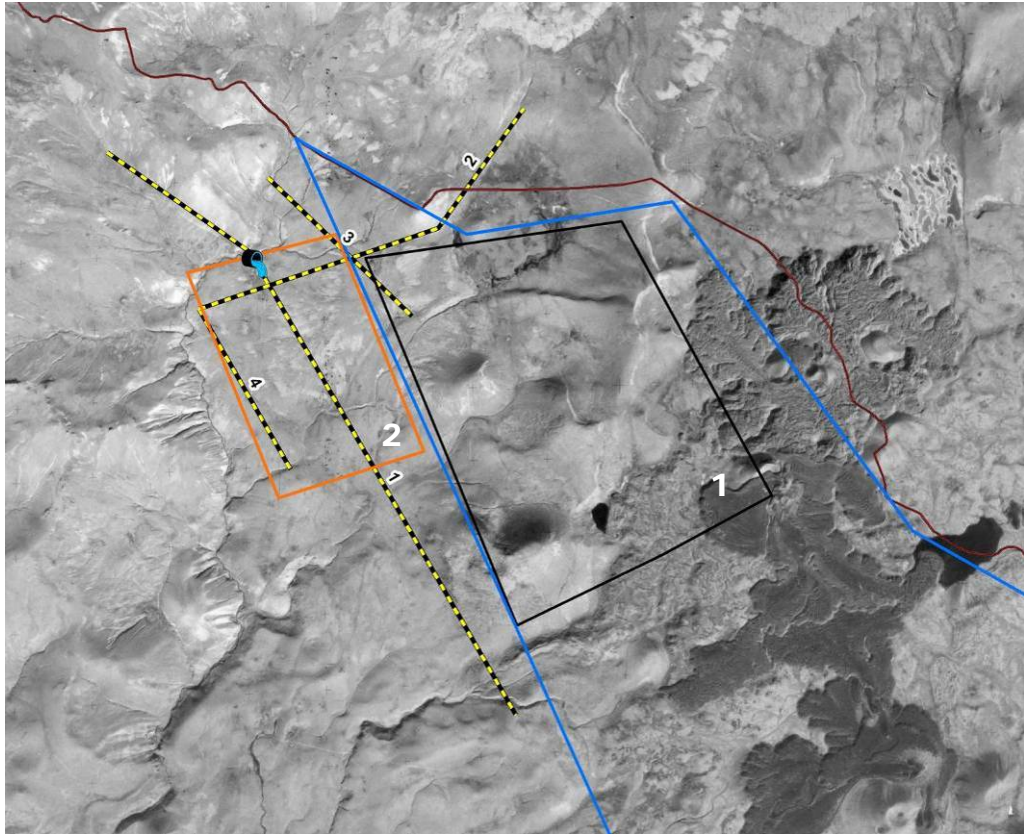
Fig.1. 2: The geometry of the Jermaghbyur site and layout of MT profiles during the survey of 2004
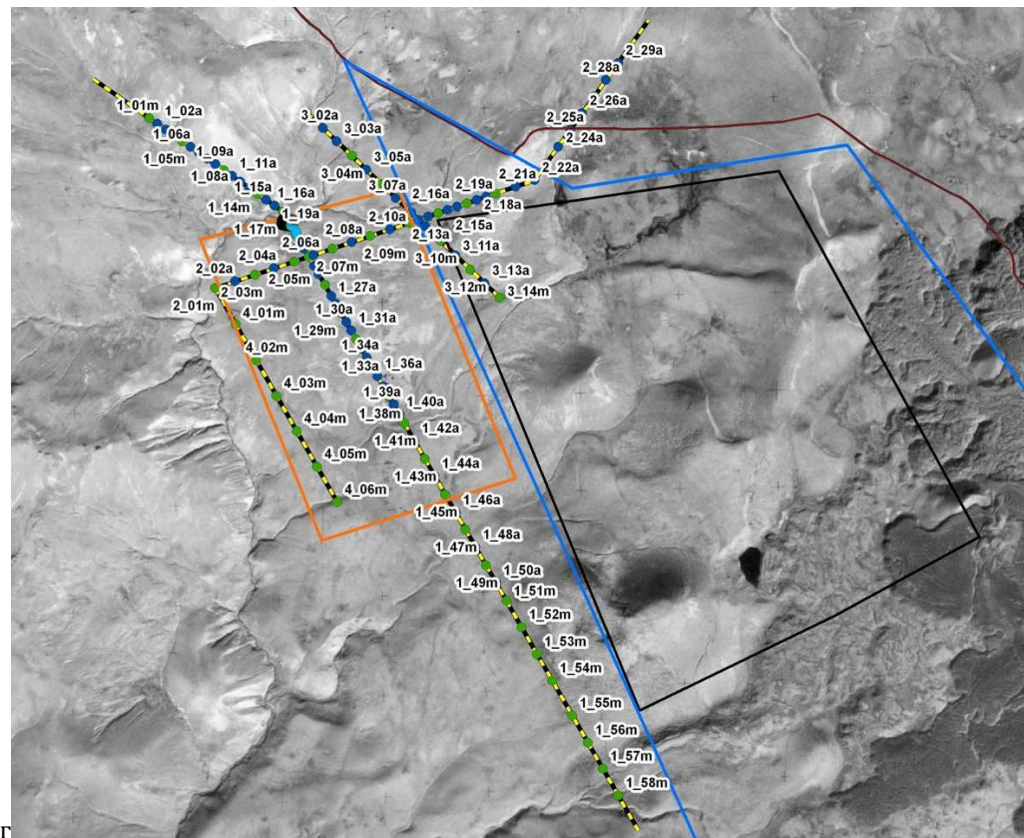
Fig. 1.3: Numbers of MT sounding points during the survey of 2004.
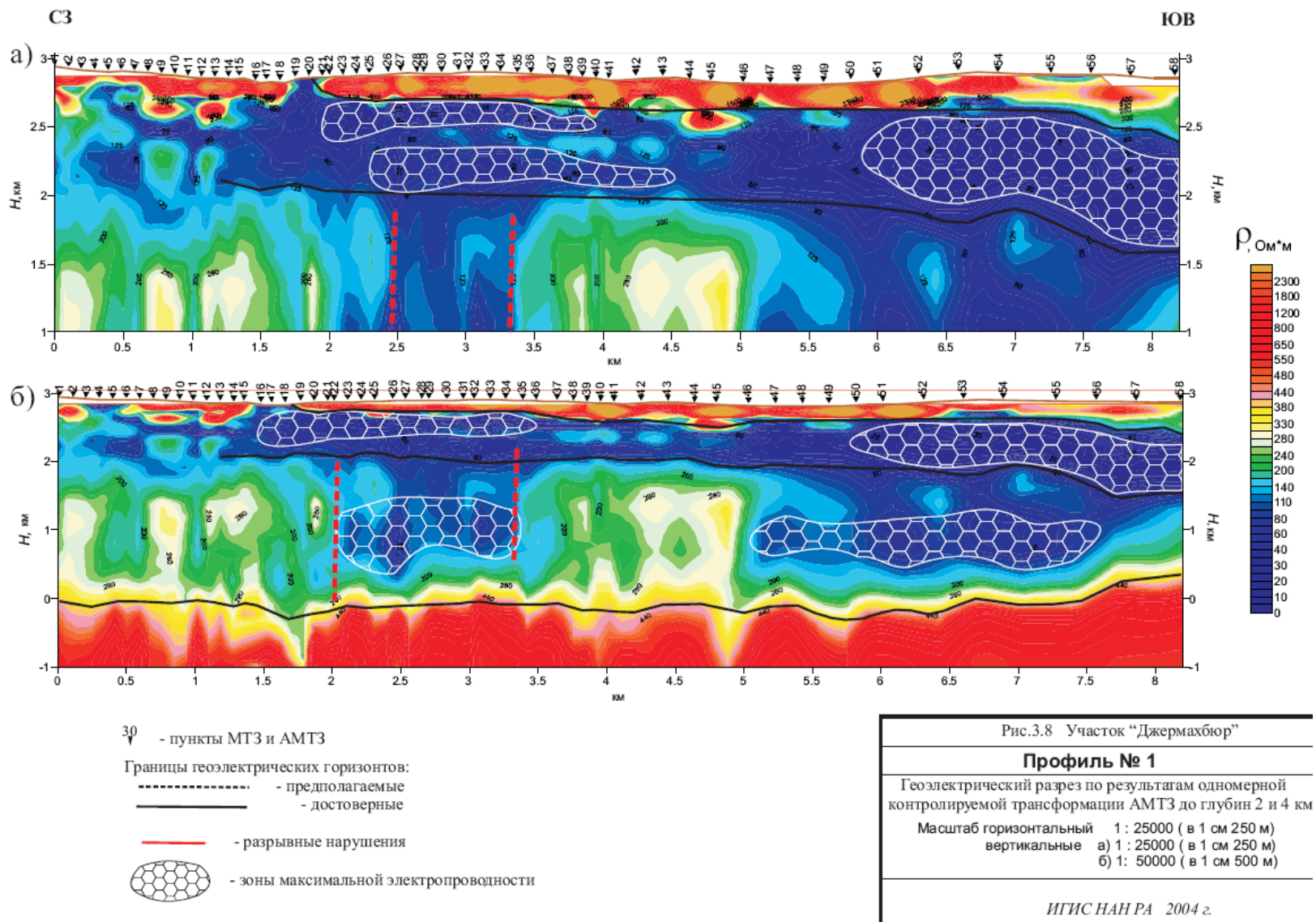
Fig. 1.4: Geo-electrical sections along Profile 1 for the depths of 2 km and 4 km surveyed in 2004

Fig. 1.5: Geo-electrical section along Profile 2 for the depth of 3 km surveyed in 2004
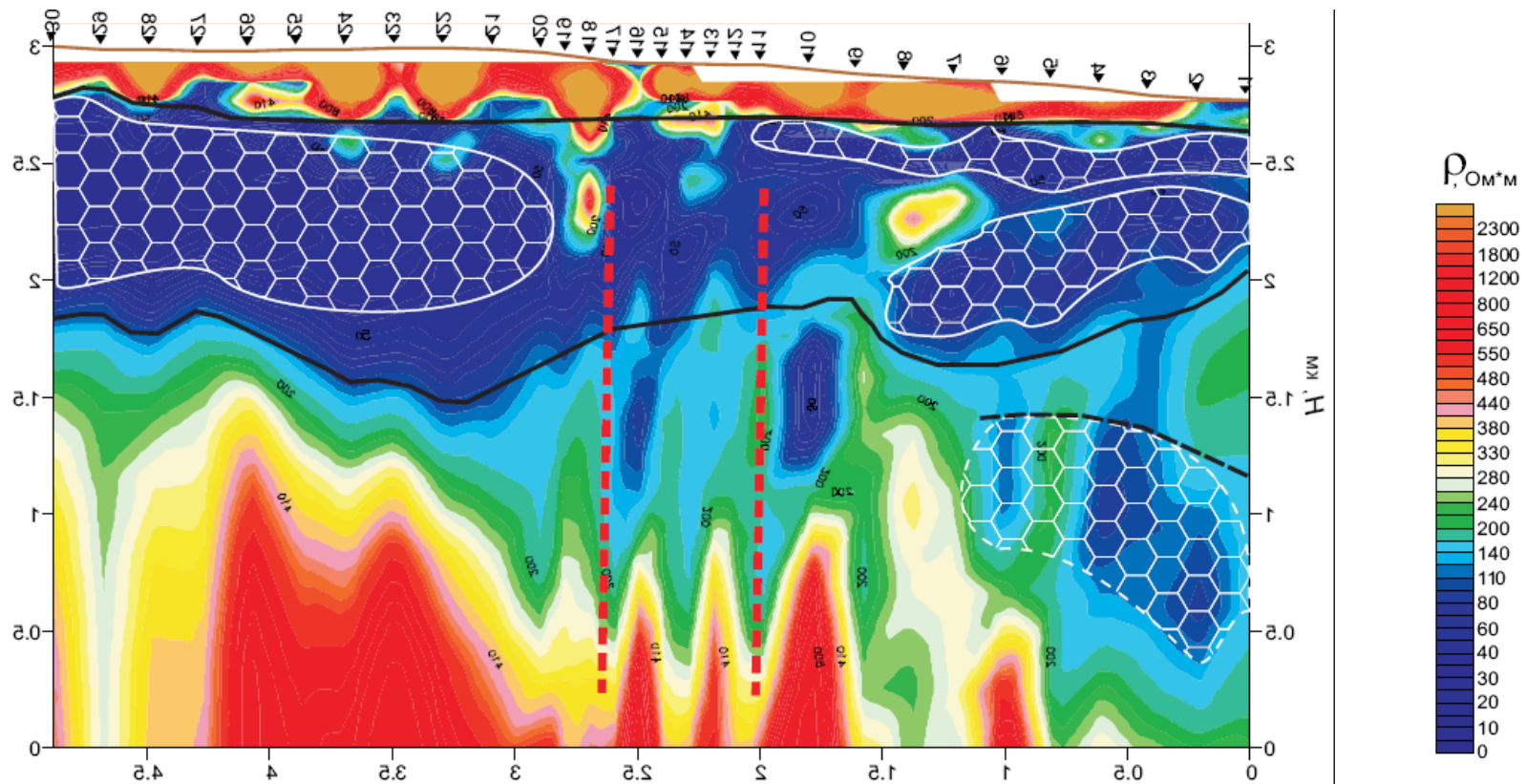
$30\atop\triangledown$ - пункты МТЗ и АМТЗ

Границы геоэлектрических горизонтов:

------------------- - предполагаемые

—————— - достоверные

—————— - предполагаемые разрывные нарушения

- зоны максимальной электропроводности

ρ, Ом*м

Рис. 3.9   Участок "Джермахбюр"

Профиль № 2

Геоэлектрический разрез по результатам одномерной контролируемой трансформации до глубин 2 и 4 км

Масштаб горизонтальный   1 : 25000 (в 1 см 250 м)
вертикальные   а) 1 : 25000 (в 1 см 250 м)

ИГИС НАН РА   2004 г.

Fig. 1. 6: Geo-electrical section along Profiles 1 and 2 for the depths of 10 km and 20 km surveyed in 2004

Fig. 1.7: Zones of low resistance of rocks – areas promising as deposits of hydrothermal waters according to the IGES (2004)
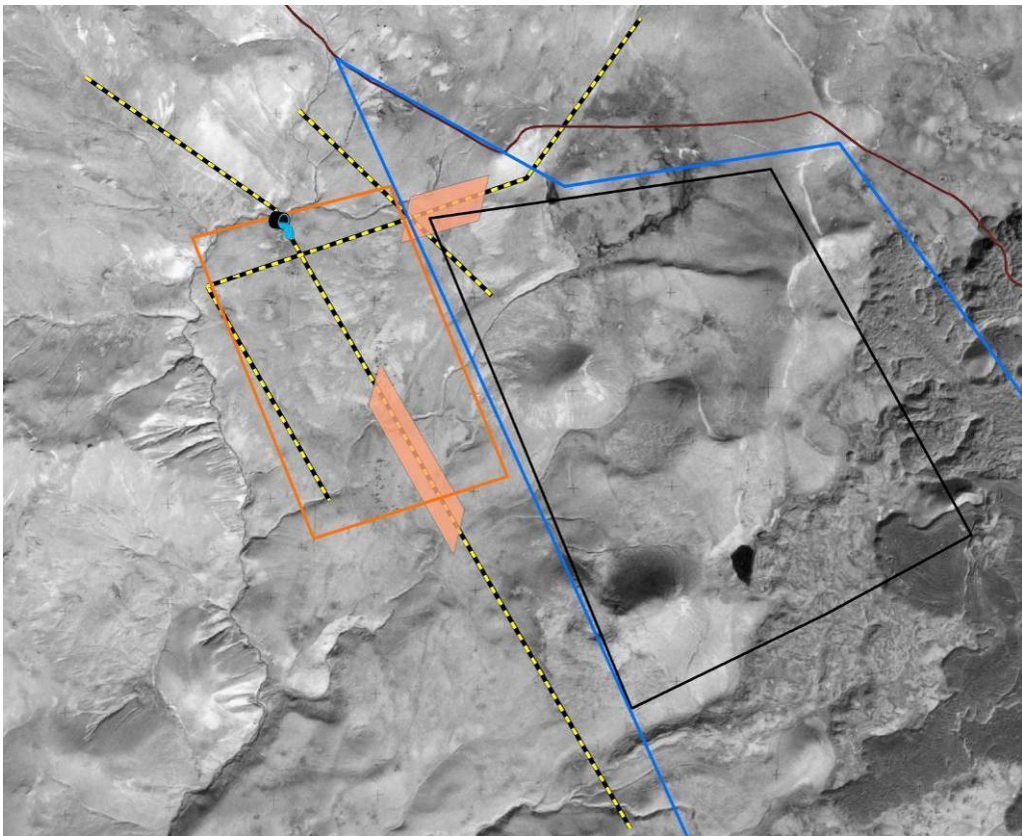
Fig. 1.8: Locations of potential presence of intrusive rocks according to the IGES (2004).
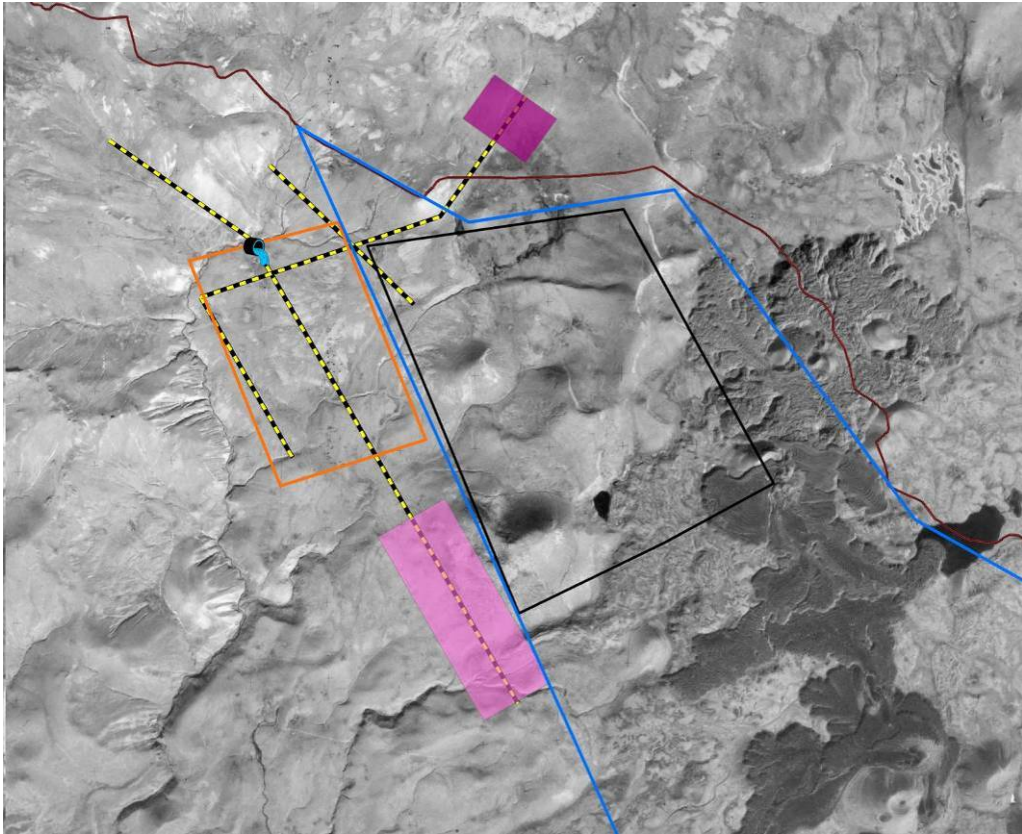
Fig. 1.9: The lowest values of rock resistance according to the IGES (2004)
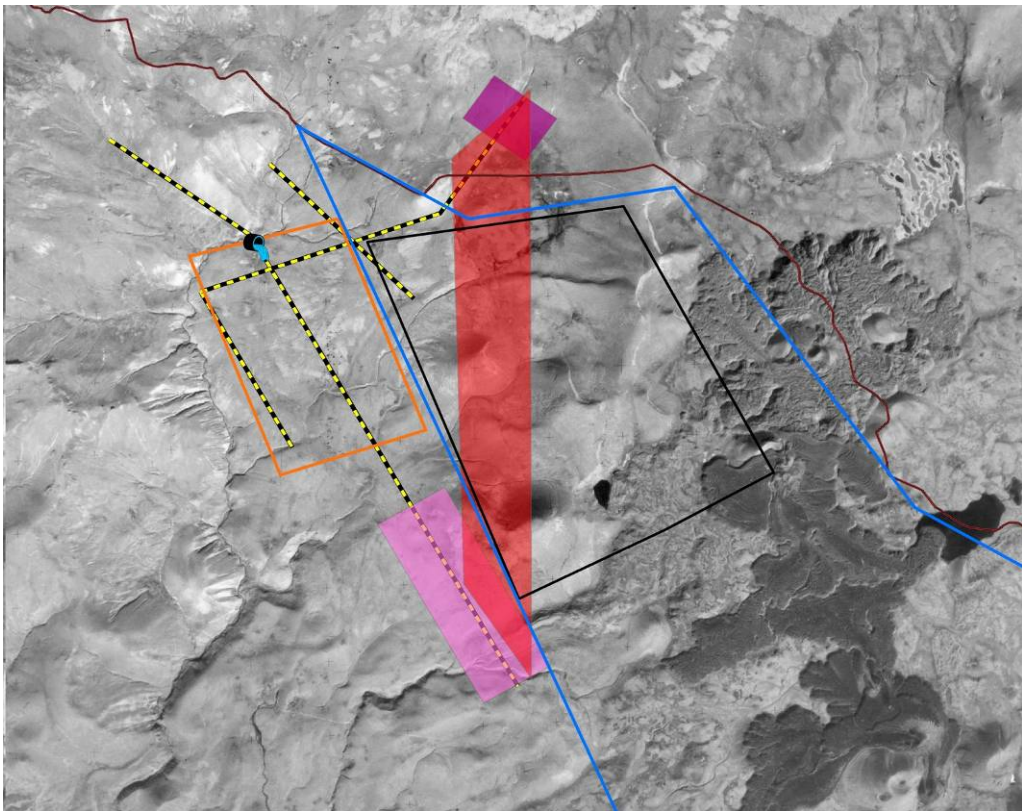
Fig. 1.10: Potential deep conductive zone according to the IGES (2004)
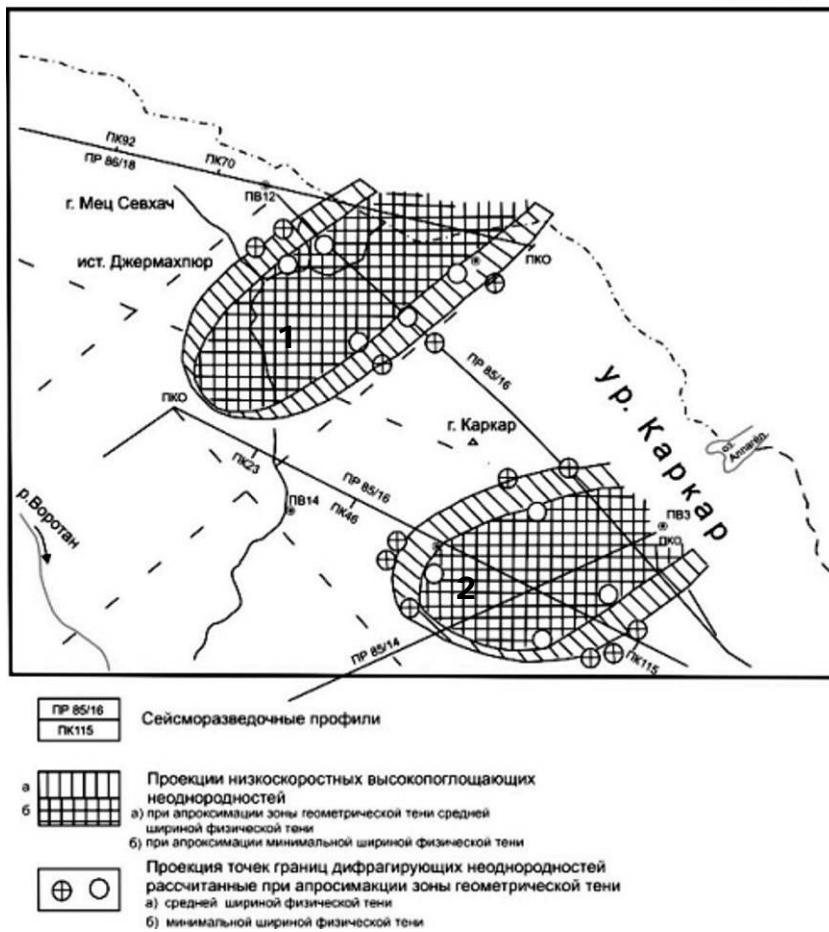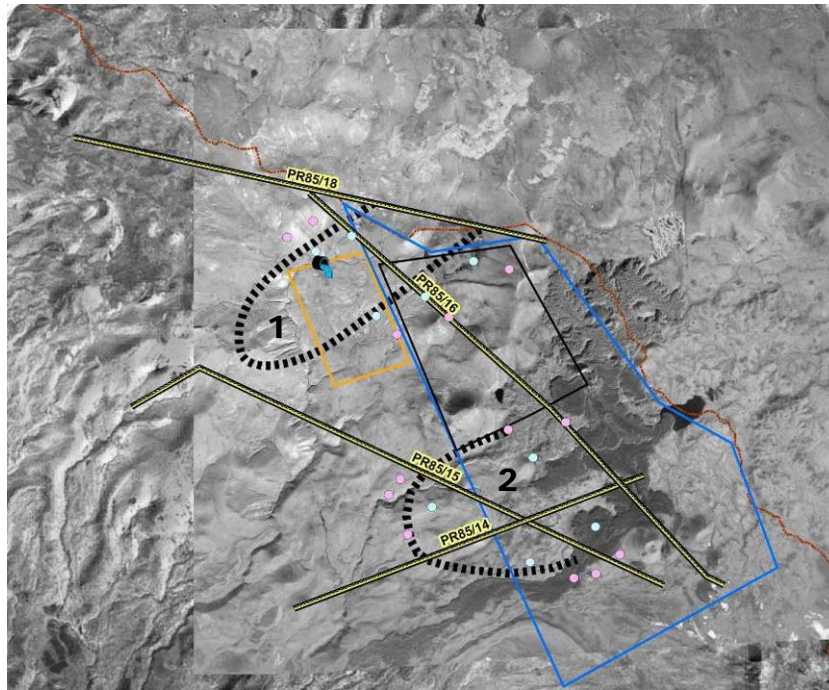
Fig. 1.11: Low-velocity seismic inhomogeneities identified in 1987/88:
1- in the region of the Jermaghbyur thermal spring, 2– in the region of the Karkar group of volcanoes
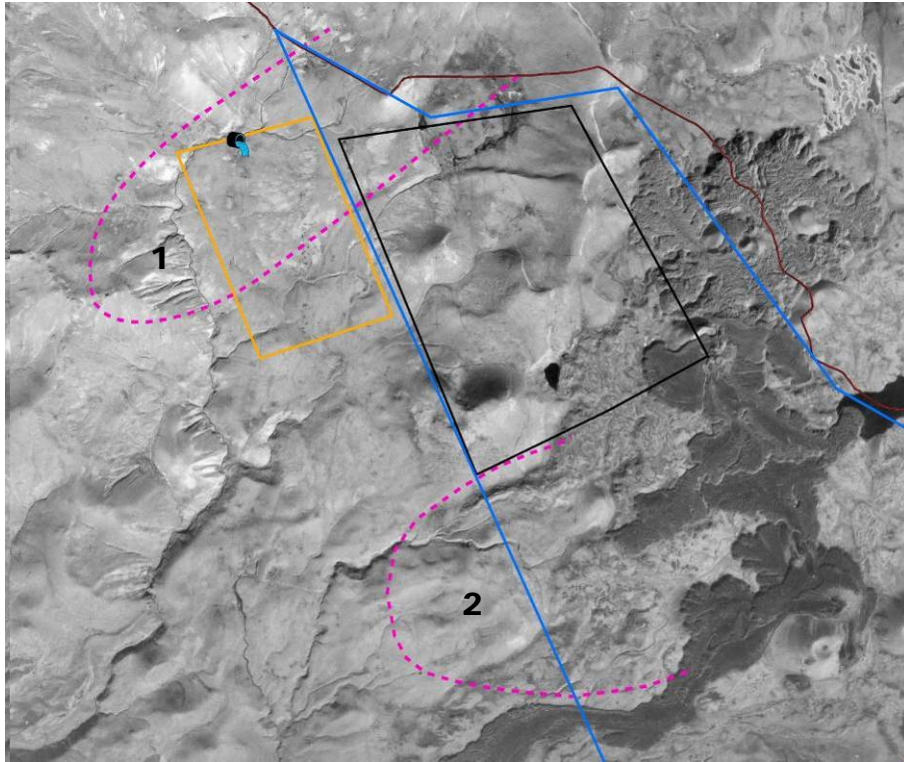
Fig. 1.12 Low-velocity seismic inhomogeneities identified in 1987/88:
1- in the region of the Jermaghbyur thermal spring, 2– in the region of the Karkar group of volcanoes
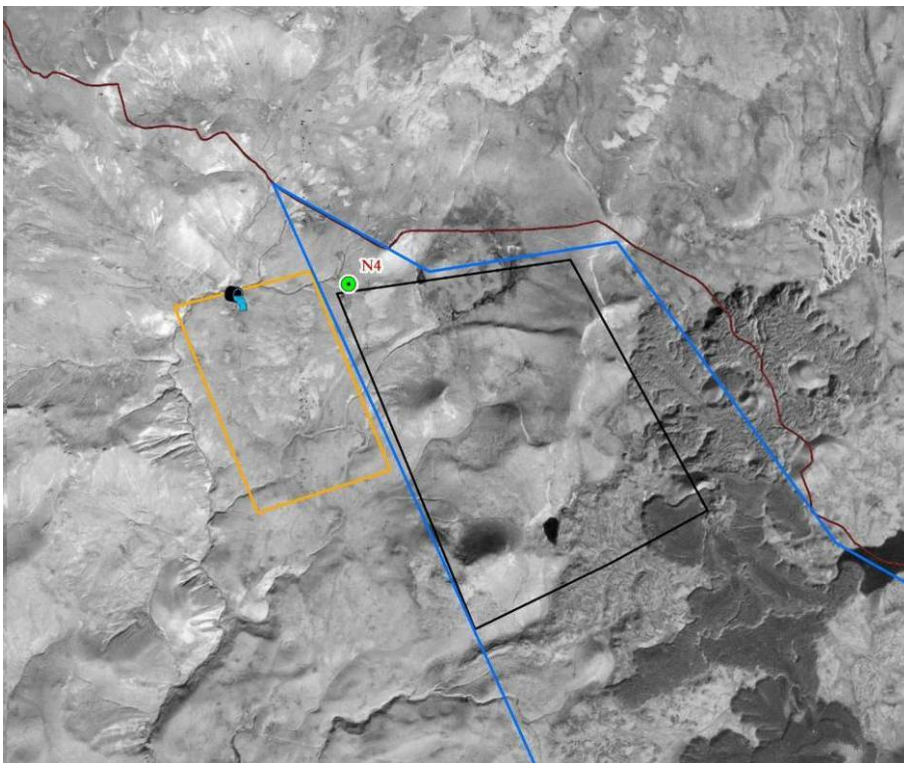
Fig. 1.13: Location of Borehole N 4.
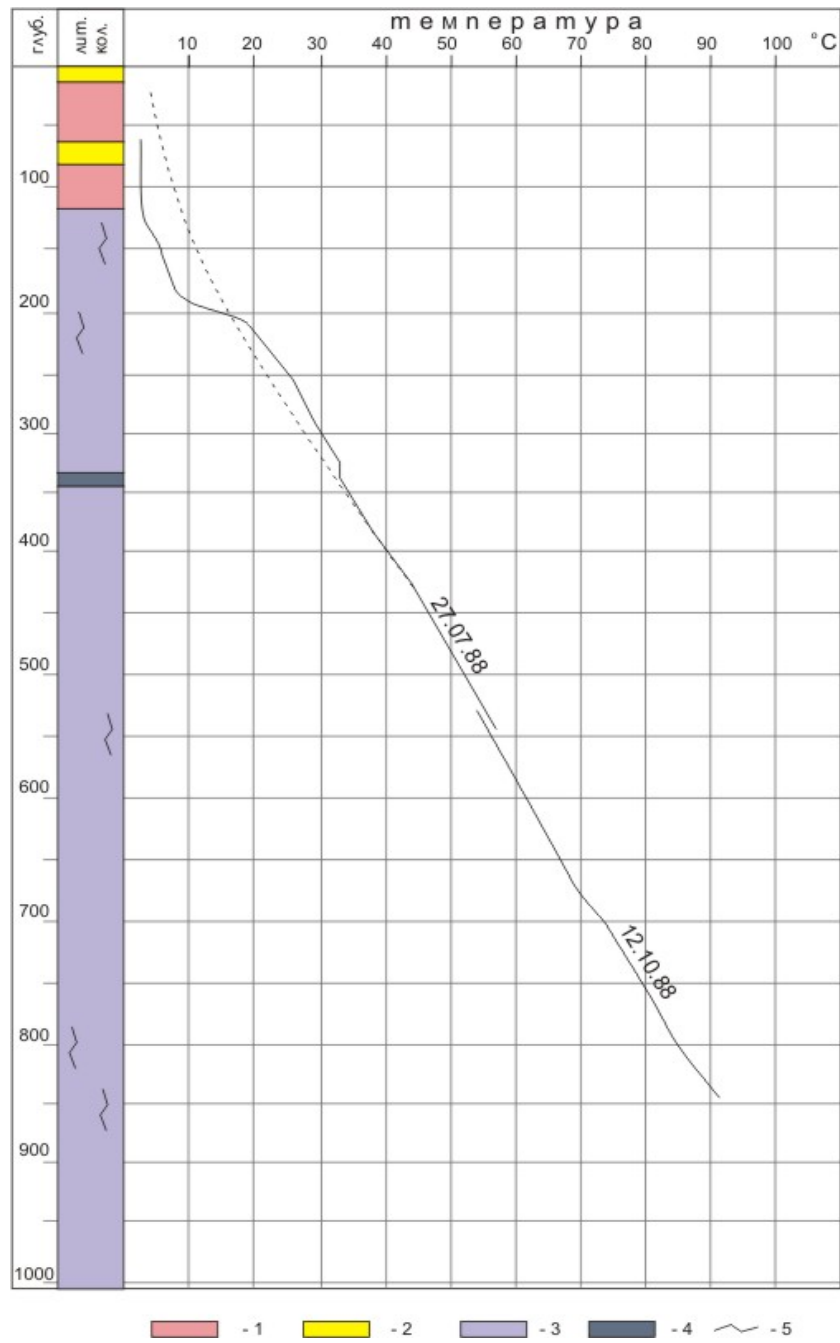
Fig. 1.14: Graph of temperature changes in Borehole no. 4 (the IGES Report, 2004).
*1 - basaltic andesite (3 4 Q −Q), 2 - alluvium-deluvium sediments, 3 - quartz monzonites,
4 - water-bearing zone, 5 - fractures.*
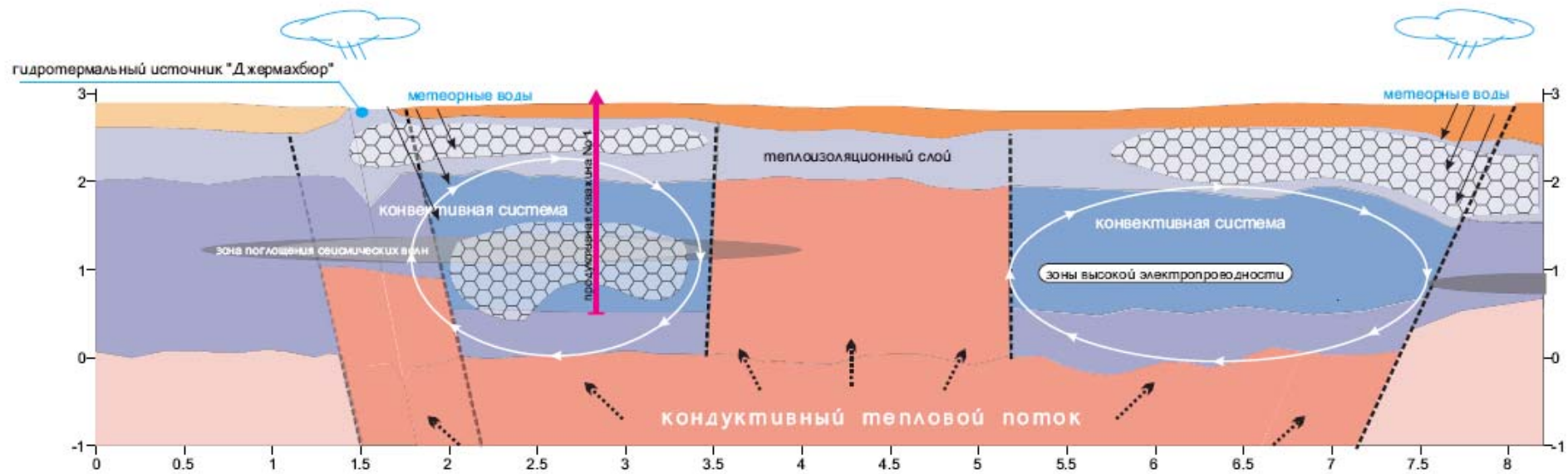
PROFILE N 1
Conceptual model of the Jermaghbyur geothermal deposit.
Horizontal scale of 1:25,000
IGES of the NAS of RA, 2004

Fig. 1.15:
1- Hydrothermal spring "Jermaghbyur", 2 - meteoric water, 3 - seismic wave absorption zone, 4 - thermal insulation layer,
5 - high electrical conductivity zones, 6 - convective system, 7 - conductive heat flow
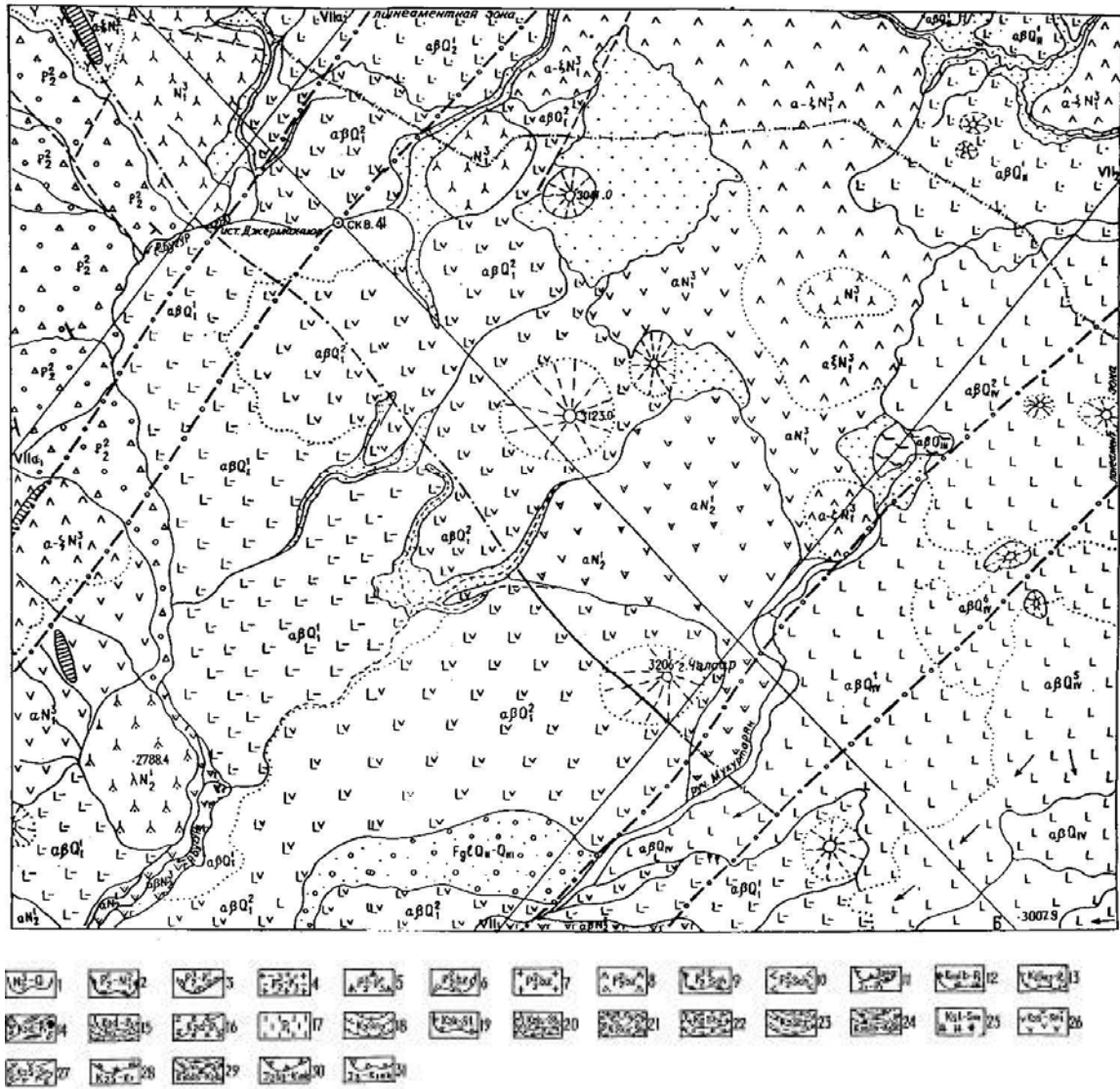
Fig. 1.16: Geological map of the upper courses of the Vorotan River (T. Toumanian, 2004)
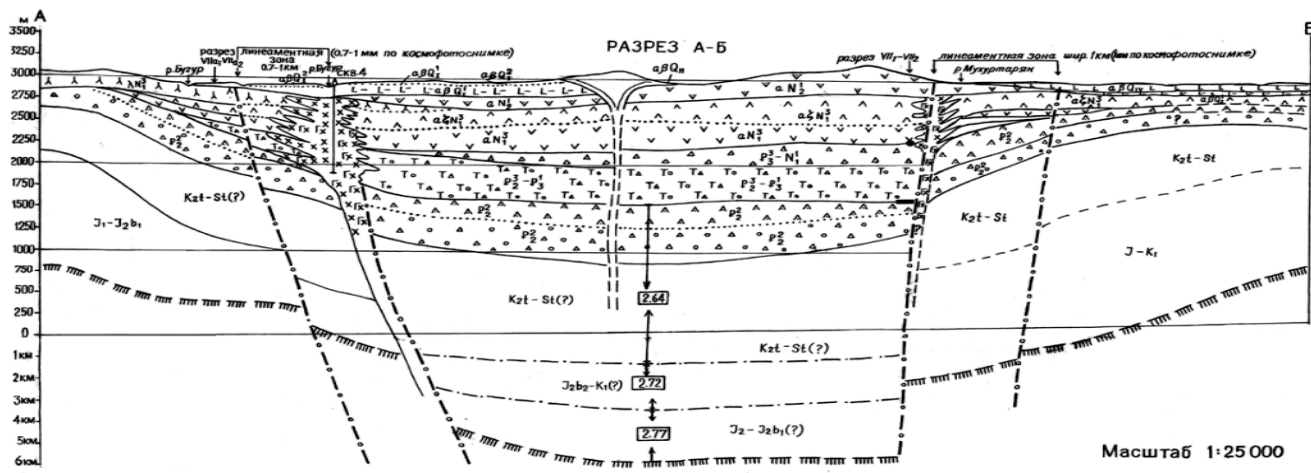
Fig. 1.17: Geological section along Line A-A from the map shown in Fig. 16, IGES (2004)
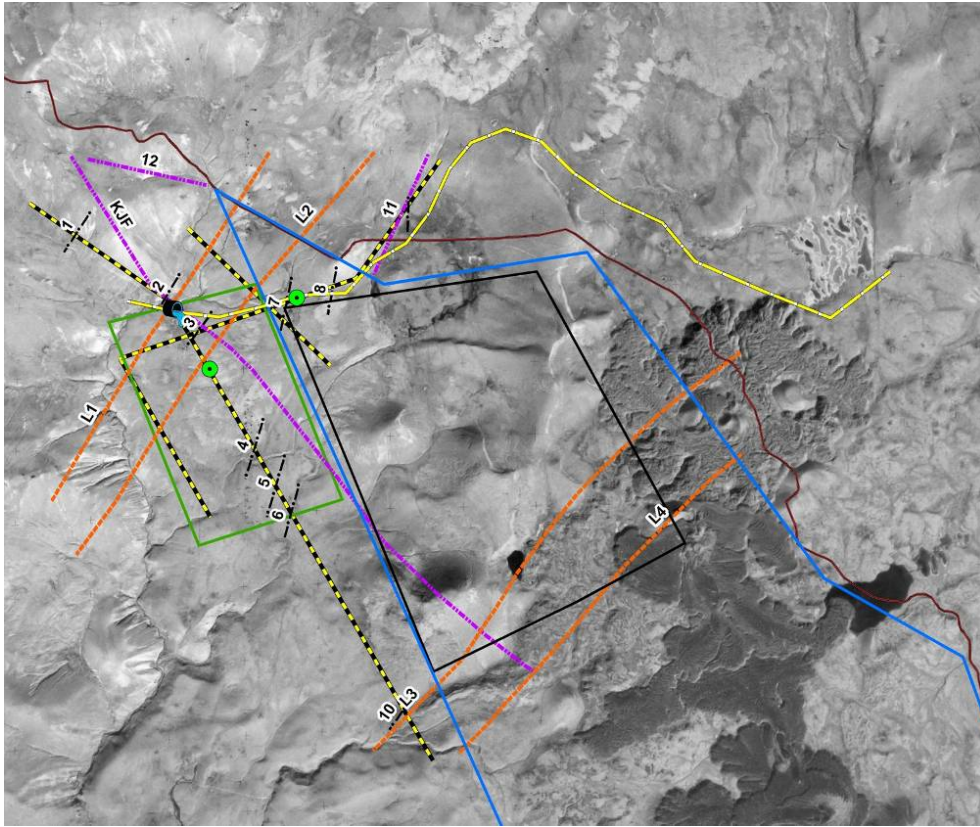
Fig. 1.18: KJF, 11, 12 – the Karkar-Jermaghbyur and other faults identified in 1987/88; L1, L2, L3 and L4 –lineaments identified in 2004.
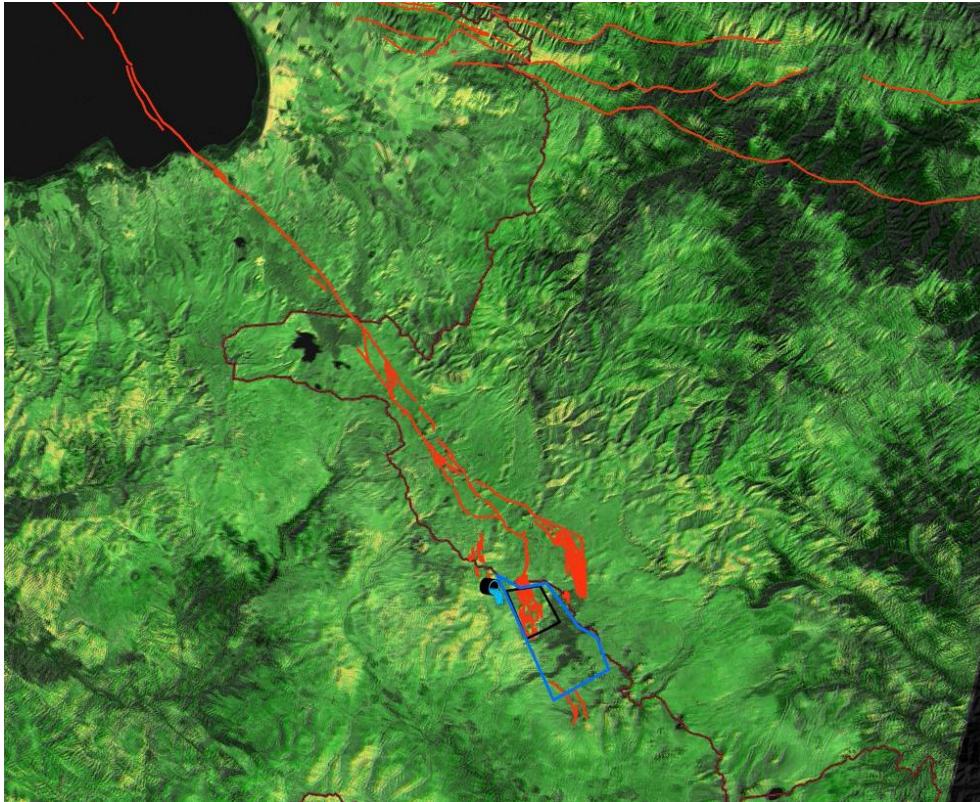
Fig. 1.19: The active Pambak-Sevan Fault.
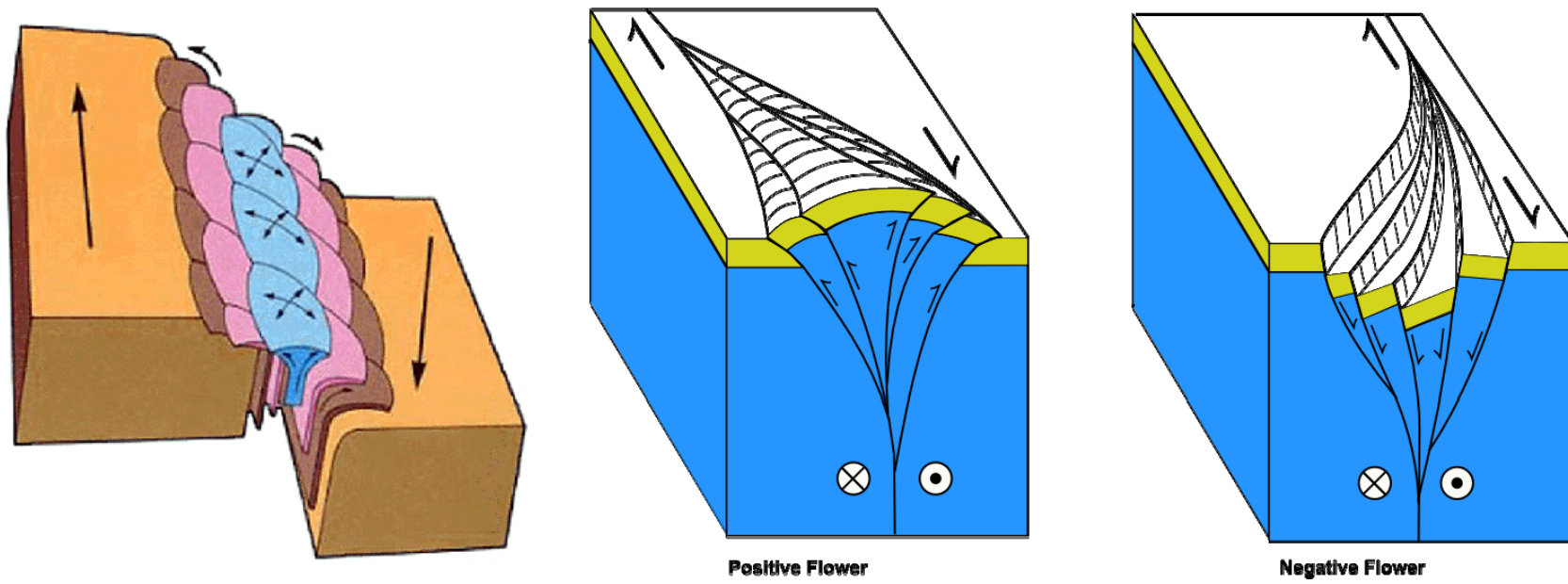
Fig. 1.20: Examples of "flower"-type structures characteristic of strike-slip fault zones.

West flank
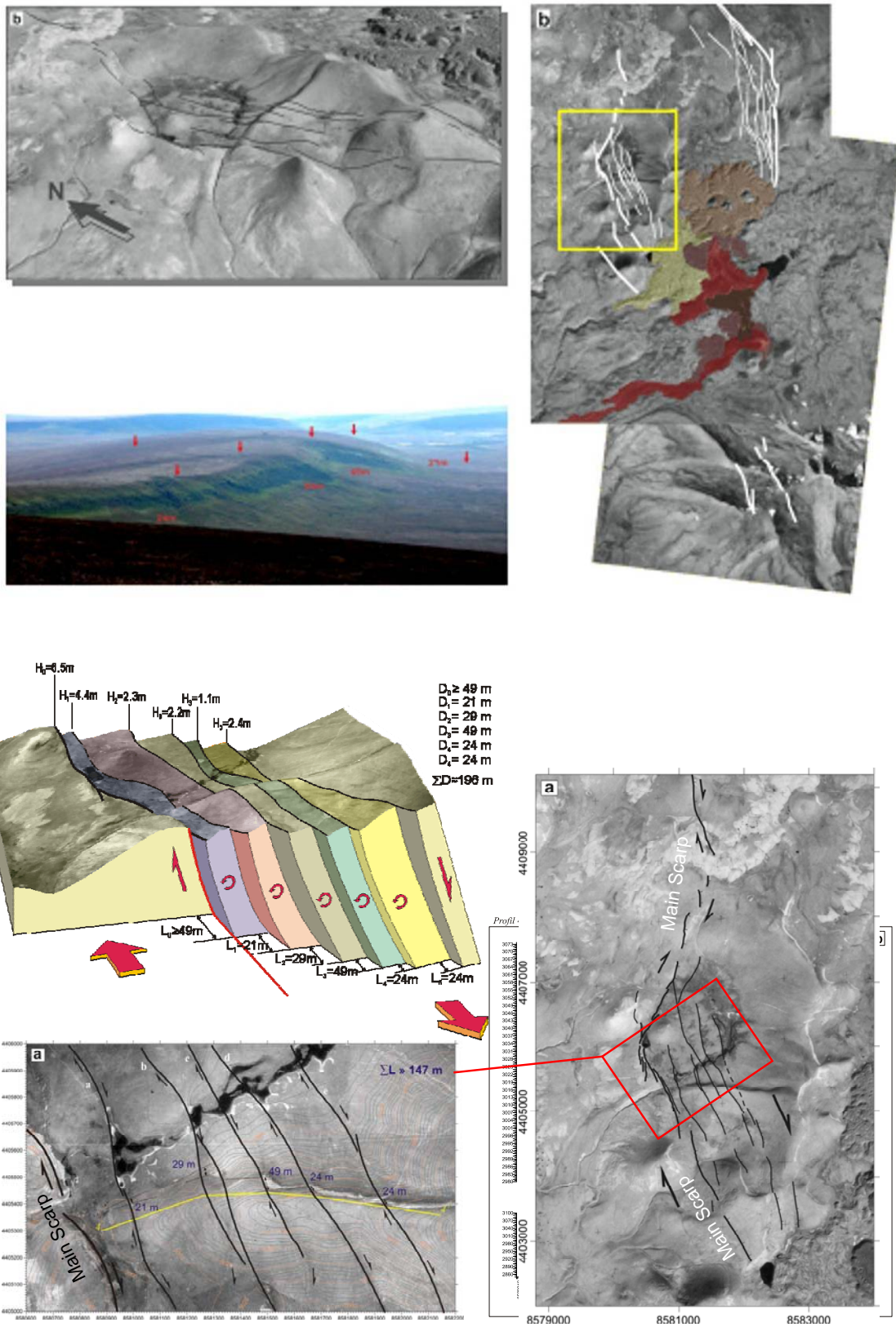
Fig. 1.21: Examples and structural model of the fault located on the western flank of the Karkar *pull-apart* basin

42

East flank
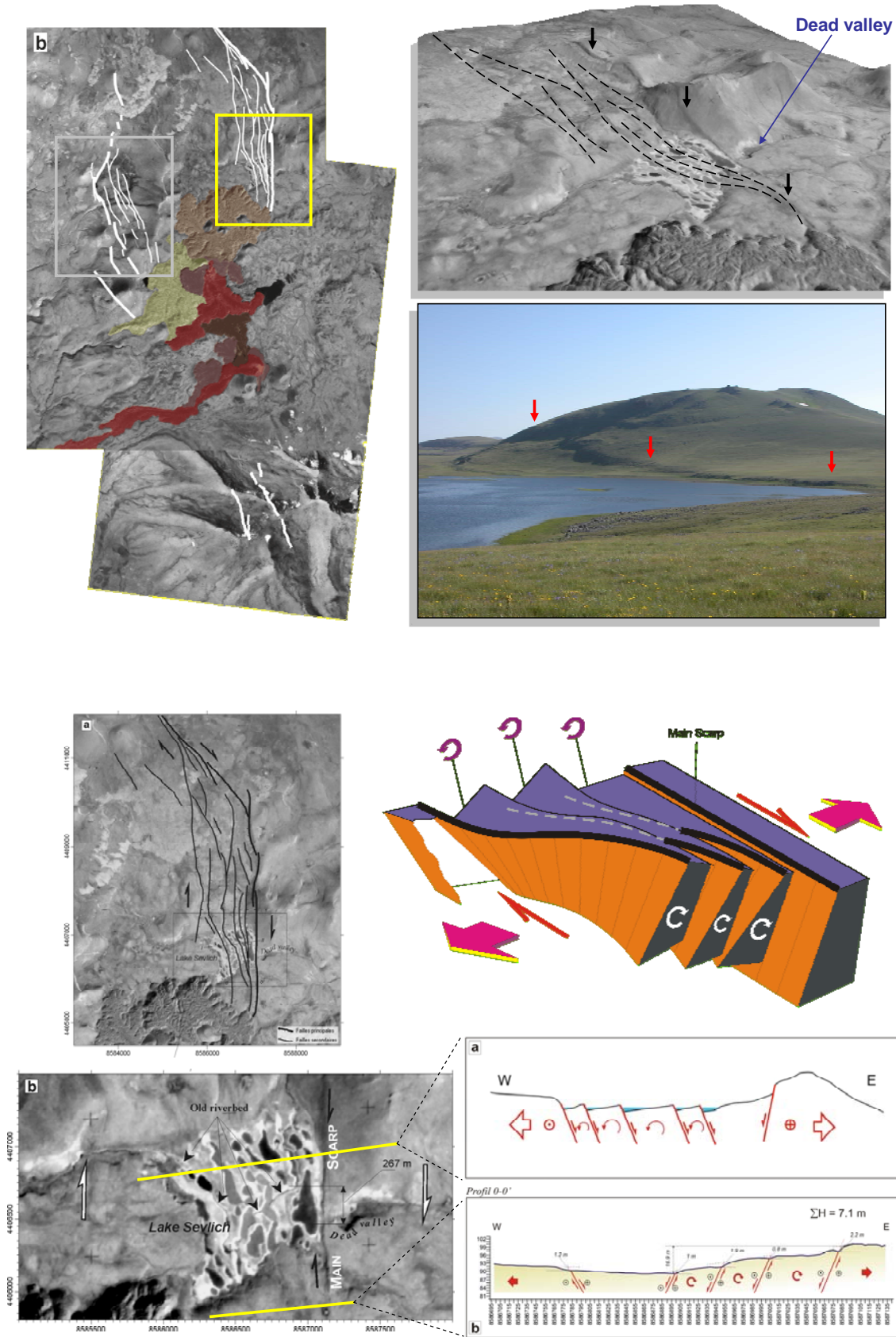
Fig.1. 22: Examples and structural model of the fault located on the eastern flank of the Karkar *pull-apart* basin

LEGEND

Depression deposits	
Olivine trachybasalts	
Amphibolic basaltic trachyandesites	
Quartz rhyolites	
Clinopyroxene-amphibole trachyandesites	

Active faults

Petrographic sampling locations

Site of geological scouting
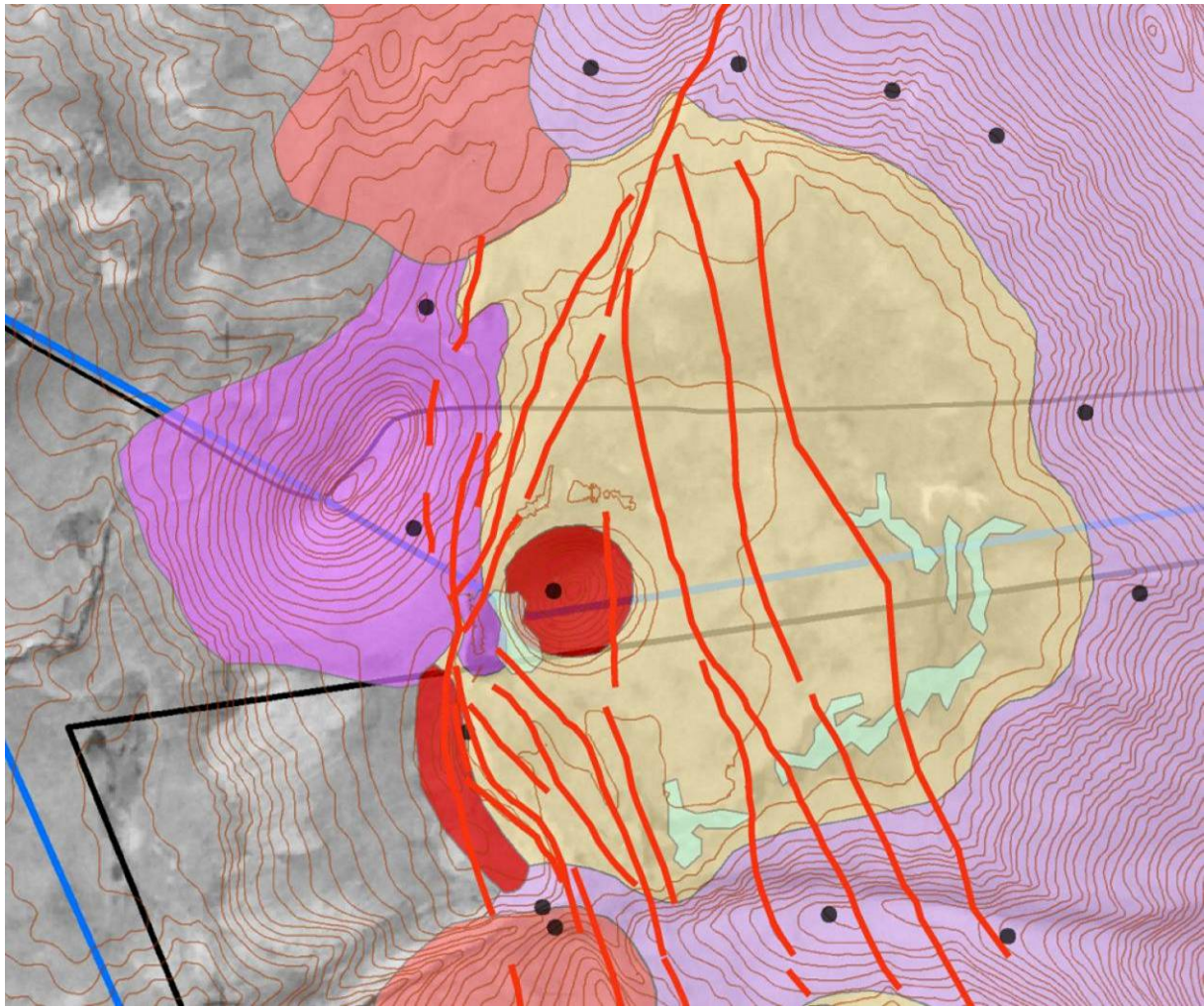
Site of MT survey

Fig. 1.23: Geological map of Depression D1
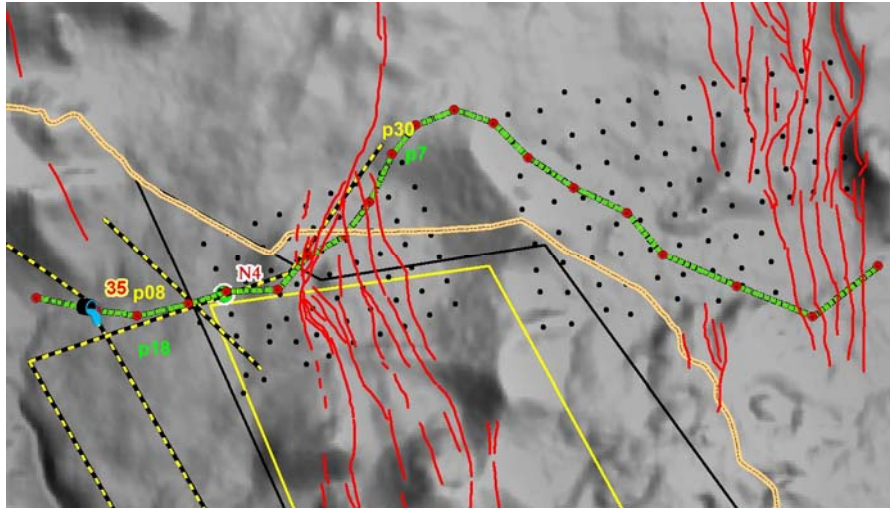
Fig. 1.24: Locations of MT survey profiles in 2004 (yellow-and-black lines);
and in 2009 (green line) and the area covered by the 3D MT survey in 2011 (black dots)
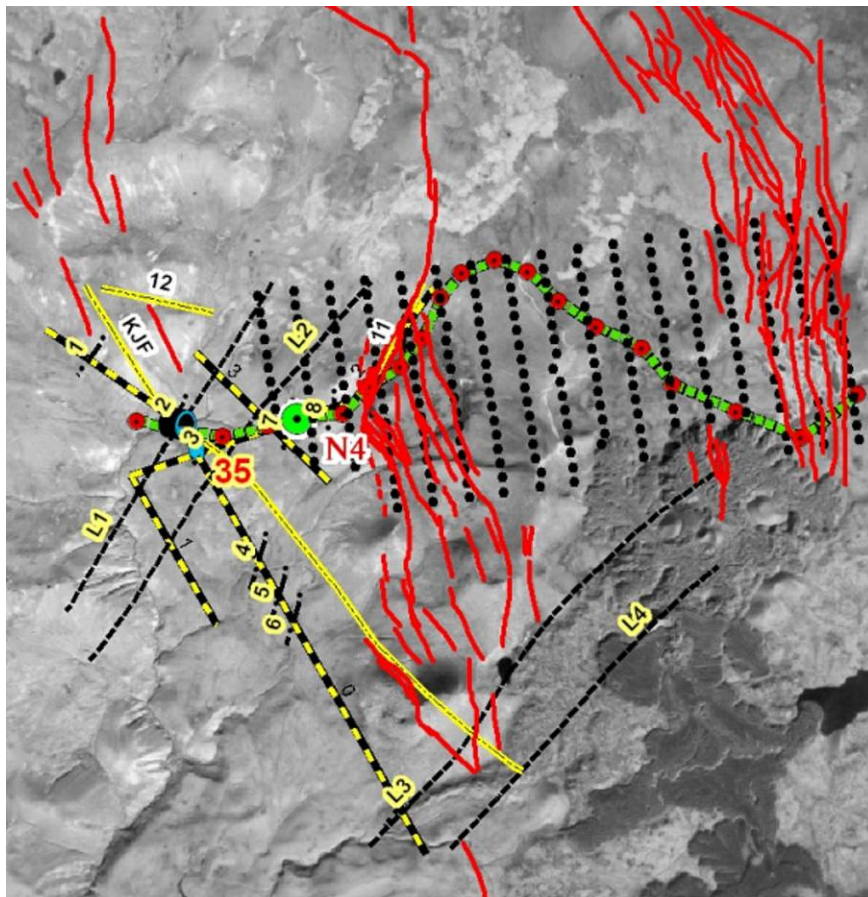
Fig. 1.25: Line of the MT survey profile in 2009 was laid across the main structures at the site.
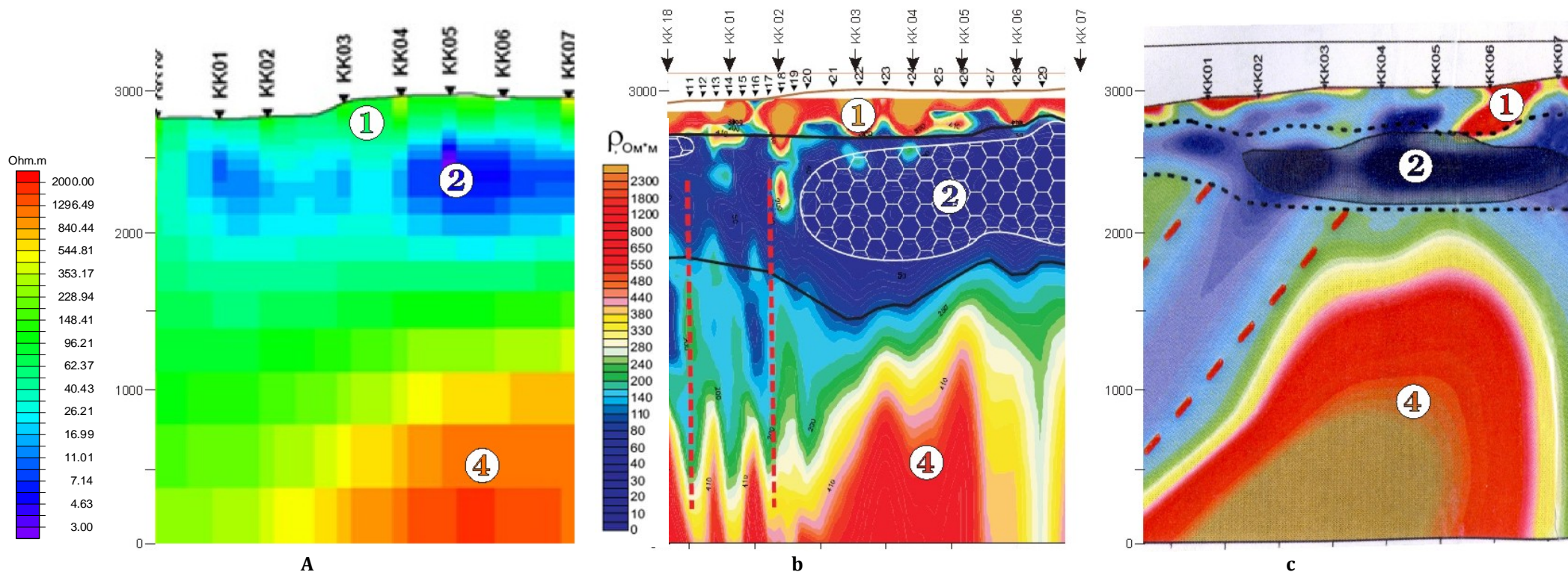
Fig. 1.26: Correlation of the results produced by interpretation of the MT survey data collected in 2004 and 2009 for the same site.

a – the survey of 2009, interpretation by the University of South Florida (USA);
b –the survey of 2004, interpretation by the «Nord-West» Company (Moscow, RF);
c –the survey of 2009, interpretation by the GEORISK/USF (Armenia/USA).

Ohm.m
- 2000.00
- 1296.49
- 840.44
- 544.81
- 353.17
- 228.94
- 148.41
- 96.21
- 62.37
- 40.43
- 26.21
- 16.99
- 11.01
- 7.14
- 4.63
- 3.00
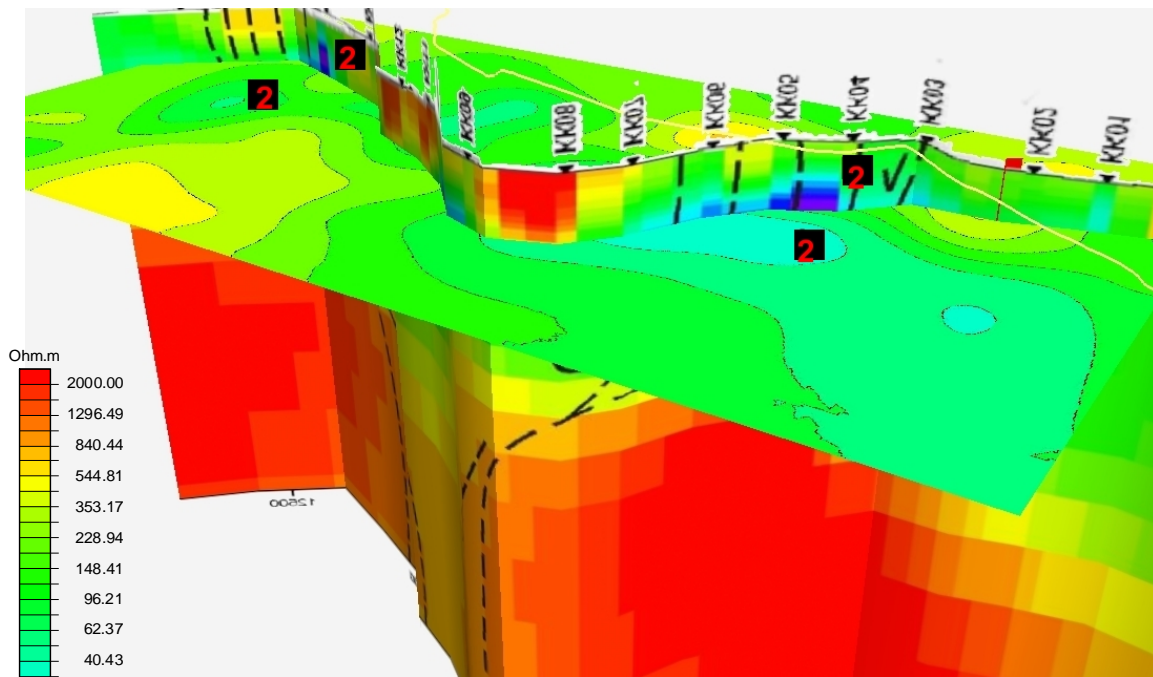
a
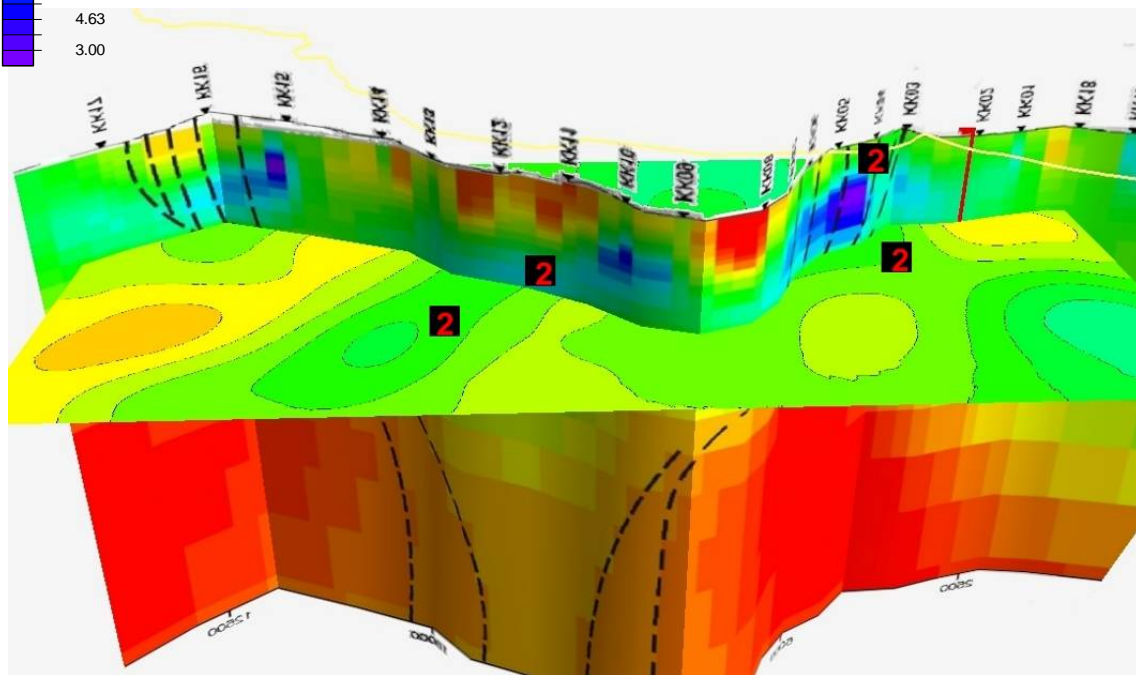
b

Fig. 1.27: Correlation of the MT sounding profile of 2009 with the horizontal sections plotted during the 3D MT survey of 2011: a – at the depth of 500 m, b – at the depth of 1000 m.
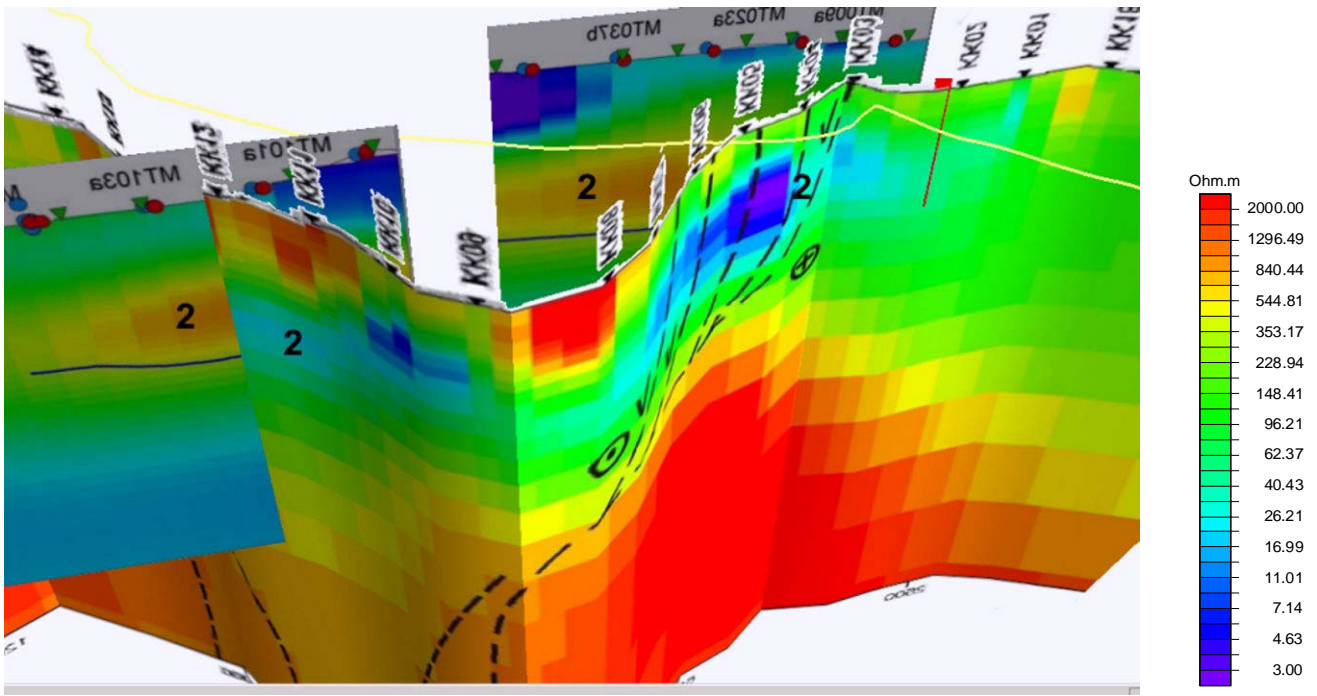
Fig. 1.28: Correlation of the MT sounding profile of 2009 with the vertical sections plotted during the 3D MT survey of 2011.
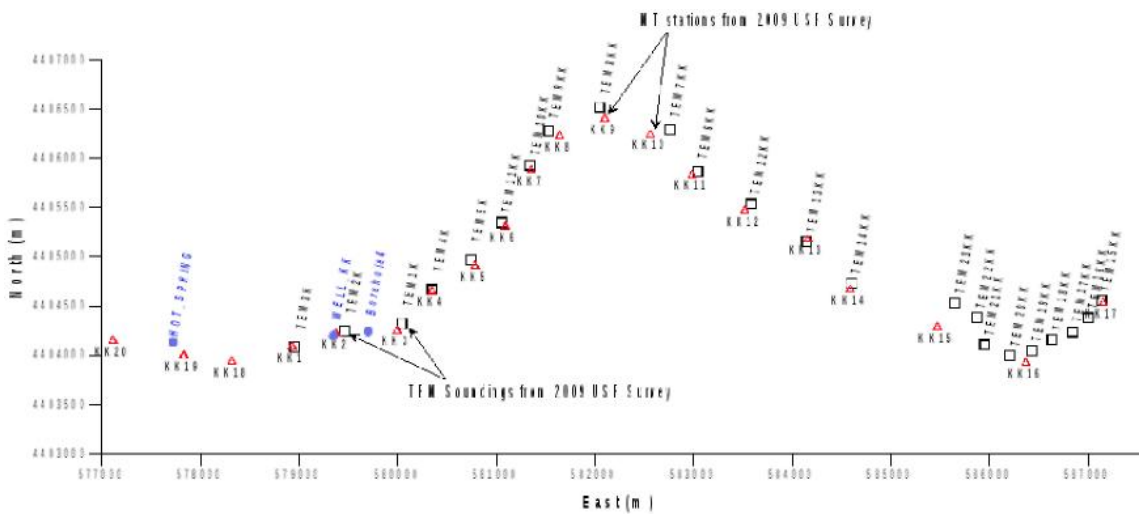
Figure 1.29: MT and TEM data acquisition sites from the GEORISK/ USF 2009 geophysical survey. Also shown are the locations of the Jermaghbyur hot spring site, and the location of Borehole4. Another well shown, WELL KK, was identified by the Armenian field crew during the 2009 survey, although the well was not actually seen by USF personnel. Further discussions indicate that it is likely that that well and Borehole 4 are the same feature.
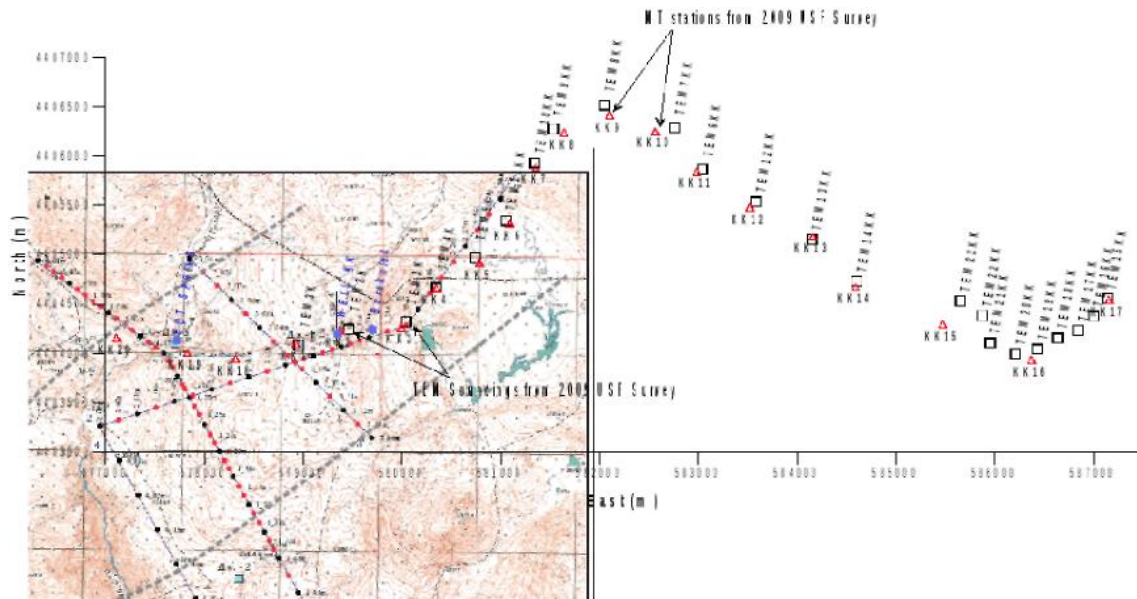
Figure 1.30: Locations of the 2004 and 2009 surveys, referenced together. This map was constructed by positioning a portion of Figure 1.28 on the Figure 1.29 map as best as possible. The actual coordinates of the 2004 data acquisition positions were not available for co-rendering.
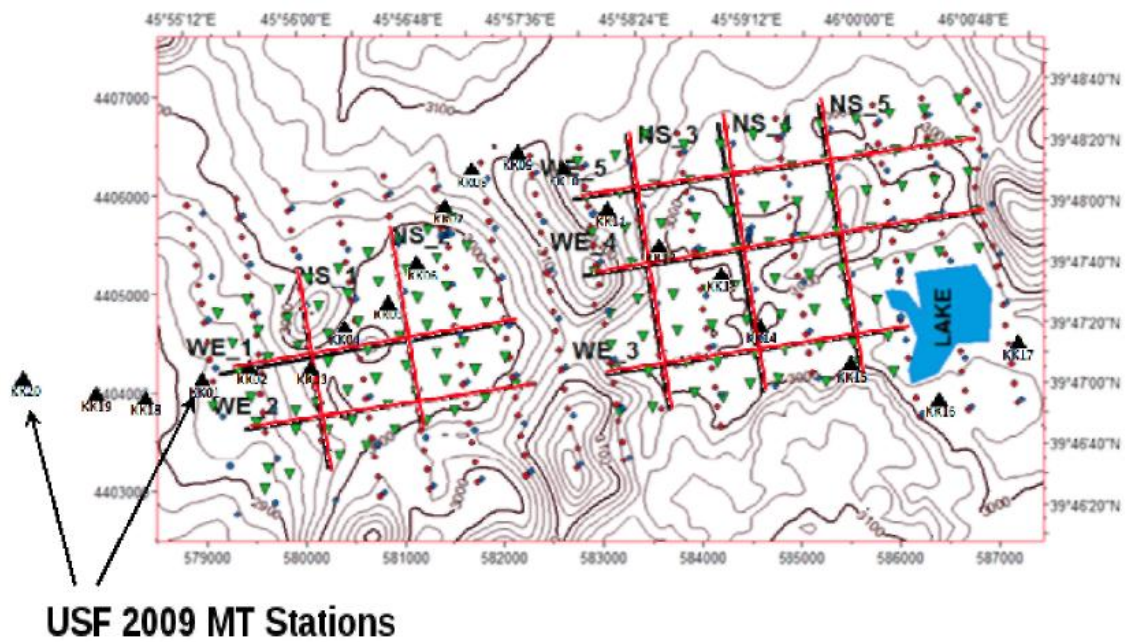

Figure 1.31: The GEORISK//USF 2009 MT stations co-located on the station location map from the WesternGeco report (2011).
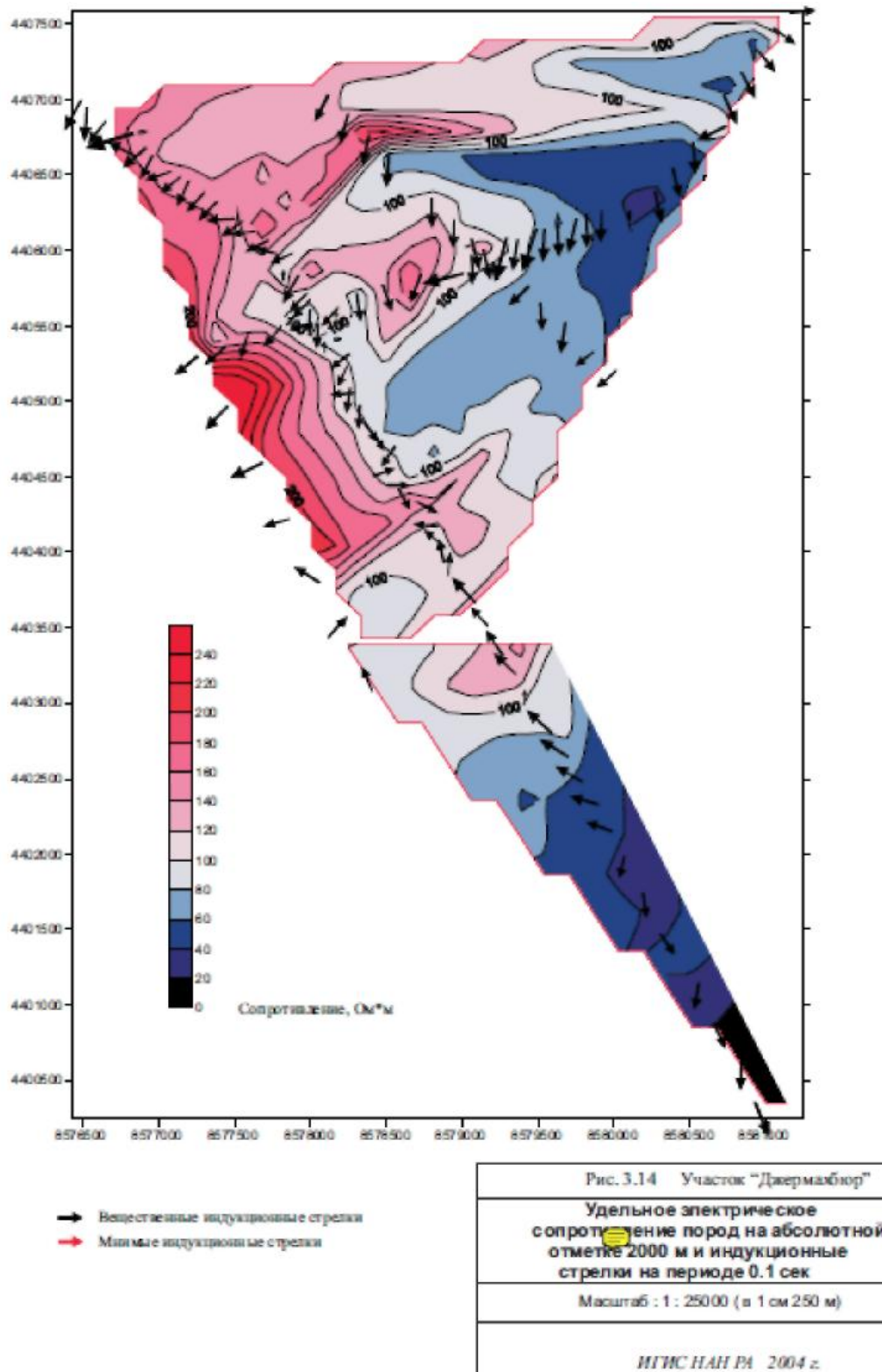
Figure 1.32: Induction arrows at 10 s period, superimposed on resistivity at 2000 m elevation from the 2004 geophysical survey.
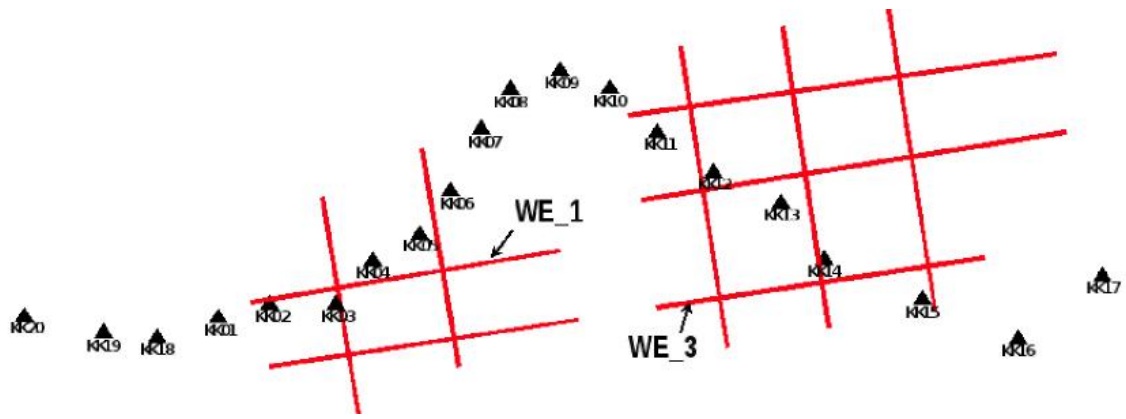
Figure 1.33: The 10 cross-sections of the WesternGeco 3D MT model presented in their report, superimposed on the MT sites from the 2009 survey. Cross-sections WE 1 and WE 3 are labeled
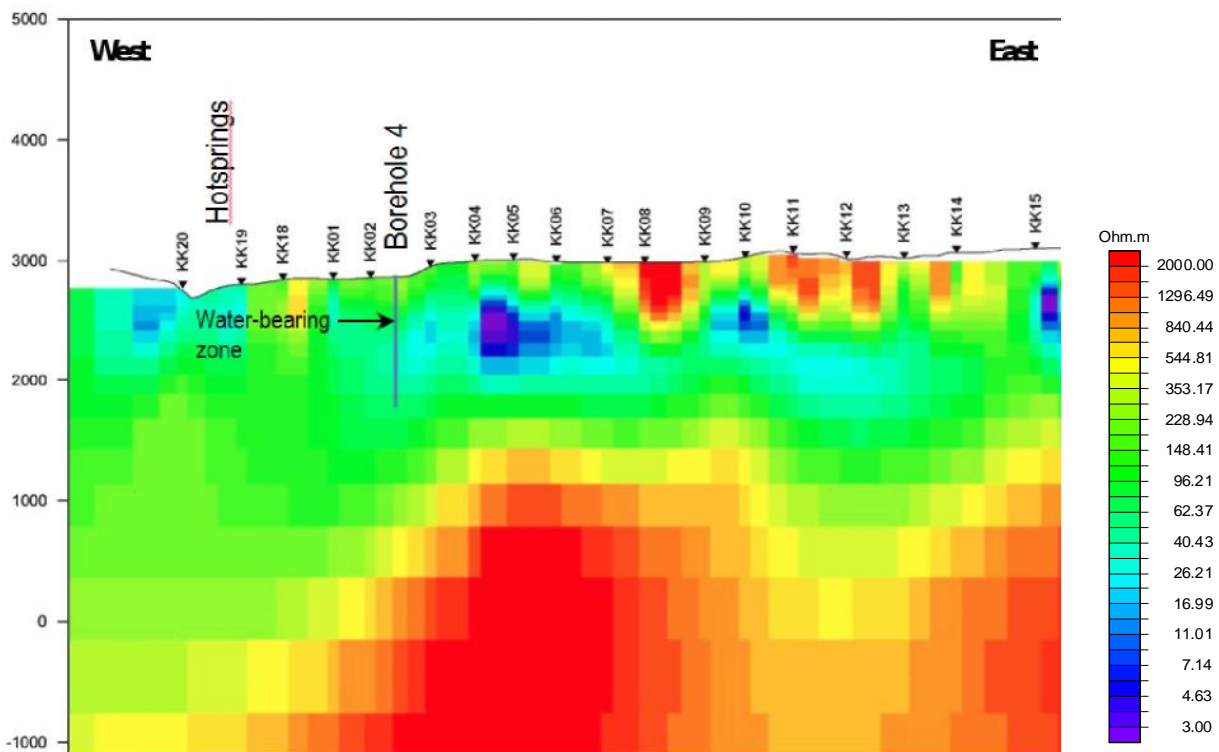

Figure 1.34: The western portion of the 2D model 3 (USF, 2009). Also shown in the figure are the locations of the hot springs, and Borehole 4. In addition, the location of an interpreted water-bearing zone encountered in the borehole is shown.
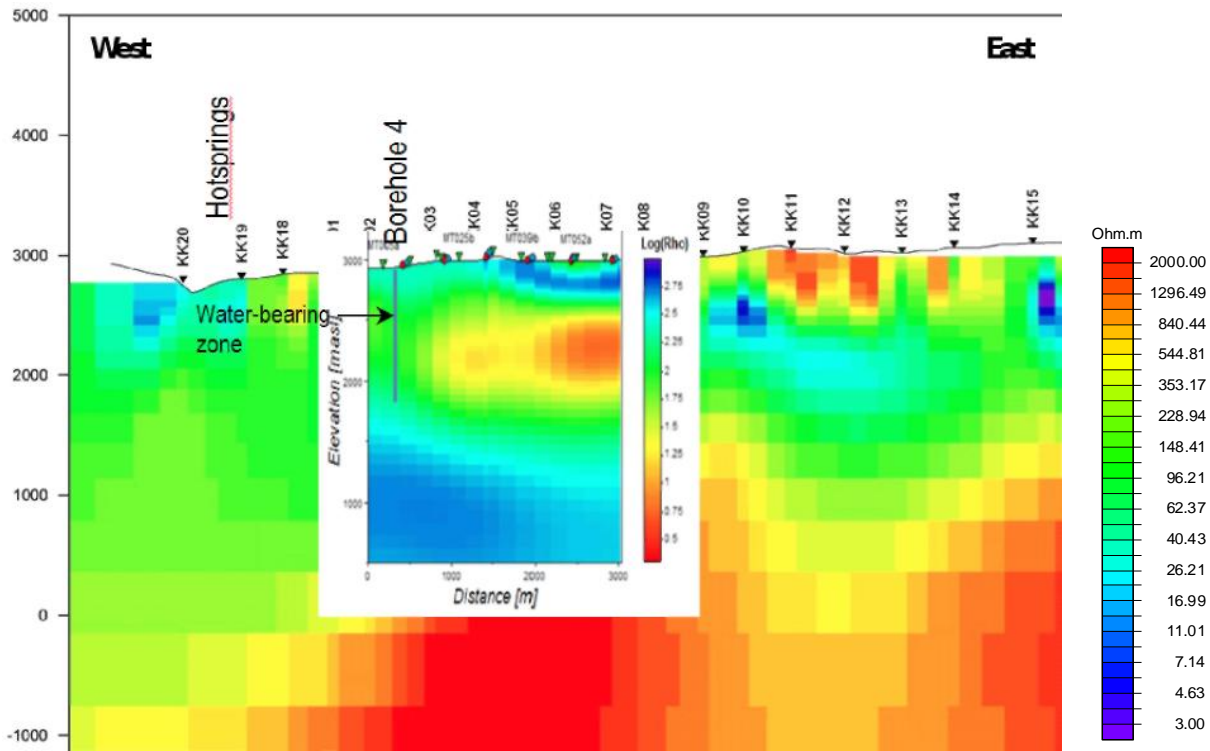
Figure 1.35: WesternGeco section WE 1 co-located on top of the 2009 GEORISK/USF model. Note that the resistivity color scales are opposite; low resistivity on the 2009 model is represented by blue and green, whereas low resistivity on the WesternGeco section is represented by red and yellow.
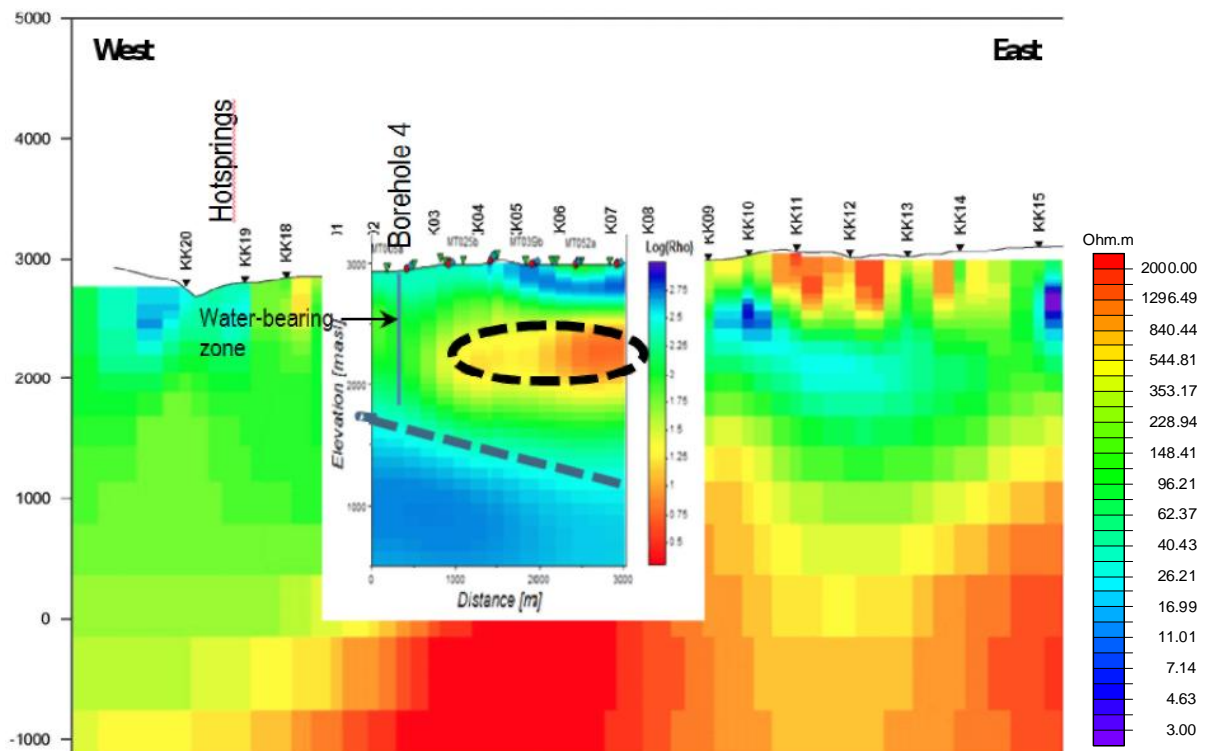

Figure 1.36: Resistivity section WE 1 co-located on top of the 2009 GEORISK/USF model, as in Figure 1.35, except interpreted features have been drawn with heavy dashed lines.
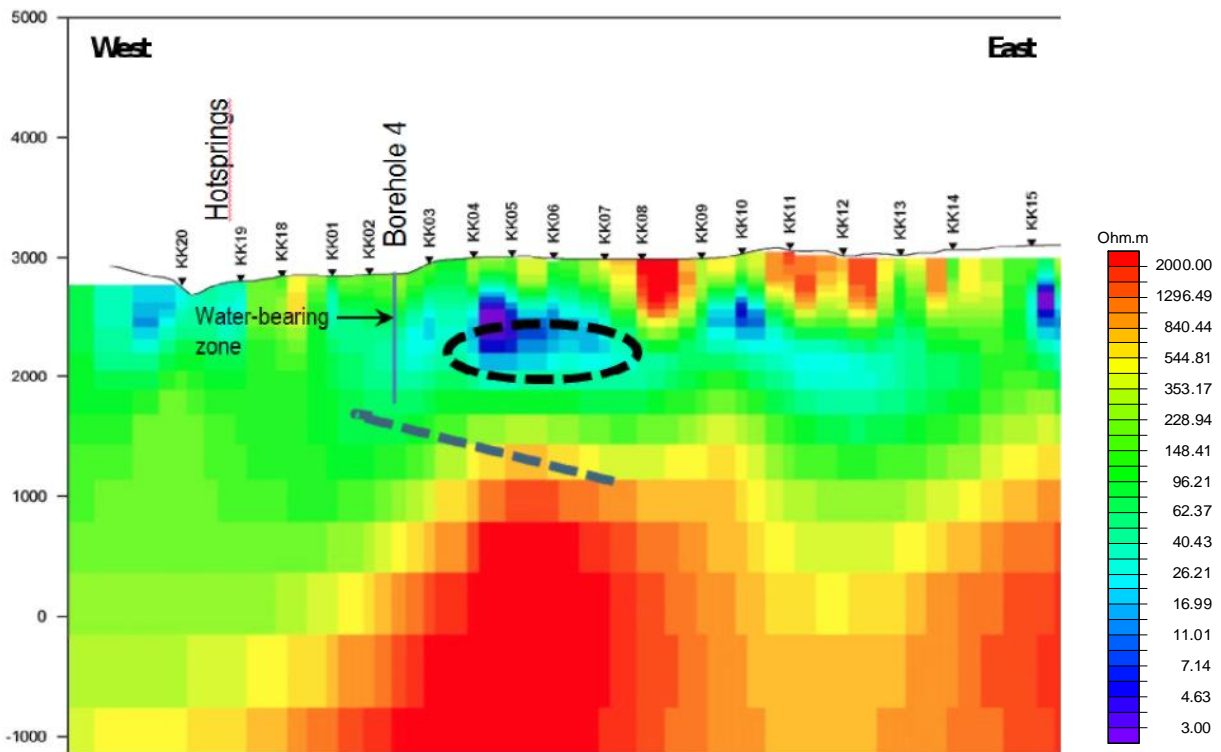
Figure 1.37: The 2D model (USF, 2009), as in Figure 1.34, except the interpreted features from Figure 1.36 have been added.
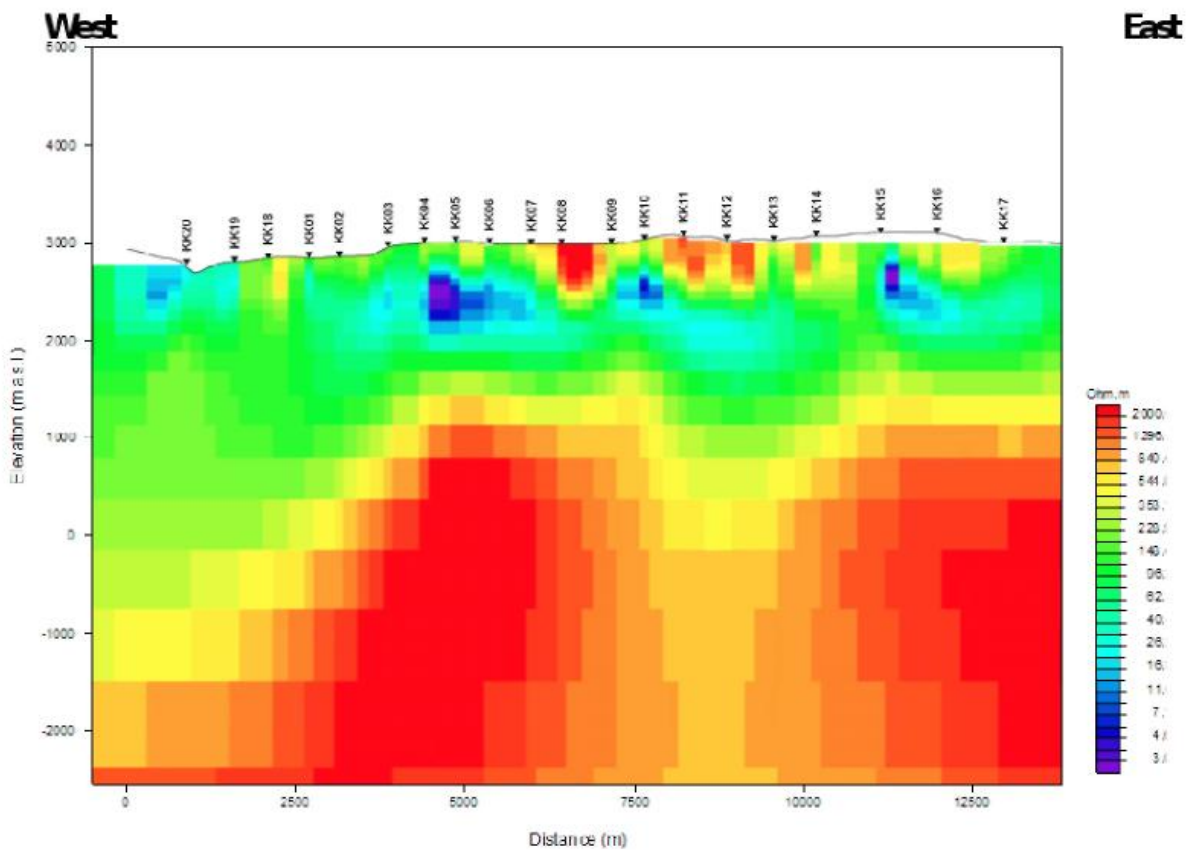

Figure 1.38: The 2009 GEORISK/USF 2D model, including its eastern portion. Note the resistivity color scale, which is the same on previous figures.
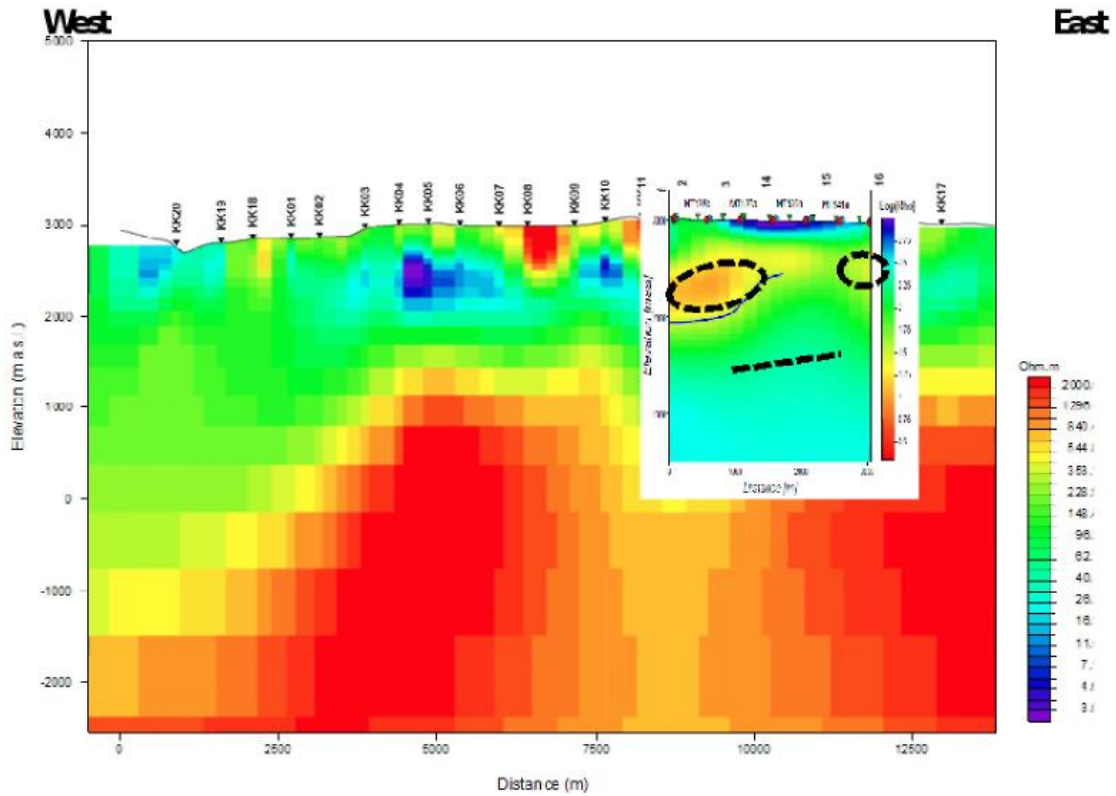
53

Figure 1.39: The 3D resistivity cross-section WE 3 is shown in its approximate position relative to the 2D model from Figure 1.38. Note that the resistivity color scales are opposite between the 2D and 3D models, as discussed in the caption for Figure 1.35. Also shown are three interpreted features as indicated by heavy dashed lines.
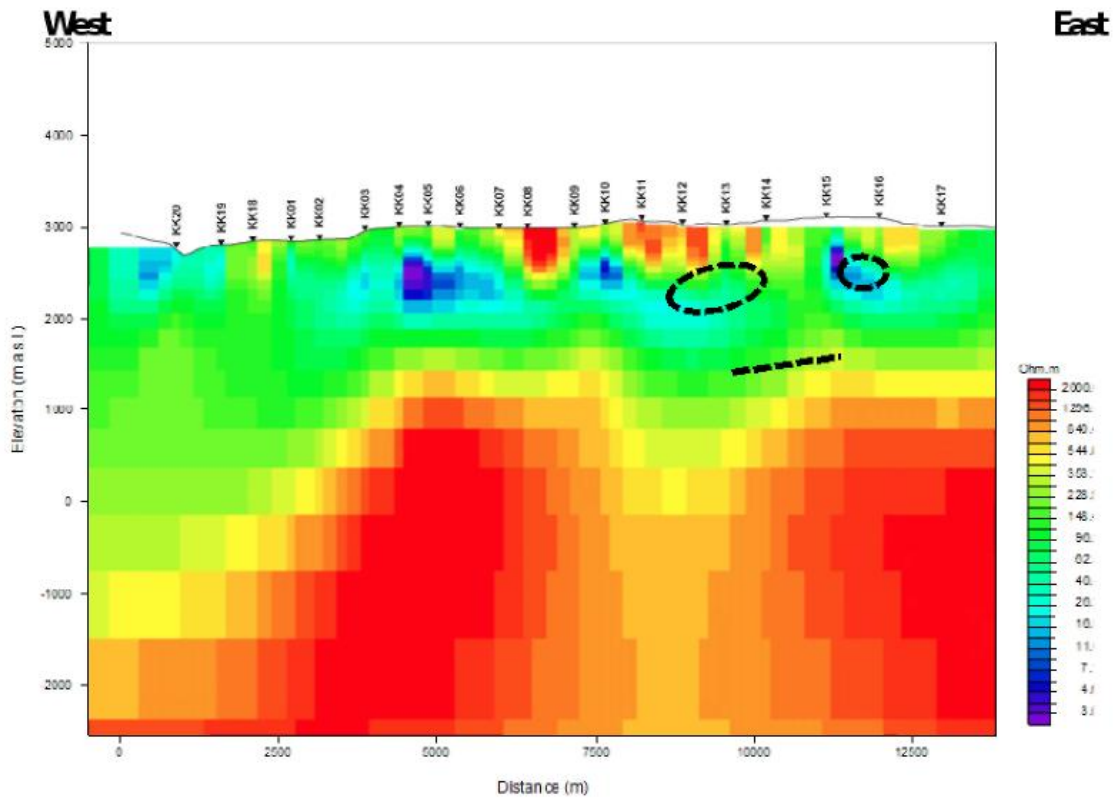

Figure 1.40: The 2D model from Figure 1.38 shown with the interpreted features, indicated by heavy dashed lines, from Figure 1.39.
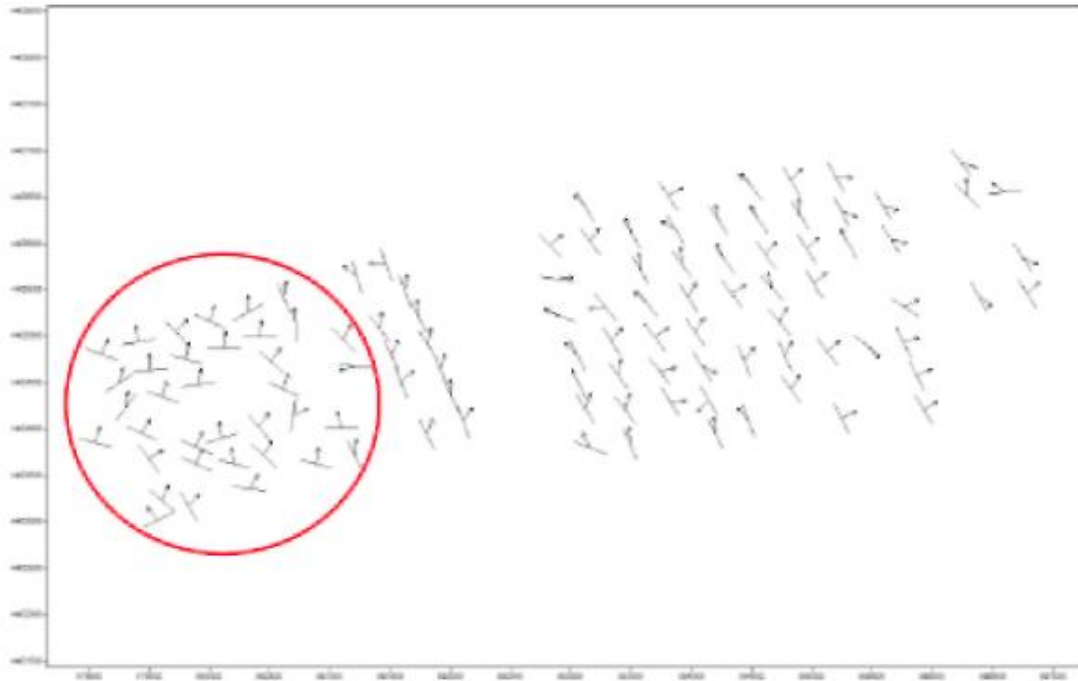
Figure 1.41: Tipper strike and induction arrows at 100s (from the WesternGeco report (2011), Figure 1.30). Also shown is a red circle outlining an anomalous area, as stated in the WesternGeco report.
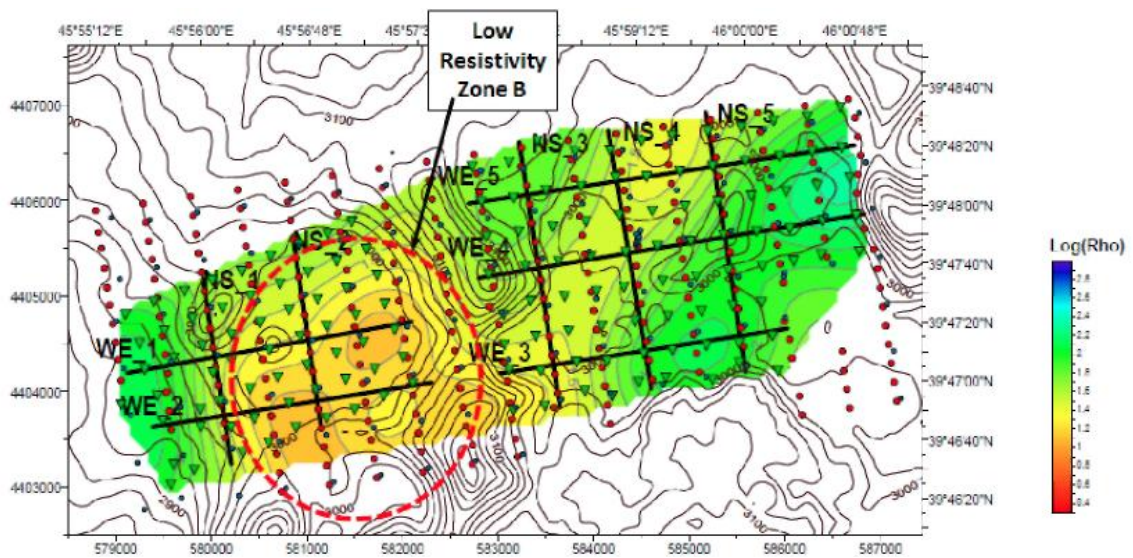

Figure 1.42: The resistivity at 2000 m elevation, extracted from the 3D model (WesternGeco Report (2011), Plate 2e. Also shown is a low resistivity Zone B, as described in the text.
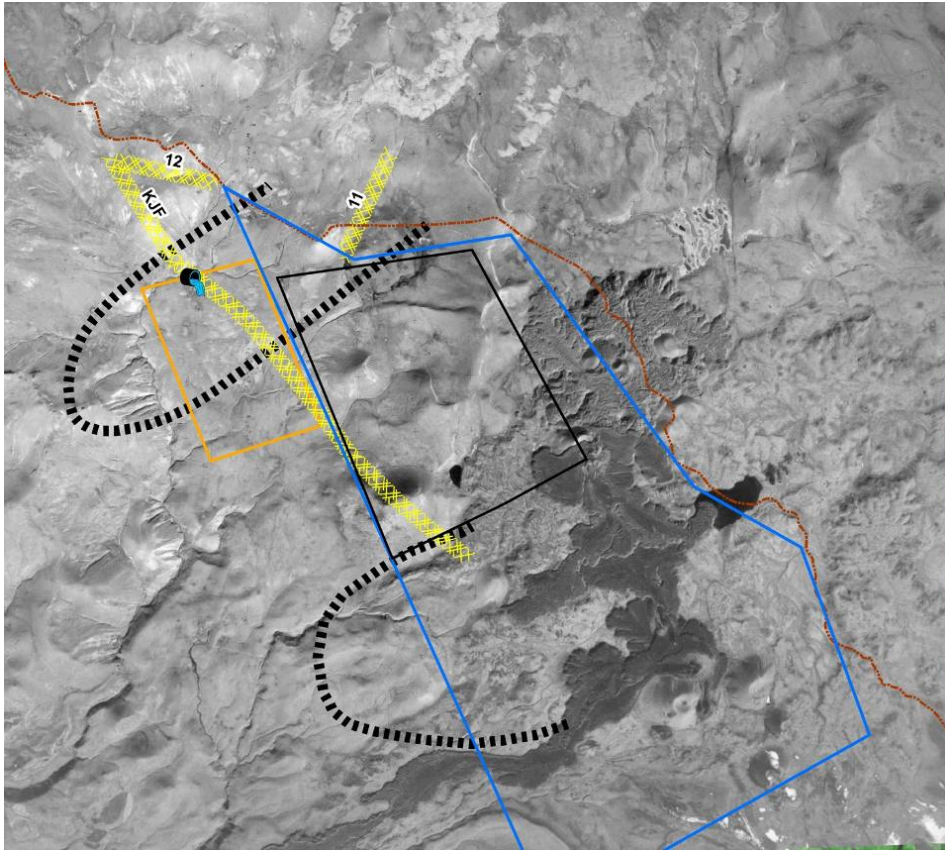
Fig. 1.43: The Structural Model 1988
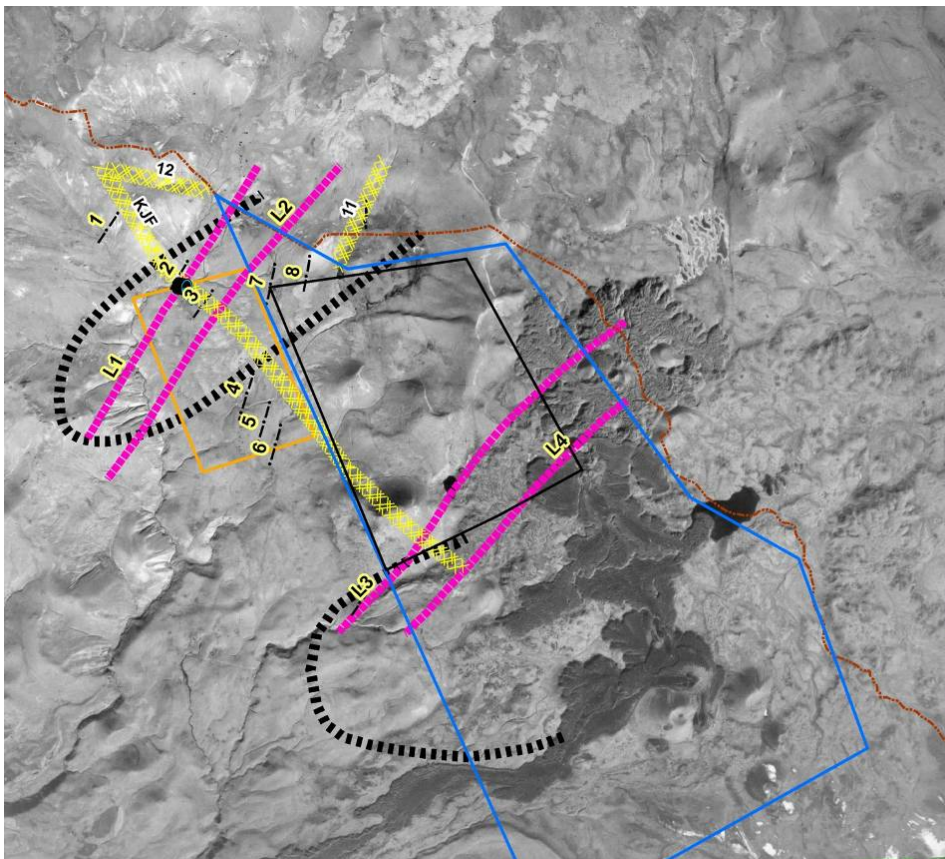
Fig. 1.44: Structural model *IGES 2004*
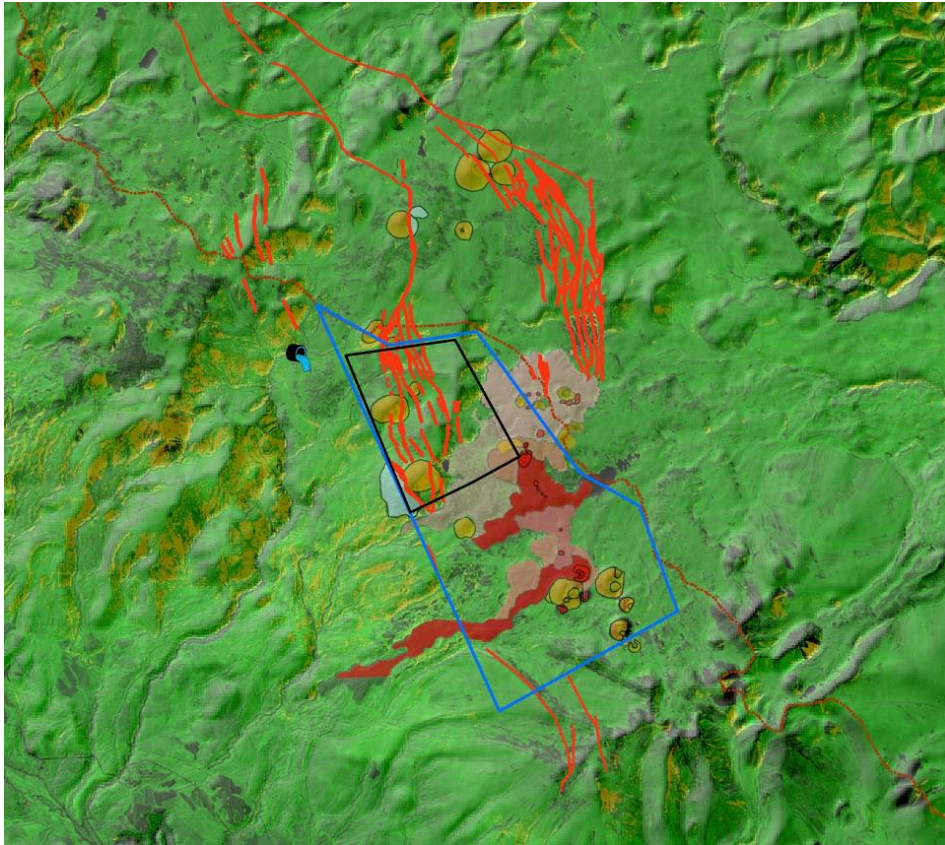
Fig. 1.45: Structural model *GEORISK 2009*
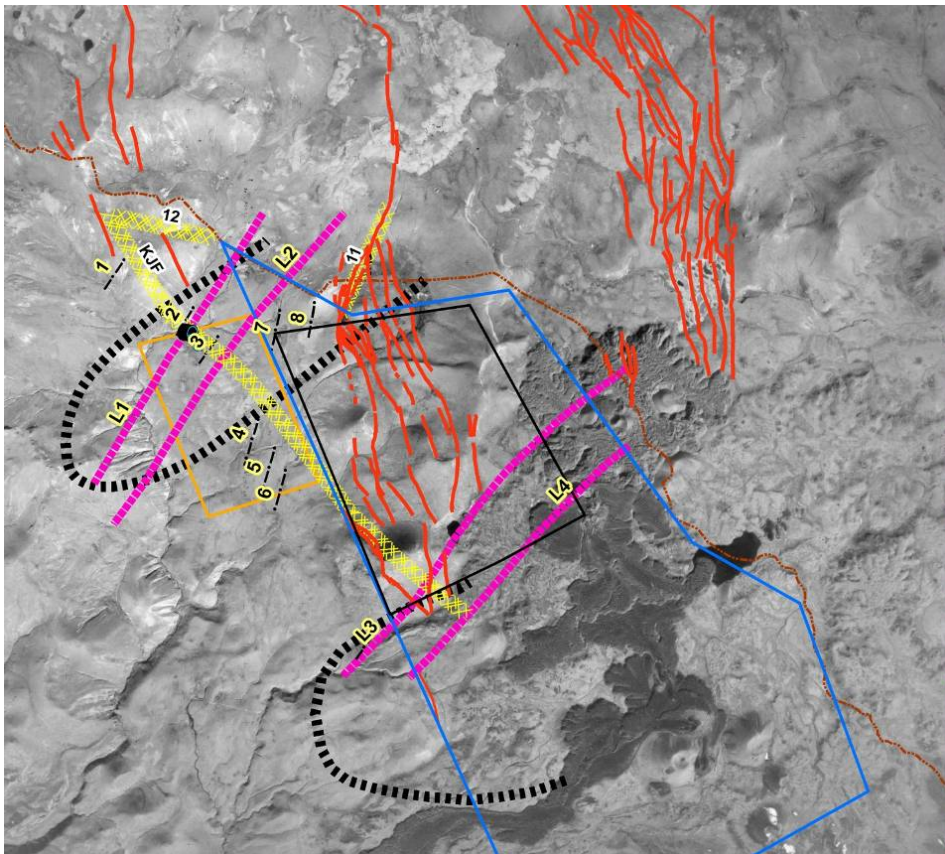
Fig. 1.46: Superposition of all three structural models.
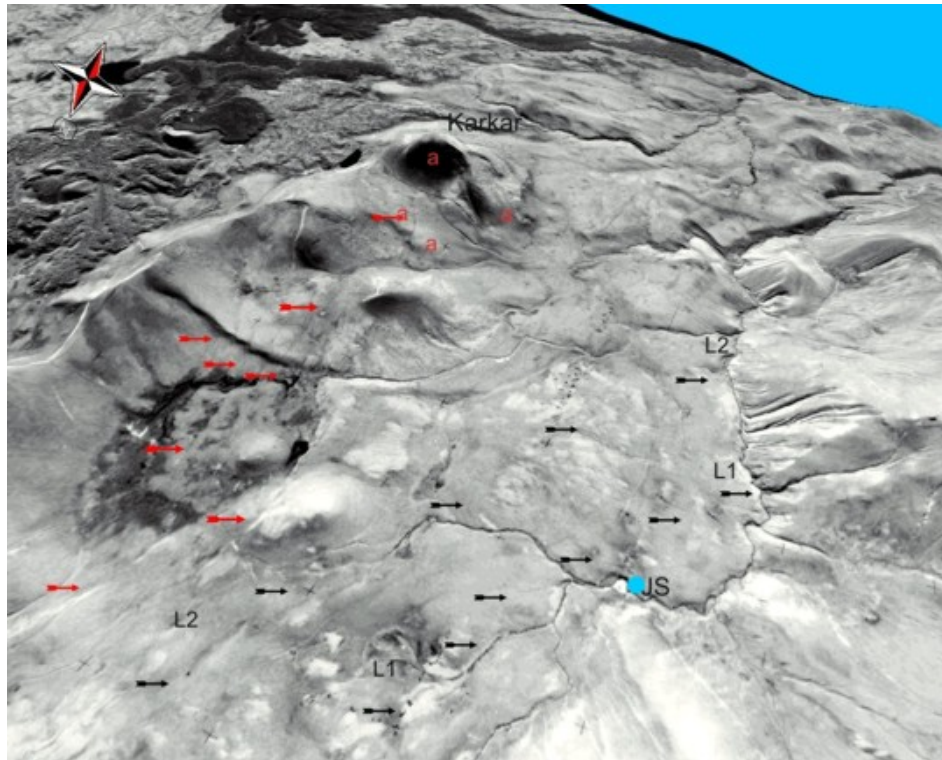
Fig. 1.47: Red arrows indicate fault routes on the western boundary of the *pull-apart* basin structure (model GEORISK 2009); black arrows indicate the routes of Lineaments L1 and L2, which, according to IGES 2004 Model, correspond to the northwestern boundary of the graben.
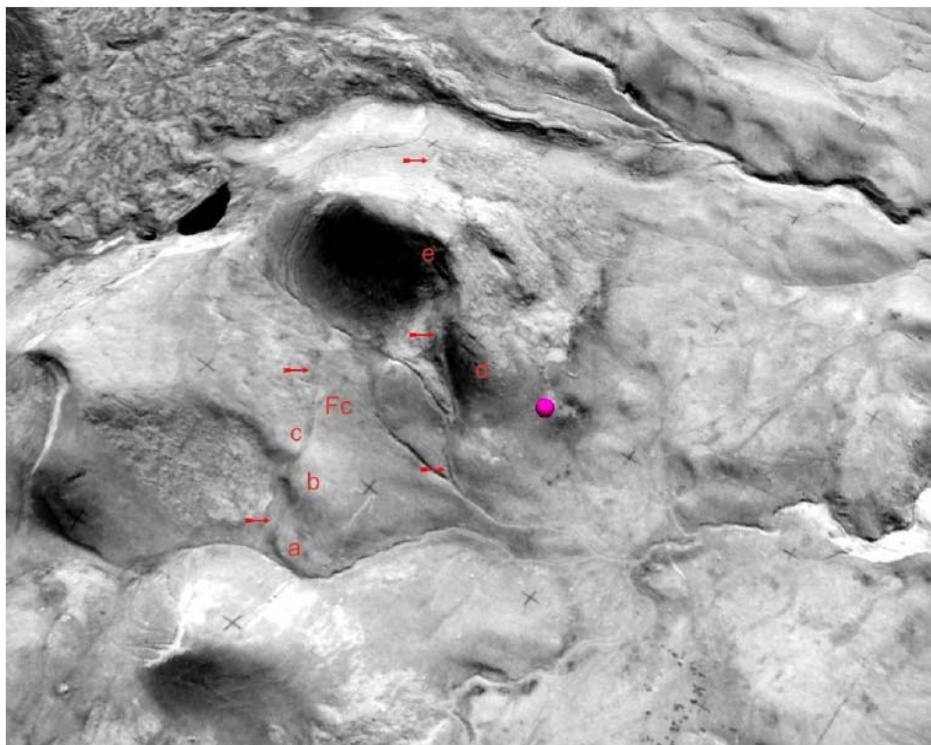
Fig. 1.48: Faults of the eastern boundary of the *pull-apart* basin. The strike-slip fault displaces margins of an erosion gully *a, b* and *c* by 320 m right-laterally. The *a–b* offset is older and has a size of 220 m, and offset *b-c* is younger and has a size of 100 m. The eastern and western branches displace the flank of the Karkar volcano by 130 m and 500-570 m, respectively
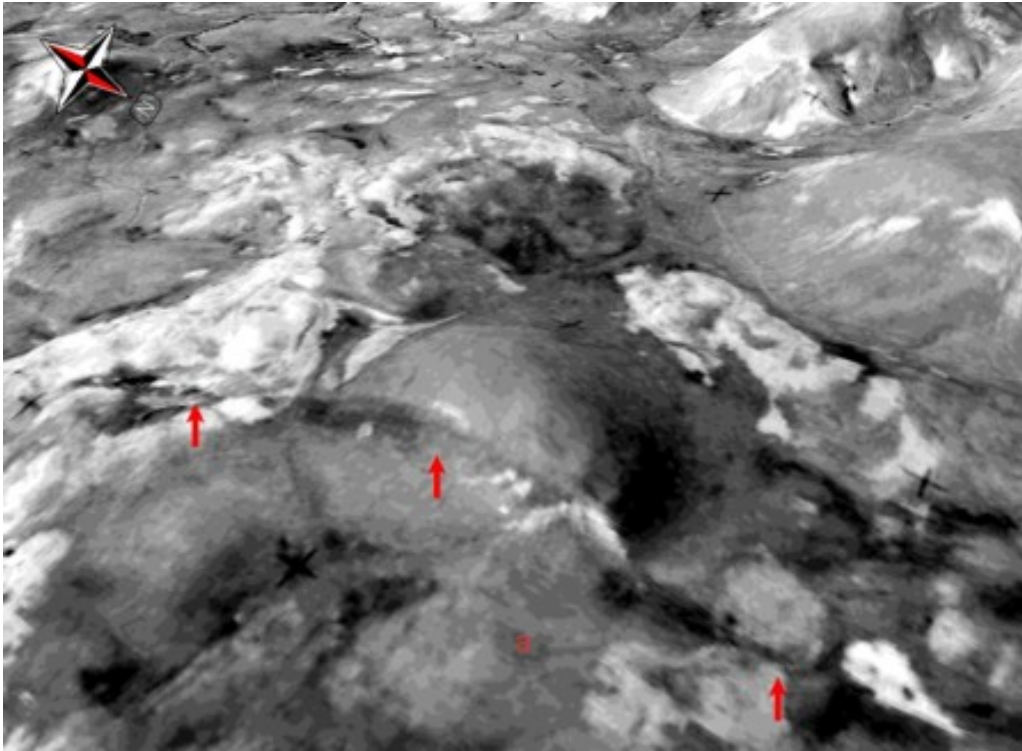
Fig. 1.49: Faults of the western sides of the *pull-apart* basin displace a cinder cone by 128 m right-laterally, and the eastern half of the volcano is downthrown vertically by 10-15 m. The northern flank of the lower eastern half was broken by a lateral fissure that ejected a small flow of basaltic andesite.
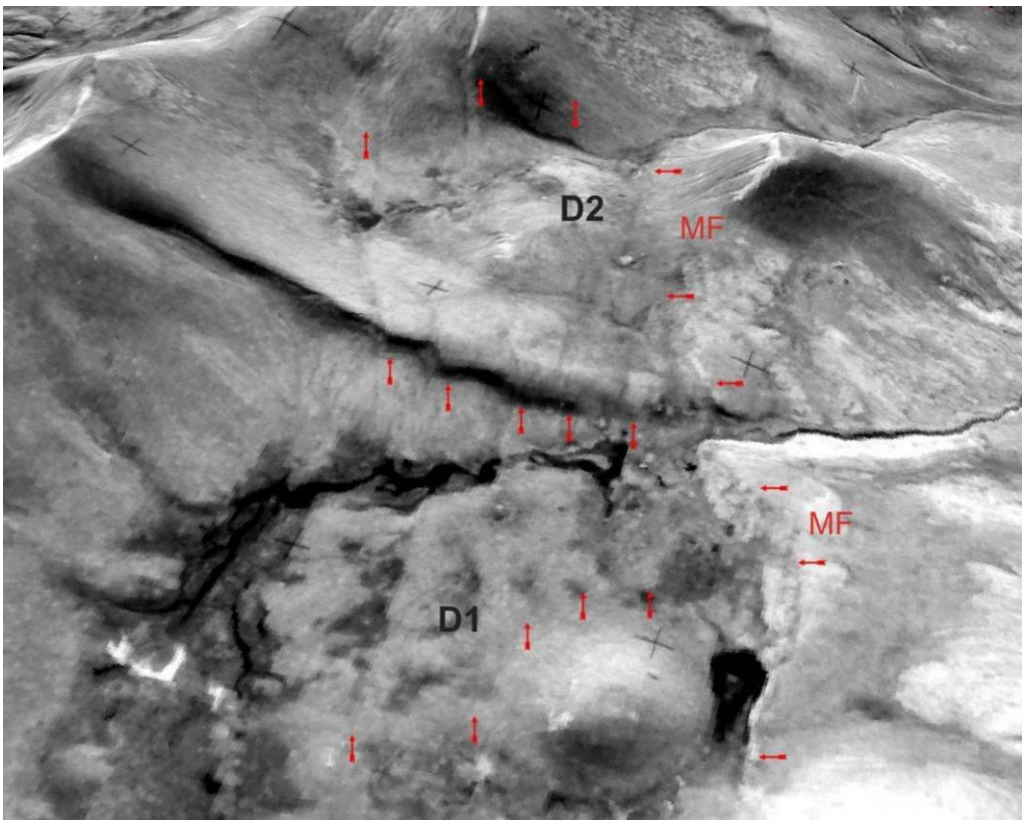
Fig. 1.50: Traversing Depression D1, the system of 8 to 10 juxtaposed sub-parallel fault branches dislocates the river and the watershed range by 230-240 m horizontally and by 24-28 m vertically.
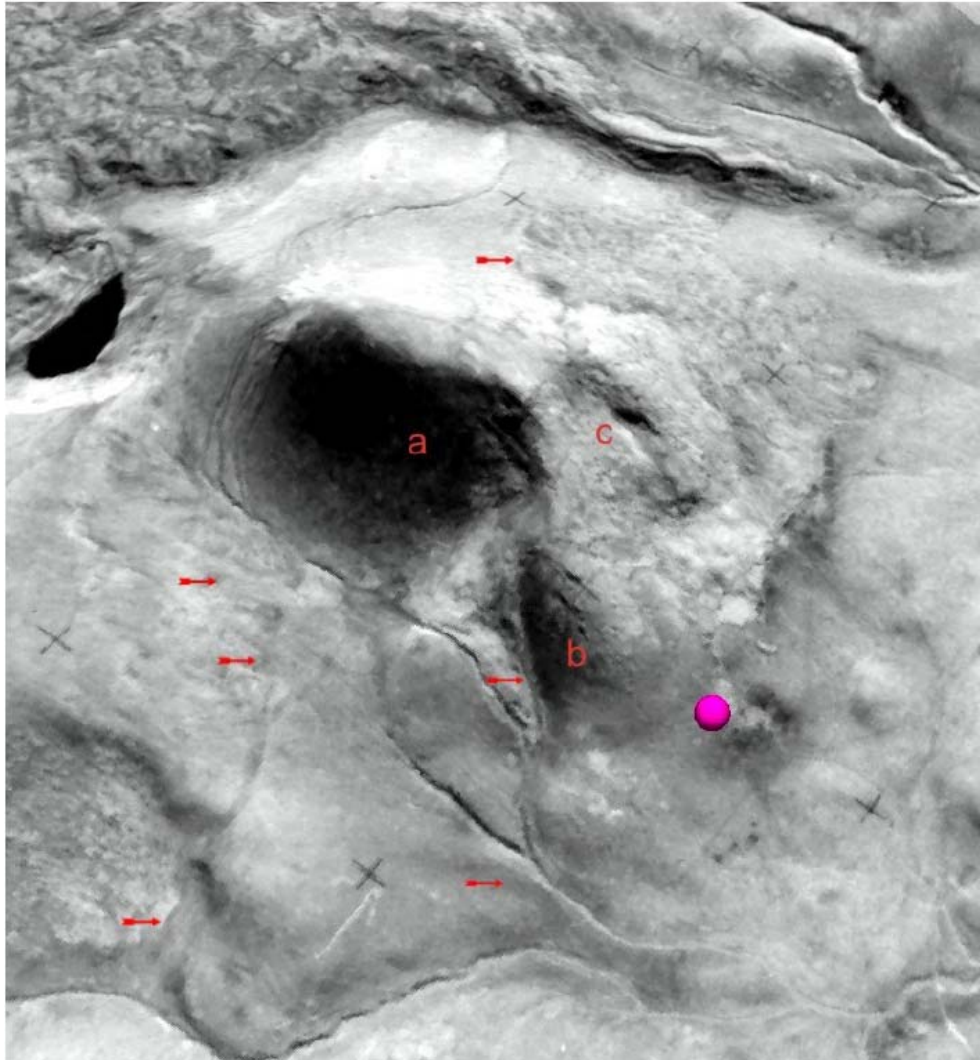
Fig. 1.51: The offset of the Karkar volcano
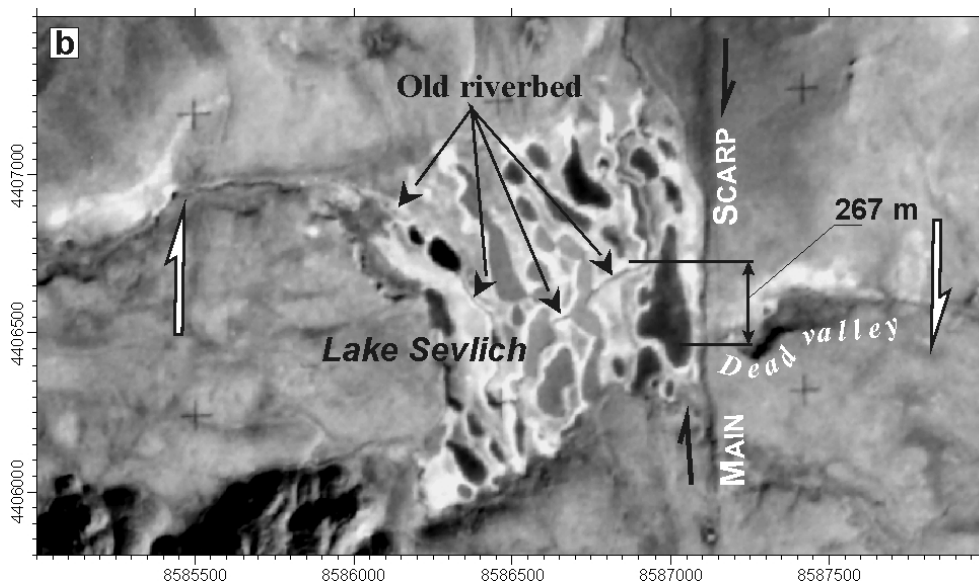
Fig. 1.52: Faults of the eastern sides of the *pull-apart* basin. Depression D3 was formed by the system of 8 to 10 faults and filled with Lake Sevlich waters. The faults caused a right-lateral offset by 267 m of a large river, created the tectonic dam on the river and shaped the dead valley.
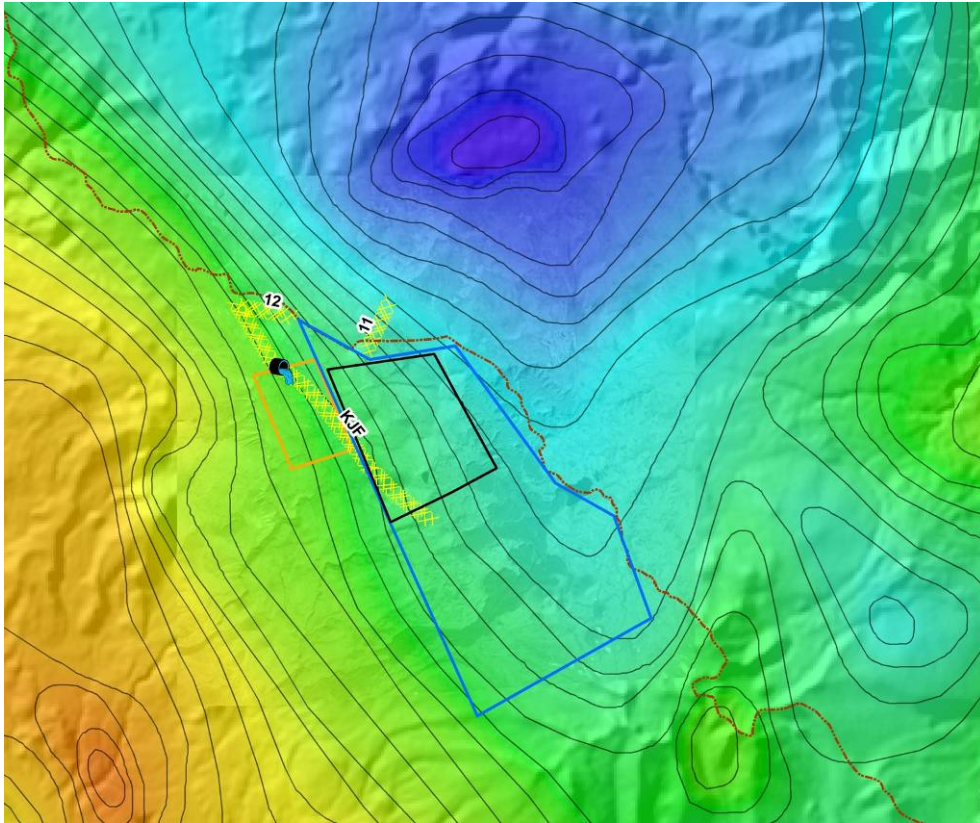
Fig. 1.53: Large negative anomaly of the gravity field, with the sites of Karkar and Jermaghbyur located on the southwestern side of its area
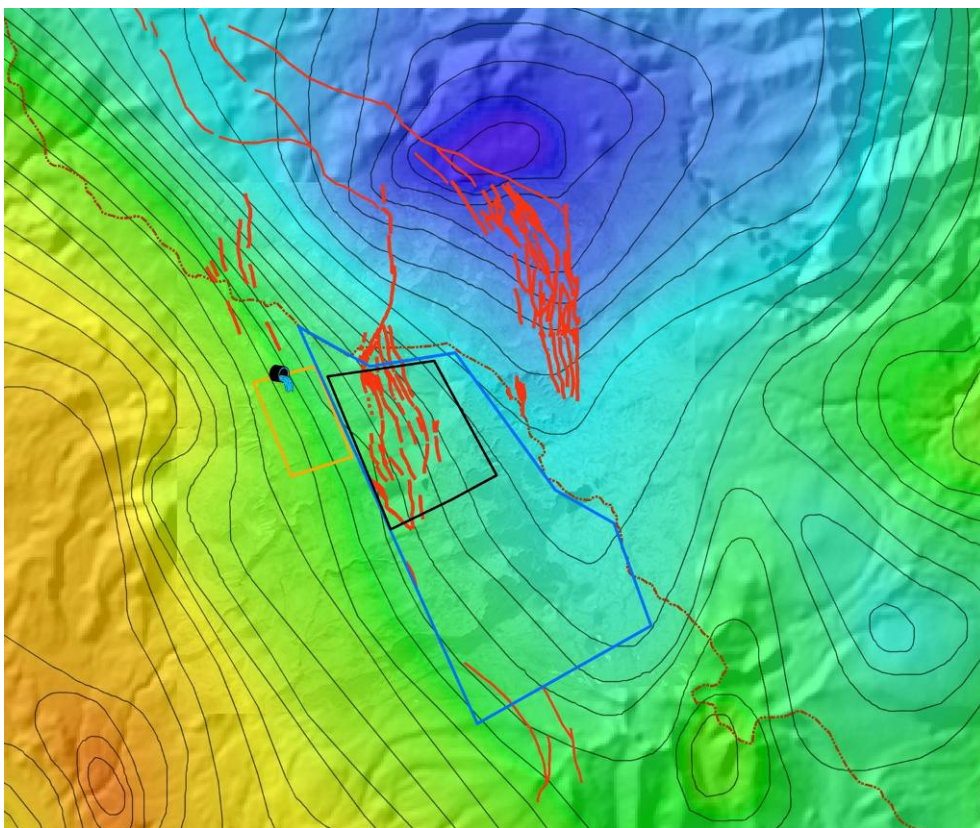
Fig. 1.54: South-elongated configuration of the gravity anomaly is similar to the geometry of the southern flank of the *pull-apart* basin structure
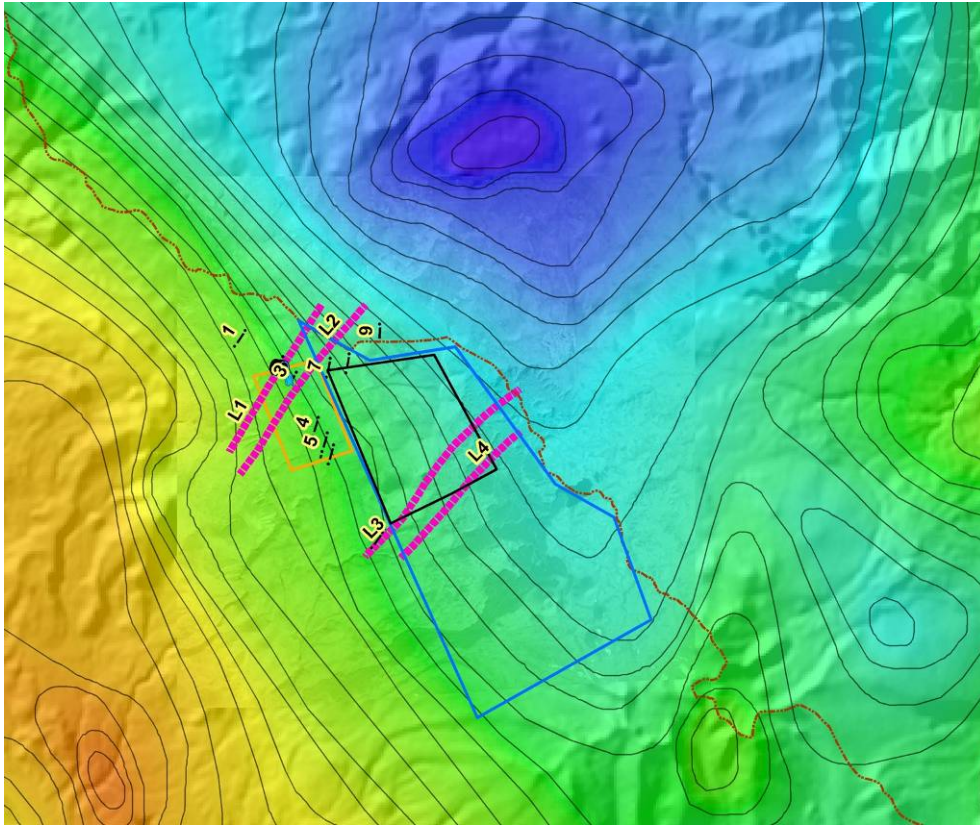
Fig. 1.55: Lineaments L1, L2, L3 and L4 in IGES 2004 Model are not reflected in the gravity field.
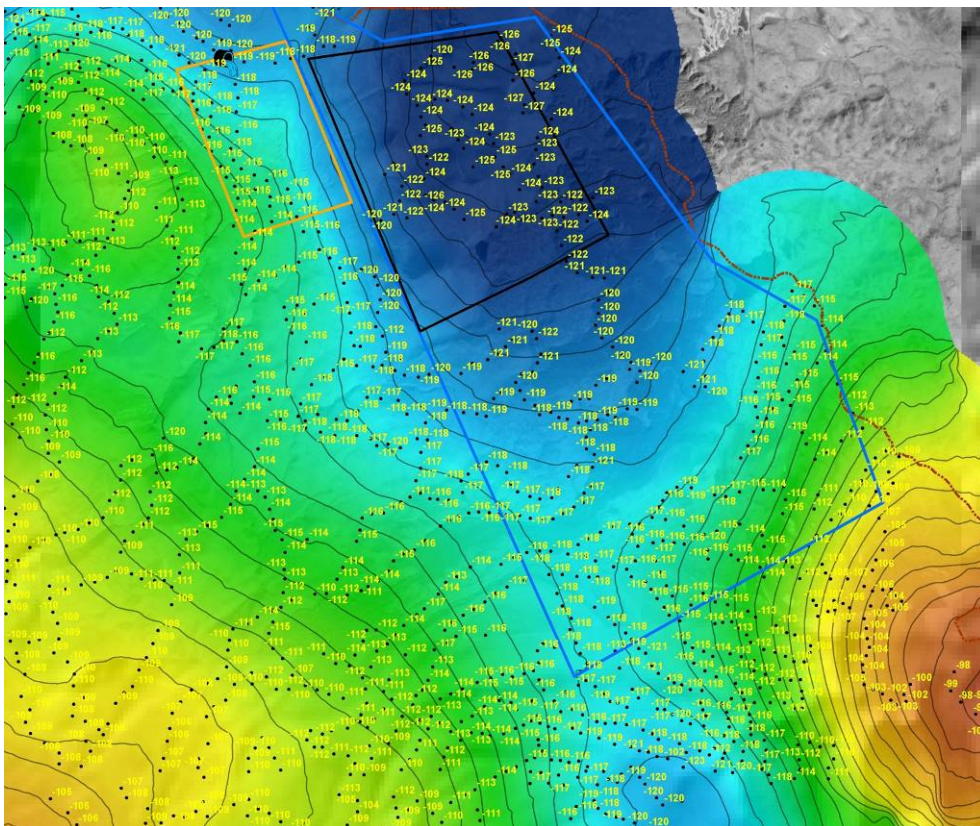
Fig. 1.56: Gravity map at the scale of 1:50,000
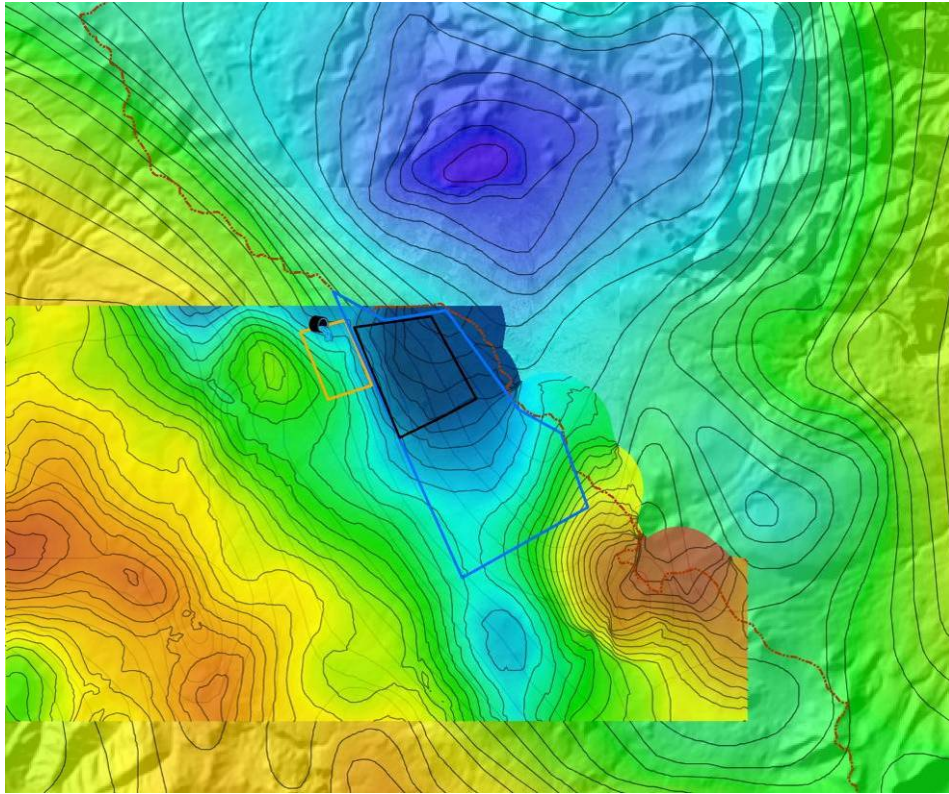
Fig. 1.57: Gravity map at the scale of 1:50,000 bears evidence of a clearly developed negative gravity anomaly stretching to the N-NW and accommodating the sites of Karkar and Jermaghbyur on its western flankp
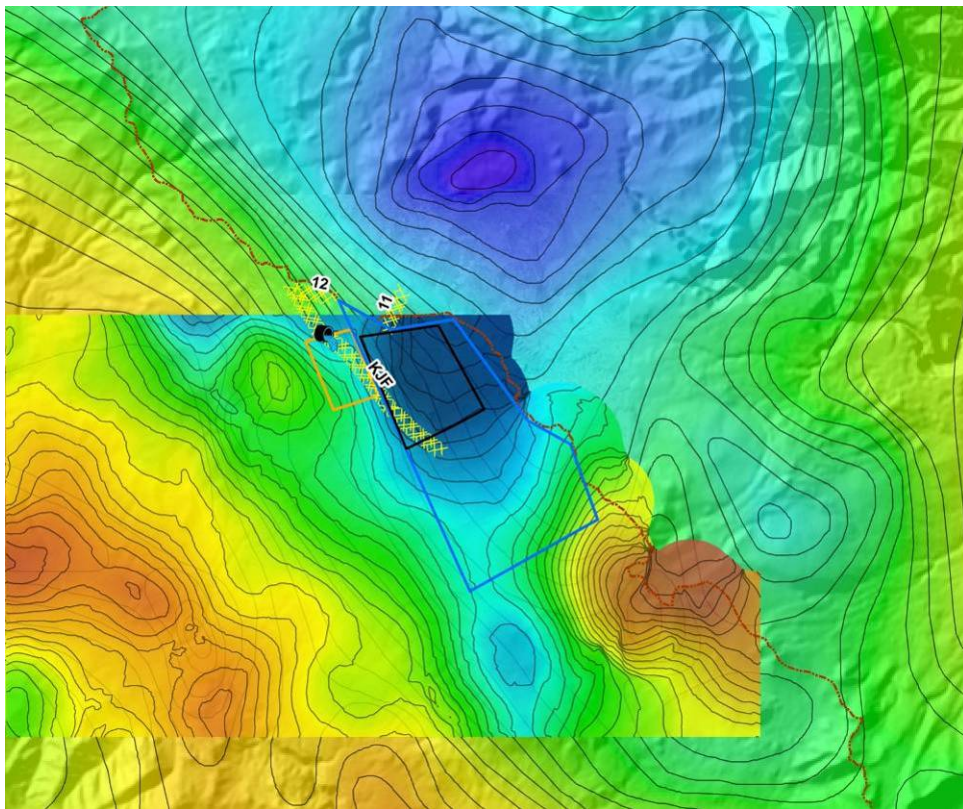
Fig. 1.58: The Karkar-Jermaghbyur Fault
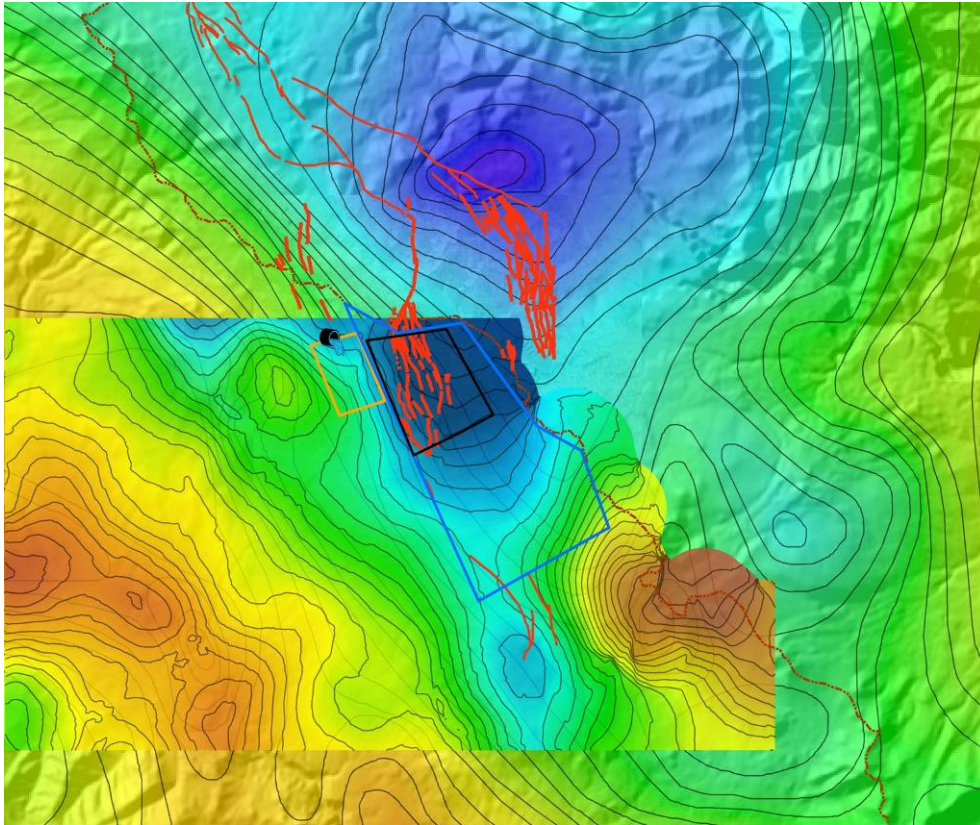
Fig. 1.59: High correlation of geometries of the western and eastern fault branches, bounding the "pull-apart" basin, and of the gravity anomaly.
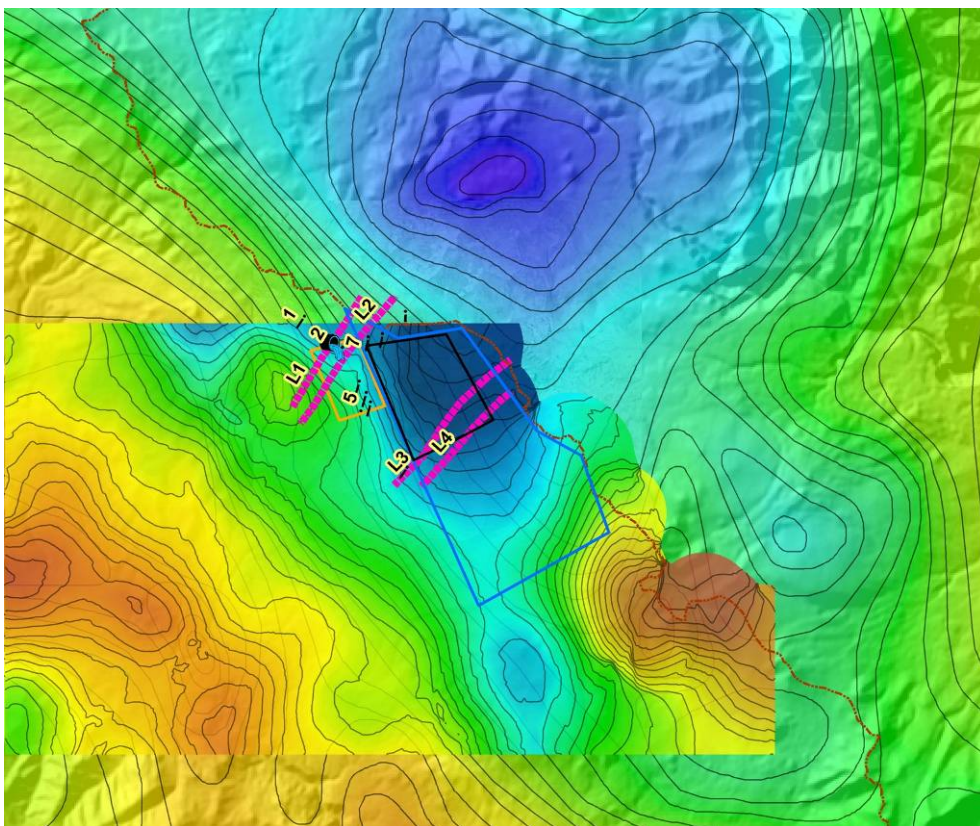
Fig. 1.60: The IGES 2004 Model is not supported by the 1:50,000 gravimetric survey data.
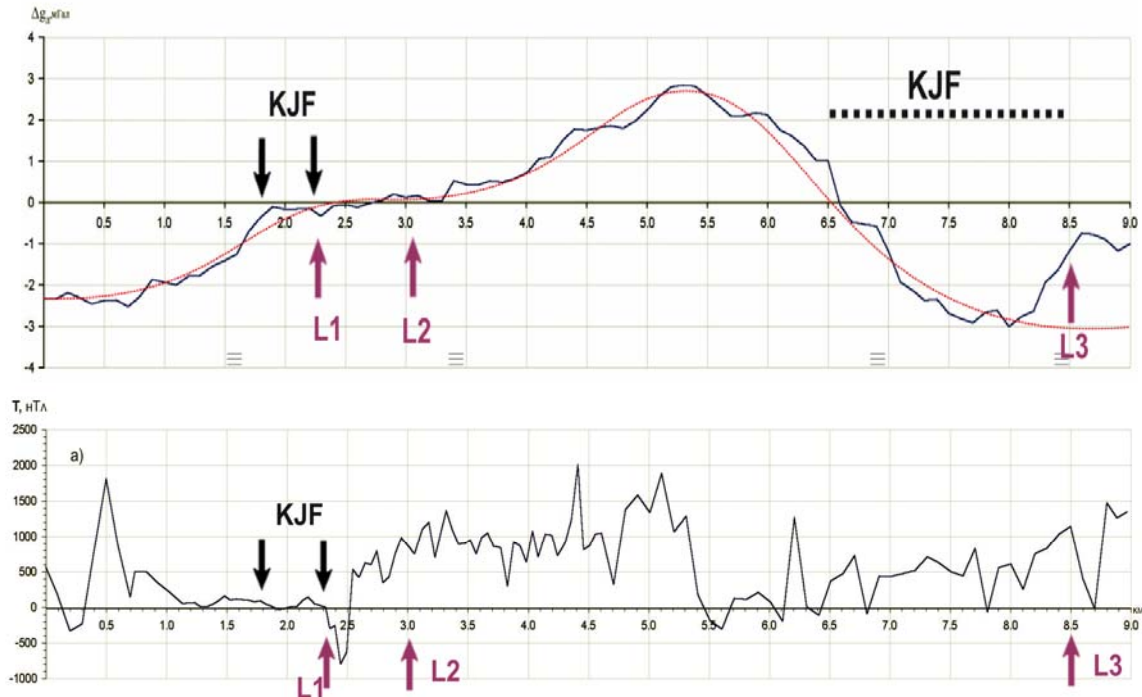
Fig.1.61a: Profile 1 reproduced from the IGES Report of 2004: gravimetric and magnetometric surveys.
KJF –the Karkar-Jermaghbyur Fault (Model 1988); L1, L2 and L3 – lineaments from the IGES 2004 Report (Model IGES 2004
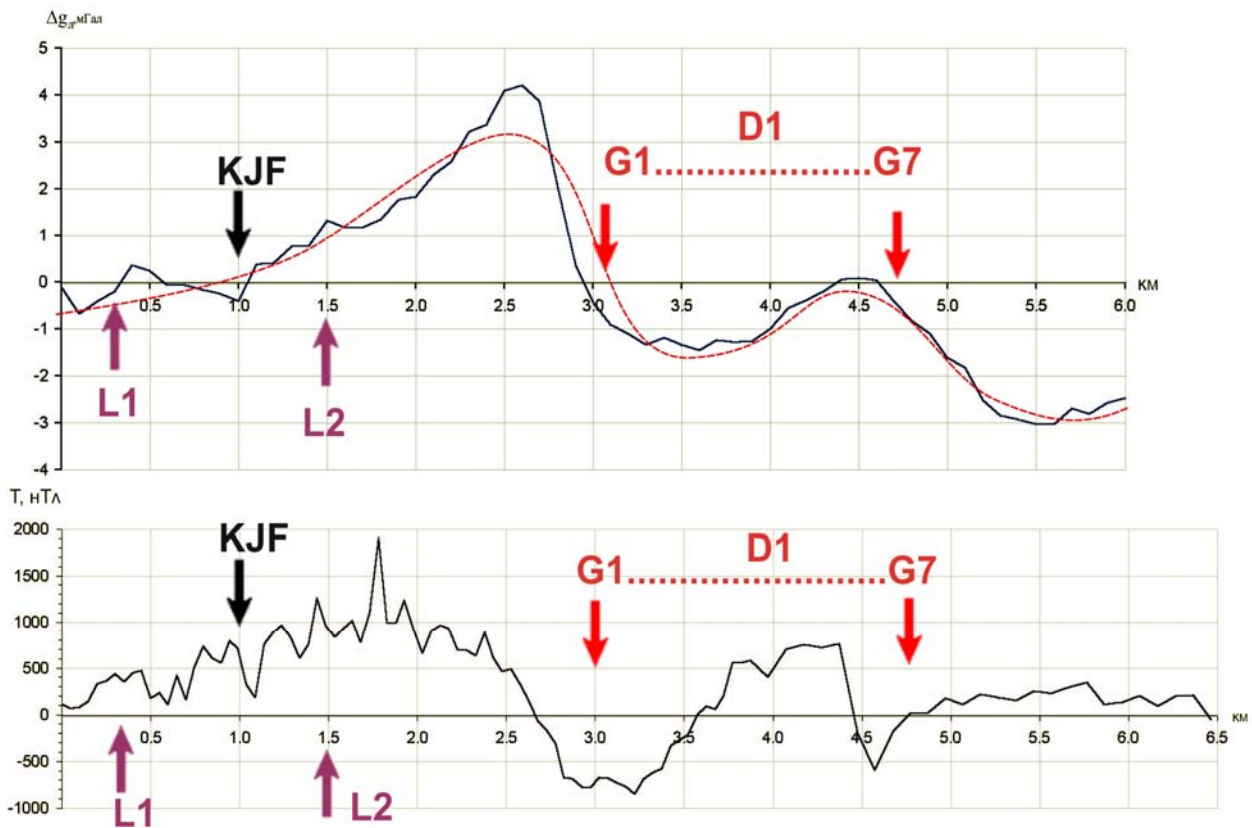
Fig. 1.61 b: Profile 2 reproduced from the IGES Report of 2004: gravimetric and magnetometric surveys.
KJF –the Karkar-Jermaghbyur Fault (Model 1988); L1 and L2– lineaments from the IGES 2004 Report (Model IGES 2004); G1…G7 – seven strike-slip faults traversing Depression D1 (Model GEORISK 2009).
.

65
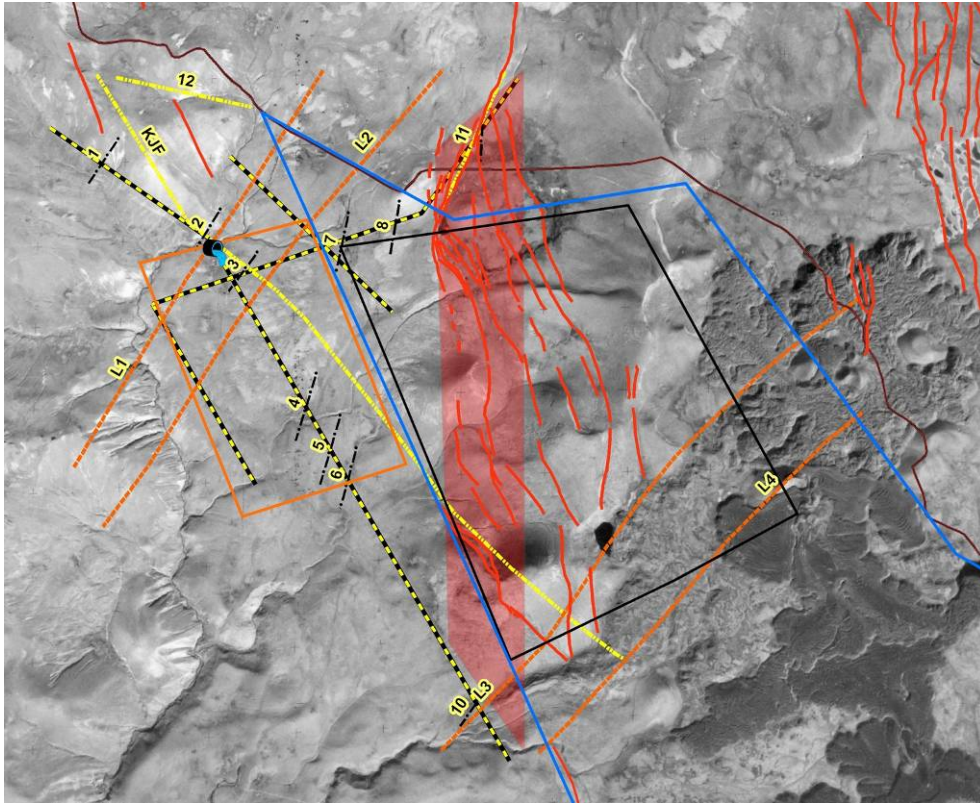
Fig. 1.62: The anomaly detected by the MT survey of 2004 and interpreted in the IGES Report 2004 as a conduit of fluids (red band). The zone coincides with the active faults that border the *pull-apart* basin in the west according to the **GEORISK 2009 Model**
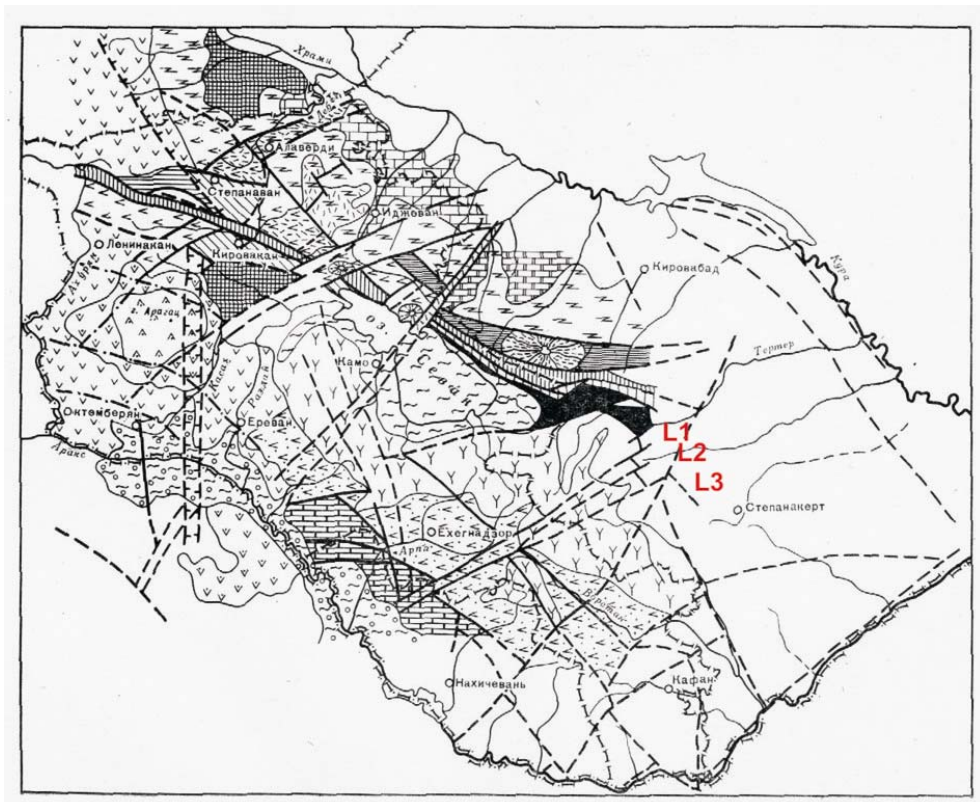
Fig. 1.63: Map of lineaments reproduced from Toumanyan (1983) that served the basis to identify Lineaments L1, L2 and L3 for the **IGES 2004 Model**

66

а

b

c
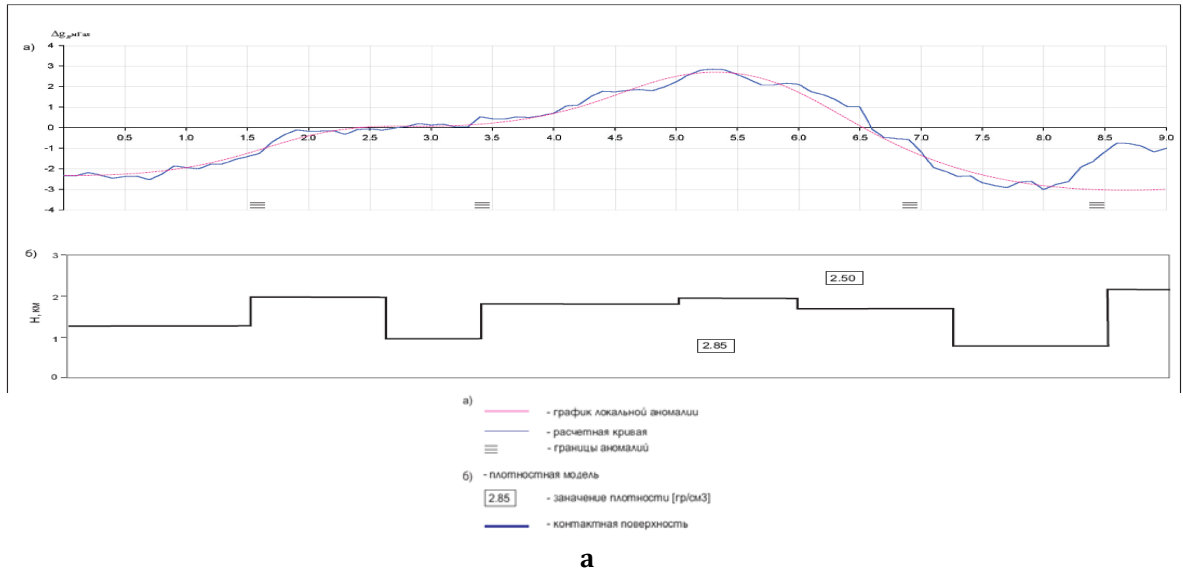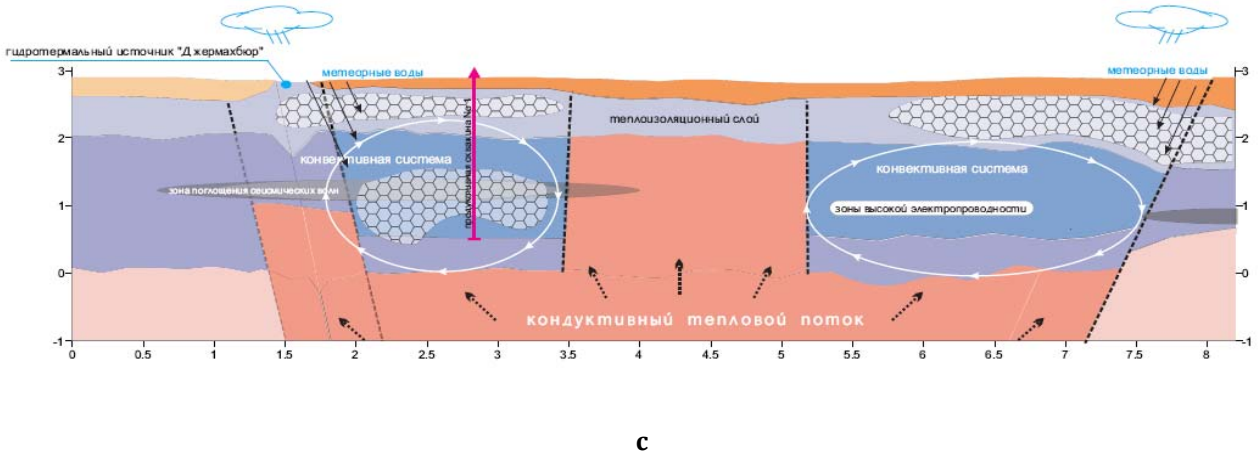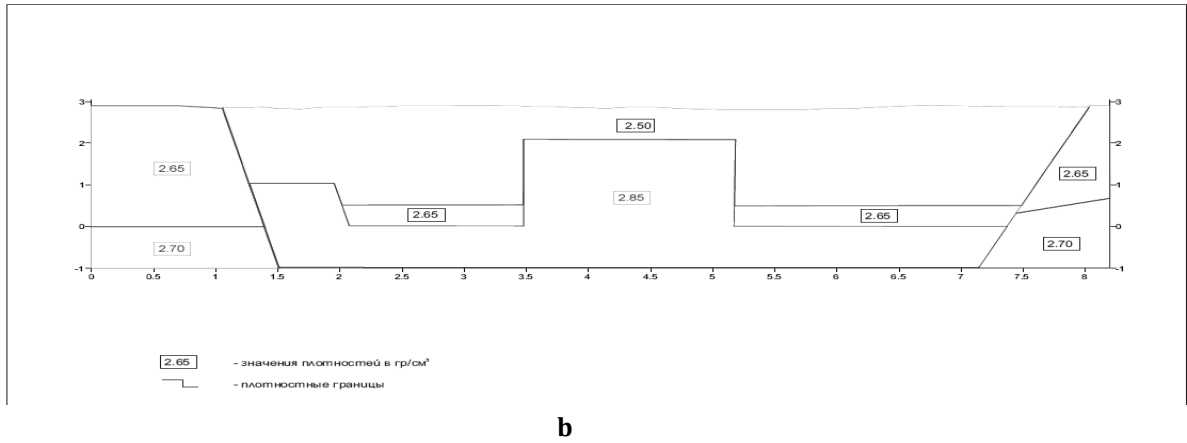
Fig. 1.64:
a: Gravity model for Profile 1, reproduced from Fig. 4.6 in the IGES Report (2004,); **b** – gravity model for the same Profile 1, but this time reproduced from the next Fig. 4.7 of the IGES Report (2004); **c** – conceptual model of the Jermaghbyur site from the IGES Report 2004 built along Profile 1. There is clear conflict between the two gravity models reproduced from Figs 4.6 and 4.7 based on the same profile. It is not clear whether the gravity model shown in Fig.1.64b served the framework for the development of the conceptual model, or, on the contrary, the conceptual model dictated the need of introducing the changes observed between the gravity models shown in Figs. 1.64a and 1.64b.

Part II

INTERPRETATION OF DATA AND CONCEPTUAL MODELING

Part 2. INTERPRETATION OF DATA FROM THE STUDIES CONDUCTED IN 2009 AND 2011 AND EARLIER; CONCEPTUAL MODELING

1. STRUCTURAL MODEL "GEORISK-2009"

The main structural concept adopted by Model GEORISK-2009 is that it identifies a large structure of *pull-apart* basin, bounded by the system of active strike-slip faults on the flanks. Intense tensile stresses appearing inside the *pull-apart* basin determined development of the Pleistocene and intense Holocene volcanism and could have facilitated origination of geodynamic settings favorable for the formation of a geothermal reservoir.

Faults bounding the structure of the pull-apart basin can be clearly distinguished on the satellite images and in the surface geological structure (see paragraphs 4.2.3, 4.2.4, 4.2.5 and Table 1). Currently, the model based on *pull-apart* basin structure is the best supported and matching the purpose of continued interpretation of the evidence collected by the geological and geophysical studies, and assessment of the geothermal potential of the Karkar site.

We note an important feature of the structures bounding the *pull-apart* basin on the sides.

Fault systems on the western and eastern sides of the *pull-apart* basin consist of 8 to 10 juxtaposed branches of active faults (Figs. 1.21, 1.22, 1.45, 1.46, and 1.47). At depth, these faults shape a *negative flower*-type structure. The center of the *flower* structure accommodates eruption channels of the Pleistocene and Holocene volcanoes and their lava fields (Fig. 2.1).

In the landscape, the systems of converging faults have developed distinct scarps with vertical displacements ranging from 3-5 to 20-50 m (1, 2, 3 and 4 in Fig. 2.2) and horizontal displacements from 270 to 1,000 m (3, 5 and 6 in Fig. 2.2. Fault planes curve helicoidally and dip inside the *pull-apart* basin (Fig. 2.1; 7 and 8 in Fig. 2.2). On the flanks of the *pull-apart* basin, these fault systems are accompanied by depressions D1 and D2 in the west, and D3 in the east. A crater-like depression D1 has a radius of 3 km and is apparently of volcano-tectonic origin. The bottom of this depression is covered by small lakes and a vast marsh (Figs. 1.47, 1.50, and 2.2). Depression D2 has similar structure. Depression D3 also has a volcano-tectonic nature, and its deepest part is filled with the water of Lake Sevlich formed by the tectonic damming of the rivers intercepted by the faults (Fig. 2.2).

In the limits of Depressions D1, D2 and D3, distances between neighboring faults range from 100 to 500 m. The faults have developed these depressions within strands that are 5 km and 8 km long (and maximum 2.3 and 2.5 km wide) on the western and eastern flanks, respectively. Blocks bounded between the faults experience tension, horizontal displacements, tilting and rotation. Northern and southern flanks of the same blocks are sometimes recorded to have been rotated in opposite directions since the fault planes are helicoidally turned (Fig. 2.2). Such pattern of structure and kinematics suggests that zones located on the lateral margins delimiting the *pull-apart* basin, where the neighboring faults and depressions have formed, are highly permeable and mobile.

Some of these faults were identified by the early studies of 1988-89 (for example, N11 in Figs. 1.43 and 1.44) and interpreted as structures formed by gravitational subsidence during volcanic eruptions, sometimes related to magma chamber empting. Such interpretation assigned a non-tectonic origin to the identified scarps and faults, and hence they were no longer accounted for in the structural models. Although this concept of volcano-gravitational origin is from time to time brought forward even now, we believe it is wrong and provide statements to reject it as the one unable to explain the faulting on the sides of the *pull-apart* basin.

It is common knowledge that failure structures may develop during and shortly after volcanic eruptions, and form surface subsidence features accompanied by surface faulting. Such structures have extremely small length, not more than the first tens, or, rarely, hundreds of meters. Moreover, they develop clear vertical offsets mostly by normal-slip kinematics, but never produce large-scale horizontal strike-slip, or strike-slip and reverse-fault displacements. In the considered study we investigate the Pambak-Sevan-Syunik fault, the largest and most active fault in Armenia. It is about 300 km long and cumulative rate of its horizontal strike-slip displacements, recorded at the Karkar Site, range up to 1 km. It has been observed to develop many offsets by strike-slip and reverse faulting, with vertical displacement (reverse-fault) components ranging up to 30-40 m. Hence, volcano-gravitational origin can not be suggested for the faults bounding the structure of the *pull-apart* basin. This inference is supported also by the gravity field that reflects the faults clearly, attesting that they penetrate to a considerable depth of many kilometers. Faults generated through volcano-gravitational subsidence do not penetrate deep or reflect in the gravity field.

Strong earthquakes generated many surface ruptures in the zone of these faults, which is another definitive proof of their tectonic origin, since the earthquakes occurred much later than the last volcanic eruptions. The paleoseismological and archaeoseismological investigations conducted in cooperation with specialists from France (Montpellier-2 University) and Russia (Geological Institute of the RAS) recorded ruptures caused by earthquakes in the magnitude range of M7.2–7.4 both on the western and eastern margins of the *pull-apart* basin. The surface ruptures produced by those strong earthquakes displaced walls of Middle and Late Bronze Age archaeological structures found on the western and eastern structural margins of the pull-apart basin (Figs. 2.3 and 2.4). The paleo-seismological studies on the southern termination of the *pull-apart* basin and age estimations by the OSL and C-14 methods helped to identify earthquakes that have ages of 3,700, 7,800 and 8,500 years BP (Figs. 2.3 and 2.4). Strong earthquakes in the range of M=7.0-7.4, accompanied by surface ruptures tens of kilometers long, were recorded along the faults located north of the Karkar Site, at the distance of 14 and 35 km far from it (Fig. 2.5).

From the statements above, it is possible to draw important inferences that will be used in the interpretation of the geothermal potential of the Karkar Site:

1. **The main structural feature of the Karkar region is the presence of a large *pull-apart basin* flanked by a system of active strike-slip faults. Strong tensile stresses within the structure of the *pull-apart* basin had been determining development of volcanism in the Pleistocene and, more intensely, in the Holocene, and could have facilitated evolution of geodynamic settings favorable for establishment of a geothermal reservoir.**
2. **The systems of 7 to 10 sub-parallel faults and depressions, filled with lake waters and located on the sides of the *pull-apart* basin, might represent the most permeable zones, enabling transportation and circulation of meteoric waters at depth, and the ascending of hot fluids to the surface.**
3. **Surface rupturing produced by earthquakes in the magnitude range of M=7.2-7.4 within the system of sub-parallel faults, delimiting the *pull-apart* basin, indicates that the faults might penetrate to a depth not less than 15-20 km, as this is the depth range of strong earthquake hypocenters and seismic focal surface in Armenia.**

2. INTERPRETATION OF THE 2D AND 3D MT STUDY DATA OF 2004, 2009 AND 2011

Sections 3.2 and 4.1 in the first part of this report demonstrate good correlation of the results from the MT surveys conducted in 2004, 2009 and 2011, as well as between the 2D finite models produced independently based on the surveys of 2009 (Figs. 1.26 - 1.28 and 1.35 -1.39). This is additionally confirmed by the pictures shown in Figures 2.6, 2.7 and 2.8 and allows considering the evidence provided by the surveys of 2004, 2009 and 2011 reliable and applicable for interpretation.

The MT data of 2004, 2009 and 2011 were introduced into *ArcScene 9.3*. The data of the 3D MT and gravity surveys, introduced into ArcScene 9.3, enabled 3D interpretation over an area of 20 km² and to the depth of up to 2 km. By applying the 2004 and 2009 2D MT survey profiles, dimensions of the interpreted site were expanded up to a band 10 km wide in the W-E direction and up to 20 km deep.

The following layers were introduced into the *ArcScene*:

- Digital elevation model at the scales of 1:25,000 and 1:10,000;
- Air photos;
- Structural models 1988, IGES 2004, and GEORISK 2009;
- Locations of Borehole no. 4, thermal springs of Jermaghbyur, Jermouk, Jermajour (Isti-Sou), Ouits and Vorotan, zones of altered rocks, Pleistocene and Holocene volcanoes and their lava flows,
- Anomalous zones with higher rates of seismic wave attenuation identified by the seismic prospecting works of 1987/88;
- Maps of gravity field anomalies at the scales of 1:200,000 and 1:50,000;
- Geology map at the scale of 1:50,000;
- **Model MT 2004** - 2D finite model from the MT 2004 survey along Profile 1 with the depths of 4 km and 20 km,
- Zones identified in the **MT Model 2004**, including zones of low resistance of rocks, promising areas of geothermal water deposits, zones of supposed intrusions, the zone interpreted as a conduit for geothermal fluids, and locations of the proposed production well;
- **Model MT 2009 "GEORISK/USF"** - 2D finite model of MT 2009 survey according to the interpretation done by "GEORISK" CJS and the University of South Florida, with the depth of 5 km (two options);
- **Model MT 2009 "Nord-West"** - 2D finite model of the 2009 MT survey according to the interpretation done by "Nord-West", with the depth of 3 km,
- **Model MT 2009 "Nord-West"** - 2D finite model of the 2009 MT survey interpreted by "Nord-West", with the depth of 10 km.
- **Data of the 3D MT survey of 2011 in the form of horizontal sections having an area of 20 km² and the depths of 0 m, 500 m, 750 m, 1000 m, 1500 m and 2000 м (Fig. 2.9);**
- **Data of the 3D MT survey of 2011 in the form of 10 vertical sections (5 sections oriented North-to-South, and 5 sections oriented West-to-East (Fig. 2.10);**
- **Based on the 3D MT survey data of 2011, three-dimensional MT grid was plotted (Fig. 2.10);**
- **Based on the 3D MT survey data of 2011, three-dimensional grid was plotted in ArcScene 9.3 (Fig. 2.11).**

Five (5) layers are clearly identified along Profile 2 in all MT survey models of 2004 and 2009.

The following layers can be identified from the top to the bottom:

- **Layer 1** is a sub-horizontal layer spreading from day surface to the depth of 250-400 m (thickness of 250-400 m); rocks with high resistance values (hundreds and thousands of Ohm-meters). Apparently, this stratum corresponds to volcanic rocks (basaltic andesite). It develops the greatest thickness and has the highest resistance values along the eastern contour of Depression D1, within areas of development of the Pleistocene volcanoes (Figs. 2.6 to 2.14).

- **Layer 2** is a sub-horizontal layer spreading in the depth interval of 300-1,000 m (400-700 m thick). The rocks have low resistance values of 10-20 Ohm-m. Models MT 2009 "GEORISK/USF" and MT 2009 "Nord-West" both record the lowest resistance values at MT profile Points NN 4-7 and 15-17. Points 4 to 7 correspond to Depression D1, and Points 15 to 17 to Depression D3 (Figs. 2.6 to 2.14). Model MT 2004 records low values of resistance also at the site of Depression D1 (Fig. 2.7). Around Points 12-11, the lower boundary (bottom) of Layer 2 plunges abruptly to a depth of 1,500-1,600 m (Figs. 2.6, 2.7, 2.8, and 2.12). The evidence of the 3D MT is also clearly indicative of Layer 2 (Figs. 2.9, 2.11, 2.12, and 2.13). The lowest resistance values and the greatest thickness of Layer 2 correspond to the region of Depression D1 (Figs. 2.11 and 2.14). Fig. 2.14 shows it clearly that Layer 2 is bordered on its flanks by the system of faults creating the structure of *pull-apart* basin. Layer 2 is interpreted as a zone of fractured and water-saturated rocks (Model "GEORISK/USF") and/or as a zone of higher content of mineralized, high-temperature thermal waters, promising for the search of geothermal energy sources (Model "Nord-West").

- **Layer 3** fills in the spaces between Layers 2 and 4 and spreads within the depth interval of 1,000-3,000 m (Figs. 2.6 to 2.14). In the east, the thickness of this layer is less than 1 km, but an in the west it is 2-2.5 km thick. Model MT 2009 "GEORISK/USF" highlights it with green color, and Model MT 2009 "Nord-West" with light-blue colors (Figs. . 2.6, 2.7, and 2.8). This divergence is explained by the difference of scales applied in the models. The layer is characterized by resistance values in the range from 200 to 50 Ohm-m. An important feature of this layer is that according to the "GEORISK/USF" model, its lower boundary (bottom) plunges to the depth of 2,500 m around Points 14-10 (Fig. 2.6). Model "Nord-West" records the lowering of the layer around Points 14-7 (Fig. 2.7). In the west, both models show Layer 3 at much lower position, matching the depth of 3,000 m. Model "Nord-West" interprets this lowering as a potential fault zone (Fig. 2.7) with rock resistance values decreased to as low as 70-100 Ohm-m. Layer 3 is well noticeable also by the results of the 3D MT sounding conducted in 2011 (Fig. 2.11).

- **Layer 4.** This layer is identified as two large blocks separated with Layer 5 (Figs. 2.6 and 2.7). The 2D and 3D models have detected the upper boundary of the blocks at the depth of about 1,500–1,800 m. It is difficult to detect the lower boundary; in the west of the Profile, Layer 4 spreads to the depth of 10,000-12,000 m and might be terminating there. Layer 4 includes rocks with very high resistance values (1,000-2,500 Ohm-m). The three models all detect gradual increase of resistances from the outer boundaries of Layer 4 toward its inner areas (Figs. 2.6, 2.7, 2.11 and 2.12). Layer 4 may be interpreted as slightly fractured blocks of metamorphic basement or intrusion, not saturated with water.

- **Layer 5** is a vertical (Model "GEORISK/USF") or east-verging (Model "Nord-West") layer spreading down to a depth of more than 10 km (Figs. 2.6, 2.7, 2.11 and 2.12). Higher to

the surface, Layer 5 joins Layers 3 and 2 around Profile Points 14-7. The layer is characterized by low resistance values of 20-30 Ohm-m. Model "Nord-West" detects the lowest resistance values in the depth range from 3,000 to 5,000 m (Figs. 2.7 and 2.8). Model "GEORISK/USF" and Model "Nord-West" both interpret Layer 5 as a large faulting zone (Figs. 2.6, 2.7, and 2.8). The "Nord-West" Model, as well as the MT 2004 Model, considers it is a deep conduit for heat carrier fluids ascending from an object located in depth up to the surface

The report from "Western Geco" company provides the results of 3D MT data inversion of 2011. The main outcome of the performed 3D inversion of new data is the recorded conductive layer, which is 600 m thick and oriented approximately SW-to-NE, its basis located, by rough estimations, at a depth of 1000 m to 1250 m. According to the data of 'Western Geco", the thickness and depth of the identified conductive layer are varying; however, it is possible to identify three distinct anomalies - A, B, and C. Fig. 2.9 from the report by "Western Geco" shows the resistivity section based on the final 3D MT model along with the full Bouguer anomaly and superimosed trace of the interpreted base of conductor. The correlation of the 3D inversions accomplished by "Western Geco" in 2012 with the 2D inversion data, produced by "Nord-West" company in 2004, and by the South Florida University and "Nord-West" in 2009 indicates that Layer 2, as identified by the 2D inversions, is matching fully Anomalies A, B and C (Figs. 1.27, 1.28, 1.35, 1.36, 1.37, 1.39, and 1.40). Table 2.1 shows a brief summary of the results of all MT investigations conducted within the period since 2004 till 2012.

Tab.2.1. Summary of the results of the 2D and 3D MT surveys conducted in the area of the Karkar Site in 2004-2011

NN	MT data	Field MT surveys realized	MT data inversion	MT inversion interpretation	Results
1	**2D MT, 2004** "Nord-West" Company (Russia)	yes	yes	yes	**Layer 2** **Layer at the depth of 400-1200 m; Abnormally low resistance horizon (40-60 Ohm×m) and** **Layer 5** **10 km-deep layer**
2	**2D MT, 2009** South Florida University (USA)	yes	yes	yes	**Layer 2** **Layer at the depth of 300-1000 m (400-700 meters thick) with low resistance of 10-20 Ohm×m**
3	**2D MT, 2009** "Nord-West" Company (Russia)	no	yes	yes	**Layer 2** **Layer at the depth of 300-1000 m (400-700 m thick) with low resistance of 10-20 Ohm×m.**
4	**3D MT, 2011** "Western Geco" Company (Italy)	yes	yes	yes	**Anomalies A, B, and C, which correspond to Layer 2** **Layer at the depth of 500-1200 m (600 m-thick) having low resistance and oriented approximately SW-to-NE**

Therefore, the 2D MT survey of 2004 and 2D MT survey of 2009, as well as the 3D MT survey of 2011, were conducted by three different groups from Armenia, Russia and USA. The 2D MT data collected in 2009 were independently interpreted also by two groups from the US and the Russian Federation. Data of 3D MT survey of 2011 had been tentatively interpreted by "Western Geco". All interpretations are similar and thus attest to the credibility of the MT survey evidence and of the interpretations.

The models developed in 2004, 2009 and 2012 indicate the following features of the Jermaghbyur and Karkar sites that are important for consequent interpretation:

- The models all record the zone of low resistance values (Layer 2 according to the 2D inversions, or Anomalies A, B, and C, according to the 3D inversion data) at depths from 500 m to 1,200 m. The lowest values of rock resistivity (10-20 Ohm×m), along with the greatest thickness of the layer, are recorded within the site of Depression D1 in Anomaly A zone, according to the evidence of 3D MT inversion.
- Around Points 7-14 of the 2009 Profile and Points 22-30 of Profile 2 surveyed in 2004, it appeared possible to record a vertical or slightly east-verging zone of Layer 5 with low resistance values of 20-30 Ohm-m, extending to a depth of more than 10 km. Closer to the surface, the vertical zone joins the horizontal zone of Layer 2, which is also characterized by low values of rock resistance. At the place of junction, the lower boundary of Layer 2 is as low as 1,500-1,600 m. The lower boundary of Layer 3 is also sinking inside the vertical zone of Layer 5.
- The vertical zone with low resistance values separates two areas in Layer 4 that have very high resistances.
- Model "Nord-West" 2009 identified a small, west-verging vertical zone with resistance values in the range of 70-100 Ohm-m. According to this model, the lower boundaries of Layers 2 and 3 are also plunging inside the vertical zone.

We suggest the following combined interpretation of the 2D MT survey data of 2004 and 2009, and the 3D MT survey of 2011. The projection of vertical Layer 5 onto the surface matches the centre of the *pull-apart* basin structure, accommodating many Pleistocene and Holocene volcanoes. The vertical Layer 5 with low resistance values could be interpreted as a fault zone located inside the *pull-apart* basin that separates the two blocks in Layer 4 and spreads more than 10 km deep (Figs. 2.6 to 2.14).

The 2004 MT Model and "Nord-West" MT Model both interpret the vertical zone in Layer 5 as a deep-seated conduit of heat carrier-fluids ascending from an object located at depth up to the surface. The vertical zone in Layer 5 is presumably the central part of the *pull-apart* basin structure. This is the zone of principal displacement (PDZ), where the greatest tension deformations concentrate and the fracturing is intense. Hence, this is the highest permeability zone. Such structural interpretation supports the assumption that the vertical zone in Layer 5 could be a conduit channeling meteoric water to the depth and the heated mineralized waters upwards.

The second vertical zone identified by the "Nord-West" MT Model might be also interpreted as a fault zone. It has much smaller size and is inclined westward. Model "Nord-West" suggests that Layer 2 is detected higher at Point 5 of the profile surveyed in 2009 and interprets this as detection of potential surface outcrop of a fault (Fig. 2.7B). The fault has been indeed recorded at Point 5 on the surface (Fig. 1.25). It is difficult to judge whether the second vertical zone is one of the faults in the system bounding the *pull-apart* basin, or corresponds to the same Karkar-Jermaghbyur Fault. Considering that neither MT Model 2004, nor Model "GEORISK/USF" identifies it, the presence of this fault is still open to question.

MT Model 2004 and MT Model "Nord-West" both interpret Layer 2 as a zone of higher content of mineralized, high-temperature thermal waters, promising for the search of a geothermal energy source.

None of the models developed in 2004, 2009 or 2012 records anything that could be interpreted as a magma chamber filled with not cooled substance and located 1.5 km deep, as suggested by the interpretations of seismic anomalies in 1989-2004 (see section 2.2 in this report). Most probably, the zone of increased seismic wave attenuation ratio identified by the studies of 1987/88 at the site of Jermaghbyur could be related to the system of 7-10 closely spaced faults and zones of fracturing in between them. We must comment that Dr. G. Grigoryan, who was the principal investigator of the seismic surveys, which identified the above anomalies in 1987-1988, characterized them saying that *«... the recognized zones of seismic wave attenuation were determined by diffraction of the seismic waves on local inhomgeneities».* What objects correspond to those local inhomgeneities is a question that has not been answered until today.

Based on this evidence, the following joint interpretation can be suggested for the 2D MT survey data of 2004 and 2009, and the 3D MT survey of 2011.

1. **The most important outcome of the MT survey of 2009 is identification of the sub-vertical zone in Layer 5, having low values of resistance (20-30 Ohm-m). The mentioned zone can be interpreted as a conduit of fluids ascending from a depth of more than 10 km. Faults, bounding the structure of the *pull-apart* basin, penetrate more than 15 km deep. The faulting and continuous motions deformed and split the monolithic and highly resistant Layer 4 into 2 separate blocks. The gap between the blocks represents a zone of developing tension deformations and intense fracturing. Tensile stresses, appearing inside the *pull-apart* basin structure, along with the rock fracturing, created a permeable vertical zone, where channels of the Pleistocene and Holocene volcanic eruptions were formed.**
2. **The two isolated high-resistance (1,000-2,500 Ohm-m) areas of Layer 4 can be interpreted as two blocks of intrusion, separated by the vertical zone of Layer 5 corresponding to the faults bounding the *pull-apart* basin.**
3. **The horizontal low-resistance zone of Layer 2, located at the depth of 500-1200 m, can be interpreted as follows. Hot mineralized waters ascending toward the surface through the vertical zone of Layer 5 could spread through the horizontal Layer 2 and mix with cold surface water. The lowest values of resistance (10-20 Ohm-m) in Layer 2 are recorded at the sites of Depressions D1 and D3, corresponding to the surface outcrops of the faults flanking the *pull-apart* basin on the sides. These faults can provide for transportation of meteoric water to depth and also for rise of hot fluids to the surface. The lower boundary of Layer 2 at points 11 and 12 on Profile-2009 plunges down to the depth of 2-2.5 km, where it joins the vertical zone of Layer 5. This may bear evidence confirming the link between Layer 2 and Layer 5.**
4. **The main three statements above are based on the results of independent interpretations of the 2D MT surveys of 2004 and 2009, as well as of the 3D MT survey of 2011, conducted by three different groups in Armenia, USA and Russian Federation. These three interpretations are mutually consistent. In aggregate, this confirms the credibility of the results of the MT surveys and that of their interpretation.**

3. GRAVITY MODEL: DATA INTERPRETATION AND MODELING

3.1. Introduction

Gravity anomalies are created by geologic structures that create lateral discontinuities in the crust. For example, faults may juxtapose rocks of different densities and therefore gravity anomalies (e.g., a change in the gradient of the gravity field) are frequently associated with faults. Gravity measurements involve collection of data at individual gravity stations where both relative change in gravity and precise location (horizontal and vertical) are determined. For the Kar Kar geothermal assessment, WesternGeco performed a gravity survey on a grid over a comparatively small area within the major area of interest. The goals of making this gravity map were to (*i*) identify geological discontinuities associated with potential fault-bounded basins, (*ii*) provide data to constrain the depth(s) of basins in the survey area, a key parameter for understanding the circulation and heating of groundwater, and (*iii*) compare gravity anomalies (and the resulting models) with resistivity anomalies identified as part of the 3D magnetotelluric (MT) survey and modeling effort. The primary origin of gravity anomalies in the region is related to the density contrast between quartz monzonite identified in Borehole 4 and the lava flow and alluvial package that fills the fault-bounded basin mapped within the survey area.

The WesternGeco gravity observation dataset included 257 gravity measurements and individual stations collected by WesternGeco. The data were collected on an approximately regular grid (Figure 2.15). The apparent low gravity anomaly is likely a result of low density sediment and relatively low density lava flows infilling the valley created by N--S trending basin-bounding faults, which juxtaposes quartz monzonite or related basement rocks against these lower density rocks. In the following, we:

1. Review the WesternGeco sampling procedures
2. Complete gravity reductions using the WesternGeco dataset and a variety of Bouguer densities, and compare the results with topographic features, thereby identifying an appropriate range of Bouguer densities for the modeling effort
3. Perform a high-dimensional gravity inversion of the WesternGeco dataset using a variety of Bouguer densities in order to construct a geological model of the basin
4. Compare the model results with MT results and discuss the impact of the model and comparison on development of the hydrothermal model.

3.2 Gravity Data

Gravity data were collected by WesternGeco during gravity surveys in summer, 2011. Review of field procedures indicates that WesternGeco staff did an excellent job of high-resolution gravity data collection. Instrument drift appears to have been minimal. High vertical precision on elevation of gravity stations was achieved. Although the report does not provide details of the terrain correction, specifically about the way local terrain differences were incorporated into the digital terrain model (DEM) based correction, the WesternGeco approach appears to have been reasonable (resulting in terrain corrections generally <1 mgal (Figure 2.16).

3.3 Gravity Reductions

Gravity reductions, and particularly the choice of density for the Bouguer corrections, have an important impact on modeling. WesternGeco staff used a density of 2700 kg m^{-3} for the Bouguer density. This is higher than values normally used in gravity modeling, especially for local gravity surveys, and may lead to correlation between modeled geological features and topography, as noted in the WesternGeco report. In fact, inspection of Figure 20 does indicate that some correlation occurs, especially with the N--S trending low gravity values and the topographic ridge in the central part of the map area. Therefore, we undertook to repeat the gravity reduction using a variety of Bouguer densities, using data provided in the WesternGeco report, in order to assess the impact of this assumption (Bouguer density of 2700 kg m^{-3}) on model results.

Drift and Tidal Corrections. WesternGeco staff report low instrument drift, thought to be linear during the sampling period. The gravity instrument used performs tidal corrections automatically, using the Longman formulas. We did not have the information, or think it necessary, to repeat drift and tidal corrections.

Theoretical Gravity (mGal). Gravity varies with latitude due to the change in diameter of the Earth with latitude and change in angular acceleration with latitude. The change of gravity with latitude is the theoretical gravity. We use the Somigliana closed-form solution to estimate theoretical gravity:

$$g_T = \frac{g_e(1 + k\sin^2\phi)}{(1 - e^2\sin^2\phi)^{\frac{1}{2}}},$$

(1)

where g_T, is the theoretical gravity on the GRS80 reference ellipsoid at latitude ϕ, g_e is normal gravity at the equator equal to 978032.67715 mGal, k is a dimensionless derived constant equal to 0.001931851353, and e being the first numerical eccentricity with e^2 having a value of 0.0066943800229.

Free Air Correction (mGal). The difference in elevation between the base station and the measurement point results in a difference in gravitational acceleration. The free air correction is applied to account for difference in gravity due to difference in measurement height. For the GRS80 ellipsoid the second-order formula for the precise free air correction is:

$$\delta g_h = -(0.3087691 - 0.0004398 sin^2\phi)h + 7.2125 \times 10^{-8}h^2,$$

(2)

where the free air correction, δg_h, is calculated in milligals and h is the elliptical elevation of the gravity station measured in meters.

Atmospheric Correction (mGal). The weight of the atmosphere varies with height and this change affects gravity measurements. The atmospheric correction accounts for the change in weight of the atmosphere between the base station and the measurement point. The formula for the atmospheric correction is:

$$\delta g_{atm} = 0.874 - 9.9 \times 10^{-5}h + 3.56 \times 10^{-9}h^2,$$

(3)

where the atmospheric correction, δg_atm, is given in milligals and h is the elliptical elevation of the gravity station in meters.

Bouguer Correction (mGal). The Bouguer correction accounts for the mass of average crust between the base station and the measurement point, given the height difference between them. The Bouguer correction used here accounts for the spherical cap-shape of this mass of rock, as described in LaFehr1991. The formula for the Bouguer correction is:

$$g_{sc} = 2\pi G\rho[(1+\mu)h - \lambda R], \tag{4}$$

where g_{sc} is the gravity correction due to the spherical cap in milligals, ρ is the density of the material making up the spherical cap, μ and λ are dimensionless coefficients, and $R=R_0+h$, where R_0 is the mean radius of the Earth and h is the elevation of the gravity station on the reference ellipsoid.

Terrain Correction (mGal). The free air and Bouguer corrections incompletely account for topographic effects on gravity measurements. The terrain correction accounts for differences produced by actual terrain and required DEM to implement. WesternGeco performed terrain corrections using a DEM and elevation differences measured near each gravity station, using a Bouguer density of 2700 kg m^{-3}.

 We are uncertain from the WesternGeco report exactly how the terrain correction was computed. Normally, the inner zone correction accounts for topographic variation within Hammer's zone C, <53.3 m from the gravity station, and is computed using the quarter-wedge method described by Nowell (1999), an improved version of the power-law approximation method of Campbell (1980). The intermediate zone correction is normally performed for DEM grid points that fall between Hammer's zone D, >53.3 m, and outer radius of Hammer's zone K, 9903 m. This terrain correction is done using the simplified gravity attraction of a prism approximated as an annular ring, described by Kane1962. The far-field terrain correction is usually performed for topographic variation >9903 m and up to the extent of the input DEM (if SRTM-derived DEM is used, up to 163 km). This far-field correction is carried out by means of the vertical line mass approximation described by Blais (1984), which is the approximation of the gravity attraction due to a prism in the far-field.

Recalculation of the Gravity Reduction. We recalculated the gravity reduction using equations 1-4. Through this procedure we verified the complete Bouguer gravity anomaly presented by WesternGeco staff in their report, using a Bouguer density of 2700 kg m^{-3}. Because we are most interested in the local variation in the gravity field (i.e., within the boundaries of the survey area), a residual gravity anomaly was computed by subtracting the complete Bouguer anomaly (the anomaly obtained after the application of the terrain correction) from an assumed regional trend, estimated by fitting a plane to the complete Bouguer anomaly map using the generalized least-squared method (Figure 2.17).

 Inspection of Figure 2.17 indicates that there is some correlation of the complete Bouguer gravity anomaly with topography, especially indicated by the low gravity values associated with a topographic ridge that extends N–S through central part of the map area. This correlation with topography suggests that the Bouguer density of 2700 kg m^{-3} is high, and that lower Bouguer densities are more appropriate for use in modeling the local gravity anomaly. This is important because the choice of the Bouguer density affects the estimated basin depth derived from the gravity data, a key parameter in the hydrothermal model.

 We note that much of the topography around the site is due to emplacement of lava flows. There are few measurements of bulk lava flow density reported in the literature. In

Hawaii, basalt density measurements in boreholes were 2000-3000 kg m^{-3}, with mean value of 2500 kg m^{-3} for water saturated lava flows Moore2001. Thus, although basalt samples have densities on order 2700-3000 kg m^{-3}, the bulk density of lavas is less due to the presence of fractures and flow vesiculation. Kar Kar lava flows should be close to this density, or perhaps slightly less for partially saturated rocks that form topographic highs in the local survey area.

Therefore, we recomputed the gravity reduction, using a range of lower values of the Bouguer density, 2200 kg m^{-3} < ρ < 2700 kg m^{-3}. We used the terrain corrections computed by WesternGeco using 2700 kg m^{-3} because terrain information, especially for the inner Hammer zone, was not available to us. This leads to a very slight over-correction for terrain effects when lower Bouguer densities are used. However, we note that the error introduced into the terrain correction is very slight (<<1 mgal), and therefore not meaningful compared with the amplitude of the computed anomaly.

Figures 2.18, 2.19 and 2.20 show example results of this re-computation using lower Bouguer densities, each time subtracting the best-fit plane from the data. Inspection of these maps shows that correlation with topography is minimized using Bouguer densities of 2300 kg m^{-3}< ρ <\$ 2550 kg m^{-3}. For lower Bouguer densities (e.g., ρ < 2300 kg m^{-3}), an anti-correlation with topography emerges. In the following, we construct a forward model using a complete Bouguer anomaly calculated with a Bouguer density of 2550 kg m^{-3}, acknowledging that slightly lower values may also be used.

3.4 Gravity Forward Model

The forward gravity model consists of 6 603 rectangular prisms aligned in a uniform grid, which is approximately centered on the dataset of observed gravity stations (Figure 2.15). Each rectangular prism is 200 × 200 meters square in the horizontal plane. Each prism extends from the surface to some depth, inferred through the inversion. The depth of each prism is adjusted during the inversion process to minimize differences between the observed complete gravity field and the calculated gravity field.

For this inversion, the density contrast of each prism was fixed at a value of \$-250.0\$ kg m^{-3}, which is assumed to represent the bulk density contrast for the valley-fill sediments, volcanoclastics and low density lava flows with the underlying quartz monzonite or comparable basement. Using the Bouguer density of 2550 kg m^{-3}, this implies a density for the quartz monzonite of 2800 kg m^{-3}, which is generally taken to have a normative bulk density (unfractured) of approximately 2770 kg m^{-3} (Daly 1935). Thus, given the uncertainties in the density of the alluvium and lava flow in-filling the basin, a model density contrast of -250.0 kg m^{-3} appears to be appropriate.

3.5 Gravity Inversion

The Gauss-Newton procedure with the Levenburg-Marquardt modification was used to invert the gravity data for the depth distribution. This depth distribution represents the depth to the quartz monzonite, given a uniform package of basin-filling sediments and lava flows. Pilot points were used as a parameterization device to reduce the dimensionality of the inverse problem, while maintaining maximum degrees of freedom. The pilot points were distributed non-uniformly throughout the forward model domain, focused near the gravity stations (Figure 2.21). A total of 431 pilot points were used to parameterize the depth distribution of the forward model grid.

Constructing an inverse problem with more degrees of freedom than observations is an under-determined problem. Solving this type of problem requires finding a pseudo-inverse

solution that meets the Moore-Penrose conditions, which is found using singular value decomposition (SVD) in combination with Tikhonov regularization. Although the SVD and regularization result a numerically tractable problem, inverting for more parameters than data requires the specification of an acceptable level of data error, or misfit. Otherwise, over-fitting of the data, which include noise from various sources, will occur. The goal of the inversion process is then to find a minimum of regularization error at the specified level of data error or misfit. Different values of acceptable misfit produce different solutions to the inverse problem. Ideally, if the observation errors are assumed to be normally distributed and the forward model does not produce any structural error (and the co-factor matrix is the identity matrix), then the acceptable level of misfit should be the product of the standard deviation of the observation error and the number of observations.

To explore the trade-off between assumed observation error and regularization error, the inversion process is wrapped in a multi-objective framework. The result is a series of solutions to the inverse problem for unique combinations of minimized regularization error and data misfit. These unique combinations are known as Pareto optimal points and the collection of these points forms the Pareto frontier, which quantitatively defines the trade-off between the two competing objectives.

3.6 Gravity Model Results

Ten Pareto optimal points were found for a range of assumed observation error standard deviation (Figure 2.22).The resulting depth distribution, as well as a comparison of observed and simulated gravity response are presented in the Appendix of this report.

Assessment of the Pareto plot suggests that an error model standard deviation of 0.3 to 0.4 mgals results in an equitable trade-off between misfit and plausibility (points 4 or 5 on Figure 2.22). In other words, the inversion does not attempt to refine models to less than this range of values, reflecting both uncertainty in the true value of gravity at observation points and additional complexities of the gravity anomaly distribution, not accounted for in the forward model

Model depths are shown in Figure 2.23 and the forward solution to the gravity calculation based on this model is shown in Figure 2.24. Although strong constraints are placed on the model because only one density contrast is used, it is clear that relatively smooth variation in basin-fill can model the observed variation in gravity. The major feature of the model is the presence of a narrow N-S trending basin through the center of the map area, reaching a maximum depth of approximately 1500 m and bounded by mapped faults. We note that the model depth at the western margin of the gravity grid, nearest Borehole 4, is approximately 150 m, in excellent agreement with the depth measured to the top of the quartz monzonite in Borehole 4 (123 m).

4. HYDROTHERMAL MODEL: DATA INTERPRETATION AND MODELING

The geophysical data and models based on the interpretation of these data place important constraints on the hydrothermal model for the Kar Kar area. The geophysical models are also consistent with observations made in Borehole 4 (Figure 2.25).

Interbedded lavas and alluvium occur in Borehole 4 to a depth of 123 m. Quartz monzonite was logged from 123 m to the bottom of the hole at approximately 1000 m depth. The thickness of alluvium and lava flows derived from the gravity model in the westernmost portion of the grid, east of Borehole 4, is approximately 150 m. This suggests that the model depths from the 3D inversion of gravity data represent the depth to basement, which at least in Borehole 4, is quartz monzonite.

The quartz monzonite in Borehole 4 is variably fractured. A water-bearing zone was identified through interpretation of the temperature log (Figure 2.25) at a depth of approximately 340 m. Temperatures of water in this zone in Borehole 4 were 30-35°C, the same temperature as the Jermaghbyur hot springs. Both the 2D MT model (GEORISK/USF, 2009) and the 3D MT model (data of WesternGeco, 2011) identify a prominent low resistivity zone east of Borehole 4 at approximately this depth. Hot fluids within a fracture zone can explain this low resistivity anomaly. It seems possible that fracture flow through the quartz monzonite rapidly delivers hot water to the springs by predominately lateral transport through this water-bearing zone from the area of the low resistivity anomaly.

The low resistivity anomaly appears to be thickest and of greatest amplitude at the projected location of steeply dipping faults bounding the western edge of the N--S trending basin. The 3D gravity model suggests that this basin rapidly deepens to approximately 1500 m east of the low resistivity anomaly. Additional low resistivity anomalies, although of lower amplitude, are identified in the 3D MT model within the basin.

Both the 2D MT model (GEORISK/USF, 2009) and the 3D MT model (data of WesternGeco, 2011) identify an increase in resistivity at a depth of approximately 1500 m beneath the low resistivity zone adjacent to the borehole. This transition may represent a change from water saturated fractured quartz monzonite to unfractured rock, and hence impermeable, rock at greater depth. The MT results from 2009 and 2011 are somewhat inconsistent about whether this zone shallows or deepens to the west. It appears that this zone deepens within the basin based on 2009 MT modeling results.

Finally, the geothermal gradient measured in Borehole 4 is clearly anomalous, reaching approximately 100°C km^{-1} in the lower half of the well. The quartz monzonite is reported to be fractured in zones throughout much of the well. The anomalous temperature gradient, the presence of fractured igneous intrusion, and the presence of the narrow N--S trending basin within the survey area all create conditions for rapid transport of hot water from within the basin from depth to the surface along permeable fractures. It is possible that this fracture flow is partially controlled by faults bounding the western margin of the basin. The water-bearing zone at 340 m depth in the well may represent a mixing zone between these up-welling fluids and meteoric recharge.

Our interpretation is that the major features of gravity and MT modeling, along with the borehole observations, indicate that meteoric water may circulate to substantial depth within the basin. A heat source at depth is required to explain the anomalous geothermal gradient in Borehole 4. It is uncertain if this heat source is localized within the fault-bounded basin, or is larger, for example extending to the west.

4.1 Hydrothermal Model Framework

A density-dependent groundwater flow and transport model was constructed to simulate advective and conductive heat transport in the shallow subsurface at the site. This model is based on results from the geophysical data analysis and gravity inversion and was parameterized using site-specific data and expected values from literature sources. Results from the model were qualitatively compared to the observed temperature distribution in Borehole 4 (Figure 2.25).

4.2 Model Domain

A two-dimensional cross-section model domain was selected for the model analysis. The domain extends parallel to the long axis of the gravity grid through the lake (a major recharge feature) in the east and just south of the borehole in the west (Figure 2.26). This domain was selected because it is representative of the general groundwater flow and heat transport pattern across the Kar Kar valley and allows inclusion of the relevant flow system features.

4.3 Conceptual Model

Based on the gravity and MT data analysis and gravity inversion, the shallow subsurface along the cross-section was simplified into three distinct geologic units (Table 2.1).

AL	alluvium and lava flows
FR	Upper quartz monzonite that is highly fractured
QZ	Lower quartz monzonite that is less fractured

Table 2.1. The 3 distinct geological units of the shallow subsurface.

These units were translated into three distinct hydrostratigraphic units for input into the hydrothermal model as regions of distinct hydraulic and transport model parameters. The basin depth, as determined from the gravity inversion, represents the contact between the upper AL and FR units (Figure 2.27). Based on the lithologic record from Borehole 4, the FR unit is conceptualized as having a thickness of 100 meters, so that the FR/QZ contact is 100 meters below the AL/FR contact. The AL unit comprises the lower density alluvium and lava flows that fill the valley, as interpreted from the gravity inversion. The FR unit is thought to be a primary transport pathway for advective heat transport from the deep part of the basin to shallower depths near Borehole 4.

4.4 Model Selection

The model code SEAWAT (Langevin et al. (2008a)) was used as the simulation engine for the hydrothermal model analysis. SEAWAT solves a density-dependent form of the groundwater flow equation and is capable of multi-species density-dependent transport. SEAWAT uses a finite-difference approximation and is capable of simulating the transport of heat by both conductive and advective processes:

$$\nabla.[\rho\frac{\mu_0}{\mu}\mathbf{K}_0(\nabla h_0 + \frac{\rho - \rho_0}{\rho_0}\nabla z)] = \rho S_{s,0}\frac{\partial h_0}{\partial t} + \theta\frac{\partial \rho}{\partial C}\frac{\partial C}{\partial t} - \rho_s\acute{q}_s \tag{5}$$

where,

ρ_0	:= fluid density at reference conditions
μ	:= dynamic viscosity
μ_0	:= dynamic viscosity at reference conditions
K_0	:= hydraulic conductivity tensor at reference conditions
h_0	:= hydraulic head at reference conditions
$S_{s,0}$	:= specific storage
t	:= time
θ	:= porosity
C	:= concentration
q_s	:= source/sink term of density ρ_s

To simulate heat transport in SEAWAT, heat is treated as a dissolved constituent. As a result, the SEAWAT framework requires specification of the following properties:

K_{dtemp} fluid-matrix thermal distribution coefficient

D_{mtemp} effective molecular diffusion coefficient for heat transport

μ (T)   viscosity dependence on temperature

The thermal distribution coefficient, K_{dtemp}, describes thermal equilibrium between the aquifer and the fluid:

$$K_{d_temp} = \frac{c_{Psolid}}{\rho c_{Pfluid}} \tag{6}$$

where,

c_{Psolid}	:= specific heat capacity of the aquifer material
c_{Pfluid}	:= specific heat capacity of the fluid
ρ	:= fluid density

The effective molecular diffusion coefficient describes the transport of heat by matrix and fluid conduction:

$$D_{m_temp} = \frac{k_{Tbulk}}{\theta\rho c_{Pfluid}} \tag{7}$$

where,

k_{Tbulk}	:= bulk thermal conductivity
θ	:= porosity

Bulk thermal conductivity, k_{Tbulk}, is calculated as the arithmetic mean of fluid and aquifer material thermal conductivity:

$$k_{Tbulk} = \theta k_{Tfluid} + (1 - \theta)k_{Tsolid} \tag{8}$$

where,

k_{Tfluid}	:= fluid thermal conductivity

83

k_{Tsolid} := aquifer material thermal conductivity

The dependence of viscosity on temperature is expressed as the ratio, μ_0/μ (Equation 5), which effects the hydraulic conductivity tensor. This dependence is implemented with the following equation:

$$\mu(T) = 239.4 \times 10^{-7} 10^{\frac{248.37}{T+133.15}} \tag{9}$$

where,

$\mu(T)$:= viscosity as a function of temperature
T := temperature of the fluid in $°C$

As presently coded, SEAWAT does not simulate multi-phase transport, so the practical upper limit of temperature is 99.0$°C$. Refer to Langevin (2008) and the references cited there in for a full description of the SEAWAT model.

4.5 Discretization

Use of finite-difference approximation requires discretization of the continuous partial differential functionals into a discrete form for numerical solution. In this case, the discretization includes both spatial discretization, which divides the model domain into cells, or nodes, as well as discretization of time into discrete solution time steps. The map cross-section selected for model analysis was discretized into cells, 25 m square (Figure 2.28), which results in 48 model layers and 320 model columns. Figure 2.29 shows the discretized hydrostratigraphic layers.

The time-stepping scheme in the model is variable. The initial time step is selected to produce a Courant number of 1.0. The subsequent time steps follow a geometric progression of increasing length to a maximum of 10 days

4.6 Boundary Condition Specification

Solution of the partial differential equations for groundwater flow and heat transport requires specification of boundary conditions that represent sources and sinks of water and heat. The groundwater flow boundary conditions included:

- Representation of the lake near the eastern edge of the model domain as a Cauchy boundary condition
- Representations of outflow at the western (down-gradient) edge of the model domain as a Dirichlet boundary condition
- Representation of Recharge as a Neumann type boundary condition
- Representation of evapotranspiration as a Cauchy boundary condition

The components of the flow boundary conditions which require specification are summarized in Table 2.2.

Boundary Condition Component	Units	Value	Source
lake stage	m	42.0	DEM
lake bed conductance	m^2/d	variable	calculated using K
stage at western boundary	m	0.786	DEM
conductance at western boundary	m^2/d	variable	calculated using K
recharge rate	m/yr	0.75	shapefile coverage
evapotranspiration rate	m/yr	0.075	10% of recharge

Table 2.2. Summary of specified flow boundary condition components

Heat-transport boundary conditions include:
Representation of geothermal heat flux into the basal model layer as a Neumann boundary condition

- Representation of a localized heat source in the bottom of the basin as a Dirichlet boundary condition
- Representation of heat transported into the model domain by lake leakage as a Dirichlet boundary condition
- Representation of heat transported into the model domain by recharge as a Dirichlet boundary condition
- Representation of heat transported out of the model domain by evapotranspiration as a Dirichlet boundary condition

The components of the heat transport boundary conditions which require specification are summarized in Table2.3.

Boundary Condition Component	Units	Value	Source
geothermal heat flux	W/m^2	0.35	calculated
localized heat source	$°C$	99.0	geothermal gradient
stage at western boundary	$°C$	1.0	Borehole 4 log
conductance at western boundary	$°C$	1.0	Borehole 4 log
recharge rate	$°C$	1.0	Borehole 4 log
evapotranspiration rate	$°C$	1.0	Borehole 4 log

Table 2.3. Summary of specified transport boundary condition components

The geothermal gradient observed at Borehole 4 and the thermal conductivity, k_{dtemp} of the basal model layer were used to calculate the basal geothermal heat flux. A temperature of $99.0°C$ was selected for the localized heat source cells based on the geothermal gradient at Borehole 4. Localized heat source cells were placed in model cells where the contact between the AL and FR is deeper than 1000.0 m (Figure 2.28). As discussed in the following, the predicted distribution of heat throughout the model domain, including the area near Borehole 4 is very sensitive to the location of the localized heat source. Placement localized heat source boundary conditions in the FR unit results in temperatures in excess of $50.0°C$ in the western potion of the model domain. Since the localized heat source has the capacity to provide infinite amounts of heat, and since the FR unit has a large flow of groundwater, the result is a large amount of heat transported down gradient of the source cells.

4.7 Property Specification

hydraulic parameters The model requires specification of several hydraulic properties for each of the three hydrostratigraphic units including hydraulic conductivity, hydraulic storage,

and porosity. The values assigned to these properties represent typical, or expected values and were determined from literature sources (Table 4).

Property	Units	AL	FR	QZ
hydraulic conductivity	*m/d*	10.0	10.0 to 100.0	0.0001
porosity	(none)	0.1	0.2	0.08
specific yield	(none)	0.08	0.12	0.0001
specific storage	*1/m*	0.0001	0.0001	0.0001

Table 2. 4. Summary of flow model parameters

transport parameters In addition to the hydraulic properties, transport-specific parameters were also specified for each of the three units, and include specific heat capacity, density, and thermal conductivity. The values assigned to these properties represent typical, or expected values and were determined from literature sources, with the exception of AL density, which is the same as was used in the Bouguer gravity reduction (Table2.5).

Property	Units	AL	FR	QZ
density	*kg/m³*	2550	2700	2770
specific heat	*J/(kg°C)* 840.0	820.0	790.0	
thermal conductivity	*W/m°C* 1.75	1.0	3.0	

Table 2.5. Summary of transport model parameters

4.8 Model scenarios

The purpose of geophysical data collection, data analysis, and hydrothermal model analysis is to determine the existence of a localized heat source at the base of the Kar Kar valley. To use the hydrothermal model in this capacity, two scenarios were constructed to bracket a possible geothermal system configuration:

Scenario	Purpose
Scenario A	localized heat source thermally coupled to FR and AL units
Scenario B	localized heat source of 99$℃$ coupled to the FR and AL units

Scenario A is designed to test the existence of a localized heat source at the base of the Kar Kar valley by removing the localized heat source boundary condition and comparing the model predicted temperature distribution at Borehole 4. With this configuration, if the predicted distribution does not agree with the observed distribution, then an additional heat source is needed.

Scenario B is designed to test the existence of a localized heat source in direct contact with the FR units by placing source cells in the FR unit at the base of the Kar Kar valley. If the predicted distribution at Borehole 4 does not agree with the observed data, then a heat source of *99.0℃* with a direct advective connection to the Borehole 4 area is not plausible.

All scenarios were non-transient, which means that flow and transport boundary condition forcing do not vary with time. The model scenarios were run forward in time until the simulated water level and heat distributions were invariant. Additionally, since the capacity

of the FR unit to serve as a heat transport pathway is uncertain, both scenarios were subjected to two parameterizations:

Parameterization	Description
Homogeneous	the hydraulic conductivity of the FR and AL unit is the same
Heterogeneous	the hydraulic conductivity of the FR is higher than the AL

For homogeneous parameterizations, the AL and FR units were given hydraulic conductivity values of 10.0 m/d. For heterogeneous parameterizations, hydraulic conductivity of the FR unit was raised to $100.0 m/d$, allowing the flow of groundwater concentrate in the FR unit. Scenario results were qualitatively compared to the observed temperature distribution at Borehole 4 to determine plausibility. If the model-predicted distribution captures the general shape and trend of the observed distribution, then the scenario is deemed plausible.

4.9 Model Results

4.9.1 Scenario A

Scenario A was completed to test the existence of an additional localized heat source by using only a basal geothermal heat flux in the model. Figures 2.30, 2.31, 2.32, and 2.33 summarize the results of this scenario. Results from both parameterizations indicate this scenario is plausible, as the predicted temperature distribution at Borehole 4 agrees with the data. This means given the current data set, the model analysis cannot prove the existence of a localized heat source. Instead a broad heat source, with respect to the entire model domain, may be present to account for the temperature anomalies observed in Borehole 4.

4.9.2 Scenario B

Scenario B was completed to test the existence of a localized heat source of $99.0 °C$ in direct contact with the FR unit. Figures 2.34, 2.35, 2.36 and 2.37 summarize the results of this scenario. Results from both parameterizations indicate this scenario is not plausible, as the predicted temperature distribution at Borehole 4 does not agree with the measured temperature gradient. This means that if a localized heat source is present near the floor of the pull-apart basin, this heat source is thermally isolated from the highly transmissive valley fill sediments and fractured monzonite. Otherwise, a higher temperature gradient would be expected in borehole 4 than was observed. In the extreme case, the heterogeneous model with a localized heat source predicts nearly isothermal conditions in Borehole 4 due to rapid advection of heat in the fractured quartz monzonite unit.

Using results from the above model analysis scenarios, existence of a localized heat source within the basin identified by gravity inversion cannot be disproved. However, given the current data set, a non-identifiability exists between the location and temperature of a localized heat source and the hydraulic conductivity of the FR and AL units. A low-temperature source located within the FR unit produces the same response as a high-temperature source located within the QZ unit. This is because the QZ unit acts as a thermal insulator, which restricts the transport of heat by conduction. This effect is increased by the low-permeability character of QZ, which results in little or no advective heat transport. The result is a weak thermal coupling between a localized heat source within the QZ and the advection dominant

FR. The existence of a high-temperature heat source within the QZ unit cannot be ruled out. However, this cannot be resolved by the model analysis using the available data.

4.10. Discussion

The WesternGeco report is a highly valuable addition to our understanding of the geothermal potential of the Kar Kar region. The quality of MT and gravity data collection and reduction, as presented in the WesternGeco report, is state-of-the-art. In the broadest sense, the WesternGeco report leads to identification of a significant low resistivity anomaly located at the western margin of a fault-bounded basin. The location of the resistivity anomaly correlates with mapped faults.

Our inversion of the gravity data collected by WesternGeco using a Bouguer density of 2550 $kg\ m^{-3}$ suggests a total basin depth of approximately 1500 m. This basin is narrow, and N-S trending, features consistent with a pull-apart structure. Thus, the faults bounding this pull-apart structure offset quartz monzonite, which is variably fractured.

The most prominent resistivity anomaly (Low Resistivity Zone A of the WesternGeco report) can be explained by the advection of deeply circulating meteoric waters up basin-bounding faults. These waters mix with shallow meteoric water within fast-path fracture zones of the quartz monzonite. Transport of these mixed, 30-35 $℃$, waters continues west, passed Borehole 4 and to the Jermaghbyur hot springs.

A major issue related to the Kar Kar geothermal development is the potential for high temperature fluids at relatively shallow depth within the fault-bounded basin. The hydrothermal model appears to rule out the *requirement* that high temperature fluids are present in the basin at depths less than 1200 m. Of the alterative models tested, a diffuse heat source resulting in elevated geothermal gradient appears to best explain the geothermal gradient on Borehole 4 and its relationship to the quartz monzonite and the basin. In this model fluids do circulate in the basin, but the overall temperature gradient is associated with conductive cooling of the quartz monzonite body or a deeper feature.

Addition of a localized heat source within the basin, using the model conductivities, increases advective heat transport and results in higher modeled temperatures in the borehole than observed. In the extreme case, close to isothermal conditions are modeled in the borehole. Given, at least, the conductivity values applied in the hydrothermal model, it seems unlikely that a considerable localized source of heat exists in the basin..

In general, the main conclusion drawn by the hydrothermal modeling is that there is not requirement for high-temperature fluids present within the basin.

The observed geothermal gradient in the borehole is best explained by a diffuse source of heat. This result is consistent with the MT data and model, and with the soil CO_2 flux data. Nevertheless, several model assumptions may create bias. For example, low permeability zones within the basin may occur. If so, then a localized heat source within the basin may still be present at depth, but isolated by the low permeability cap-rock. Alternatively, the quartz monzonite (?) under the basin may be anomalously warm, but also relatively impermeable. We emphasize that although these alternative models are possible, there is no evidence from the borehole data or models to support them.

5. CORRELATION AND JOINT INTERPRETATION OF ALL INTERIM MODELS AND DEVELOPMENT OF A CONCEPTUAL MODEL

Structural, gravimetric and MT models, like all other geophysical data collected in the period of 2004 – 2011, are well compatible and inter-correlative. Models built on the basis of those data have demonstrated that there is a *pull-apart*-type basin in the Karkar Site. The basin is flanked by a system of 7 to 10 steeply dipping faults

The upper part of the basin is filled with alluvial deposits and lava flows that are from 300 m (on the flanks) to 1,200 m (in the centre) thick. These deposits might be underlain with quartz monzonite. The faults, bounding the *pull-apart* basin, offset quartz monzonite that is variably fractured. The anomaly of low resistances (Layer 2 with resistance values from 2 to 50 Ohm×m) could be explained by advection of meteoric waters, circulating at depth, up toward the basin-bounding faults. These waters mix with shallow meteoric water within fast-path fracture zones of the quartz monzonite. Transport of these mixed, 30-35 ℃, waters continues west, passed Borehole 4 and to the Jermaghbyur hot springs.

The main issue considered by the geothermal model is potential absence or presence of high-temperature fluids within Layer 2, displaying resistance values from 2 to 50 Ohm×m at the depths of 300-1000 m within the fault-bounded basin. The presence or absence of high-temperature fluids within Layer 2 plays significant role for the choice of a conceptual model, assessment of geothermal potential of the Karkar Site and selection of the place for exploratory well drilling.

The hydrothermal modeling considered two possible scenarios.

<u>Scenario A – Diffuse Heat Source</u>. The scenario provides that the anomalies observed in Borehole 4 could be explained by mere existence of an extensive, with respect to the model domain, heat source

<u>Scenario B – Localized Heat Source</u>. The scenario provides that the anomalies observed in Borehole 4 could be explained by mere existence of a localized heat source within the upper part of the fractured quartz monzonite (depths less than 1500 m) just beneath the base of the basin filled with alluvium and lava.

The parameterization results for both models confirm Scenario A and indicate that Scenario B is unlikely, as the predicted temperature distribution in Borehole 4 does not agree with the measured temperature gradient.

Considering the importance of assessing heat source location and type, and recognizing that the hydrothermal modeling is based on the data of gravity inversion, a part of MT data, and data from Borehole 4, below we proceed with analysis and interpretation of both hydrothermal modeling scenarios together with additional geological and geophysical evidence.

5.1. Model A – Diffuse source of heat

As we noted above, Model A provides that anomalies detected in Borehole 4 could be explained only by existing extensive, relative to the entire model domain, source of heat. In this model, temperature of fluids circulating within the basin at depths of 300-1200 m is below 100°C, and the temperature gradient in Borehole 4 is associated with conductive cooling of the quartz monzonite body or some deeper object.

As already mentioned in section 4.2.3 of this report, the regional gravimetry map at the scale of 1:200,000 indicates presence of a well-manifested, large negative anomaly, the southwestern side of which accommodates the sites of Karkar and Jermaghbyur (Figs. 1.53 and

2.38). The size of this anomaly is 35 km in the north-southern and 25 km in the east-western directions. Many studies interpreted the northern part of the gravity anomaly as a reflection of the large Dalidagh intrusion (Nikolsky and Milay, 1975, Mousayev, 1983).

The part of the Dalidagh intrusion exposed on the surface is 20 km long and 8 km wide, and its area is about 150 km^2 (1 and 2 in Fig. 2.38). The intrusion is situated at the distance of 6 km to the north of the Karkar Site and is bounded by the Terter Fault in the north (Figs. 2.38 and 2.39). It is assumed that the southern part of the intrusion plunges beneath the Quaternary lava (Nikolsky and Milay, 1975, Mousayev, 1983).

Below we provide a few characteristics of the Dalidagh intrusion that are important for the further interpretation

1. Phase 1 of the intrusion cuts through the Middle-Late Eocene deposits. The estimates by the *K-Ar* isotope method establish its age within 30-35 Ma (Mousayev, 1983).
2. Rocks of the three phases are distinguished in the intrusion. **Phase 1 (ø$^3_2$–ø$^1_3$)** is represented by monzonites, quartz syenites, syenite-diorites and diorites (1 in Figs. 2.38 and 2.39). **Phase 2 (N$^1_1$)** is represented by porphyraceous granodiorites and granosyenites (2 in Fig. 2.38 and 2.39). Small extrusions of rhyolites with the estimated age of 3 Ma, located at the contact of the intrusion with the Terter Fault, correspond to **Phase 3 (N$^1_2$)** (Mousayev, 1983).
3. The second, Early Miocene phase of the Dalidagh intrusion is similar to the Early Miocene phase of the Vohji complex in the Meghri Intrusion located 60 km to the south. The Vohji complex of porphyraceous granites with an age of 22-24 Ma (estimated by *K-Ar*, *Pb-Sr*) is related to the unit of sub-volcanic granite formed 1-3 km deep. Similar depth is suggested for the second phase of the Dalidagh Intrusion (Mousayev, 1983).
4. Abnormally high concentrations of *U* and *Th* are characteristic geochemical features of the Dalidagh Intrusion. In Phase 1 rocks, the average contents of *U* and *Th* are 7.1 g/t and 25 g/t, respectively, and in Phase 2 rocks, content of *U* is 8.9 g/t and that of *Th* is 45 g/t, which is 2.5 times higher than the clarke contents.

The length of the southern extension of the Dalidagh Intrusion is unknown. However, if we base on the location of the southern margin of the gravity anomaly, the intrusion must spread up to the site of Karkar (Fig. 2.38 and 2.39).

The 2D models of MT survey interpretation developed both by "Georisk/USF" and by "Nord-West" identify Layer 4 with rocks of very high resistance values (1,000 to 2,500 Ohm-m) at depths ranging from 1,500–1,800 m to 10,000 m (Figs. 2.6 and 2.7). According to the interpretation of Georisk/USF it might correspond to blocks of either metamorphic basement, or intrusion. In Armenia, the crystalline basement is everywhere reflected by relative maxima of gravity field, and intrusions mostly correspond to the minima. The negative gravity field anomaly coinciding with the Dalidagh intrusion was traversed by the 2004 and 2009 MT survey profiles and the blocks of high-resistance of Layer 4 were detected just at these areas.

Therefore, it is possible to suggest that the high-resistance Layer 4 identified at the depth of 1.5–10 km corresponds to intrusive rocks and may represent an extension of the Dalidagh intrusion to the south.

Such suggestion is supported by a few additional facts.
1. Borehole no. 4 drilled in the northwestern corner of the Karkar Site in 1987/88 had cut through quartz monzonites and granosyenites within depth interval from 123 m to 1 km, when the drilling was stopped. By the stratigraphy description, the intrusive rocks drilled in by Borehole no. 4 are similar to Phase 1 rocks of the Dalidagh intrusion.

2. The gamma-logging of Borehole no. 4 recorded an abnormally high rate of background radioactivity (50μR/h) of the drilled intrusive rocks, which is 2.5-3 times higher than the common background rates. The recalculation of the obtained values by the uranium equivalent yields values about 40 g/t. These values are typical for the Dalidagh intrusion rocks.

3. Small outcrops of the Early Miocene porphyraceous granodiorites are recorded on the surface of Quaternary lava at the distances of 0.7 and 2.5 km to the north of Point 17 on the 2009 MT survey profile. These rocks are related to Phase 2 of the Dalidagh intrusion and are located 4 and 6.5 km far from it (Figs. 2.39 and 2.40). It is noteworthy that both intrusion outcrops are broken by Quaternary volcanoes (Fig. 2.40).

4. West of the Karkar and Jermaghbyur sites, more than 25 small exposures of intrusions are recorded among the Quaternary lava on the left bank of the Vorotan River. These rocks are represented by monzonites, granosyenites and granodiorites of the Early Oligocene (Fig. 2.39). Many of these rocks have features similar to the Dalidagh intrusion (Abovyan and Malkhasyan, 1961, Mousayev, 1983).

5. A dome-shaped exposure of rhyolites is located 250 north of the Karkar Site and has the size of 1,000 x 600 m. The rhyolitic dome is located 100 m north of Point 3 of the 2009 MT survey profile and 400 m east of Borehole N4 (1 in Fig. 2.41). By the petrographic description, rocks in this rhyolitic dome are very similar to Phase 3 rhyolites in the Dalidagh Intrusion.

We suggest that the rhyolitic dome could have been intruded along the fault zone bounding the western side of the *pull-apart* basin (2 in Fig, 2.41). Bodies of olivine trachybasalts are intruded along the same fault system nearby (3 in Fig. 2.41).

The petrographic analysis of a thin section sample from the rhyolitic dome indicates high rate of secondary silicification of the rock (see Annex 1). The chemical analysis of the same sample reveals that it has high (up to 6%) content of sulfur, while the x-ray structure analysis indicates that the high sulfur content is related to the presence of alunite mineral in the rock. Therefore, the rocks of the rhyolitic dome were exposed to strong hydrothermal alteration involving both silicification and alunitization, which was associated with exposure to post-volcanic processes such as impacts of solfatara solutions and fumaroles.

Therefore, the gravity field anomalies, and the drilling and gamma-logging data from borehole no. 4, outcrops of porphyraceous granodiorites near to the sites and all over the region, along with the petrographic, chemical and X-ray structure analysis of the rhyolithic dome, all suggest that the high-resistance Layer 4 identified 1.5–10 km deep beneath the Karkar-Jermaghbyur site could correspond to the intrusive rocks and represent the southern extension of the Dalidagh intrusion.

Signs of hydrothermal alteration of rocks in the rhyolitic dome, manifested in silicification and alunitization, are related to the concurrent post-volcanic processes such as exposure to effects of solfatara solutions and fumaroles.

Sixteen (16) km north of the Karkar Site, at the contact of the Dalidagh intrusion with Quaternary lava, there is a Jermajour group of thermal springs (Isti-Sou Springs, Fig. 2.42). On the surface, spring water temperatures range up to 72°C, with flow rates of about 1000 m³ per day. The Dalidagh intrusion has been considered the most probable heat source for the Jermajour Springs group.

The Jermouk group of thermal springs is located farther westward, at the distance of 22 km from the Karkar Site. In those springs, surface water temperatures range up to 64°C (Fig.

2.42). Jermouk group springs follow the contact between the Jermouk intrusion and the Quaternary lava. The Jermouk intrusion is represented by monzonites and monzo-diorites of the Early Oligocene. Drilled wells allowed detecting temperatures of 60-62°C at the depth of 600-650 m, and the geothermal well gradient varied from 4.5 to 12.5 m/°C depending on the well. The heated intrusive rocks have been considered the source of heat for the Jermouk group.

These facts all bear evidence supporting the southern extension of the Dalidagh intrusion up to the Karkar Site and farther southward, and confirm Hydrothermal Model A, assuming presence of a vast diffuse source of heat located beyond the limits of the *pull-apart* **basin and conductive cooling of the quartz-monzonite body or some deeper object.**

The cause of the abnormally heated condition of the quartz monzonite intrusion is apparently related to certain features of the regional intrusive and effusive volcanism developing in the Syunik Volcanic Highland and will be considered below, under the section addressing the conceptual model.

5.2. Model B – Localized source of heat

Hydrothermal Model B provides for presence of a localized heat source within the *pull-apart basin*, on the boundary of the fractured monzonite layer (FR) and the sedimentary basin filled with lava and alluvium (AL). The parameterization of Model B demonstrated that presence of a high-temperature source in the layer (FR) was unlikely, but it did not exclude that a low-temperature heat source could have been present there. In the meantime, two uncertainties still have been preserved in the assumptions made for Model B, namely:

1. Layer (QZ) does not have any high permeability or fracturing zone capable of transporting heat and heated waters toward upper layers.

2. The layer of non-fractured monzonites (QZ) does not contain any high-temperature source, as the low-temperature source within Layer (FR) gives the same result as the high-temperature source in Layer (QZ). This could happen because Layer (QZ) behaves as thermal insulator limiting the heat transfer.

In general, the conclusions of the hydrothermal modeling with respect to Model B are certainly justified. It is unlikely, indeed, that the low resistivity zone, detected by all MT models (Zone 2) on the boundary of Layers (AL) and (FR), accommodates a high-temperature source of heat. However, it is still possible that a high-temperature source could be located deeper within Layer QZ, while Layer QZ itself hosts a fracturing zone that realizes the transport of heated water to the upper layers (AL) and (FR), where it mixes with cool meteoric waters and forms some relatively lower temperature horizon of Zone (FR).

Let us consider presence of a fractured permeable zone within the monzonites that could have played the role of a channel to transport high-temperature water.

Depression D1, apparently representing volcanic caldera with the diameter of 3.5 km, is located 500 m east of Borehole 4 (Fig. 2.43 a, b). The western flank of the caldera is cut with a rhyolite dome as large as 1 000 m × 600 m. The rhyolite dome falls within the area studied by the MT surveys of 2004, 2009 and 2011, and is located 400 m east of Borehole N4 (1 in Fig. 2.41). Petrographic description of rocks in this rhyolitic dome shows high correlation with Phase 3 rhyolites of the Dalidagh intrusion. The maximum thickness of the low-resistivity

Layer 2 is recorded by the MT data just beneath Caldera D1 and the rhyolitic dome (Fig. 2.44). Certainly, both the rhyolitic dome, and the caldera itself, cut through the layers of monzonite (FZ and QZ) and could have developed fracturing zones. Two to four kilometers south of the site covered by the MT studies, there is a North-to-South elongating system of 21 Holocene volcanoes that should have cut through monzonite Layers FZ and QZ (Fig. 2.44). Volcanic edifices recorded 800 m NE of the 3D MT survey area accompany outcrops of the Early Miocene porphyraceaous granodiorites related to Phase 2 of the Dalidagh Intrusion. In both cases, intrusion outcroppings are broken through by Quaternary volcanoes (Fig. 2.40). Therefore, abundant volcanic apparatuses, many of which are of Holocene age, might help to demonstrate it in principle that the monzonite layer could have been broken through and that potential fracturing zones could have been present.

Additionally, the present system of active faults forming the *pull-apart basin* structure, and the pattern of gravity data that emphasizes this structure in Fig. 2.38 attest that permeability and fracturing zones penetrating to the deep can exist also. Eight hundred (800) meters east of Borehole 4, on the western side of Depression D1, one of the active faults is manifested as a scarp generated by surface rupturing during a strong earthquake. The surface rupture broke through the ancient burial mound (*kurgan*) dated back to the 12th-11th centuries BC, and dislocated the *kurgan* and its wall by 8 m by right-lateral strike-slip (Fig. 2.45). The depth of strong earthquake hypocenters in Armenia varies from 15 to 20 km; therefore, the active faults forming the *pull-apart basin* penetrate at least to a comparable depth from the surface. The faults bounding the *pull-apart basin* often shape a *flower*-type structure and, converging at depth even join one another in the centre of the *pull-apart* (Fig.1.20). This pattern could be considered also for the Karkar *pull-apart basin*, and the central zone where the faults converge (PDZ - principal displacement zone) could represent the channel that provides for connection between moderately hot surface waters and relatively higher-temperature source of heat at depth.

To support such a hypothesis, the 2D MT survey data for 2009 and 2004 can be very important. In the central part of the Karkar *pull-apart basin*, all models developed by the data of 2D MT and 3D MT surveys have identified Zone 4 with very high resistivity values ranging up to 2000 Ohm×m (Figs. 2.6, 2.7, 2.8, and 2.12). This zone is interpreted by all models as a monzonite intrusion. However, in the centre of this zone, the MT data have recorded Zone 5 that has much lower resistivity values (Figs. 2.6, 2.7, 2.8, and 2.12). The most plausible interpretation of low-resistance Zone 5 could be the *flower*-type structure of converging faults that bound the *pull-apart basin* (Figs. 2.6, 2.7, and 2.8). Models Georisk/USF-2009 assign resistivity values of 500-400 Ohm×m to this zone while Models «Nord-West»-2004 and «Nord-West»-2009 record much lower resistivity values (Figs. 2.6, 2.7, and 2.8). On the model built by the 3D MT survey data in Fig.2.12, Zone 5 is recorded much less clearly (Fig. 2.12). As demonstrated in Part 1, Sections 4.1.1 and 4.1.2 of this Report, all data from the MT surveys of 2004, 2009 and 2011 show good rate of consistency. The divergence of geometry assessments and resistivity values estimated for Zone 5 can be explained if we consider that the models accounted for different depths. Models «Nord-West»- 2004 and «Nord-West»- 2009 were built to the depth of 12 km, Model «Georisk/USF»- 2009 covered the depth of 6 km, and the 3D MT model spread to the depth of 2 km.

Models «Nord-West»-2004 and «Nord-West»-2009 clearly record a zone of low resistivity beneath the central part of the *pull-apart basin*, which spreads to the depth of more than 12 km (Figs. 2.7 and 2.8). At the depths of 4 to 5 km, resistivity values in the zone drop to 20-30 Ohm×m. Such pattern could be interpreted by presence of permeability and fracturing zone in the depth interval from 4 to 12 km and farther in the central part of the *pull-apart basin* structure. Most probably, this zone of fracturing is controlled by the *pull-apart* basin-bounding

93

faults that converge at depth to shape a *flower*-type structure. Low resistivity values in this zone can be interpreted by transport of heated water from the deep. The MT survey data all record increase of resistivity at the depths of about 2000-1500 m. This depth interval could have a shielding layer, isolating the subsurface zone of low resistances (Zone 2) from the deeper zone of low resistances (Zone 5). It is difficult to judge how much impermeable is this shielding layer and whether there is a possibility of water circulation between Zone 5 and Zone 2. On one hand, the 3D MT data have demonstrated lack of low resistivity zones at the depth of 2000-1500 m all over the area surveyed in 2011. The shielding layer of high resistance values between Zones 2 and 5 is noticeable also in the MT data of 2004 (see Fig. 2.6c). On the other hand, the findings of the 2D MT interpretation by 'Nord-West" in 2009 and partly those of the Georisk/USF-2009 show the plunging of Layer 2 in the central part of the *pull-apart basin*, just above Zone 5 (Figs. 2.6b, and 2.7b,c). Even with lack of connection between Zones 5 and 2, the insulating layer of monzonite at the depth of 2000– 500 m might appear heated enough to serve an additional localized source of heat.

Therefore, the analysis of geological and MT data indicates that a permeable channel /conduit/ may be present under the central part of the *pull-apart basin* structure. Most probably, this zone of fracturing is controlled by the *pull-apart basin*-bounding faults that converge at depth, forming a *flower*-type structure. Low resistance values in this zone may be interpreted by transfer of heated water from the deep. The MT survey data have indicated that an insulating shield could be present at the depth of 2000 -1500 m, isolating the subsurface zone of low resistance (Zone 2) from the deep zone of low resistances (Zone 5). However, even if there is no communication between Zones 5 and 2, the insulating layer of monzonite in the interval of 2000–1500 m could appear to be heated enough to serve as an additional localized source of heat. These facts allow us to suggest that Model B, assuming a localized source of heat, may appear likely, provided that a high-temperature source exists in Layer QZ more than 2000 m deep.

A combination of Models A and B is also plausible: the primary diffuse source of heat is located beyond the Karkar Site, and the structure of the *pull-apart basin* forms an additional localized source of heat.

5.3. Conceptual model

5.3.1. Regional Model for the Syunik region

Manifestations of concurrent effects of the intrusive and effusive magmatism are important features to consider when assessing the geothermal potential of the study region as a whole. A large intrusion was embedded 1.5-10 km deep at the Karkar Site. Deeper, the intrusion was split into two blocks by the system of active faults bounding the *pull-apart* basin structure. The interpretation of the MT surveys suggests that the site of intrusion split by the faults represents a permeable vertical channel that could have provided for transportation of meteoric water inward and rise of hot fluids up to the surface.

The rhyolithic extrusion was embedded along the linear surface outcrop of the permeable channel, aligned by many centers of Pleistocene and Holocene volcanic eruptions.

This suggests that the permeable vertical conduit, produced by the *pull-apart* basin faults, was associated with the embedding of two phases (35-22 Ma) of the Dalidagh intrusion and of the third phase (3 Ma) as the rhyolithic extrusion. Later on (1.5-0.01 Ma), eruption

channels of the Pleistocene and Holocene volcanoes formed in the same vertical permeable zone.

Abovyan and Malkhasyan (1961) published other example of such combination between intrusive and effusive volcanism. At the distance of 10 km to the west of the Karkar Site, there is a small outcrop of granosyenite intrusion, 2.2 x 1.9 km in size. The intrusion is broken by a Quaternary volcano, of which a crater with the central neck has been well preserved. A 5 km-long and 1 km-wide lava flow stretches from this crater towards the SE. Abovyan and Malkhasyan (1961) suggest that rocks of this intrusion are similar to the granosyenites of the southern termination of the Jermouk and Dalidagh intrusions.

The large-scale Dalidagh and Meghri intrusions, along with a series of numerous intervening smaller intrusions and extrusions, shape a distinct north-trending zone (Fig.2.46). The presence of this zone and its important role in the geodynamics, magmatism and metallogeny of the Southern Armenia were mentioned by Meliksetyan et al (1975). In the north of the region, the meridian-oriented north-trending zone contains concentrated intrusions (red color in Fig. 2.47) and joins the area of intense Quaternary volcanism developed across the Syunik Highland, accommodating the Karkar and Jermaghbyur sites in its center. The meridian zone of the intrusive and effusive magmatism is bounded with large faults on both sides. The eastern of the faults is the Pambak-Sevan Fault that forms the *pull-apart* basin at the Karkar site. Well-known thermal springs such as Jermaghbyur (32°C), Jermajour (72°C), Jermouk (64.5°C, 52°C) and Vorotan (42°C) are confined to the meridian-oriented zone and the faults that bound it (Fig. 2.47).

The analyses of rhyolite samples collected on the volcanoes located in the vicinity of the Karkar site (Fig. 2.47) were conducted at the Leeds University (UK) and in the IGS of the NAS (Armenia) in 2009. The results of these tests indicate higher contents of incoherent lithophilous elements (*Rb*, *Th*, *U*, *Cs* and *Pb*) and high-grade elements (*Zr*, *Hf*, *Nb* and *Ta*).

The character of distribution of the lithophilous *Pb*, *Sr*, *Ba*, *Th*, *U* and the high-grade *Zr*, *Hf*, *Ta* and *Nb* in volcanic rocks of the basaltoid group (tephrite, basalt, trachybasalt), which are common in the region, indicate that their origin is related to a metasomatically enriched mantle source with parameters different of those of volcanism sources in Aragats and Gheham

Variations of isotopic tags of the basaltoids ($^{87}Sr/^{86}Sr=0.70411-0.70476$) and of the rhyolites ($^{87}Sr/^{86}Sr=0.70493-0.70593$) attest that the effusive volcanism throughout the entire region was associated with a mantle source, and small crustal contribution is detected for the rhyolitic extrusions.

We believe that association of the north-trending zone of intense intrusive, extrusive and effusive volcanic evolution with a mantle source is an important evidence for the interpretation.

By applying the seismic tomography method, many recent studies have detected local areas of rising of the upper mantle in the Eastern Anatolia, Caucasus and Iran (Al-lazki et al., 2003; Toksoz et al., 2007; Zor, 2008; Ozacar et al, 2008). Areas of local rising of the upper mantle were recognized also in the region of the Syunik volcanic ridge that accommodates the north-trending zone of intense intrusive, extrusive and effusive volcanism (Figs. 2.48 and 2.49). Much earlier, Orovetsky and Yegorkina (1983) analyzed the data of seismic prospecting performed by the method of converted earthquake waves and concluded that a deep magmatic diapir, with high geothermal potential, was present in Central Armenia.

Considering the above, the conceptual model for the regions surrounding the Karkar and Jermaghbyur sites could be the following. A magma source could be located 40-50 km deep and associated with the abnormally uplifted upper mantle. The magma source became a source that embedded Phases 1 and 2 of the Dalidagh intrusion within the depth interval of 0-12 km (Fig. 2.50). According to estimates, Phases 1 and 2 were embedded between 35 and 22 Ma. The

rhyolitic extrusions were embedded around 3 Ma ago, and one of their domes is located just at the Karkar Site. It is possible that intermediate magma sources existed for all three phases of the injection (Fig. 2.50).

The Dalidagh intrusion is outlined by the Terter Fault in the north and the Pambak-Sevan Fault in the south. Active strike-slip fault deformations along the Pambak-Sevan Fault formed the structure of *pull-apart* basin at the Karkar site and developed the vertical conduit that channeled volcanic eruptions in the Pleistocene (1.5 Ma) and Holocene (0.001 Ma) (Fig. 2.50).

This attests to a long-time, developing association between the evolution of magmatic and tectonic processes confined within the same region.

Therefore, the sites of Karkar and Jermaghbyur represent just a small part of a large tectono-magmatic association. The area of the negative gravity anomaly that could emphasize the distribution of the Dalidagh intrusion is 420-430 km^2. The time when this magma structure started to form is estimated at 35 million years, and it was active almost until recently (5-6 thousand years BP). Most probably, the last eruptions of the Holocene volcanoes at the site have a near-historical age, as their lava covered petroglyphs. The features of geochemistry and isotopic tags $^{87}Sr/^{86}Sr$, as well as the seismic tomography indicate that intrusion channels of the intrusive and effusive magmatism were linked with the mantle. The Pambak-Sevan Fault and the *pull-apart* basin structure have been active until the present, and, according to the seismological evidence, penetrate at least to the depth of 15 km. The boundaries of the tectono-magmatic association are emphasized by the outlets of thermal springs in the regions of Isti-Sou, Jermaghbyur and, possibly, in Jermouk, Ouits and Vorotan. Signs of intense hydrothermal alteration of rocks related to exposure to such post-volcanic effects as solfatara and fumaroles are observed at the site of Karkar and Jermaghbyur.

The aggregate of this evidence attests to the presence of a large structure with long-continued tectono-magmatic evolution. The recent manifestations of magmatic activity of this structure are only few thousands years old, while the tectonic and hydrothermal activity has been preserved until the present time. Therefore, the geothermal potential of the area as a whole may appear quite high and certainly extends far beyond the limits of the Karkar and Jermaghbyur sites. Large structure of this size, which underwent a long-term tectono-magmatic evolution, could provide for the heating of a large portion of the crust stretching from the thermal springs of Jermaghbyur in the north up to the Ouits-Vorotan springs in the south, thus confirming Hydrothermal Model A that assumes a diffuse source of heat within the Karkar Site.

Figs. 2.51 to 2.55 demonstrate examples of conceptual models suggested worldwide for geothermal deposits located in tectono-magmatic settings similar to the ones present in the Syunik region.

5.3.2. Local Model for the Karkar Site

The evidence collected by the geological and geophysical studies conducted in 2004, 2009 and 2011 enable us to propose conceptual model for the Karkar Site. The Karkar Site is situated on the southern flank of the large Dalidagh-Syunik magmatic structure with a long-term evolution history. The geochemical features and seismic tomography data bear evidence of association between the mantle and the channels of embedding of intrusive and effusive magmatism in the Dalidagh-Syunik structure.

The Karkar Site is accommodated within the western flank of the *pull-apart basin* structure, shaped by the active Pambak-Sevan Fault. As attested by the data of boreholes,

geological investigations, MT and gravity survey data the following structural units can be identified in the limits of the Karkar Site:

1. **Layer 1 (AL)** spreads from the day-surface to the depths of 250-500 m and is represented by high-resistance rocks (hundred and thousands Ohm ×m). Apparently, the layer corresponds to the sedimentary basin filled with Quaternary lava and alluvium, as indicated by the gravity model and the log of Borehole 4. The greatest thickness and highest resistance values in Layer 1 are recorded on the eastern margin of Depression D1 and over the sites of development of the Pleistocene volcanoes (Fig. 2.56).

2. **Layer 2 (FR)** spreads within the depth interval of 500-1200 m (thickness of 600-700 m). Layer 2 is represented by low-resistance rocks with 10-20 Ohm×m. The lowest resistance values and the greatest thickness of Layer 2 are recorded in Depression D1. Layer 2 is interpreted as a zone of fractured quartz monzonites with possible content of mineralized, low-temperature waters (Fig. 2.56).

3. **Layer 3 (QZ)** fills in the spaces between Layers 2 and 4, and spreads within the depth interval of 1000-3000 m (Fig. 2.56). The layer is about 500-800 m thick in the center of the *pull-apart basin* structure. Easterly, Layer 2 rises and its thickness is less than 1 km, while in the west it plunges down to the depth of 3 to 4.5 km. Layer 3 is characterized by resistance values from 200 to 50 Ohm×m and is interpreted as less fractured quartz monzonite. An important feature of this layer is that its lower boundary (bottom) plunges in the centre of the *pull-apart basin* structure and in the west (within the region of the Jermaghbyur spring) downward to the depths of 2500 m and 4 km, respectively (Fig. 2.56).

4. **Layer 4 (MZ) –** The layer is identified as two large blocks separated with Layer 5 (Fig. 2.56). Based on the 2D and 3D models, the upper boundary of the blocks is recorded at the depth of about 1500–1800 м. It is difficult to distinguish the lower boundary: in the west of the profile, Layer 4 spreads to the depth of about 10-12 km, where it might be terminating. Layer 4 is represented by very high-resistance rocks (1000-2500 Ohm×m). The three models all record gradual increase of resistance from the outer boundaries of Layer 4 toward its inner areas (Fig. 2.56). Layer 4 can be interpreted as monolithic blocks of intrusion not saturated with water.

5. **Layer 5 (PDZ) –** This layer is oriented vertically according to Model "GEORISK/USF", or inclined eastward according to "Nord-West" Model. The layer has been recorded from the depth of 3 km and traced to the depth of more than 10 km (Fig. 2.56). In areas closer to the surface, Layer 5 joins Layers 3 and 2 in the centre of the *pull-apart basin* structure, at the depth of about 3 km.

The MT interpretation models are all consistent identifying geometries of Layers 1 to 4 and provide similar values of resistance in those layers. Disagreement appears in the estimations of resistance values for Layer 5. Actually, the 3D MT data allowed identification of the uppermost parts of Layer 5 only, as the interpretation procedure was cut-off at the depth of 2-2.5 km (Fig. 2.12).

Model Georisk/USF-2009 suggested that Layer 5 had vertically-oriented geometry, and estimated resistance values in the layer at 500 - 800 Ohm × m (Fig. 2.6b).

Model "Nord-West"-2009 suggested an eastward-verging geometry for the layer, and estimated its resistance at the depth of 3-5 km at 20×30 Ohm × m (Fig. 2.7 b, c). Model "Nord-West"- 2004 also estimated resistance values in Layer 5 at 20×30 Ohm × m (Fig. 2.6c).

Models "Nord-West" 2009 and 2004 both have supposed that Layer 5 represents a deep conduit transporting hear-carrier fluids from some deep object up toward the surface. If low resistance values are assumed for Layer 5, its general geometry may be indeed interpreted as a fractured conductive zone present in the place of converging faults, bounding the flanks of the *pull-apart basin.*

Therefore, two slightly different conceptual models could be proposed for the Karkar Site currently. Both models consider the 3D MT, gravity survey and hydrothermal modeling data to the same degree, but apply different interpretation of the 2D MT data collected in 2009 and 2004.

Model Karkar A considers the interpretation of 2D MT data according to Model Georisk/USF-2009 and assumes that low resistance values are not present in the zone of Layer 5 (PDZ). In such case, Model Karkar A would provide only for a diffuse source of heat (Hydrothermal Model A) and characterize Layer 2 (FZ) as a reservoir of moderately warm waters (less than 100ºC). According to Model Karkar A, quartz monzonite in Layers 4 (MZ) and 5 (PDZ) might appear abnormally heated. In the meantime, hot water horizon might be lacking from Layers 4 and 5, and the abnormal heat could be confined solely to the monzonite massif. Model Karkar A is shown in Fig. 2.57.

Model Karkar B considers the interpretation of 2D MT data according to Models "Nord-West"- 2009 and 2004 and assumes that low resistance values of 20-30 Ohm×m may be present in Layer 5 (PDZ). In such case, Model Karkar B would provide for a localized high-temperature source of heat in Layer 5 (PDZ). Along with this, if Layer 3 (QZ) is permeable, Layer 2 (FZ) could be characterized as a reservoir of high-temperature water (more than 200ºC). In case Layer 3 (QZ) is impermeable, then Layer 2 (FZ) would contain relatively warm waters (less than 100ºC), while high-temperature waters within Layer 5 would be shielded /isolated/ with Layer 3 (QZ). Model Karkar B is shown in Fig. 2.58.

We can not exclude that there might be a combination of models A and B and the Karkar Site could accommodate some diffuse source of heat fed by the regional heating of monzonite within the Dalidagh-Syunik magmatic structure, or that there could be a localized high-temperature source of heat in Layer 5 superimposed over the diffuse one.

Figures 2.59 to 2.60 demonstrate examples of conceptual models of geothermal deposits in the settings similar to the Karkar Site.

5.3.3. Selection of location for the drilling of an exploratory well

The abnormal temperature gradient in Borehole 4, presence of fractured volcanic intrusion and narrow, N-to-S elongating *pull-apart basin* within the Karkar Site - all these factors in general create conditions favorable for rapid transport of hot water from the depth to the surface along permeable fractures. This fracture flow could be controlled by faults bounding the *pull-apart basin.* The water-bearing zone at the depth of 340 m in Borehole 4 may reflect areas of mixing between the ascending fluids and atmospheric /meteoric/ recharge.

Evidence provided by the studies conducted during 1988-1990, results of the MT sounding of 2004, as well as the data of the 2D and 3D MT and gravimetric surveys conducted in 2011 attest that exploratory drilling within the Karkar Site holds promises.

The large objects identified by the gravimetric and MT modeling, along with borehole observations, indicate that atmospheric /meteoric/ water can circulate down to considerable depth within the basin. To explain the anomalous temperature gradient observed in Borehole 4, a heat source should be available at depth. However, it is not clear if the heat source exists within the fault-bounded *pull-apart basin*, or beyond it.

As indicated above there might be certain ambiguity in the choice of adequate conceptual model for the Karkar Site. As a consequence of diverging resistance estimates derived for Zone 5 by Models Georisk/USF-2009, and "Nord-West"-2004/"Nord-West"-2009, two sub-models A and B could be suggested to offer different assessment of heat sources. Two actions are required to test both models:

Action 1 – The 3D MT soundings done by WesternGeco in 2011 are of very high quality, but WesternGeco modeled them to the depth of 2 km only. These soundings could be used to interpret resistances at relatively bigger depths than those represented in the report by WesternGeco, namely, to the depths of 10-12 km. Such interpretation could enable us to choose between sub-models A and B for the Karkar site. The 3D modeling results (modeled resistance values as a function of mapped location and depth) should be obtained from WesternGeco. This will enable more precise correlation of resistance anomalies at great depth before the drilling of exploratory wells is started.

Action 2 – It is recommended to drill two exploratory wells.

Exploration Well 1 – Model Karkar A provides for the presence of a diffuse source of heat located beyond the limits of the Karkar Site and for abnormal heating of the monzonite massif. To test Model Karkar A, it is necessary to drill an exploratory well in the region of Borehole 4. The exploratory well should be not less than 2 km deep. Drilling such a borehole will enable testing all data collected during the drilling of Borehole 4 in 1988, and also to check the possibility of abnormal heating of monzonites assumed by the diffuse Model A. Supposed location of drilling area for Exploratory Well 1 (B1) is shown in Figs. 2.61 and 2.62, at the site with the coordinates of N39°47'20.15" , E45°55'32.24". The location of well should be determined more specifically during reconnaissance studies to precede the drilling.

Exploration Well 2 – Model Karkar B provides for the presence of a localized source of heat within Layer 5 and for a potential presence of high-temperature waters (200°C) in the reservoir Layer 2. Drilling of Exploratory Well 2 should be provided within the area of Depression D1, on its eastern flank, where the lowest values of rock resistance (10-20 Ohm×m) are recorded at the depth of 0.8-1.2 km for Layer 2. This exploratory well should be not less than 1500-1800 m deep. It will enable to check Model A and Model B at the same time. If high-temperature water will be encountered in the course of drilling of the 2nd well in Layer 2, this would imply credibility of Model B, or that of a combined option of Models A and B. In such case, drilling of the area of Exploration Well 2 could be cancelled. Therefore it is supposed first to drill Exploration Well 2, and then, if the need appears, to drill the second well. Supposed location of drilling area for Exploratory Well 2 (B2) falls within Depression D1 and is shown in Figs. 2.61 and 2.62, at the site with coordinates of **N39°47'15.34", E45°56'53.85".** Figs. 2.63, 2.64, 2.65 and 2.66 show location of the proposed exploratory well B2, superimposed over the results of 3 independently conducted 2D MT inversions, based on the survey data from 2004 and 2009, and the 3D MT data inversion based on the 2011 survey records. Figs. 2.67 and

2.68 show location of the proposed Exploratory Well B2, superimposed over the 3D inversion data and correlated with the gravity model and fault data.

The location of well should be determined more specifically during reconnaissance studies to precede he drilling.

CONCLUSION

The interpretation of the results of studies conducted in 2004, 2009 and 2011 has led us to the following main conclusions:

- **The main structural feature of the Karkar Site is the large structure of *pull-apart* basin, bounded by a system of active strike-slip faults on the flanks. Intense tensile stresses developing inside the *pull-apart* basin determined the Pleistocene and the Holocene volcanism and might have been facilitating establishment of geodynamic settings that were favorable for origination of a geothermal reservoir.**

- **The systems of 7 to 10 sub-parallel faults, and depressions D1, D2 and D3, filled with lake waters, located on the sides of the *pull-apart* basin, might appear to be the most permeable zones capable of transporting meteoric water downward and enabling its circulation inside, as well as heat-and-mass transfer from deeper horizons and formation of heat- carrier reservoirs.**

- **The 2D MT surveys of 2009 and 2004, and the 3D MT survey of 2011 were conducted by three different groups from Russia, USA and Italy. The data of the 2009 MT survey were also independently interpreted by two groups – one from USA and one from the Russian Federation. The results generated by all interpretations are similar and bear evidence of the credibility of all MT surveys and of their interpretations.**

  - **The geophysical studies of 2011 enabled development of the gravity model that indicates that a 300 to 1500 m-deep sedimentary basin is present between two branches of faults bounding the structure of the *pull-apart basin.***

  - **The hydrogeological modeling suggested two models of heat sources. Model A provided for the presence of a diffuse source of heat that is located beyond the structure of the *pull-apart basin.***

  - **The sites of Jermaghbyur and Karkar represent a small part of a large tectono-magmatic association with long-time tectono-magmatic evolution. The magmatic activity of this structure manifested itself as late as a few thousands years ago, while the tectonic and hydrothermal activity has preserved until today. Hence, the geothermal potential of this area as a whole may extend far beyond the limits of the Karkar and Jermaghbyur sites, but additional studies would be required for the adequate assessment of this potential**

  - **According to the data of drilling, geological investigations, MT and gravimetric surveys within the Karkar site, it is possible to identify the following structural units:**

    1. **Layer 1 (AL) spreads from the day-surface to the depths of 250-500 m and is represented by high-resistance rocks (hundred and thousands Ohm ×m). Apparently, the layer corresponds to the sedimentary basin filled with Quaternary lava and alluvium, as indicated by the gravity model and the log of Borehole 4. The greatest thickness and highest resistance values in**

Layer 1 are recorded on the eastern margin of Depression D1 and over the sites of development of the Pleistocene volcanoes (Fig. 2.56).

2. **Layer 2 (FR)** spreads within the depth interval of 500-1200 m (thickness of 400-700 m). Layer 2 is represented by low-resistance rocks with 10-20 Ohm×m. The lowest resistance values and the greatest thickness of Layer 2 are recorded in Depression D1. Layer 2 is interpreted as a zone of fractured quartz monzonites with possible content of mineralized, low-temperature waters (Fig. 2.56).

3. **Layer 3 (QZ)** fills in the spaces between Layers 2 and 4, and spreads within the depth interval of 1000-3000 m (Fig. 2.56). The layer is about 500-800 m thick in the center of the *pull-apart basin* structure. Easterly, Layer 2 rises and its thickness is less than 1 km, while in the west it plunges down to the depth of 3 to 4.5 km. Layer 3 is characterized by resistance values from 200 to 50 Ohm×m and is interpreted as less fractured quartz monzonite. An important feature of this layer is that its lower boundary (bottom) plunges in the centre of the *pull-apart basin* structure and in the west, within the region of the Jermaghbyur spring, to the depths of 2500 m and up to 4 km, respectively (Fig. 2.56).

4. **Layer 4 (MZ)** - The layer is identified as two large blocks separated with Layer 5 (Fig. 2.56). Based on 2D and 3D models, the upper boundary of the blocks is recorded at the depth of about 1500–1800 м. It is difficult to distinguish the lower boundary: in the west of the profile, Layer 4 spreads to the depth of about 10-12 km, where it might be terminating. Layer 4 is represented by very high-resistance rocks (1000-2500 Ohm×m). The three models all record gradual increase of resistance from the outer boundaries of Layer 4 toward its inner areas (Fig. 2.56). Layer 4 can be interpreted as monolithic blocks of intrusion not saturated with water.

5. **Layer 5 (PDZ)** – This layer is oriented vertically according to Model "GEORISK/USF", or inclined eastward according to "Nord-West" Model. The layer has been recorded from the depth of 3 km and traced to the depth of more than 10 km (Fig. 2.56). In areas closer to the surface, Layer 5 joins Layers 3 and 2 in the centre of the *pull-apart basin* structure, at the depth of about 3 km.

Therefore, two slightly different conceptual models could be proposed for the Karkar Site currently. Both models consider the 3D MT, gravity survey and hydrothermal modeling data to the same degree, but apply different interpretation of the 2D MT data collected in 2009 and 2004.

Model Karkar A considers the interpretation of 2D MT data according to Model Georisk/USF-2009 and assumes that low resistance values are not present in the zone of Layer 5 (PDZ). In such case, Model Karkar A would provide only for a diffuse source of heat (Hydrothermal Model A) and characterize Layer 2 (FZ) as a reservoir of moderately warm waters (less than 100ºC). According to Model Karkar A, quartz monzonite in Layers 4

(MZ) and 5 (PDZ) might appear abnormally heated. In the meantime, hot water horizon might be lacking from Layers 4 and 5, and the abnormal heat could be confined to the monzonite massif solely. Model Karkar A is shown in Fig. 2.57.

Model Karkar B considers interpretation of 2D MT data according to Models "Nord-West"- 2009 and 2004 and assumes that low resistance values of 20-30 Ohm×m may be present in Layer 5 (PDZ). In such case, Model Karkar B would provide for a localized high-temperature source of heat in Layer 5 (PDZ). Along with this, if Layer 3 (QZ) is permeable, Layer 2 (FZ) could be characterized as a reservoir of high-temperature water (more than 200°C). In case Layer 3 (QZ) is impermeable, then Layer 2 (FZ) would contain relatively warm waters (less than 100°C), while high-temperature waters within Layer 5 would be shielded /isolated/ with Layer 3 (QZ). Model Karkar B is shown in Fig. 2.58.

We can not exclude that there might be a combination of models A and B and the Karkar Site could accommodate some diffuse source of heat fed by the regional heating of monzonite within the Dalidagh-Syunik magmatic structure, or there could be a localized high-temperature source of heat in Layer 5 superimposed over the diffuse one.

- The report of WesternGeco represents valuable addition to our understanding of the geothermal potential of the Karkar region. The quality of MT and gravity data collection and processing presented in the report prepared by WesternGeco are of state-of-the-art standard. In a broader sense, the report of WesternGeco leads to identification of a considerable anomaly of low resistance on the western margin of the fault-bounded basin. Location of the resistance anomaly correlates with the mapped faults.

- Data of the investigations conducted in the period of 1988-1990, results of the MT sounding of 2004, as well as the data of the 2D and 3D MT and gravimetry surveys of 2011 attest that exploratory drilling at the Karkar Site is promising.

RECOMMENDATIONS

- The 3D MT soundings done by WesternGeco in 2011 are of very high quality, but WesternGeco modeled them to the depth of 2 km only. These soundings can be used to interpret resistances at relatively bigger depths than those represented in the report by WesternGeco, namely, to the depths of 10-12 km. Such interpretation could enable us to choose between sub-models A and B for the Karkar site. The 3D modeling results (modeled resistance values as function of mapped location and depth) should be obtained from WesternGeco. This will enable to carry out more precise correlation of resistance anomalies at great depth before the drilling of exploratory wells is started.

- It is recommended to drill two exploratory wells.

Exploration Well 1 – Model Karkar A provides for the presence of a diffuse source of heat located beyond the limits of the Karkar Site and for abnormal heating of the monzonite massif. To test Model Karkar A, it is necessary to drill an exploratory well in the region of Borehole 4. The exploratory well should be not less than 2 km deep, Drilling such a borehole will enable testing all data collected during the drilling of Borehole 4 in 1988, and also to check the possibility of abnormal heating of monzonites assumed by the diffuse Model A. Supposed location of drilling area for Exploratory Well 1 (B1) is shown in Figs. 2.61 and 2.62, at the site with the coordinates of N39°47'20.15" , E45°55'32.24". The location of well should be determined more specifically during reconnaissance studies preceding the drilling.

Exploration Well 2 – Model Karkar B provides for the presence of a localized source of heat within Layer 5 and for a potential presence of high-temperature waters (200°C) in the reservoir Layer 2. Drilling of Exploratory Well 2 should be provided within the area of Depression D1, on its eastern flank, where the lowest values of rock resistance (10-20 Ohm×m) are recorded at the depth of 0.8-1.2 km for Layer 2. This exploratory well should be not less than 1500-1800 m deep. It will enable to check Model A and Model B at the same time. If high-temperature water will be encountered in the course of drilling of the 2nd well in Layer 2, this would imply credibility of Model B, or of a combined option of Models A and B. In such case, drilling of the area of Exploration Well 2 could be cancelled. Therefore it is supposed first to drill Exploration Well 2, and then, if the need appears, to drill the second well. Supposed location of drilling area for Exploratory Well 2 (B2) falls within Depression D1 and is shown in Figs. 2.61 and 2.62, at the site with coordinates of N39°47'15.34", E45°56'53.85". The location of well should be determined more specifically during reconnaissance studies to precede he drilling.

- Considering that presence of a diffuse source of heat, possibly linked with the large Dalidagh-Syunik magmatic structure, can not be ruled out, we can not exclude also that the Syunik-Dalidagh magmatic structure can represent a geothermal resource of much greater dimensions that those of the Karkar and Jermaghbyur sites and would therefore recommend conducting study of geothermal potential of the Dalidagh-Syunik structure.

- We recommend a study of the geothermal potential of thermal springs in the village of Ouits (52°C) and in the Vorotan village (42°C).
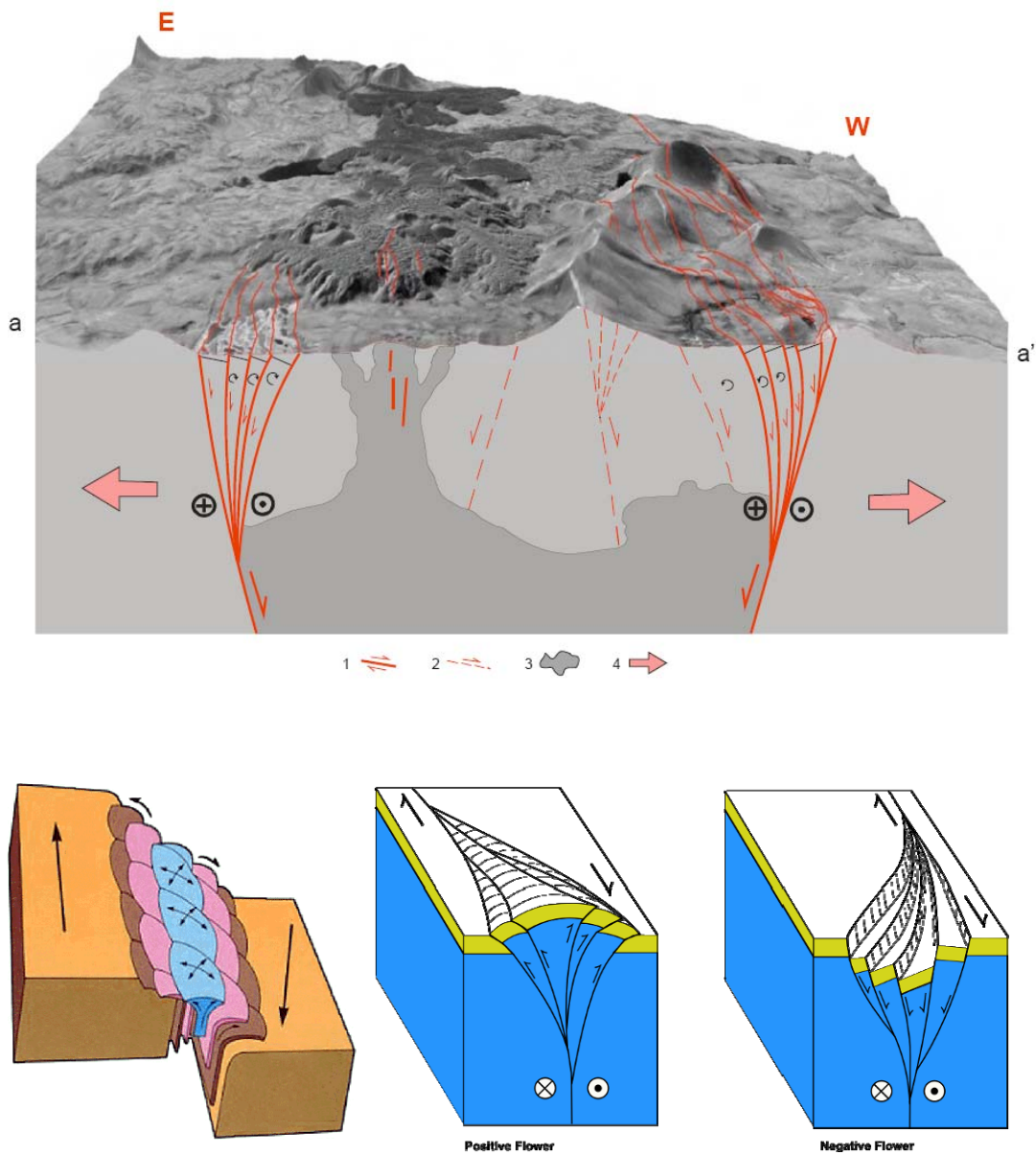
Fig. 2.1: The western and eastern sides of the *pull-apart* basin are bounded by the fault systems consisting of 8 to 10 juxtaposed branches of active faults. The faults shape a negative *flower* structure at depth, in the center of which the channels of Pleistocene and Holocene volcanic eruptions and their lava fields are located.

Western flank of the "pull-apart" basin	Eastern flank of the "pull-apart" basin
1	2
3	4
5	6
8	7
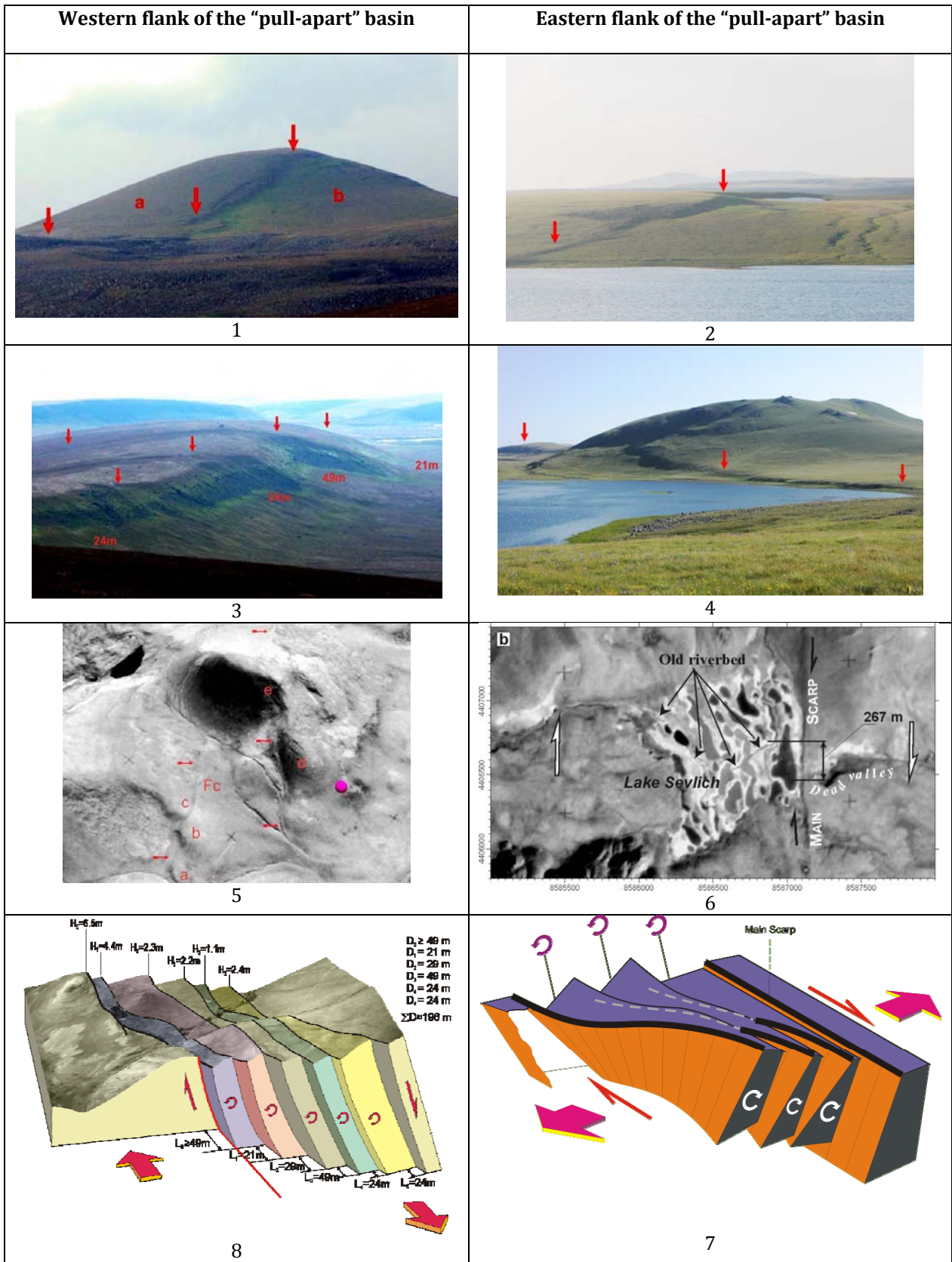
Fig. 2.2 Faults bounding the western and eastern sides of the *pull-apart* basin structure.
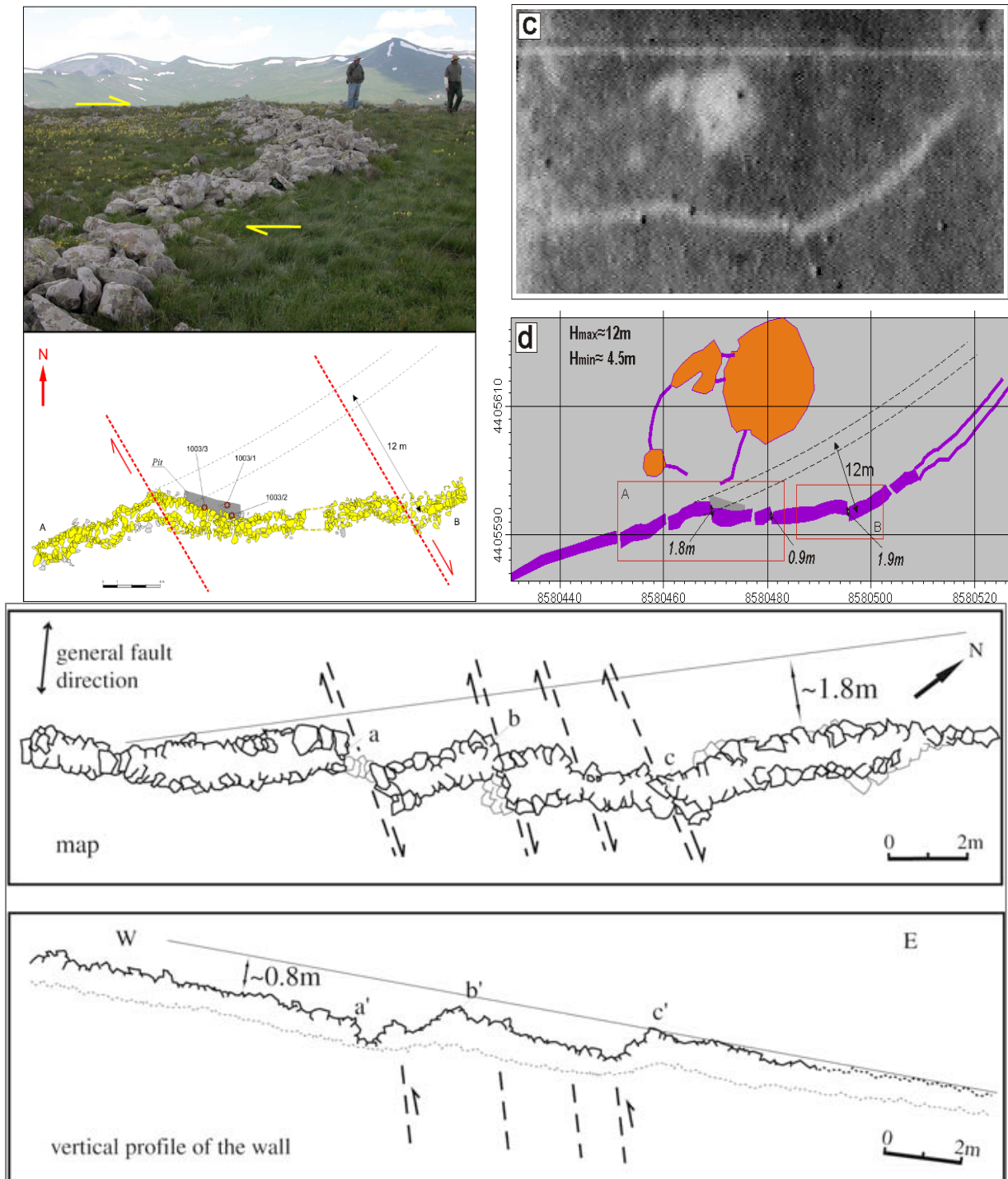
Fig. 2.3: Surface ruptures generated by strong earthquakes, which caused offsets of archaeological structures related to the period of the Middle and Late Bronze Age, located on the western boundary of the *pull-apart* basin structure.
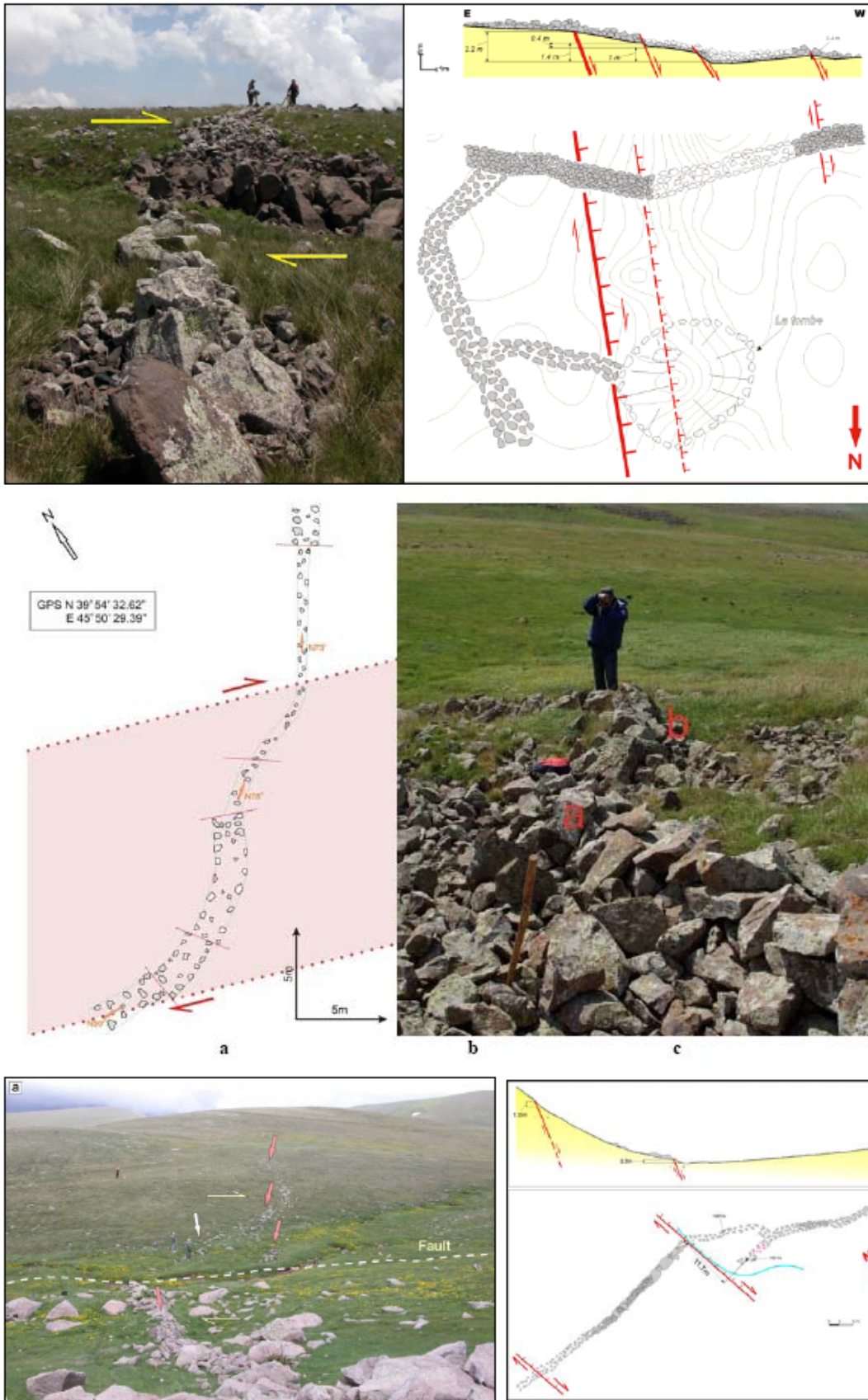
Fig. 2.4a: Surface ruptures generated by strong earthquakes, which caused offsets of archaeological structures related to the period of the Middle and Late Bronze Age, located on the eastern boundary of the *pull-apart* basin structure.
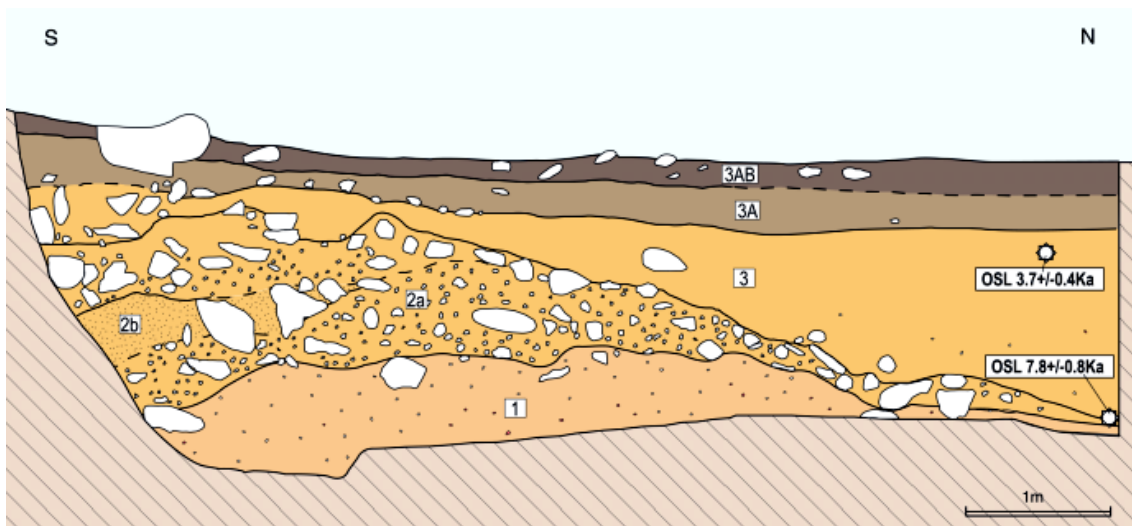
Fig. 2.4b: Surface rupture generated by strong earthquakes on the southern boundary of the *pull-apart* basin and the paleoseismological trench that provided earthquake dates constrained by the radiocarbon and OSL age estimates.
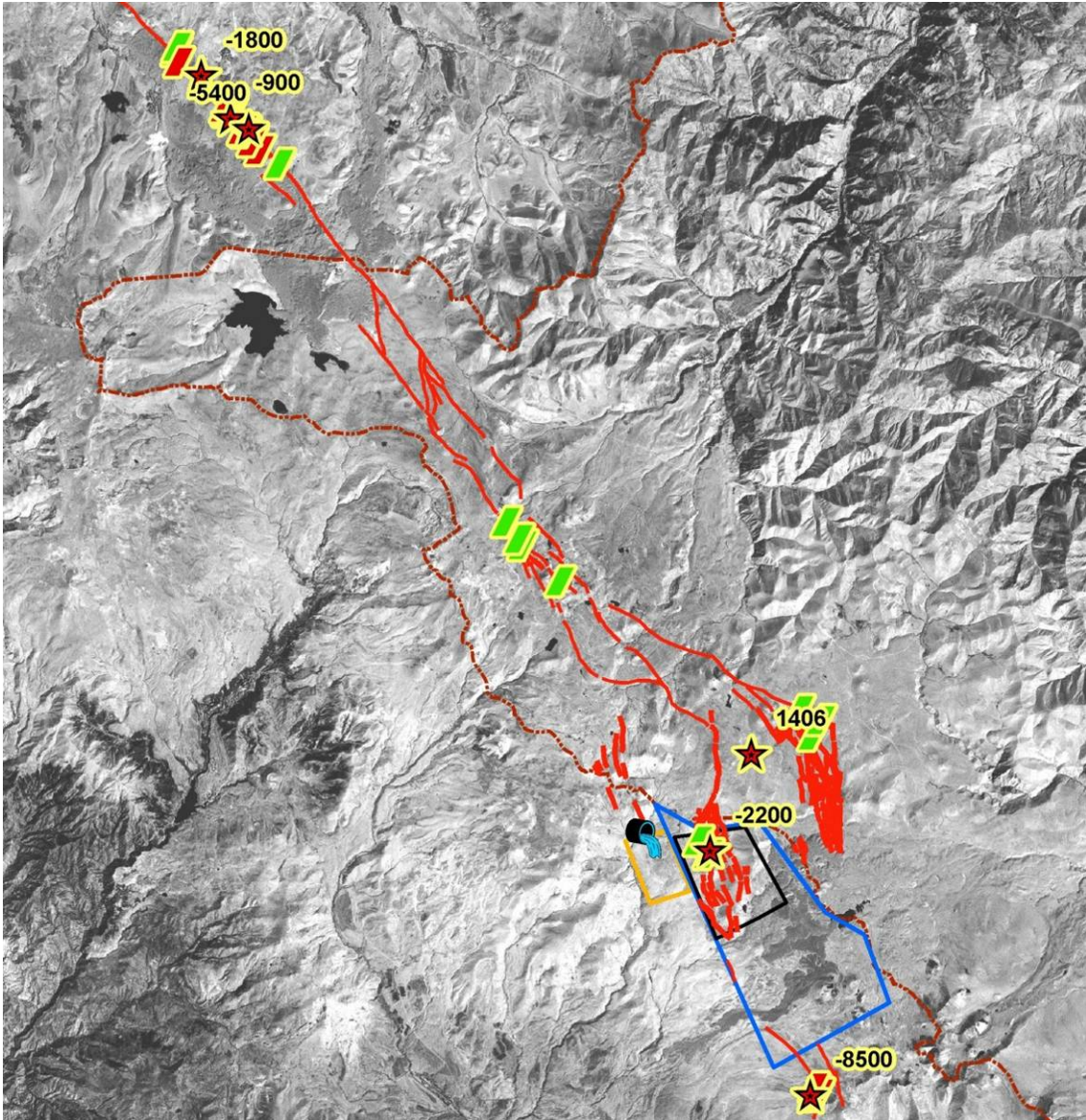
Fig. 2.5: The active Pambak-Sevan Fault at the site of Karkar and Jermaghbyur with indicated locations of paleoseismological trenches and date estimates of the paleo-earthquakes (BP)
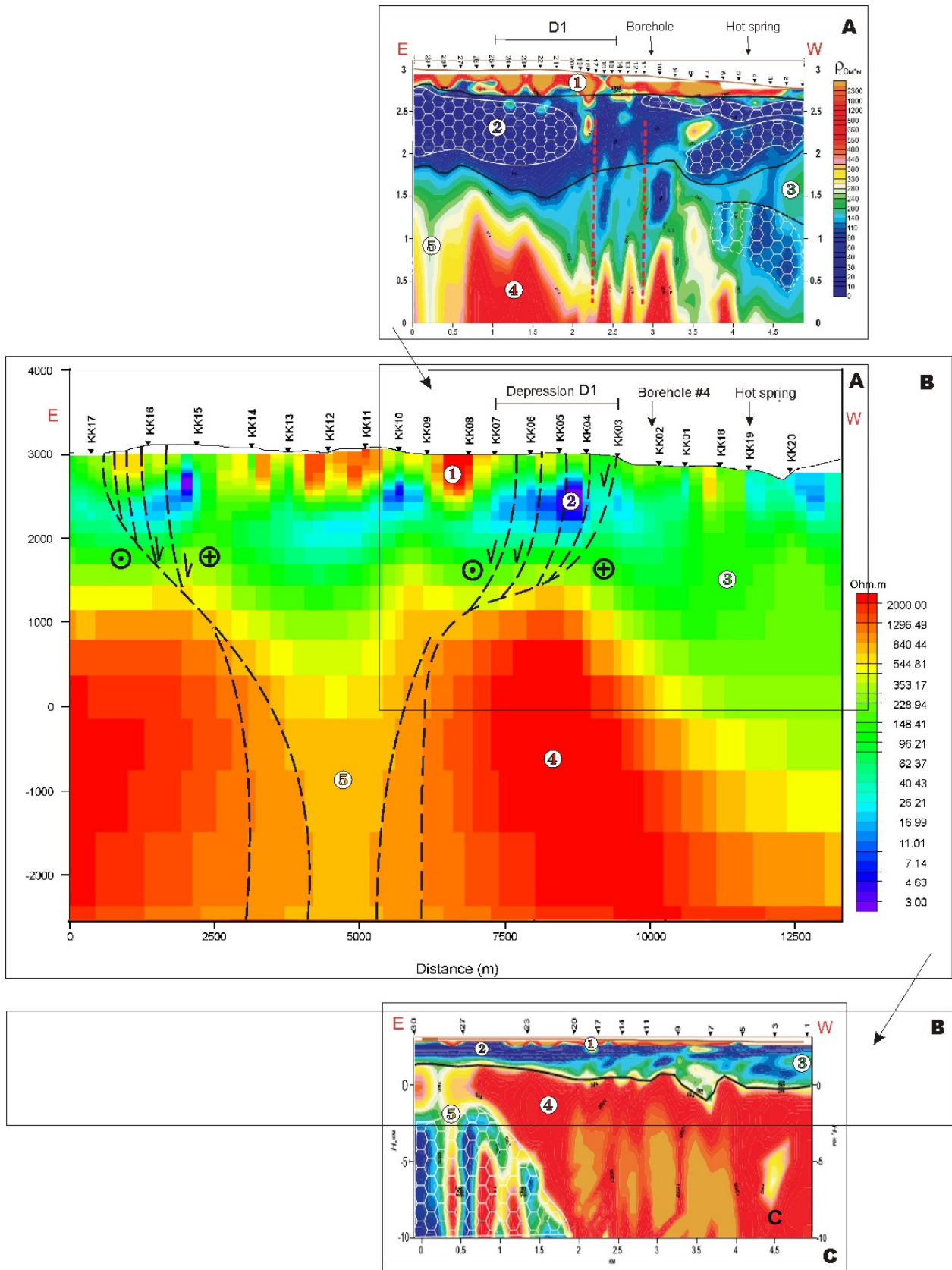
Fig. 2.6: Correlation between the finite 2D models produced by interpretation of MT surveys of 2004 and 2009
A – 2D model on Profile 2 ("Nord-West") of 2004 to the depth of 3 km;
B - 2D model along the 2009 Profile to the depth of 5 km ("USF");
C- 2D model on Profile 2 ("Nord-West") of 2004 for the depth of 10 km.
.
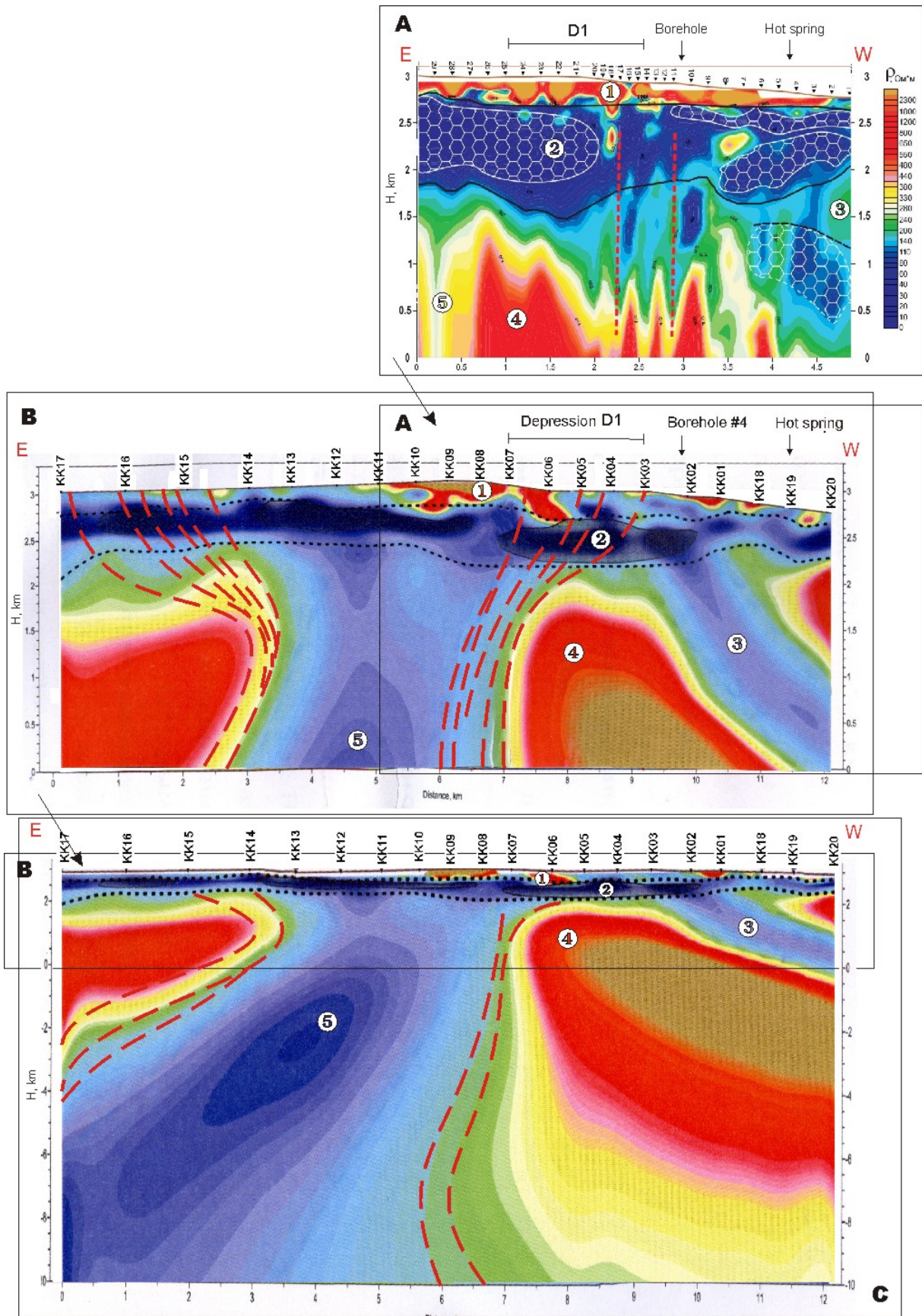
Fig. 2.7: 2D finite models of interpretation of the MT survey in 2009, developed by the *Nord-West* Company for the depths of 3 km and 10 km.
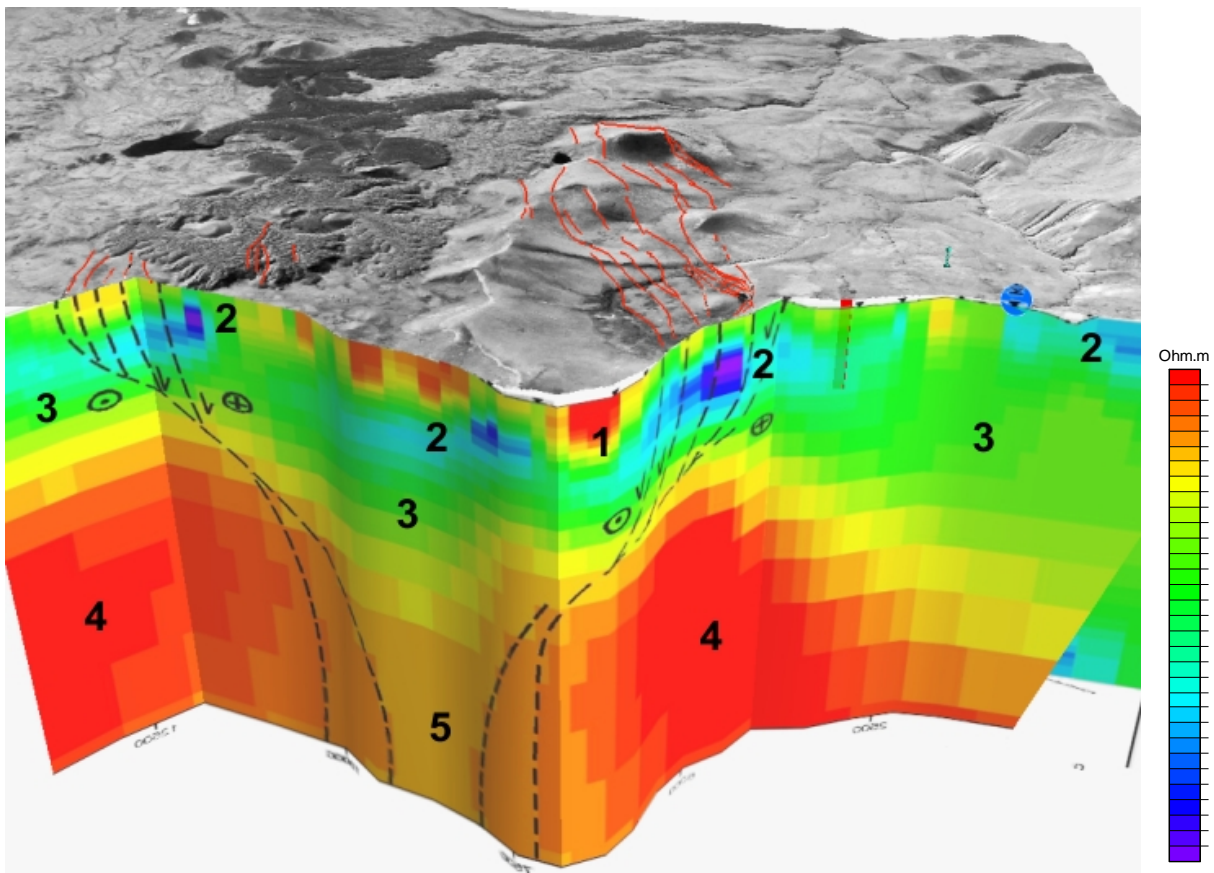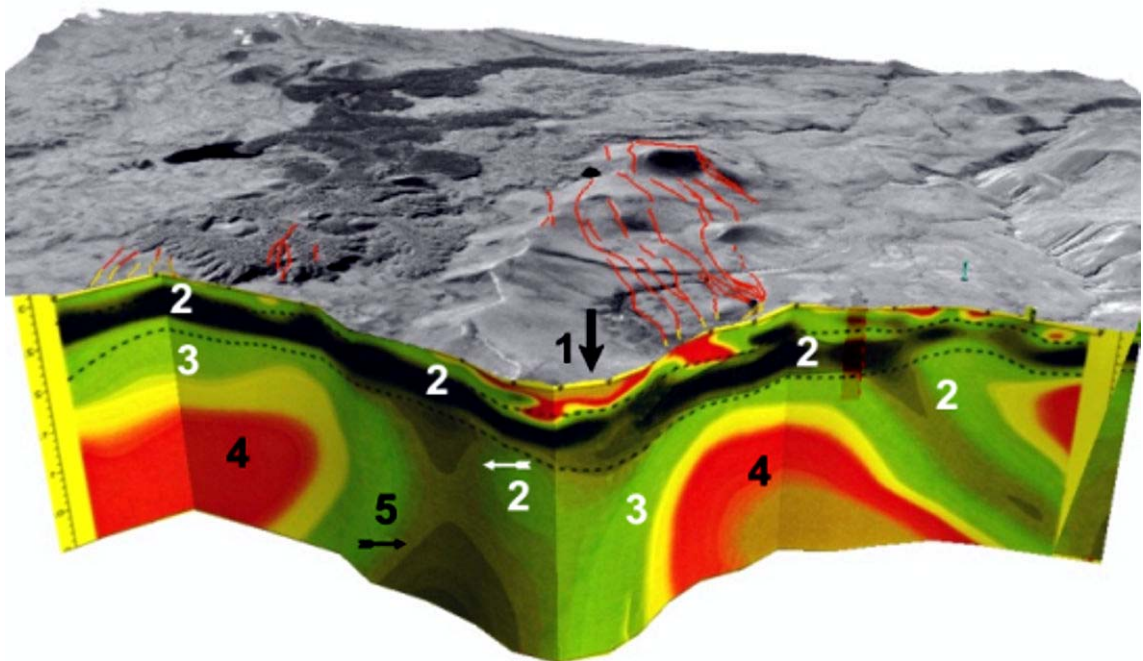
Fig. 2.8: 3D models built by means of GIS software *ArcScene 9.3*:
a – interpretation by the University of South Florida (USA); b – interpretation by the Nord-West Company (RF).
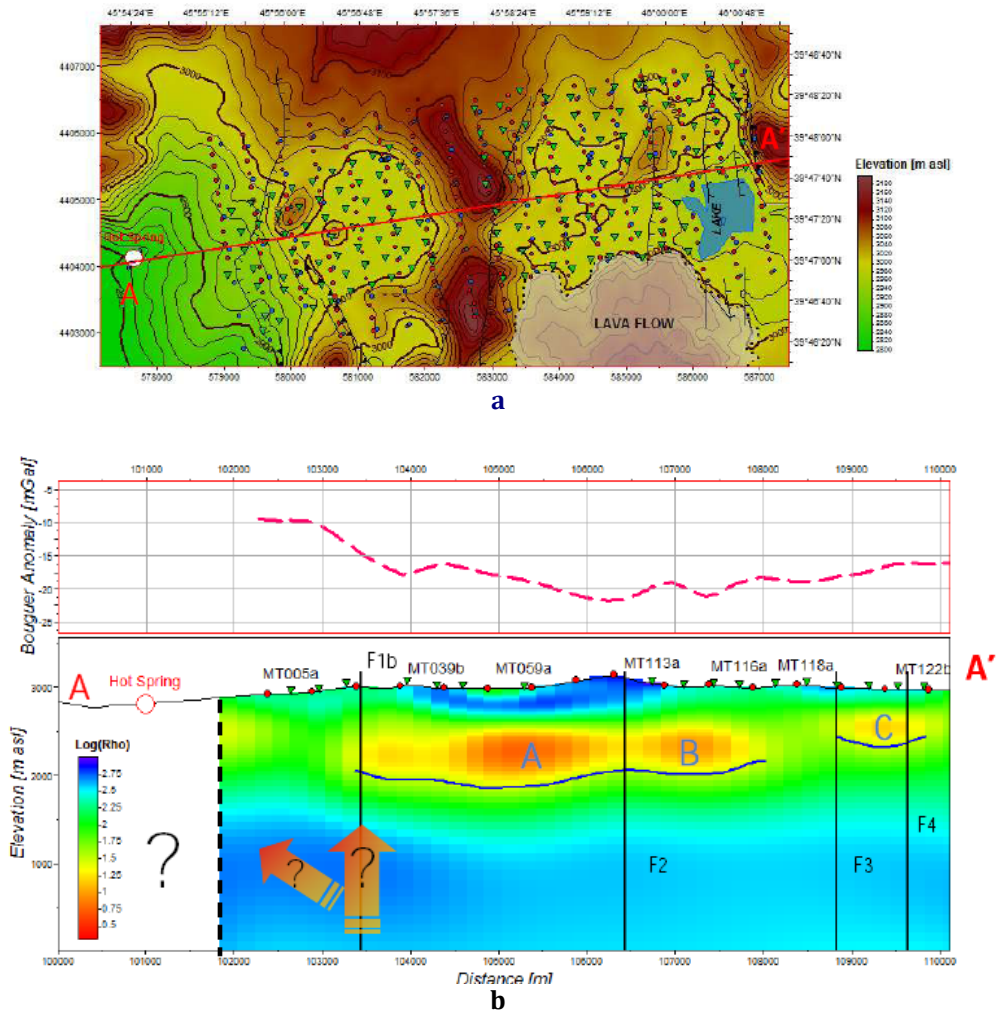
Fig. 2.9: a - 3D MT, gravimetry and soil gas measurement points: the red line indicates section **AA'**, shown in Fig. 2.9; **b –** resistivity model with Bouguer anomaly points and thermal manifestations, plotted along Line **A-A/.** Both figures are reproduced from the "Western Geco" report («Western Geco», 2012).
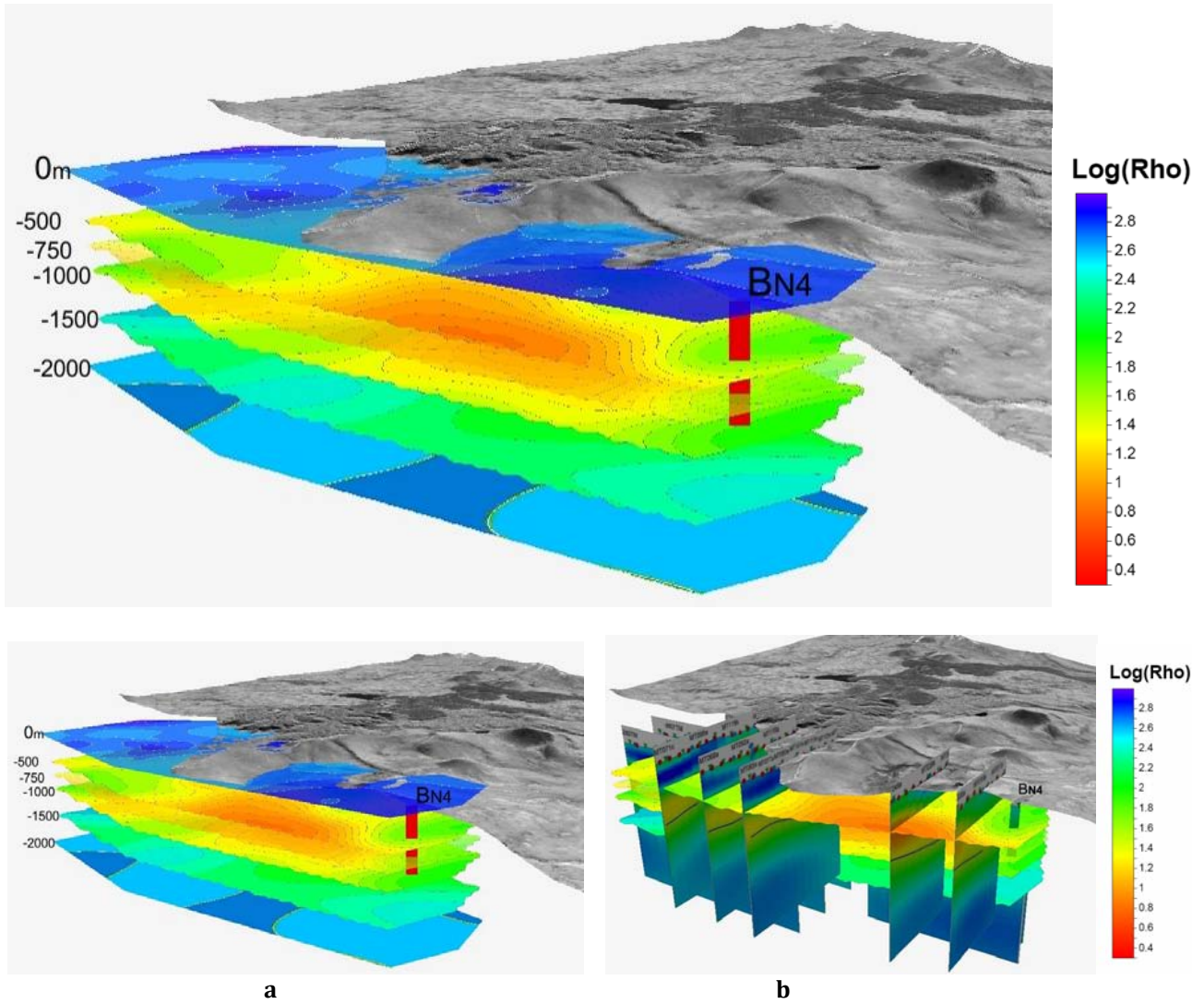
Fig. 2.10: a - Data of the 3D MT survey of 2011in the form of horizontal sections for an area of 20 km² and to the depths of: 0 m, 500 m, 750 m, 1,000 m, 1,500 m and 2,000 m.; **b -** Data of the 3D MT survey of 2011 in the form of 10 vertical sections (5 sections oriented N-S, and 5 sections oriented W-E).
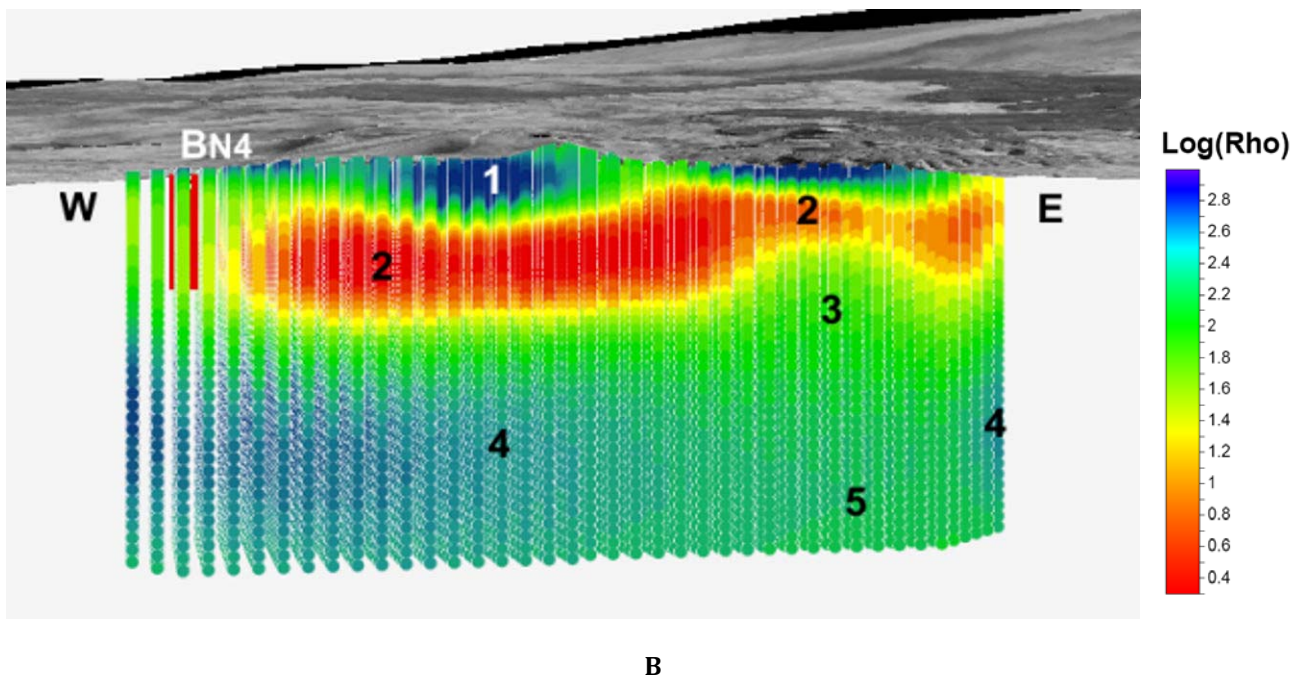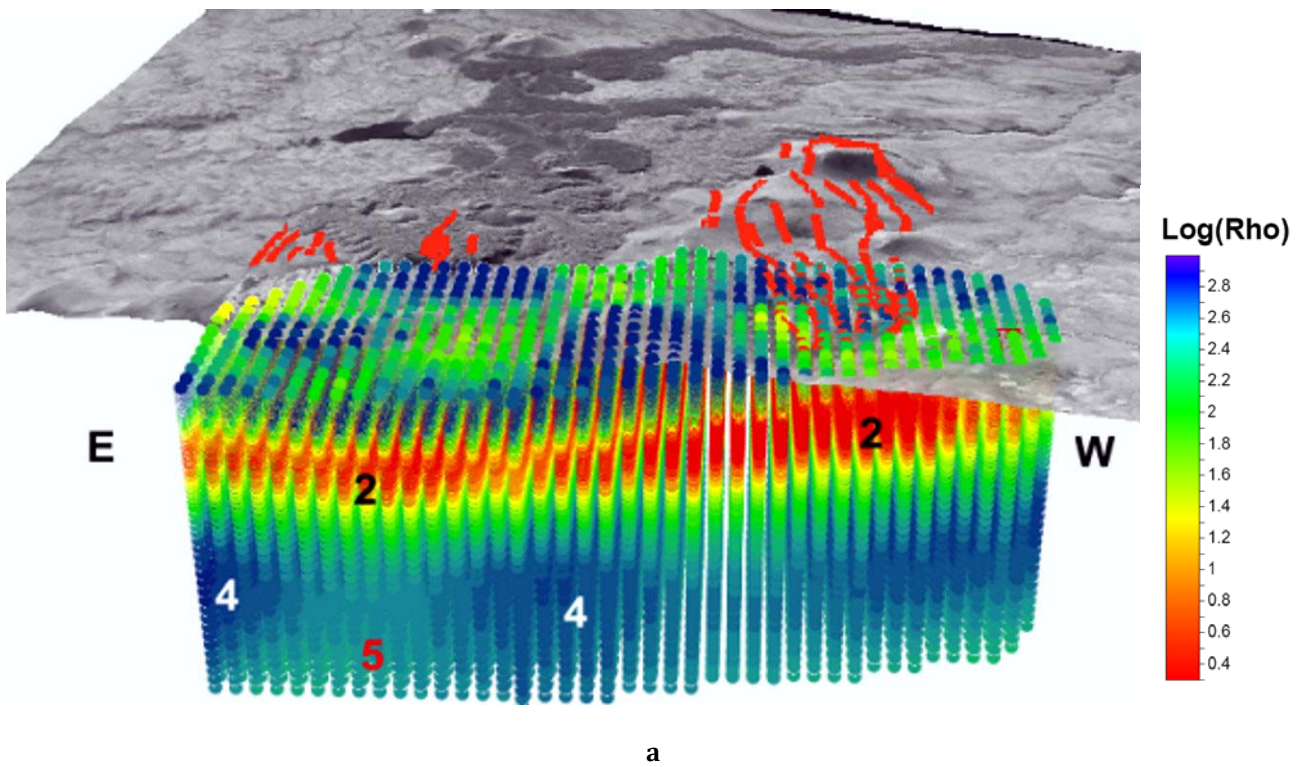
Fig. 2.11: Three-dimensional grid of data from the 3D MT survey of 2011: a – viewed North-to-South; b – viewed South-to-North. Numbers indicate Layers 1, 2, 3, 4 and 5, identified by the data of 2D MT inversions, which correlate with the data derived by the 3D MT inversion.
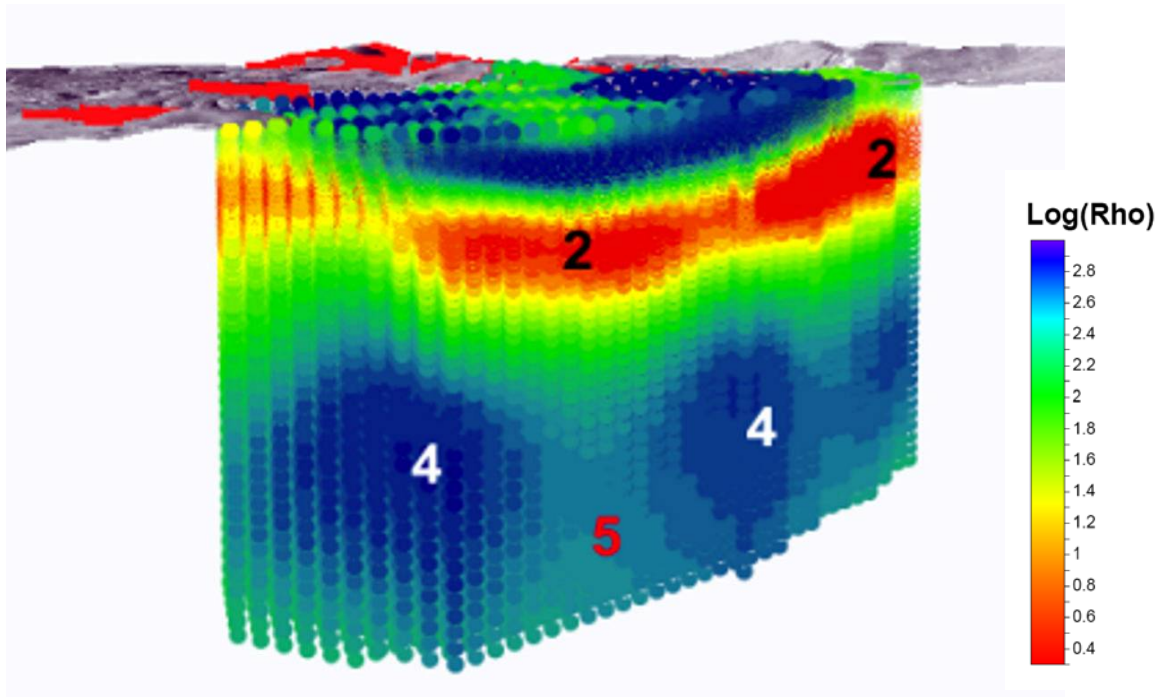
Fig. 2.12: Three-dimensional grid of 3D MT survey data collected in 2011, viewed from the East. Numbers indicate Layers 2, 4 and 5, identified by the 2D MT inversion data, which correlate with the 3D MT inversion data.
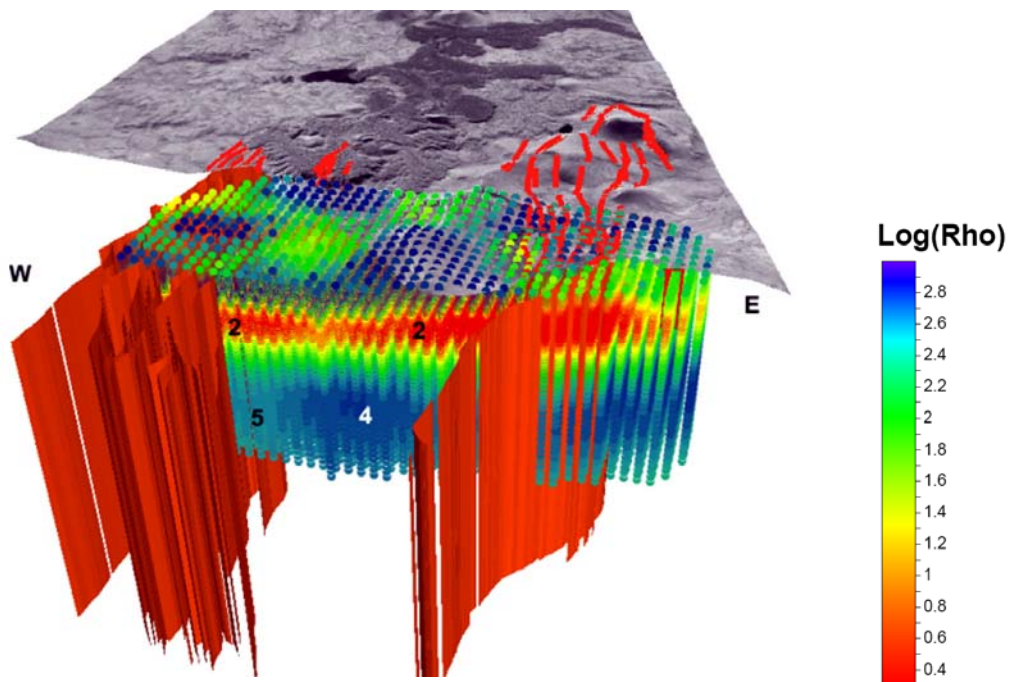
Fig. 2.13: Three-dimensional grid of the 3D MT survey data collected in 2011, demonstrated jointly with the segments of the Pambak-Sevan Fault shaping the structure of the *pull-apart* basin**.** Numbers indicate Layers 2, 4 and 5, identified by the 2D MT inversion data, which correlate with the 3D MT inversion data.

Layer 1 on ground surface

Layer 2 at the depth of 500 m

Layer 2 at the depth of 750 m.

Layer 2 at the depth of 1,000 m

Layer 3 at the depth of 1,500 m

Layer 3 at the depth of 2,000 m
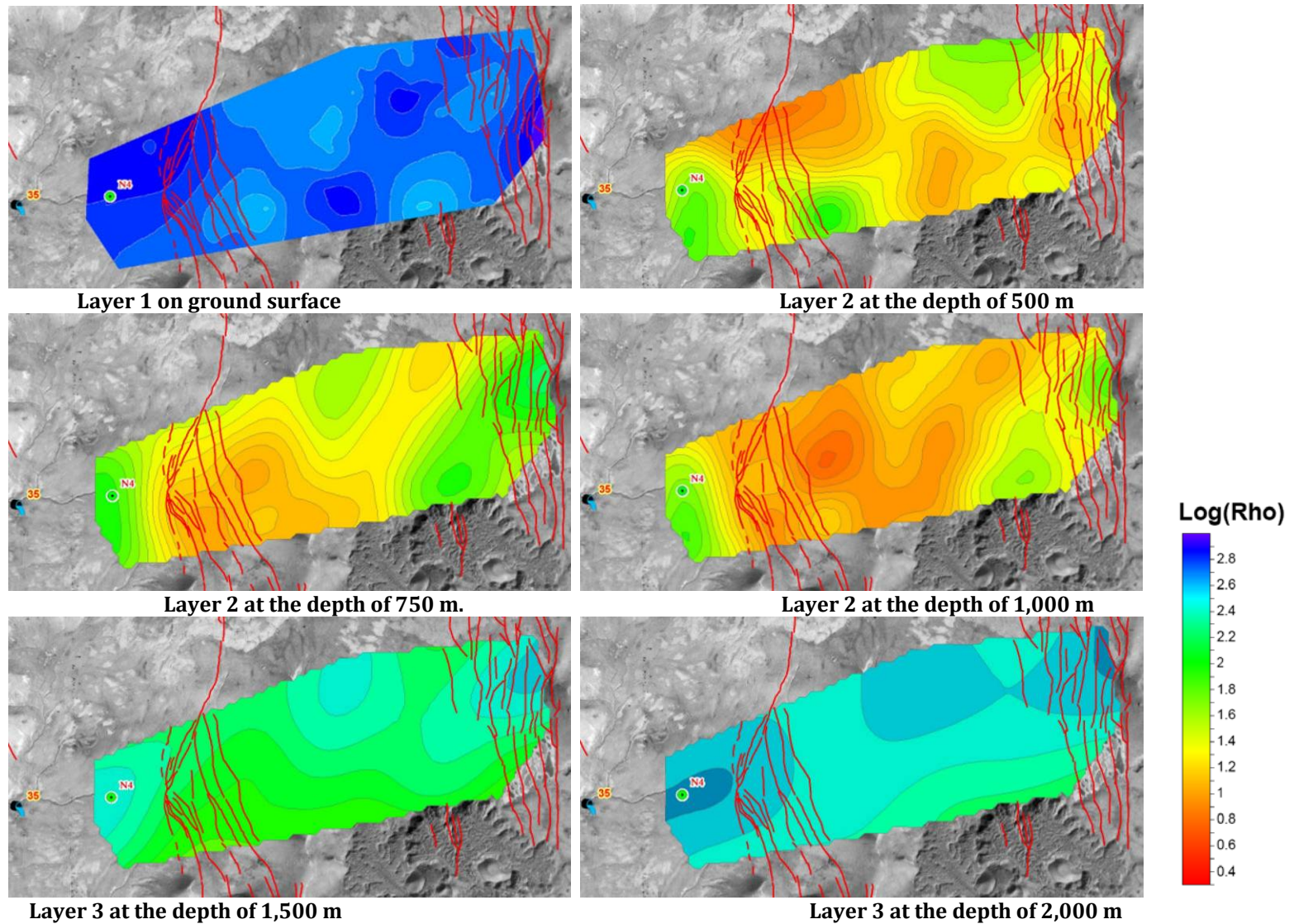
Fig. 2.14: Horizontal sections through the data of the 3D MT survey of 2011 at various depths, indicating geometries of layers with different resistivity values.
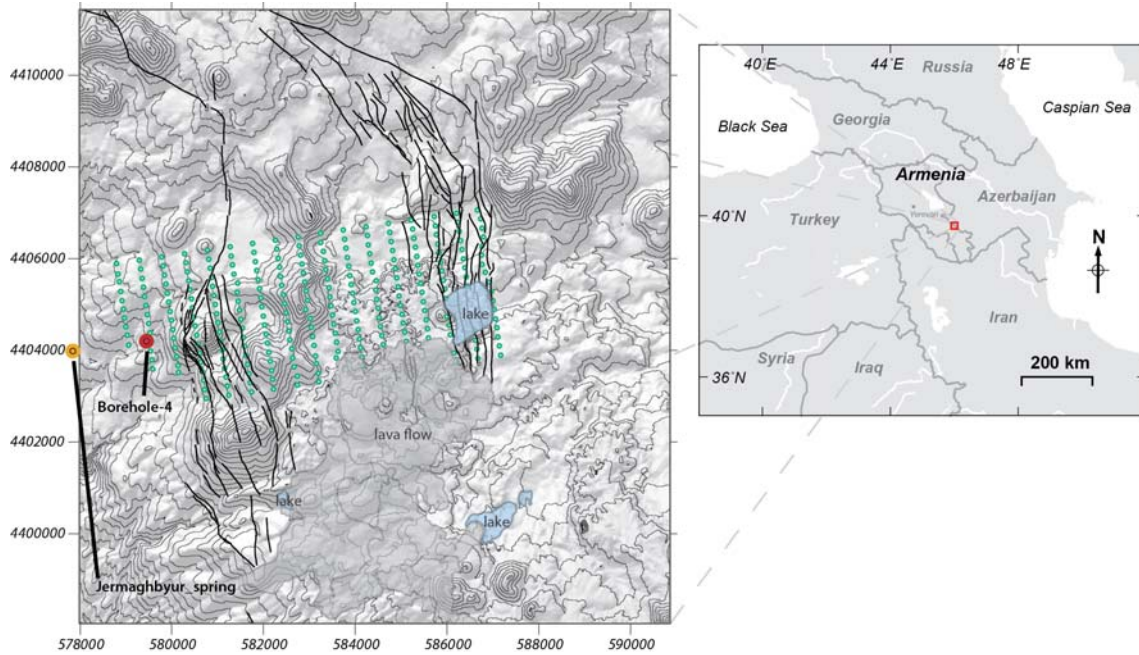
Fig.2.15: Gravity station locations for the survey grid created by WesternGeco staff (solid circles). Mapped faults shown as heavy solid lines; topography is contoured with light solid lines; superimposed on shaded relief DEM. Borehole 4 (solid red circle) lies within the western portion of this grid. Lakes and a young (Holocene?) lava flow are also shown. The hot springs lie west of the grid. UTM projection WGS84.
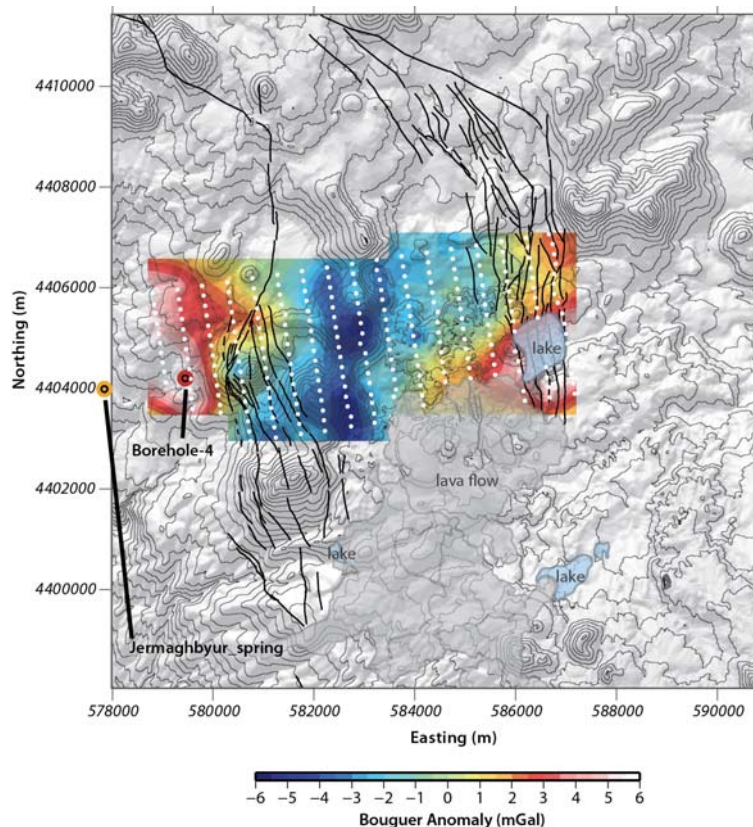
Fig.2.16. Complete Bouguer gravity anomaly mapped by WesternGeco staff (color-shaded region). Mapped faults shown as heavy solid lines; topography is contoured with light solid lines; superimposed on shaded relief DEM. Borehole 4 (solid red circle) lies within the western portion of this grid. Lakes and a young (Holocene?) lava flow are also shown. The hot springs lie west of the grid. UTM projection WGS84.

119
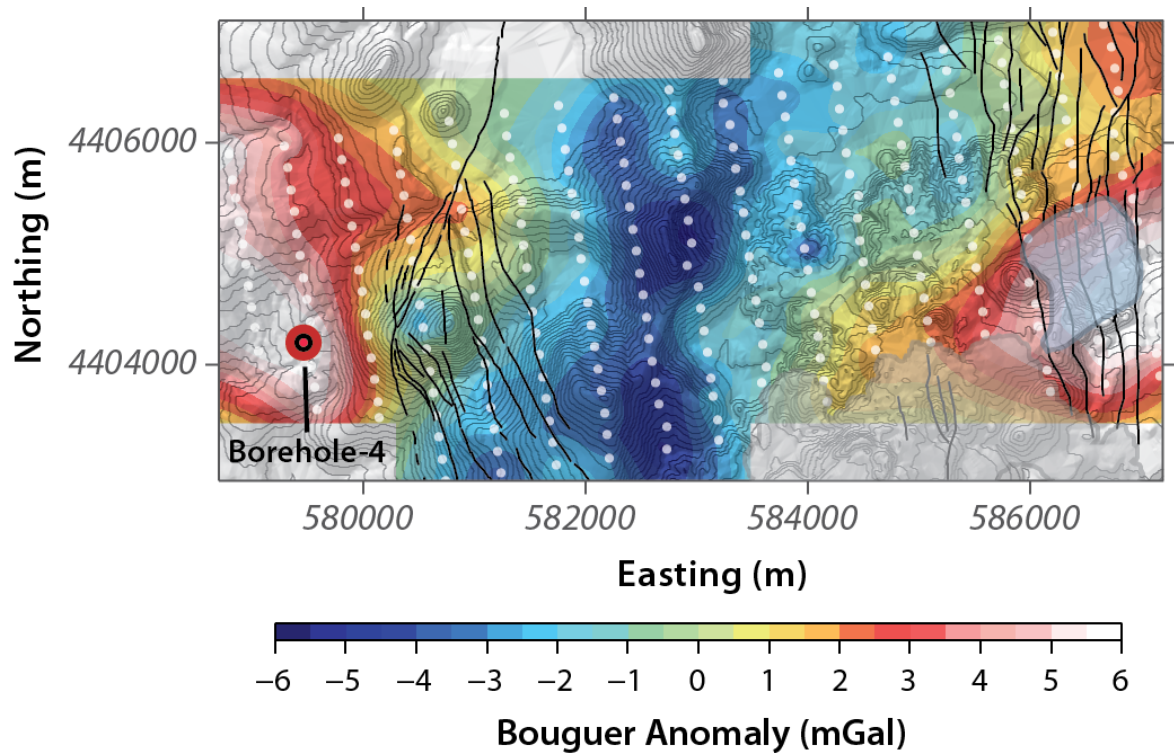
Fig. 2.17: Complete Bouguer gravity anomaly (color-shaded) calculated using a density of 2700 kg m^{-3} and with a best-fit plane subtracted. Note the correlation of gravity anomalies with topography (contour lines) indicating this Bouguer density is high. Mapped faults shown as solid lines; gravity stations shown as solid circles; superimposed on shaded relief DEM. UTM projection WGS84.
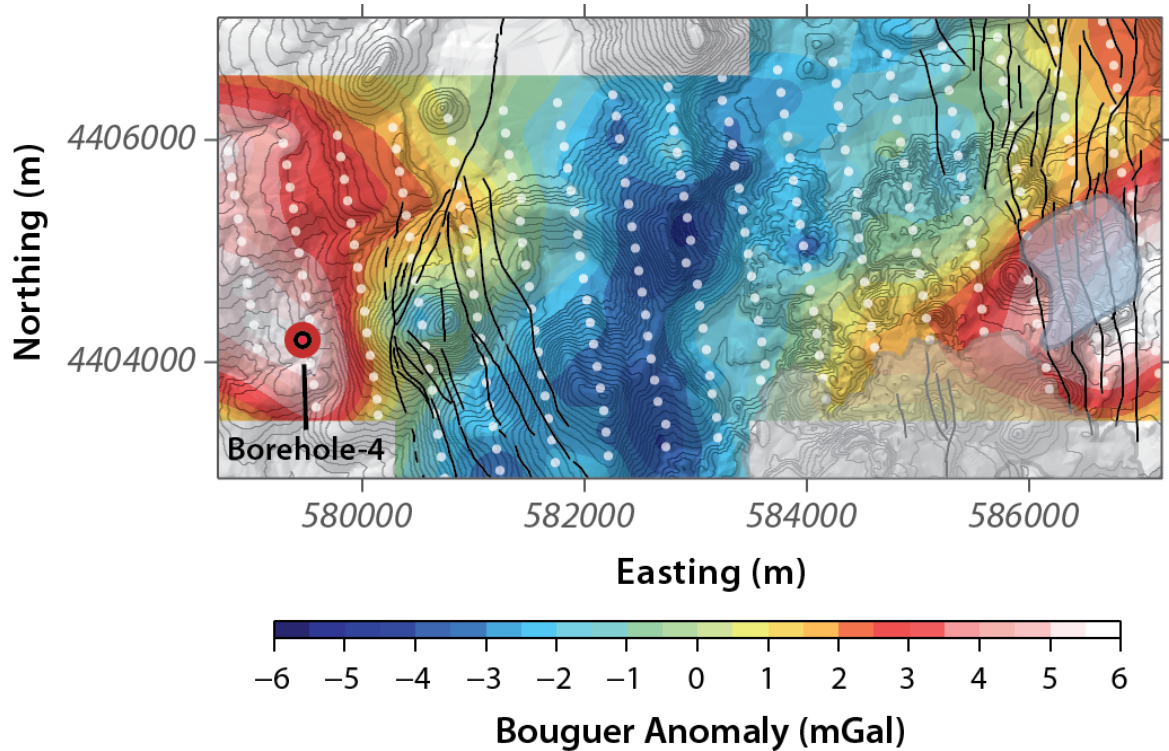
Fig. 2.18: Complete Bouguer gravity anomaly (color shaded) calculated using a density of 2550 kg m^{-3} and with a best-fit plane subtracted. This complete Bouguer gravity reduction was selected for modeling. Other map symbols as in Figure 2.17.
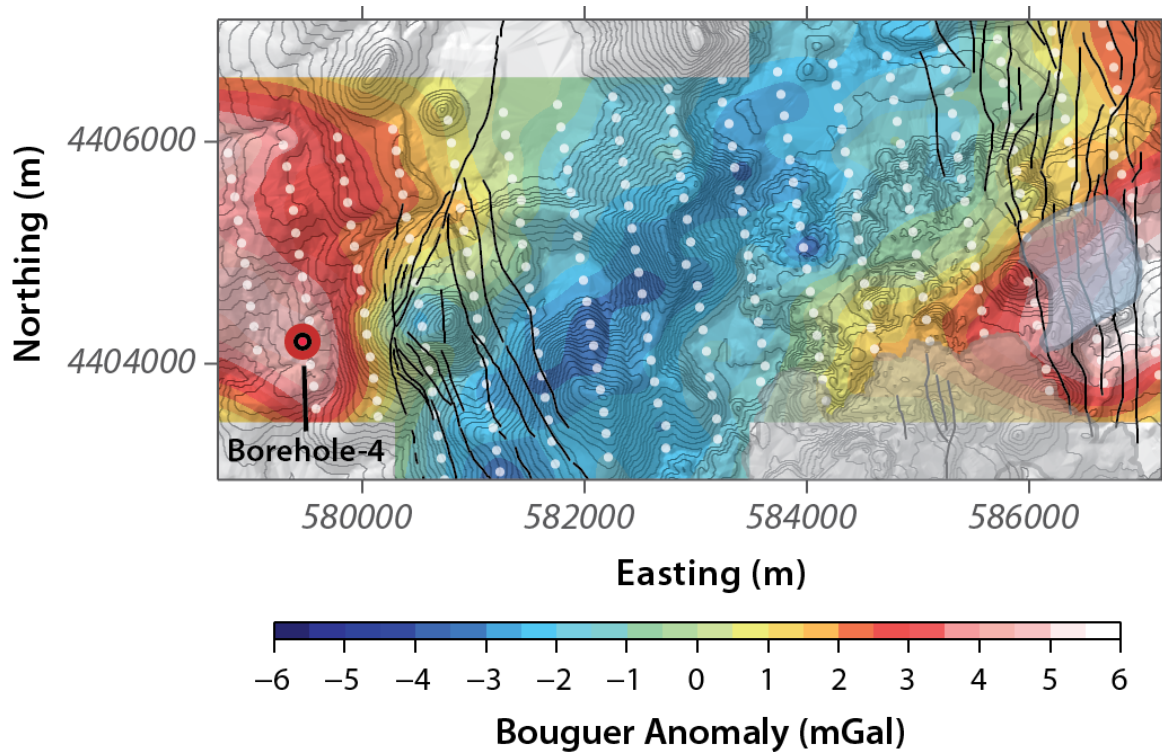
Fig. 2.19: Complete Bouguer gravity anomaly (color shaded) calculated using a density of 2400 kg m^{-3} and with a best-fit plane subtracted. This complete Bouguer gravity is not well correlated to topography, indicating that this Bouguer density is acceptable for modeling. Other map symbols as in Figure 2.17.
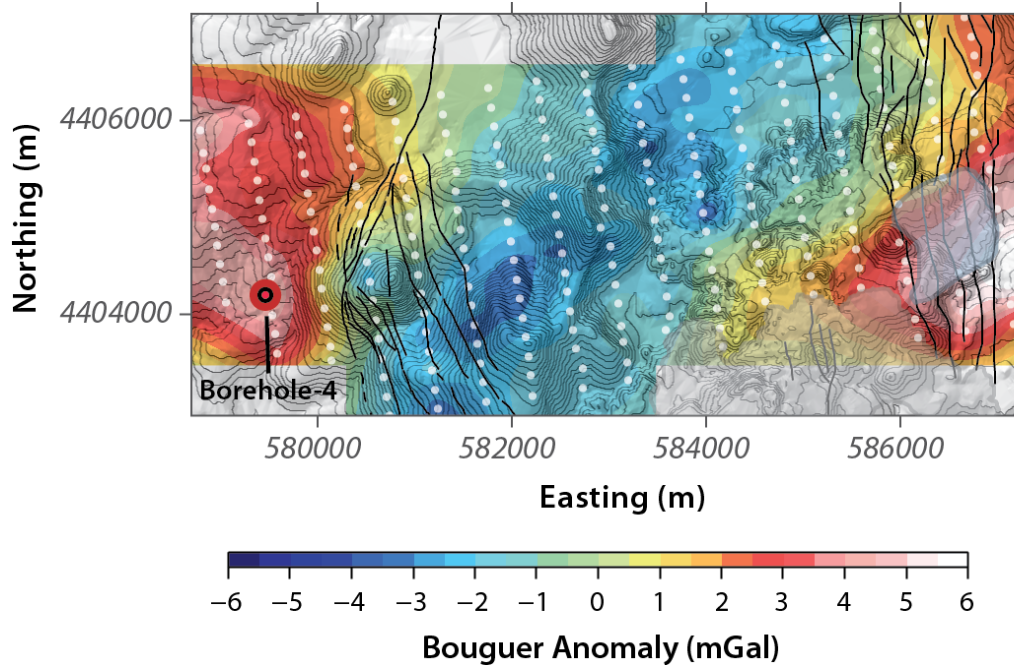
Fig. 2.20: Complete Bouguer gravity anomaly (color shaded) calculated using a density of 2300 kg m^{-3} and with a best-fit plane subtracted. This complete Bouguer gravity shows signs of anti-correlation with topography, indicating that this Bouguer density is relatively low. Other map symbols as in Figure 2.17.
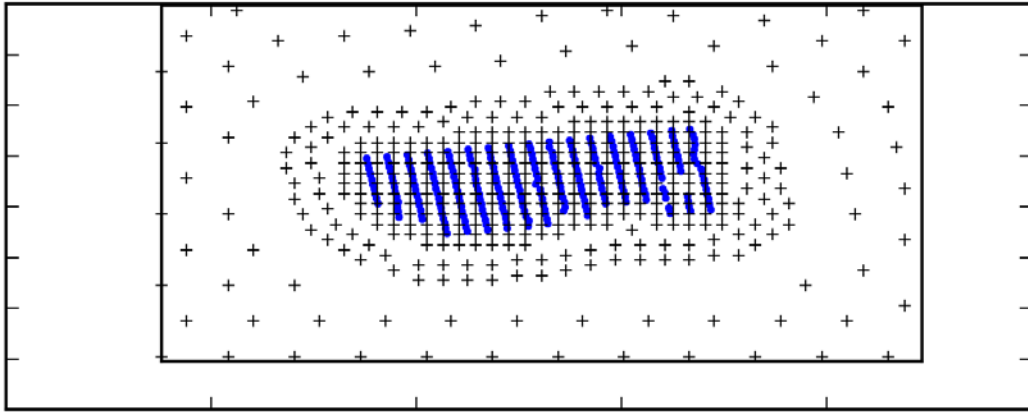
Fig. 2.21: Location of pilot points (black crosses) and gravity stations (blue points) within the forward model domain.
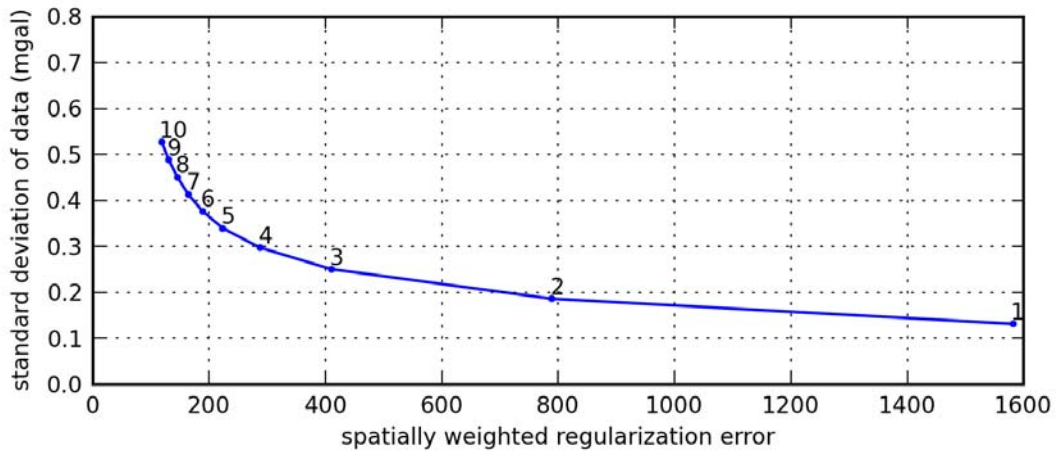
Fig. 2.22: The Pareto frontier between assumed observation error standard deviation and regularization error.
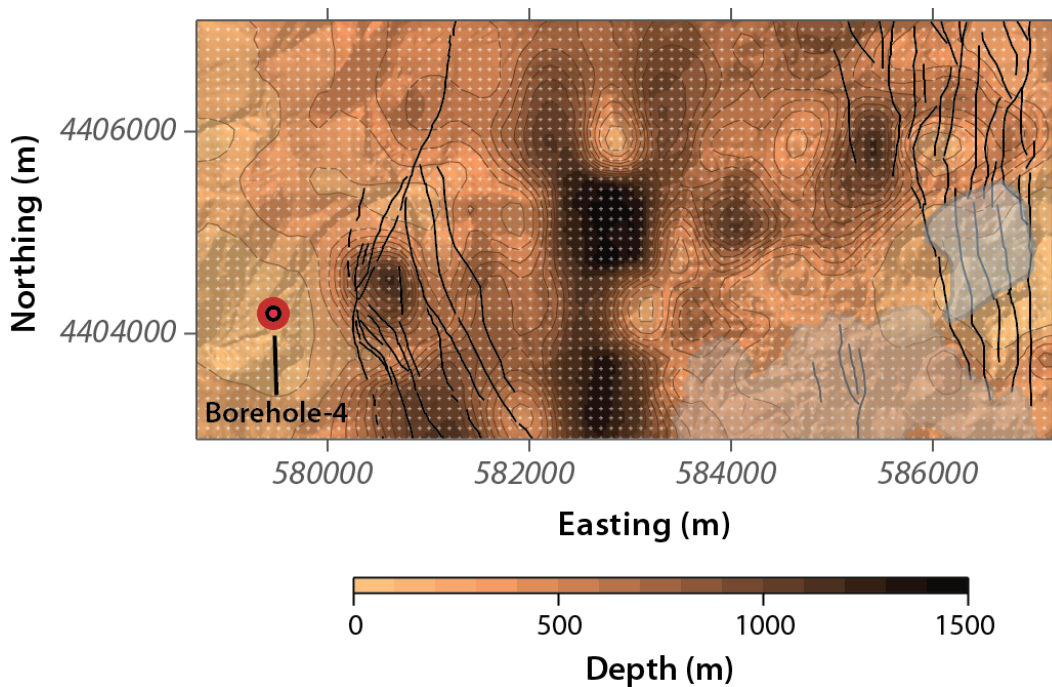
Fig. 2.23: Depth distribution of base of basin-fill (lavas, alluvium, volcaniclastics), and top of basement (quartz monzonite?) in the survey area based on inversion of the gravity anomaly with Bouguer density 2550 kg m^{-3}. Small solid circles indicate the positions of centroids of model prisms. Other symbols as in Figure 2.17.

122
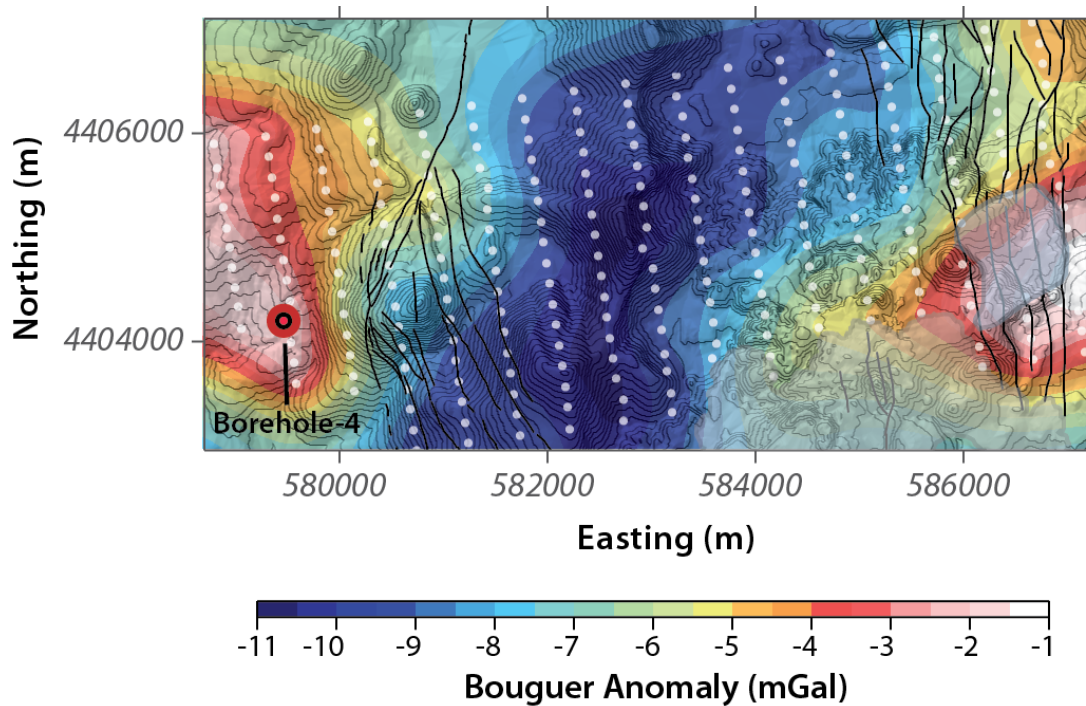
Fig. 2.24: Forward model of the gravity anomaly calculated using the depth model shown in Figure 2.23. All other map symbols as in Figure 2.17.
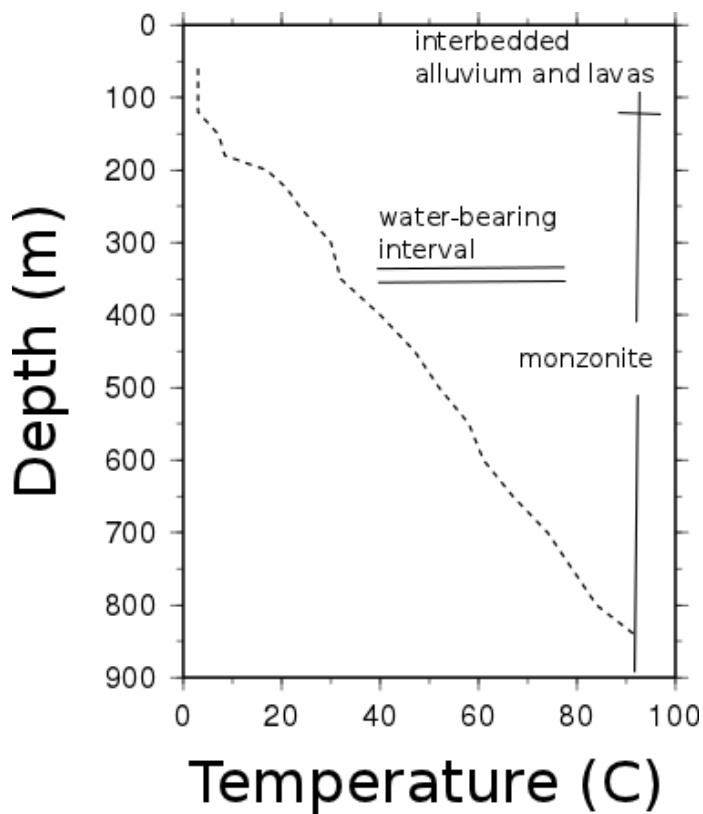
Fig. 2.25: Temperatures logged in Borehole 4. A water-bearing zone corresponds to isothermal conditions at a depth of approximately 340 m. Interbedded alluvium and lava flows were reported in the well at depths less than 123 m; quartz monzonite occurs in the well from 123 m to its total depth, approximately 1000 m.
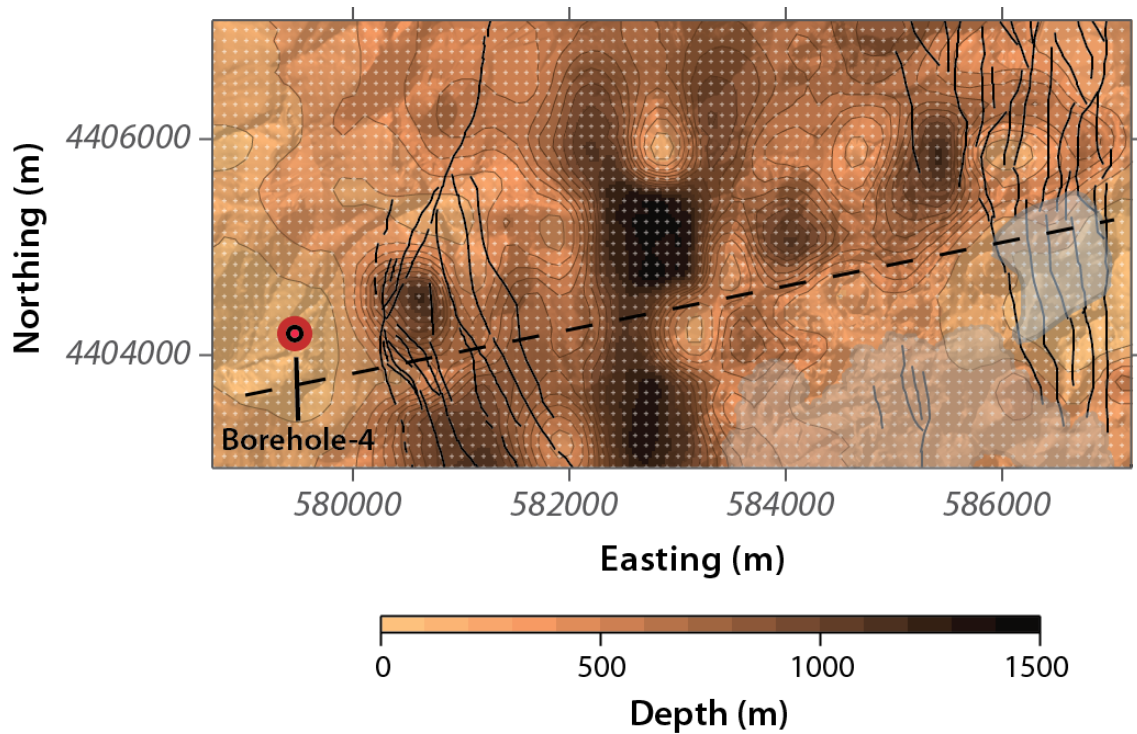
Fig. 2.26: Location of the cross section used for development of the hydrothermal transport model (straight dashed line), superimposed on depth distribution of base of basin-fill (lavas, alluvium, volcaniclastics), and top of basement (quartz monzonite?) in the survey area based on inversion of the gravity anomaly with Bouguer density 2550 kg m^{-3}. Small solid circles indicate the positions of centroids of gravity model prisms. Other symbols as in Figure.**2.17**.
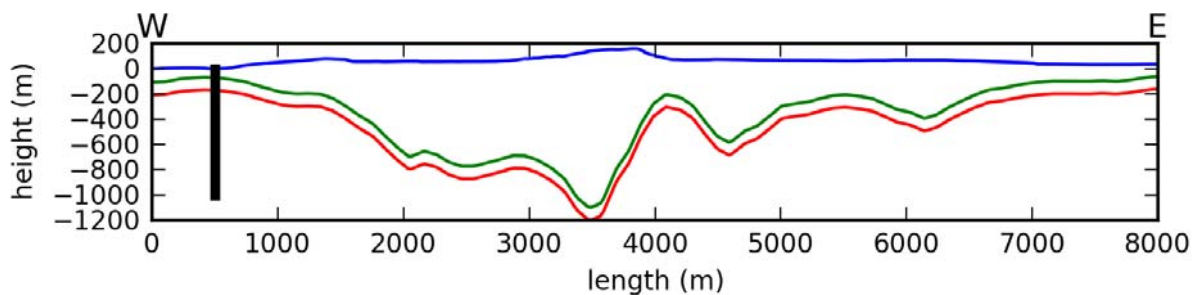
Fig. 2.27: Orientation of the three geologic units represented in the hydrothermal model. The contact between the AL and the FR (green line) is defined by the gravity inversion. The contact between the FR and the QZ (red line) is 100 meters below the AL-FR contact. Borehole 4 is shown as a heavy black line near the western edge
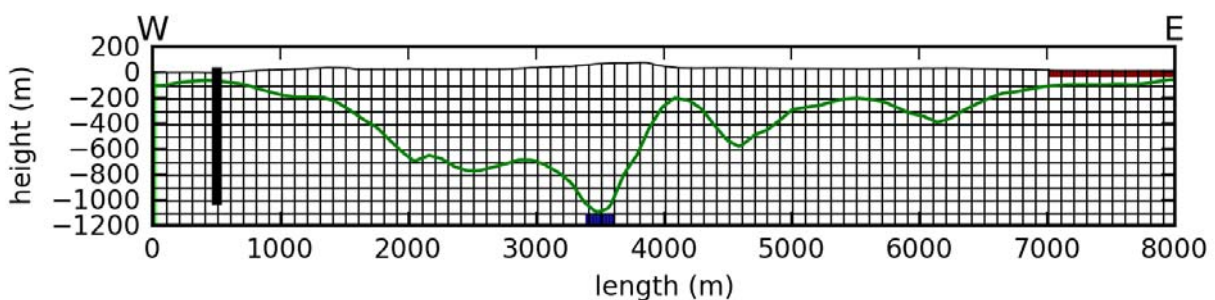
Fig. 2.28: The discretized model domain (every forth column and layer shown). The blue dashed line marks the AL-FR contact. The localized heat-source cells (blue) and the lake cells (red) are also shown.

124
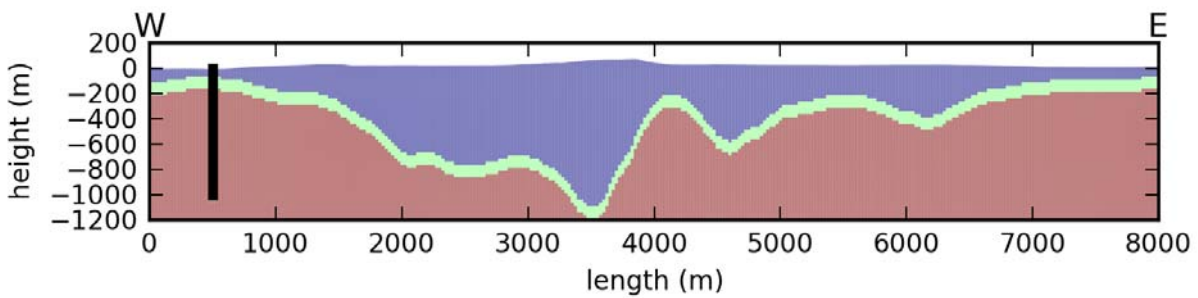
Fig. 2.29: Discretized hydrostratigraphic units in the hydrothermal model. The contact between the AL (blue) and the FR (green) is defined by the gravity inversion. The contact between the FR and the QZ (red) is 100 m below the AL-FR contact. Borehole 4 is shown as a heavy black line near the western edge of the plot.
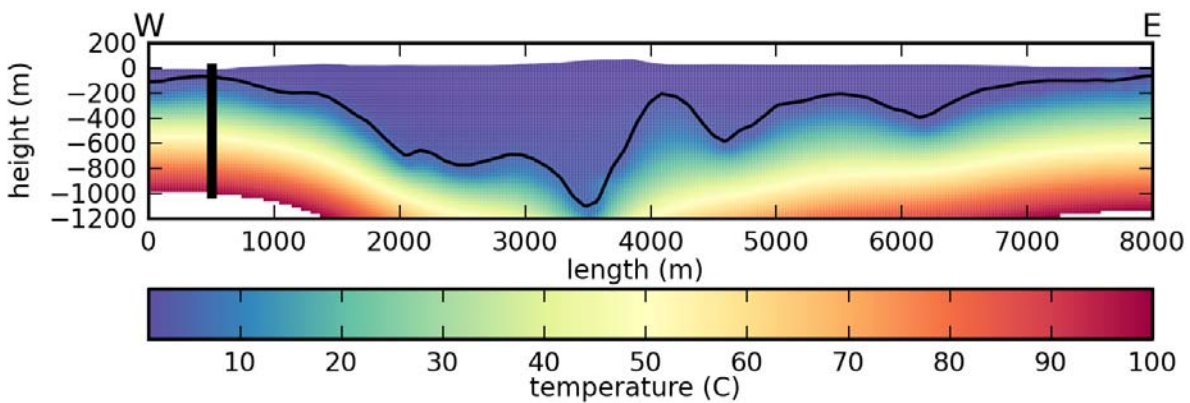
Fig. 2.30: Model domain temperature distributions from ScenarioA - homogeneous parameterization.
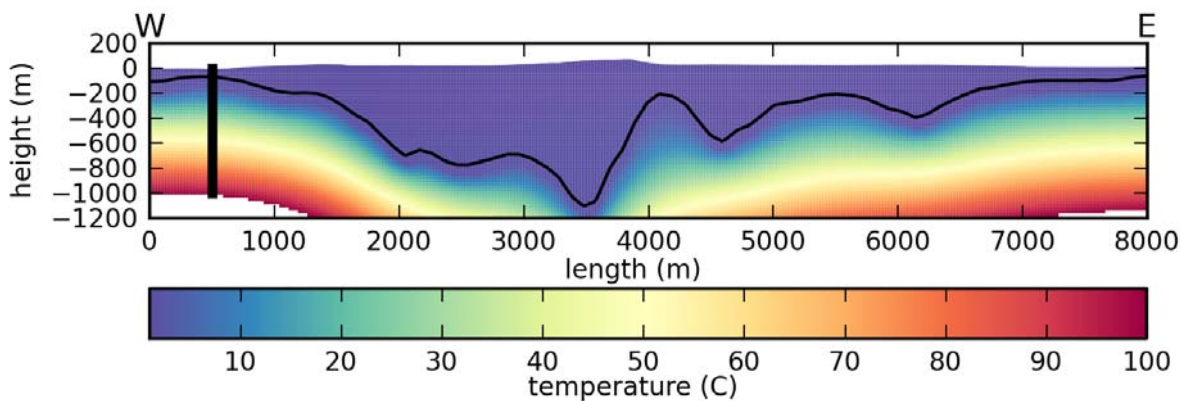
Fig. 2.31: Model domain temperature distributions from ScenarioA - heterogeneous Parameterization

125
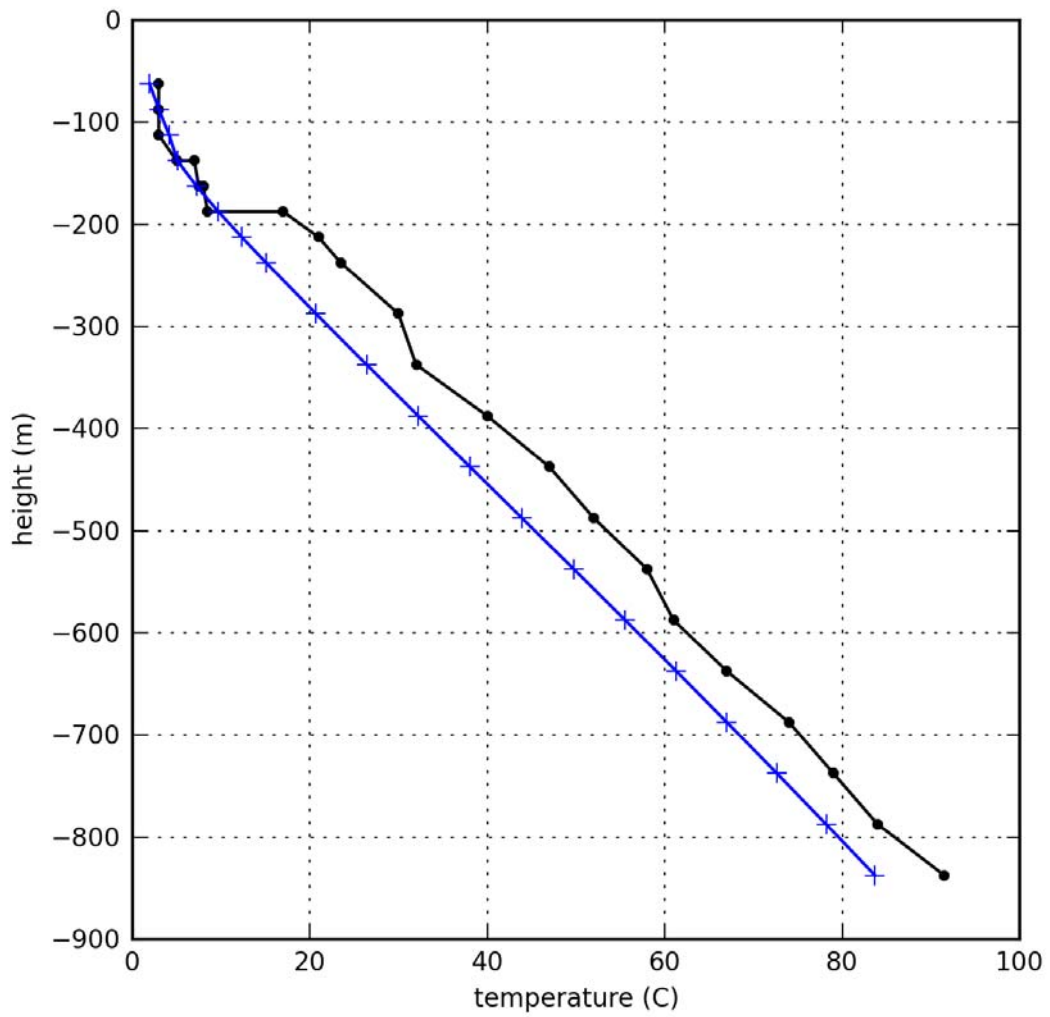
Fig. 2.32: Borehole 4 observed (black circles) and predicted (blue crosses) temperature distributions from ScenarioA - homogeneous parameterization.
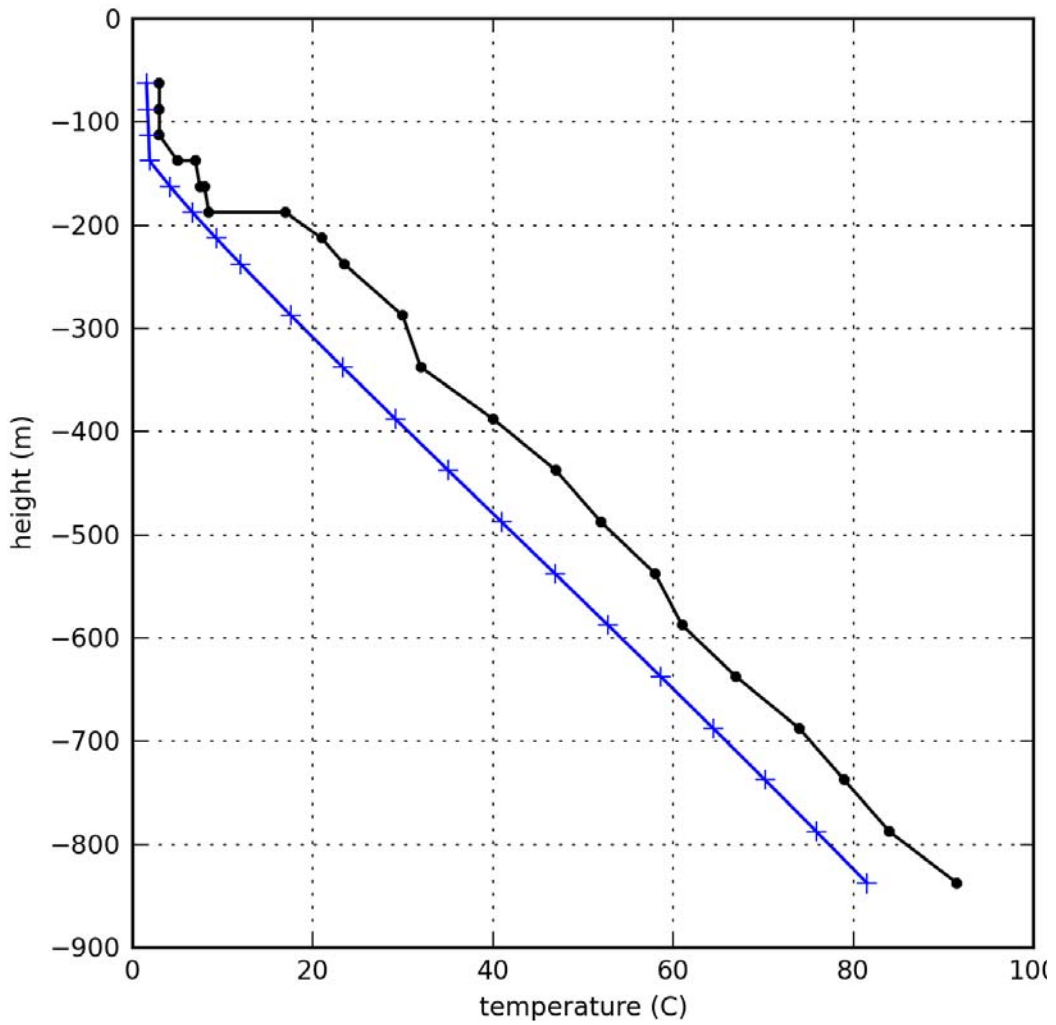
Fig. 2.33: Borehole 4 observed (black circles) and predicted (blue crosses) temperature distributions from ScenarioA–heterogeneous parameterization.
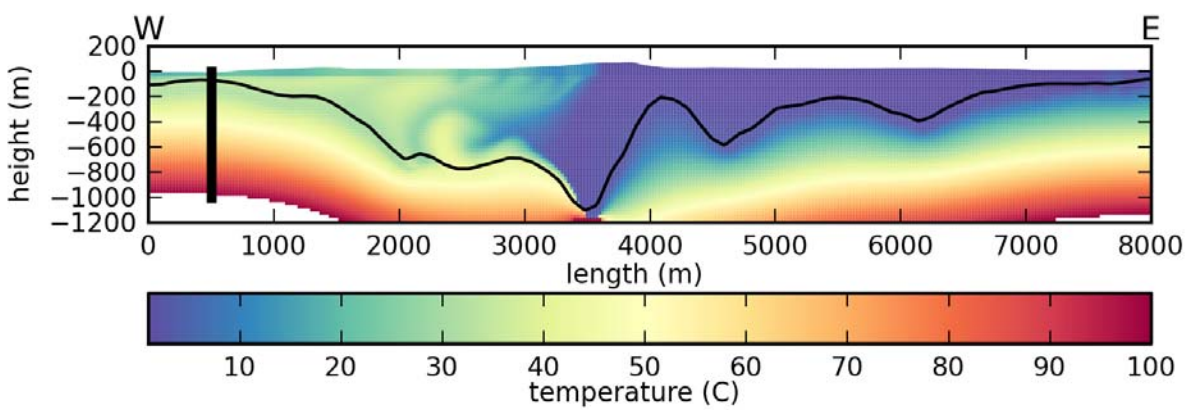
Fig. 2.34: Model domain temperature distributions from ScenarioB - homogeneous parameterization.

127
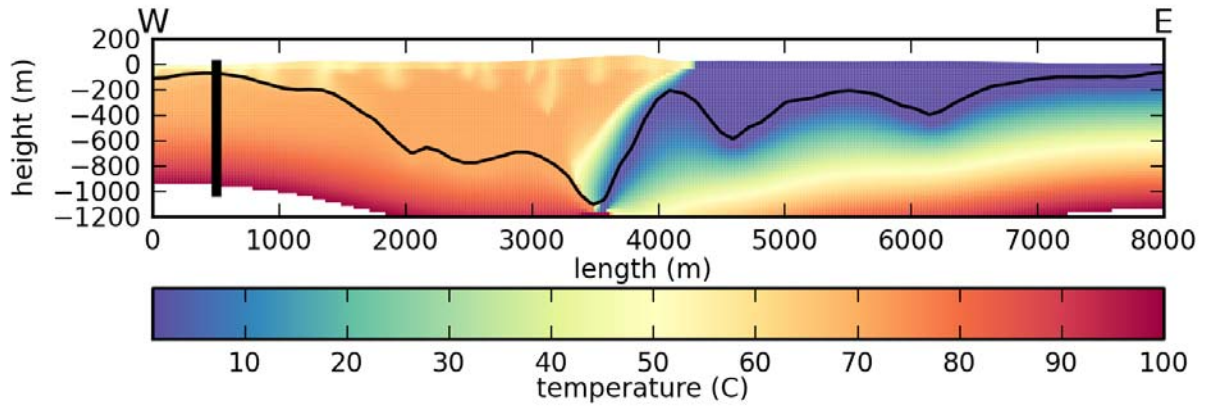
Fig. 2.35: Model domain temperature distributions from ScenarioB - heterogeneous parameterization.
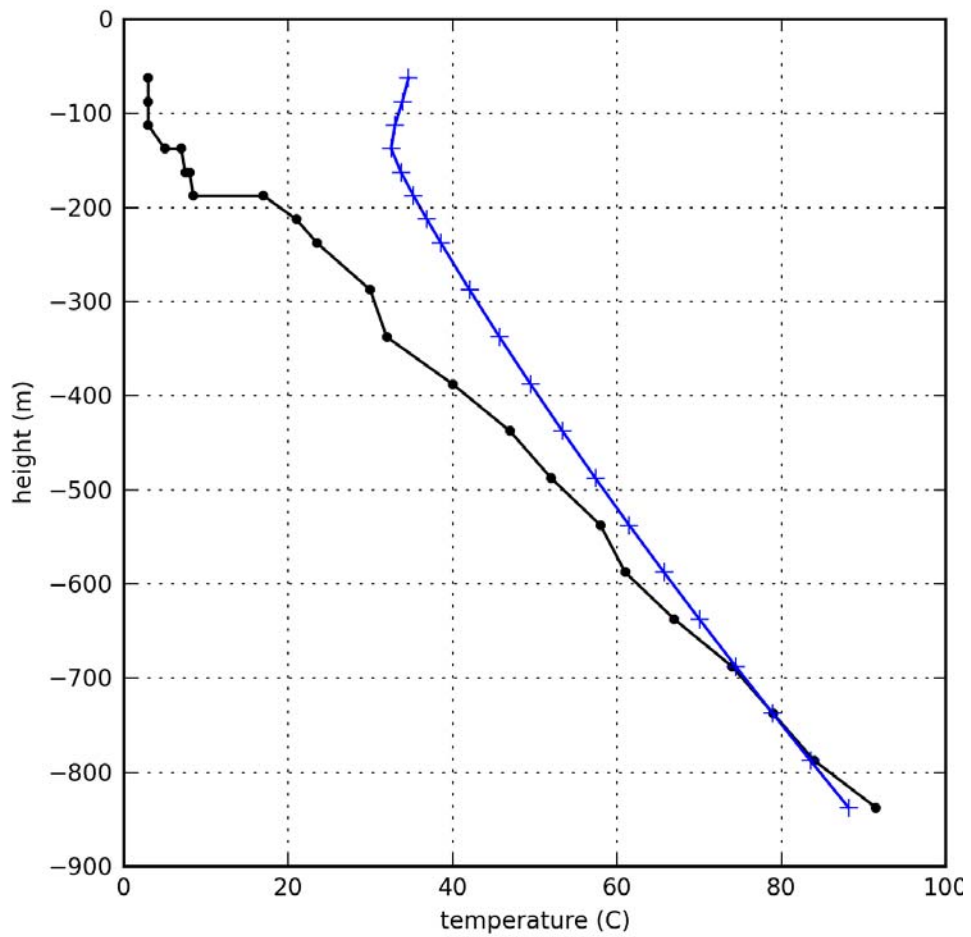
Fig. 2.36: Borehole 4 observed (black circles) and predicted (blue crosses) temperature distributions from ScenarioB - homogeneous parameterization.

Fig. 2.37: Borehole 4 observed (black circles) and predicted (blue crosses) temperature distributions from Scenario B - heterogeneous parameterization.

Fig. 2.38: Dalidagh intrusion and regional gravity map at the scale of 1:200,000

1- Phase 1of the Dalidagh intrusion; 2 –Phase 2 of the Dalidagh intrusion
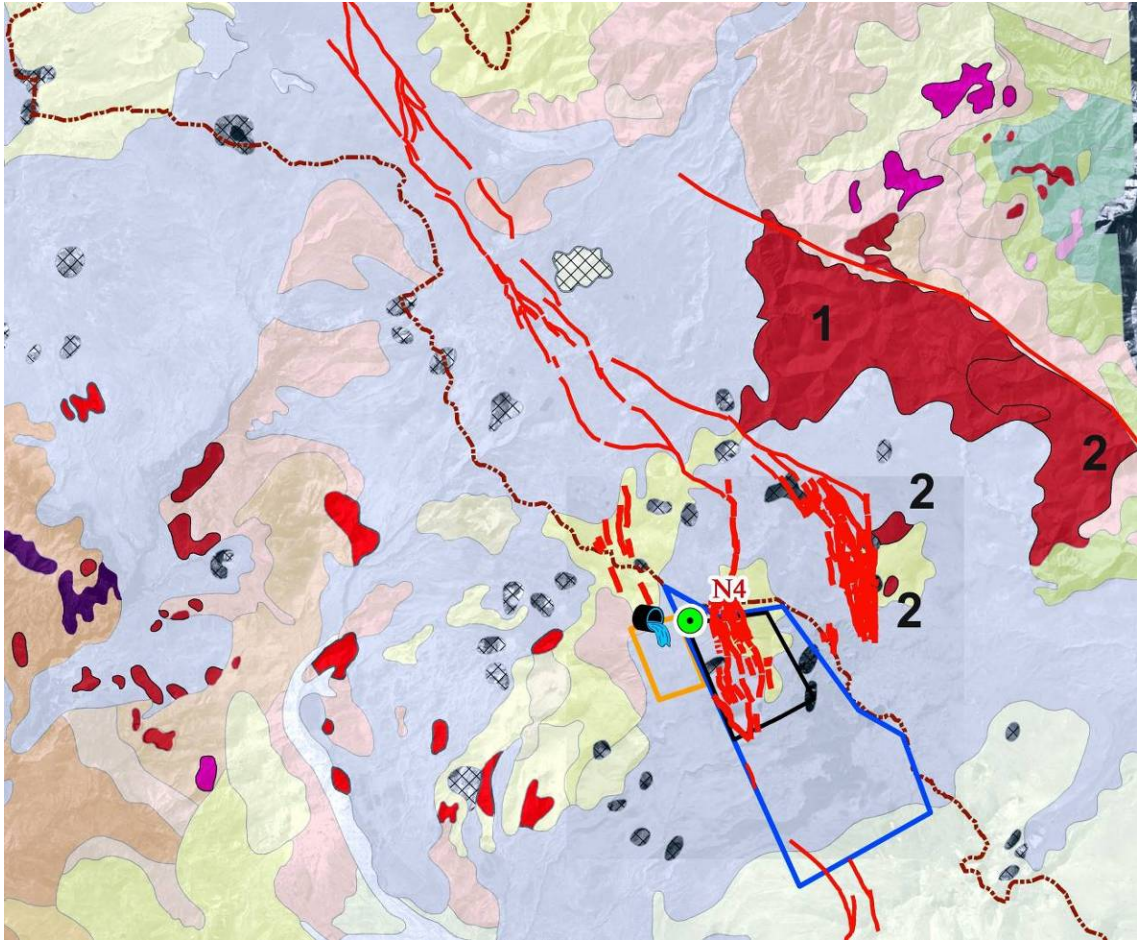
Fig. 2.39: Geological map at the scale of 1:50,000.

1 – Phase 1 of the Dalidagh intrusion; 2 –Phase 2 of the Dalidagh intrusion.
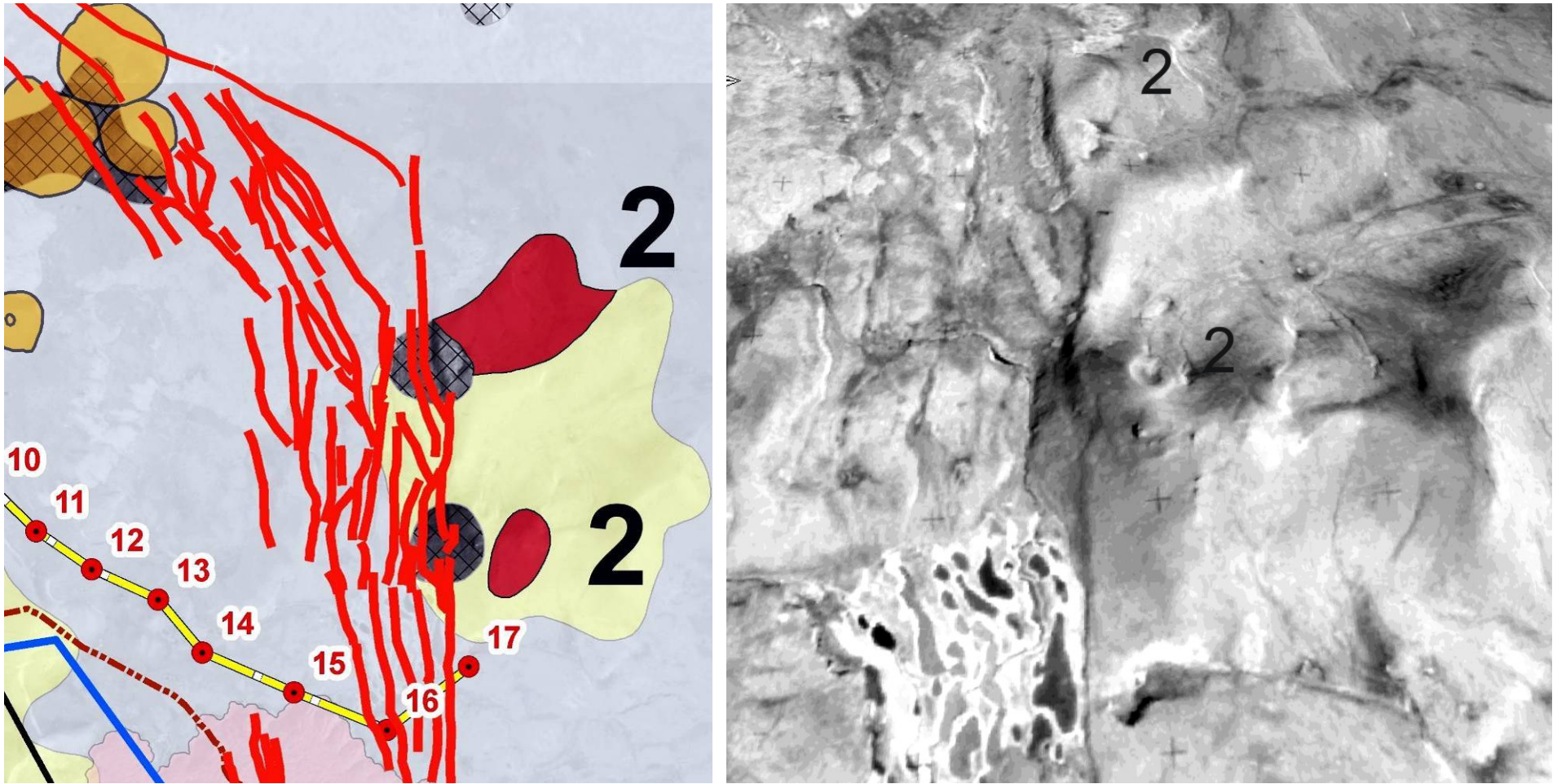
Fig. 2.40: Small outcrops of the early Miocene porphyraceous granodiorite located on the surface, among Quaternary lava, at the distances of 0.7 and 2.5 km north of Point 17 on the MT Profile of 2009. The outcrops are related to Phase 2 of the Dalidagh intrusion, situated 4 and 6.5 km far from it. In both cases, intrusion outcrops are broken through by Quaternary volcanoes.

LEGEND

▭ (tan)	Depression deposits
▭ (dark red)	Olivine trachybasalts
▭ (pink)	Amphibolic basaltic trachyandesites
▭ (light purple)	Quartz rhyolites
▭ (purple)	Clinopyroxene-amphibole trachyandesites

⟿ (red line)	Active faults
●	Petrographic sampling locations
▭ (blue outline)	Site of geological scouting
▭ (black outline)	Site of MT survey
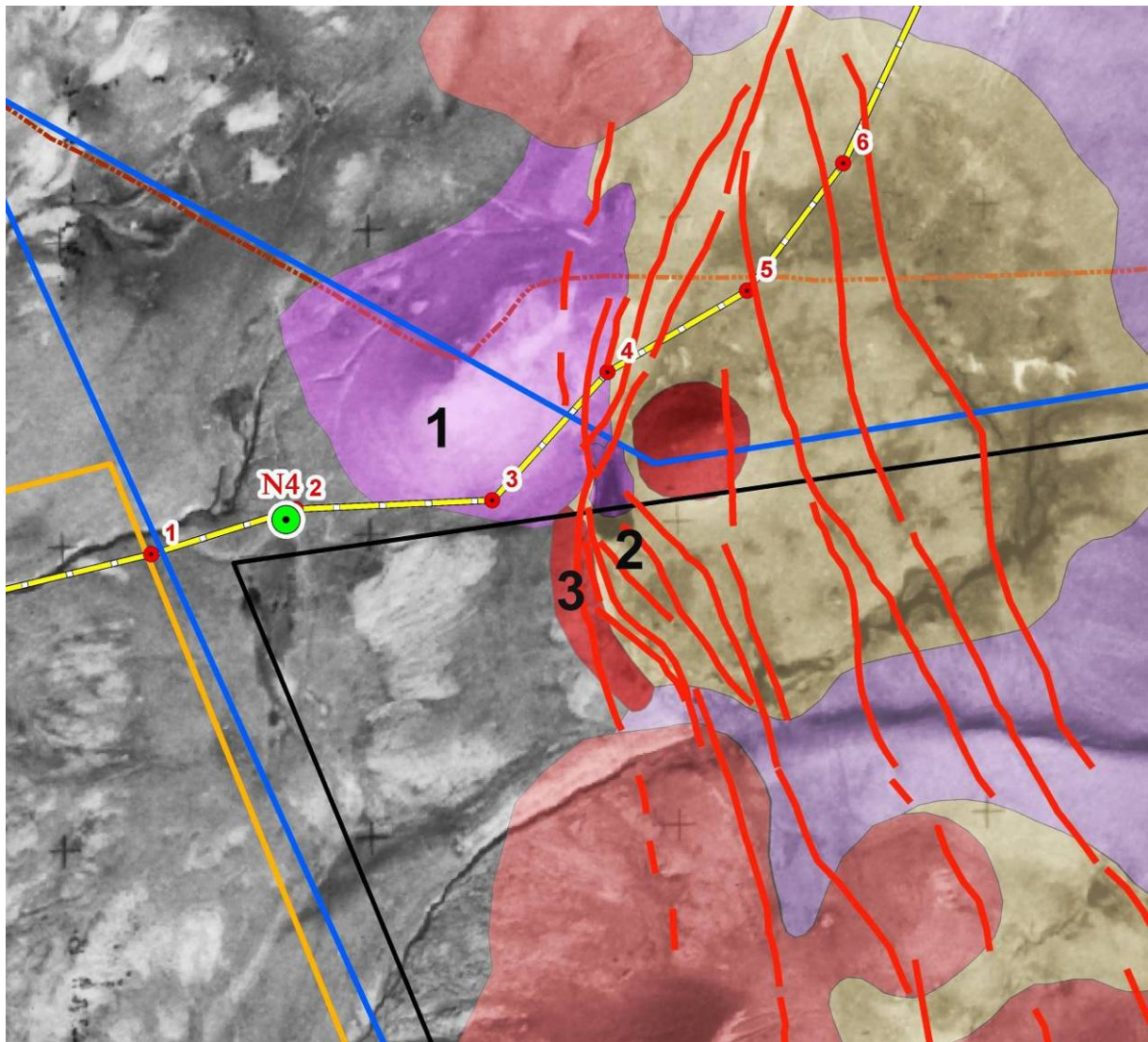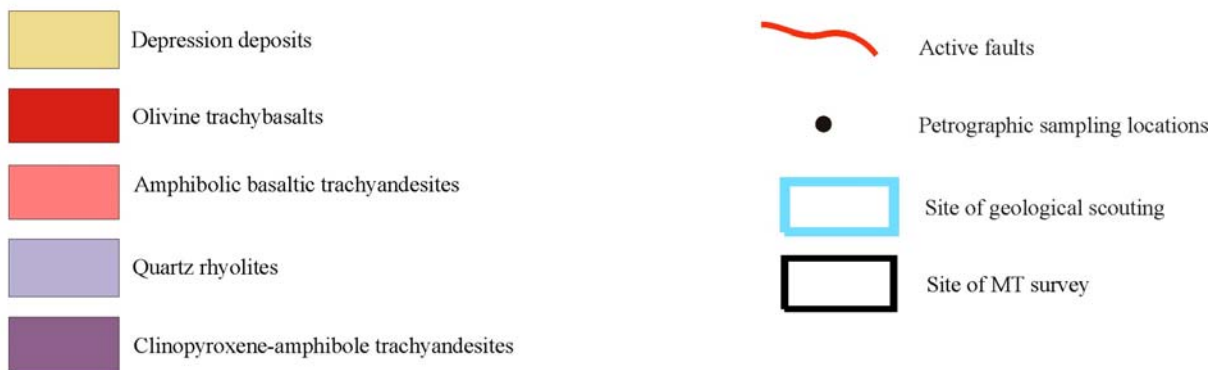
Fig. 2.41: Dome-like outcrop of rhyolites located 250 m north of the Karkar Site.
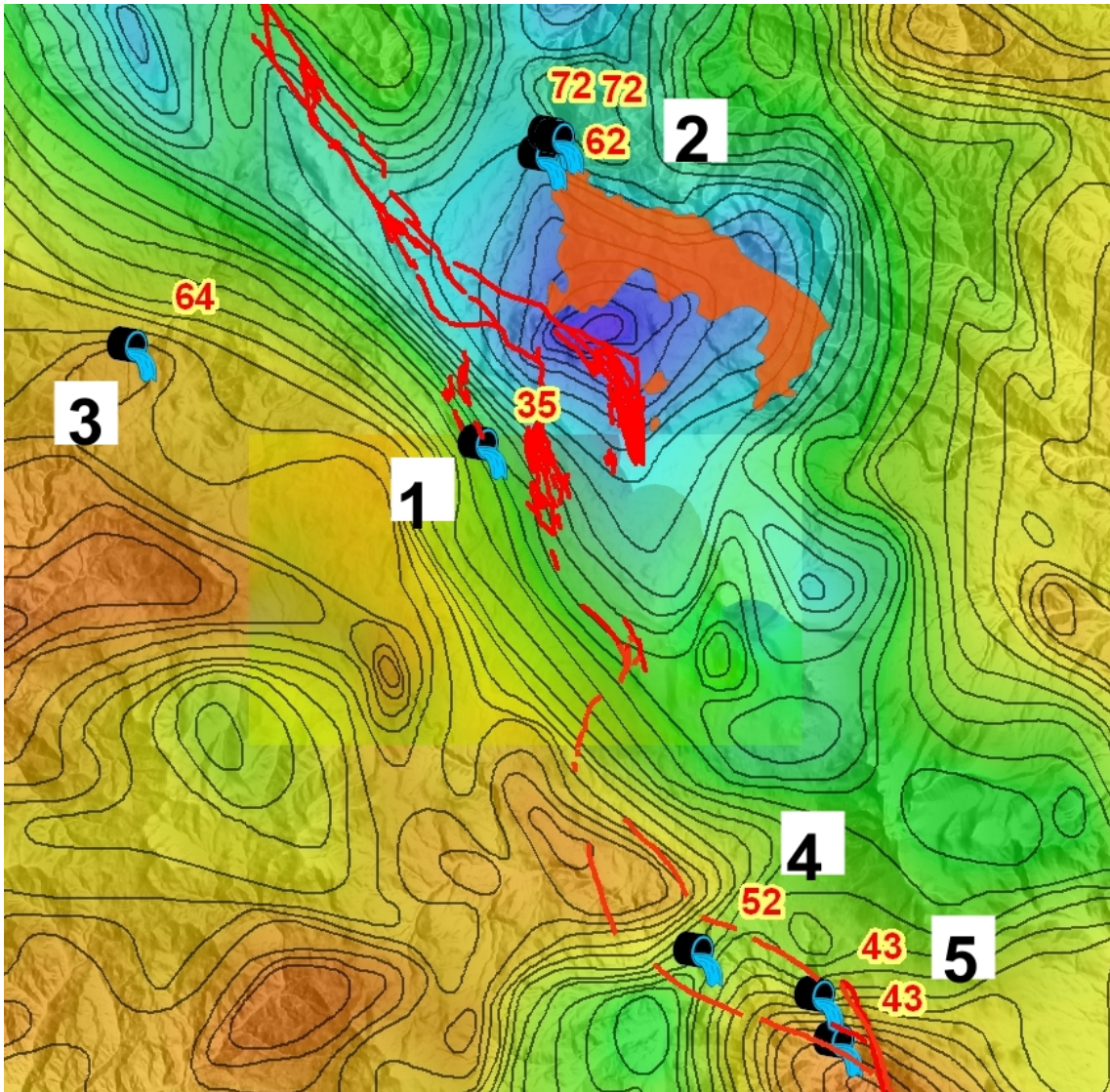
Fig. 2.42: Disposition of thermal springs around the Karkar Site. 1 – Jermaghbyur; 2 – Jermajour (Isti-Sou); 3- Jermouk; 4 – Ouits; 5 – Ouit.

a
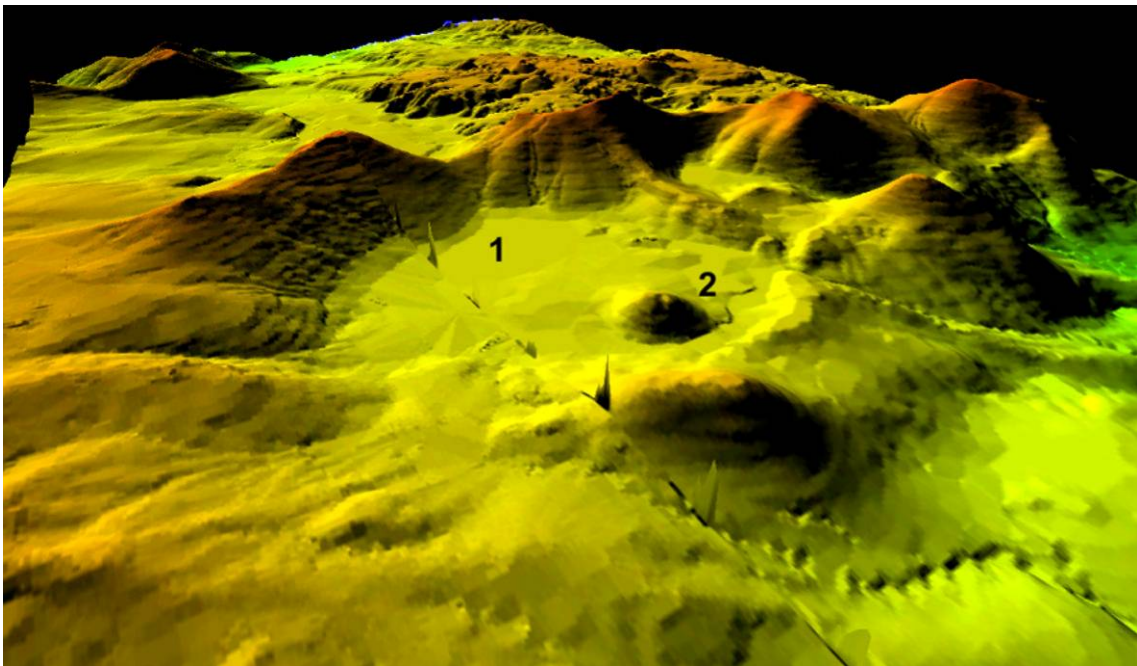
b

Fig. 2.43: Depression D1: 1 – depression; 2 – rhyolitic dome; a –air photo; b – DEM with resolution of 1 m.
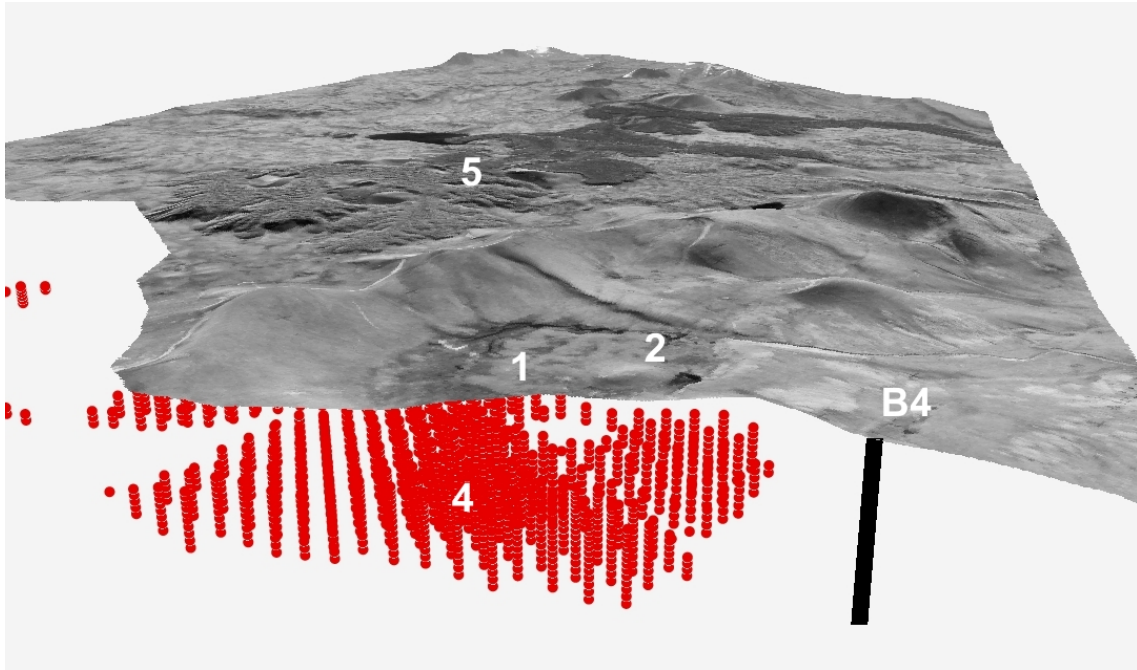
Fig. 2.44: Depression D1. 1 – depression; 2 – rhyolitic dome; 4 – low-resistance Layer 2; 5 – Holocene volcanoes.
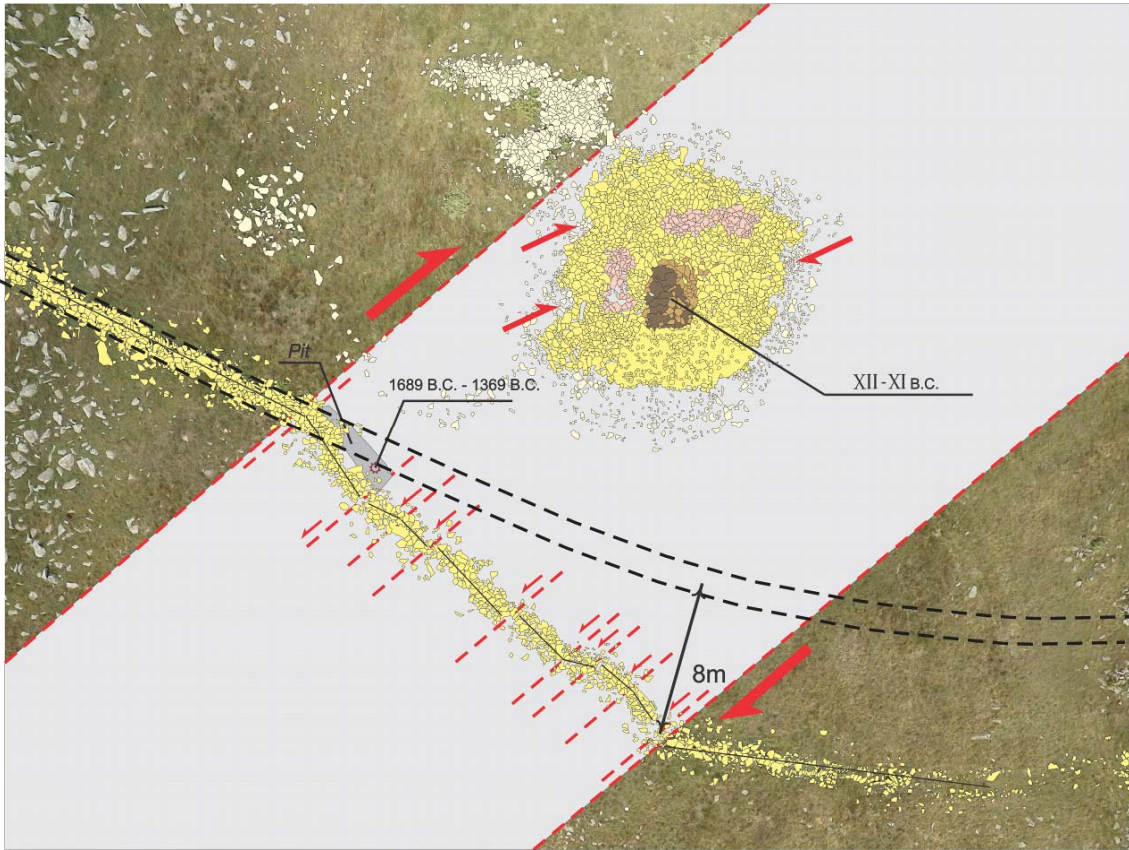
Fig. 2.45: Old burial mound, located 800 m far from Borehole 4; surface rupture by a strong earthquake dislocated the burial mound by 8 m.
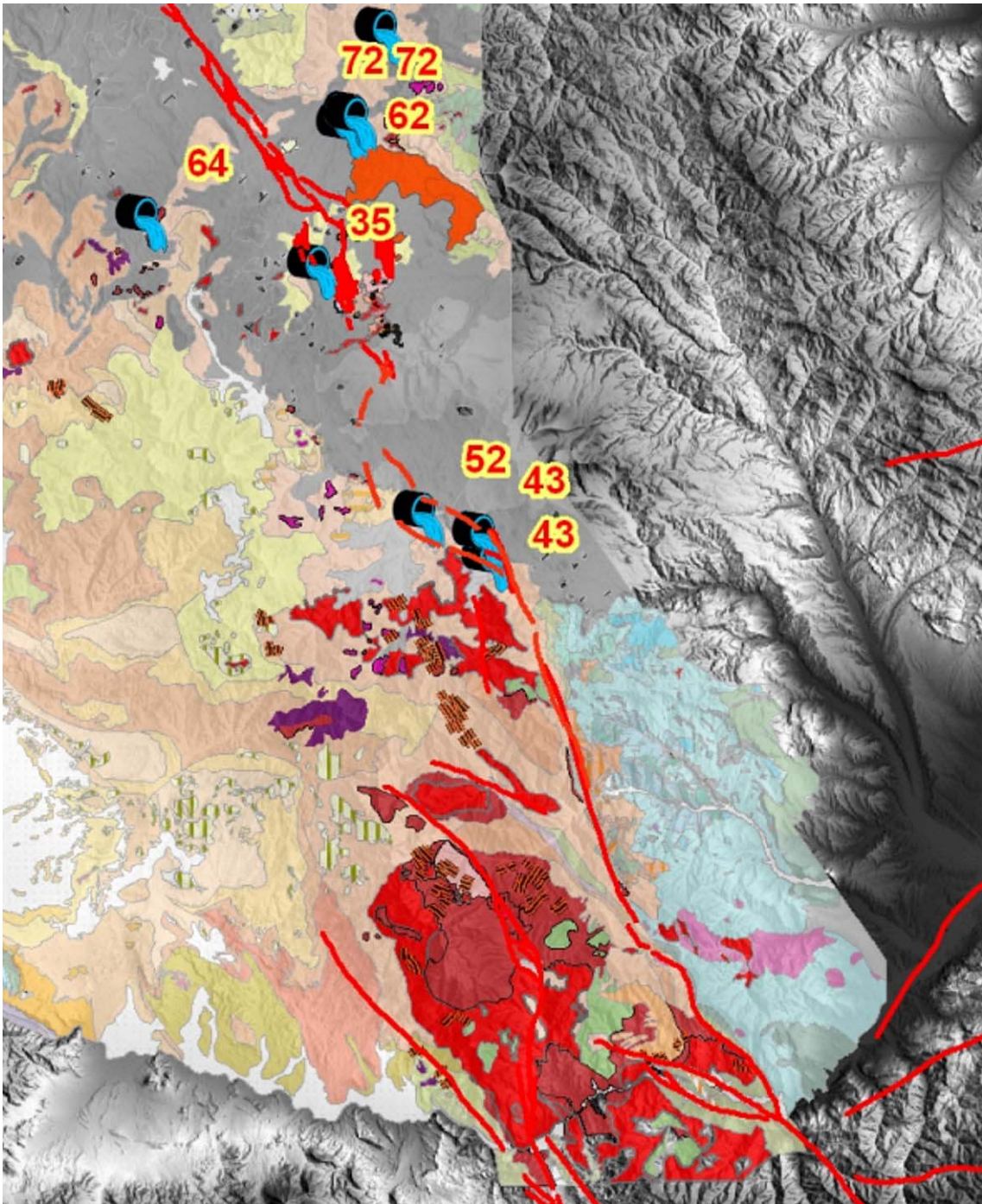
Fig. 2.46: Large Dalidagh and Meghri intrusions and a series of numerous smaller intervening intrusive and extrusive bodies shape a distinct north-trending zone.
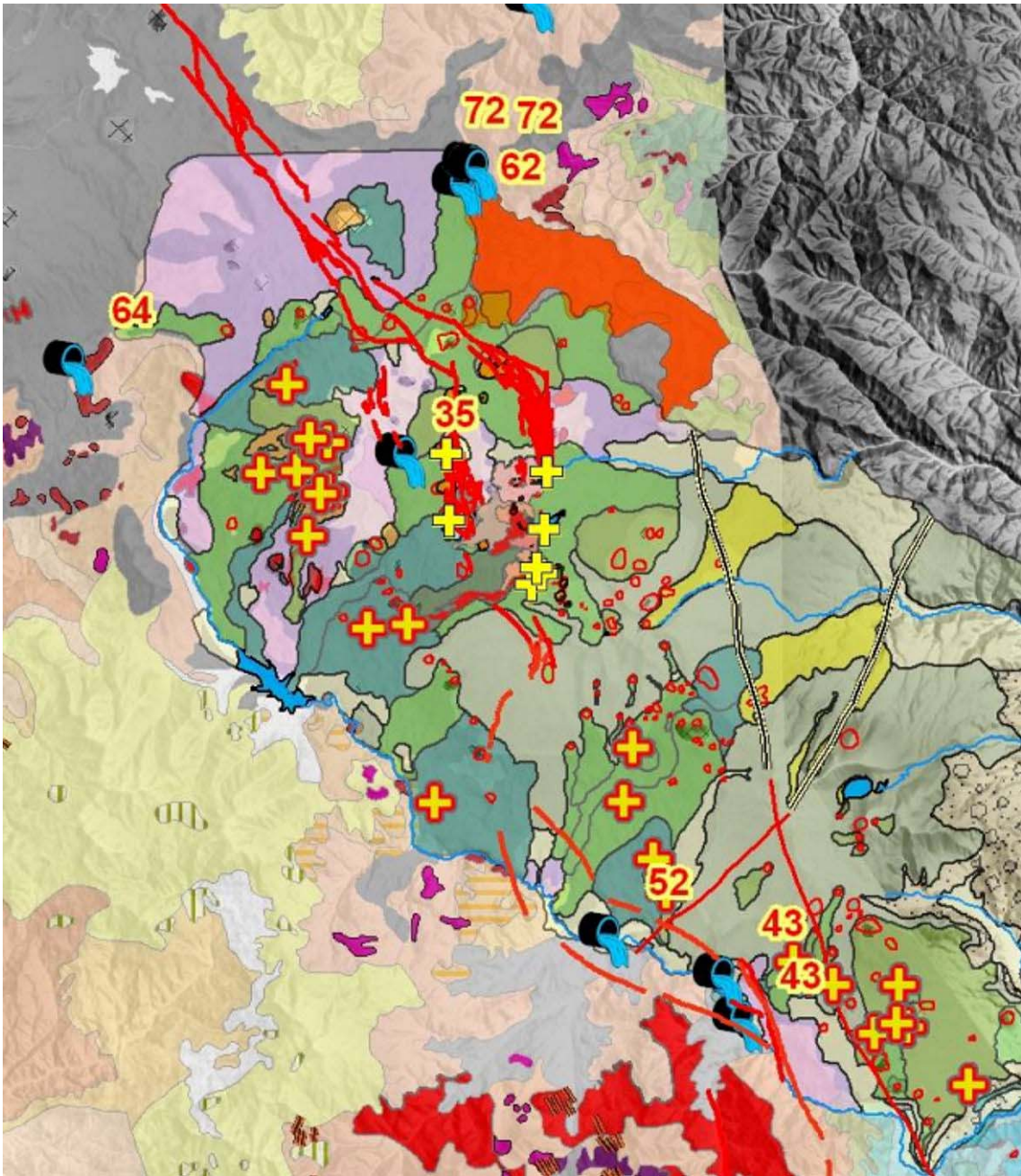
Fig. 2.47: Large Dalidagh and Meghri intrusions and a series of numerous smaller intervening intrusive and extrusive bodies shape a distinct north-trending zone. In the north of the region, the north-trending zone with concentrated intrusions (red color) joins the area of intense Quaternary volcanism in the Syunik Highland (grey-colored area with the sites of Karkar and Jermaghbyur in the center). Crosses indicate locations of sampling for the isotope analysis.

137
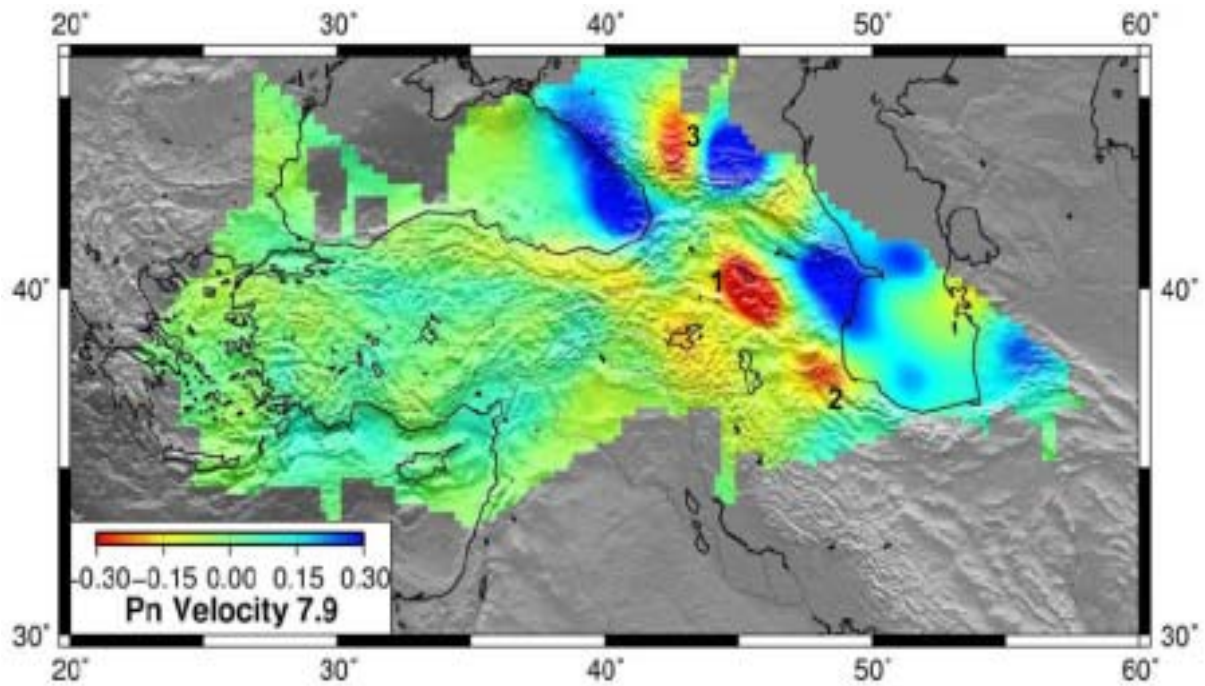
Fig. 2.48: Anomalies of P-wave velocities. Areas of lower velocities, interpreted as provinces of partly melted, higher mantle, are indicated with red color:

1 – area of volcanic highlands of Gegham, Vardenis and Syunik; 2 – Sahand Volcano (Iran);
3 – Elbrus Volcano (Toksoz et al., 2007)
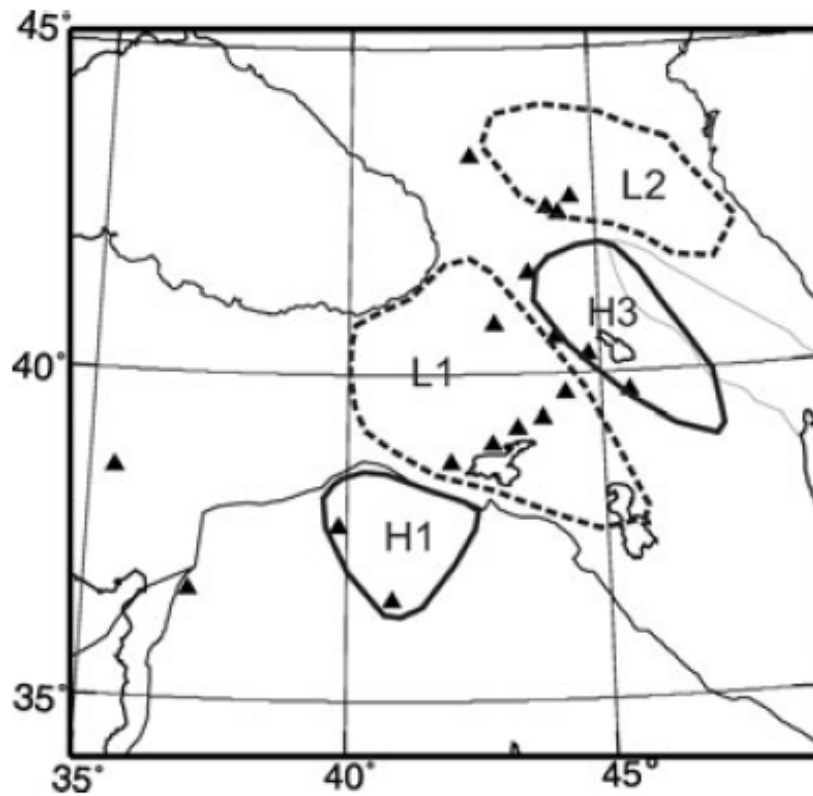
Fig. 2.49: Anomalies of P-wave velocities (Zor, 2008).

H1, H3, L1 and L2 are the velocity anomalies in the shallow part of the upper mantle (left).
Thick grey lines show major plate boundaries.

138
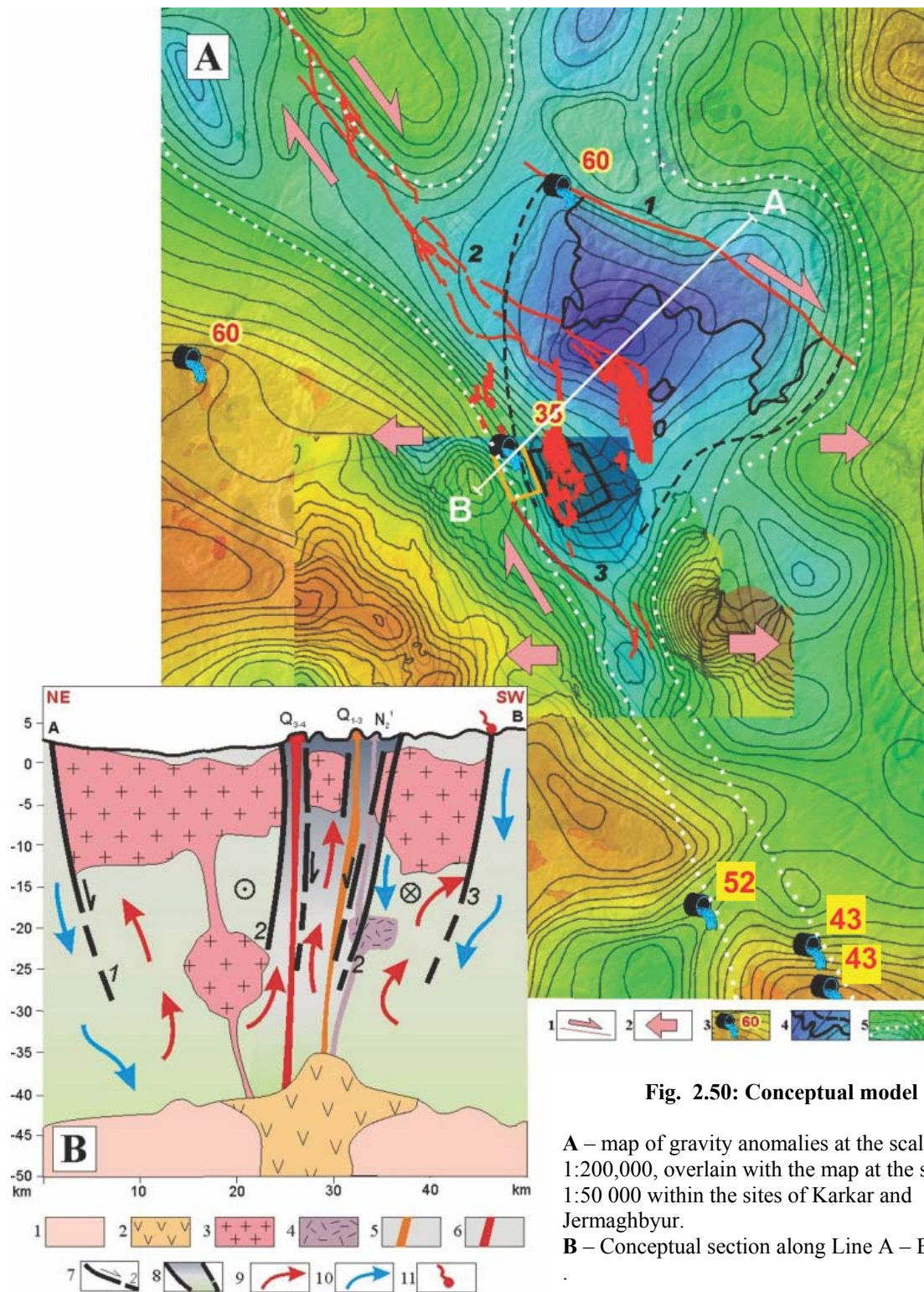
Fig. 2.50: Conceptual model

A – map of gravity anomalies at the scale of 1:200,000, overlain with the map at the scale of 1:50 000 within the sites of Karkar and Jermaghbyur.

B – Conceptual section along Line A – B
.

Legend A: 1 – active Pambak-Sevan Fault (right-lateral strike-slip); 2 – extension areas at the site of the pull-apart basin; 3 – thermalsprings with indications of temperatures; 4 – Dalidagh intrusion (solid lines contour the surface exposure of the intrusive body); 5 –area promising in terms of exploration of geothermal reservoirs.

Legend B: 1 – zone of abnormally heated mantle, 2 – potential magma source, 3 – Dalidagh intrusion: Phases 1 and 2 together (Pg2 –N1), 4 – rhyolites: Phase 3 of the Dalidagh intrusion (N2), 5 – Pleistocene volcanoes in Karkar (Q1-3), 6 – Holocene volcanoes in Karkar (Q4), 7- faults in the Pambak-Sevan system (1 – Terter Fault, 2 – Karkar pull-apart, 3- Karkar-Jermaghbyur Fault); 8 – vertical permeable zone, bounded by the faults of the Karkar pull-apart basin; 9 – thermal mineralized waters; 10 – cold meteoric waters, 11 – thermal spring Jermaghbyur..
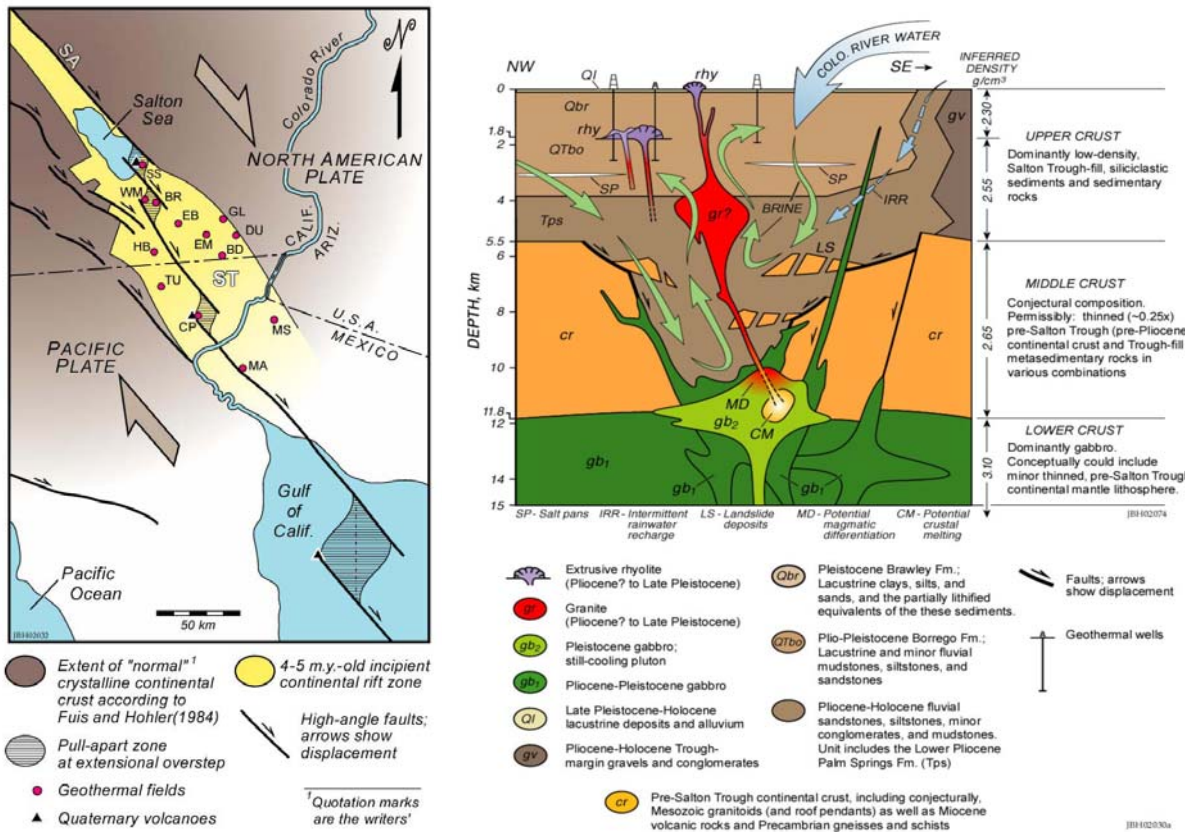
Fig. 2.51: Conceptual model of the geothermal field of the Salton Sea Imperial valley, California.
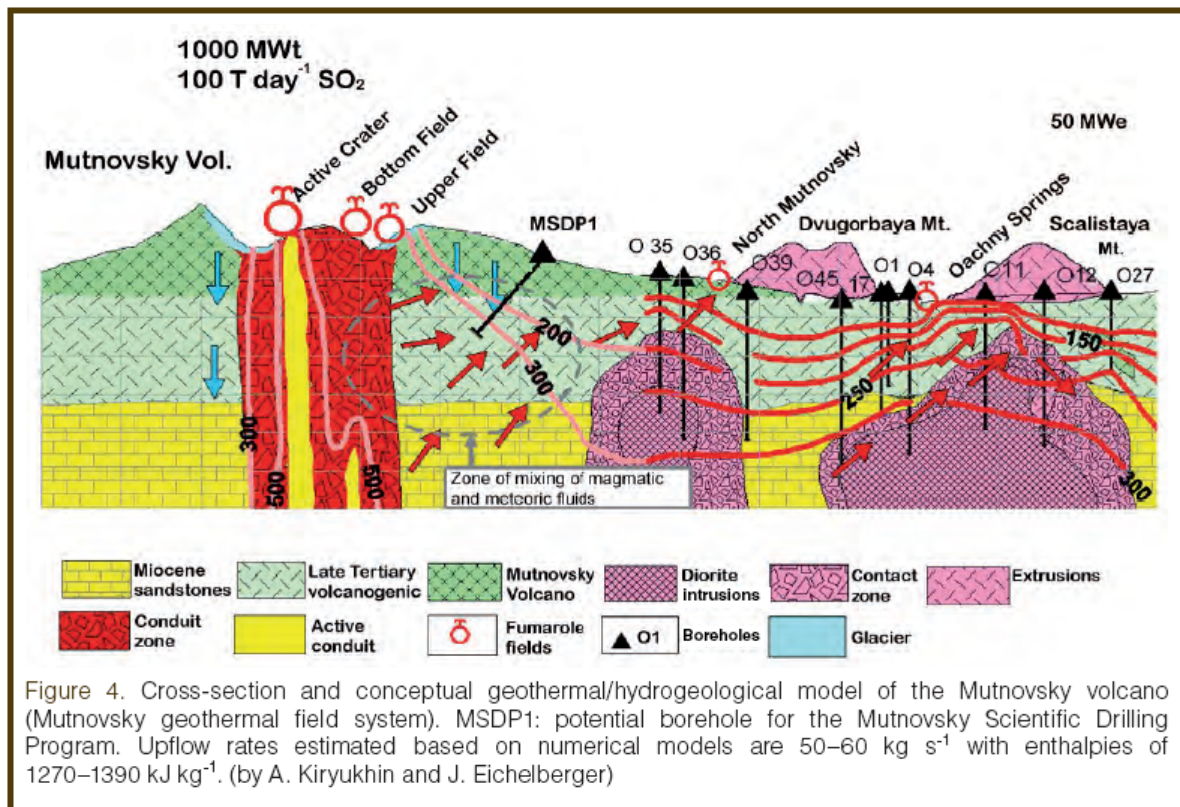
Figure 4. Cross-section and conceptual geothermal/hydrogeological model of the Mutnovsky volcano (Mutnovsky geothermal field system). MSDP1: potential borehole for the Mutnovsky Scientific Drilling Program. Upflow rates estimated based on numerical models are 50–60 kg s^{-1} with enthalpies of 1270–1390 kJ kg^{-1}. (by A. Kiryukhin and J. Eichelberger)

Fig. 2.52: Conceptual model of the Mutovsky deposit in Kamchatka.
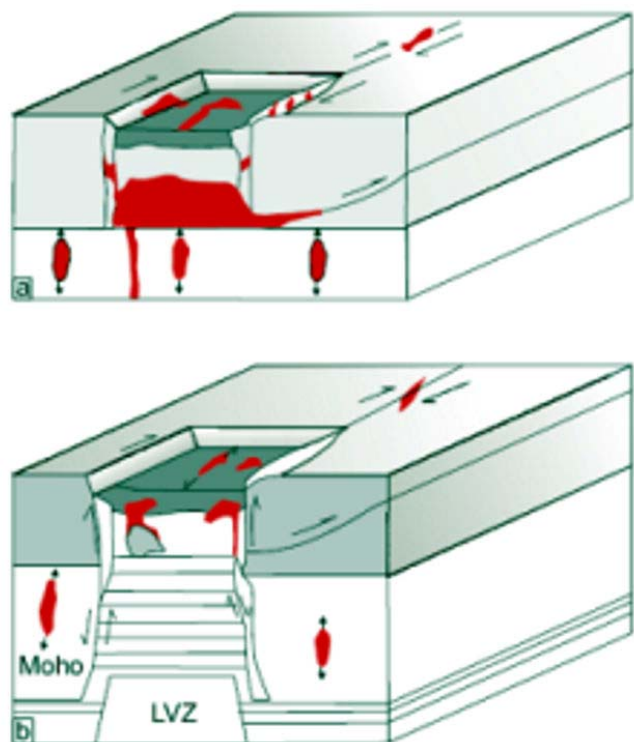
Fig. 2.53: Schematic strike-slip pull-apart basins involving (a) only the elastic lid (basement symbol), and (b) the whole lithosphere (slightly modified from Dewey et al., 1986).
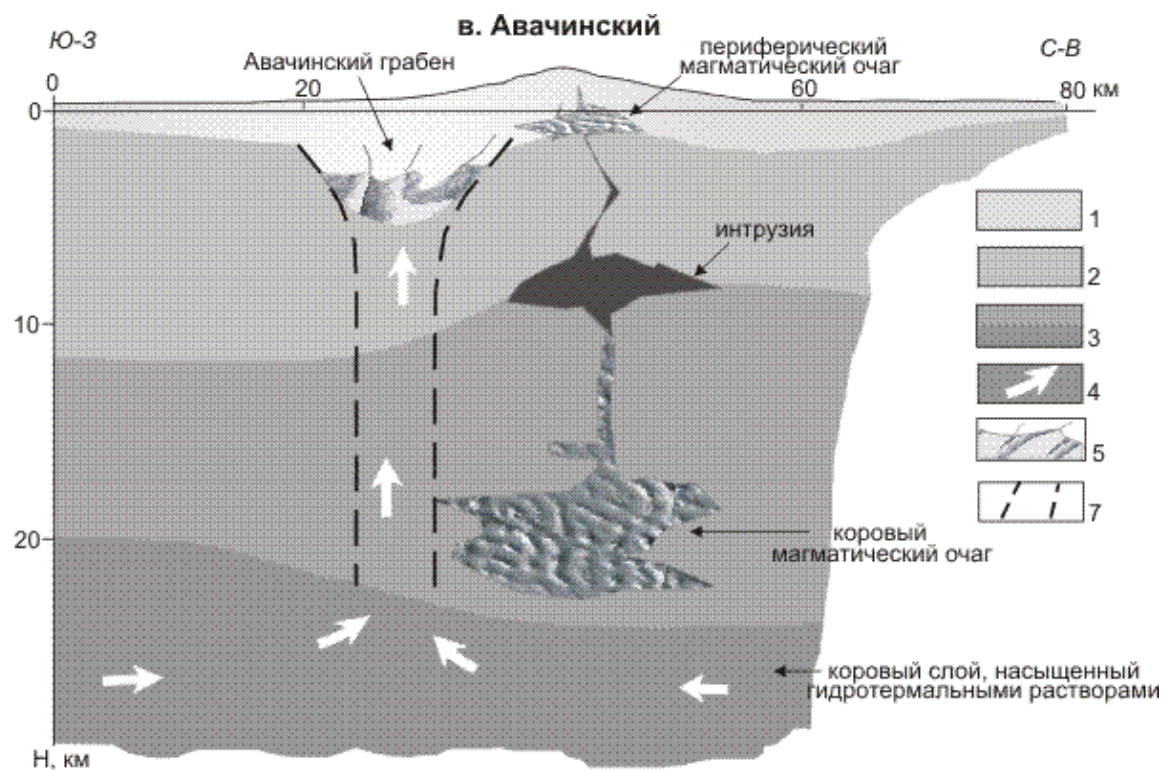
Fig. 2.54: The geological-geophysical models of Avachinsky Volcano
1 – sedimentary-volcanogenic cap; 2 and 3 –Cretaceous and crystalline basements, and the lower crust stratum; 4 – potential tracks of fluids; 5 –anomalous zone on the graben bottom; 6 – presumed deep-seated fault

.

Fig. 2.55: A huge hot-water (280-360°C) geothermal system occurs at Cerro Prieto along an offshore segment of East Pacific plates. This field now produces 720 MW of electricity from geothermal reservoirs as deep as 4000 m.
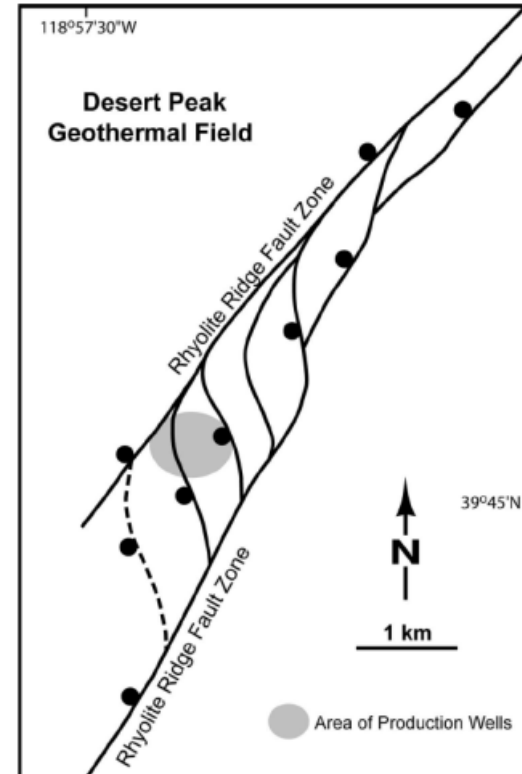
Structural map of the Desert Peak geothermal field (from Faulds and Garside, 2003). Production wells occur within a left step of the Rhyolite Ridge fault zone, where multiple fault strands connect the major overlapping fault segments. The faults shown with solid lines are defined by offset strata and/or well logs. Balls are shown on downthrown sides of normal faults. More detail is shown for the Desert Peak field (as compared to others discussed in this paper), because detailed geologic mapping and compilation of well data has been completed in this area. Numerous wells in the Hot Springs Mountains also facilitate more comprehensive subsurface interpretations as compared to most other geothermal fields within the Great Basin.
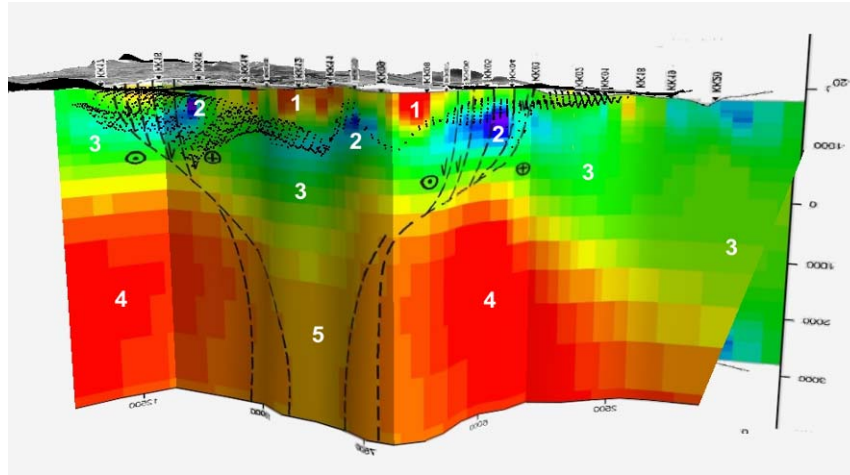
Fig. 2.56: Structural units identified at the Karkar Site by the data of geological investigations, MT and gravimetric surveys. 1, 2, 3, 4, and 5 are different layers described in the text. Black dots show the gravimetric model that detects the bottom of Layer AL – sedimentary basin filled with lava and alluvium.
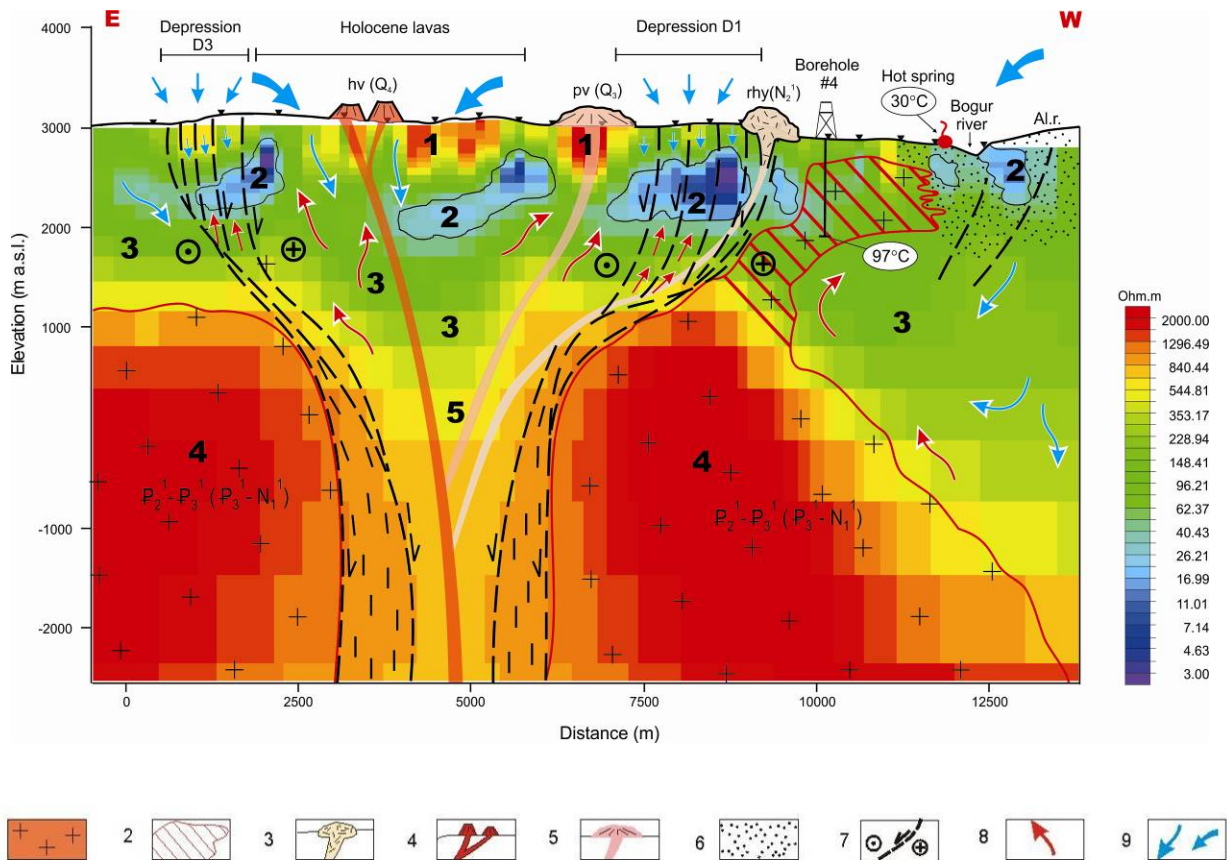
Fig. 2.57: Model Karkar A for a depth of 5 km considers the interpretation of the 2D MT data by Model Georisk/USF and assumes lack of low resistance values in the zone of Layer 5 (PDZ).
Legend: 1 – Dalidagh intrusion: Phases 1 and 2 together (Pg3 2 –N1 1) by the Mt survey data; 2 – inferred distribution of Dalidagh Intrusion Phase 1 according to borehole data; 3 – rhyolites – Phase 3 of the Ddalidagh Intrusion (N2); - 4 -Pleistocene volcanoes in Karkar (Q1-3), 5 – Holocene volcanoes in Karkar (Q4), 6 – zone of hydrothermal silicification and alunitization; 7 – faults of the Pambak-Sevan system; 8 – thermal mineralized waters; 9 – cold meteoric waters. 1-5 –structural units as layers of varying resistance according to the MT survey data.

143
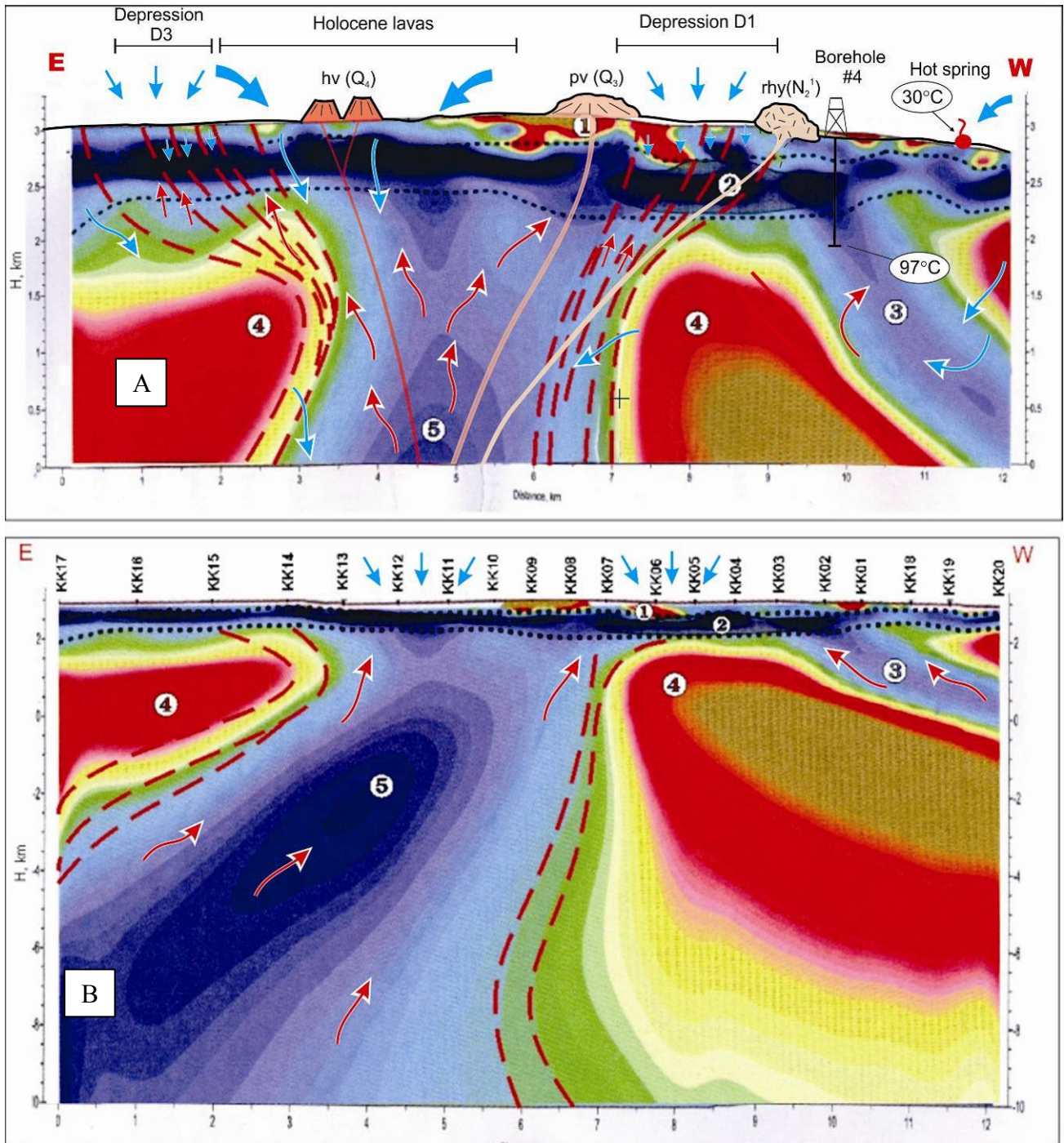
Fig. 2.58: Model Karkar **B, A** – for the depth of 3.5 km, and **B** – for the depth of 10 km, considering the interpretation of the 2D MT data by Models "Nord-West"-2009 and 2004, and assuming presence of low resistance values of 20-30 Ohm x m in the zone of Layer 5 (PDZ). The legend is the same as in Fig. 2.57.
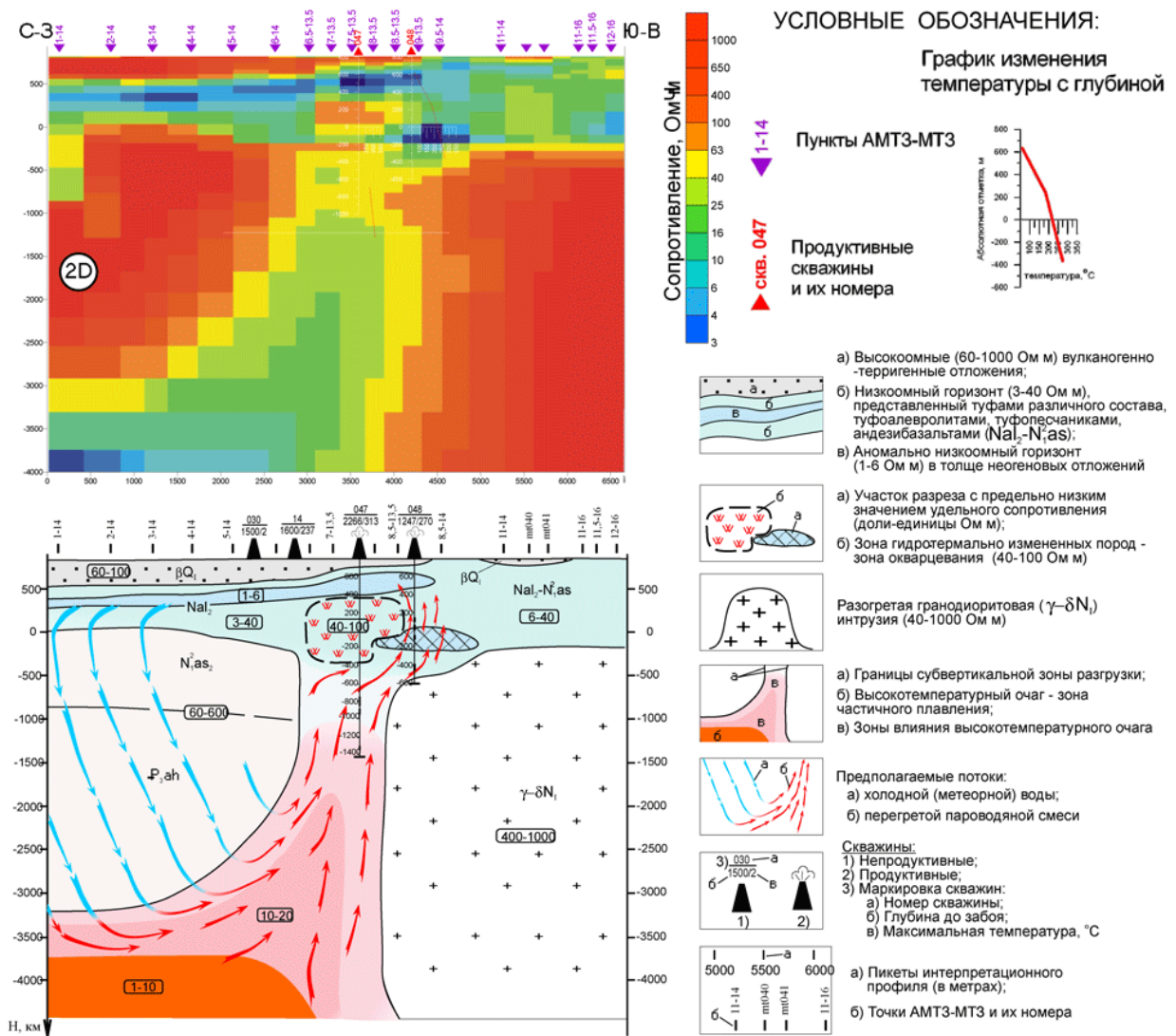
Fig. 2.59: The conceptual model of the Mutovsky geothermal deposit (Results…, 2008).
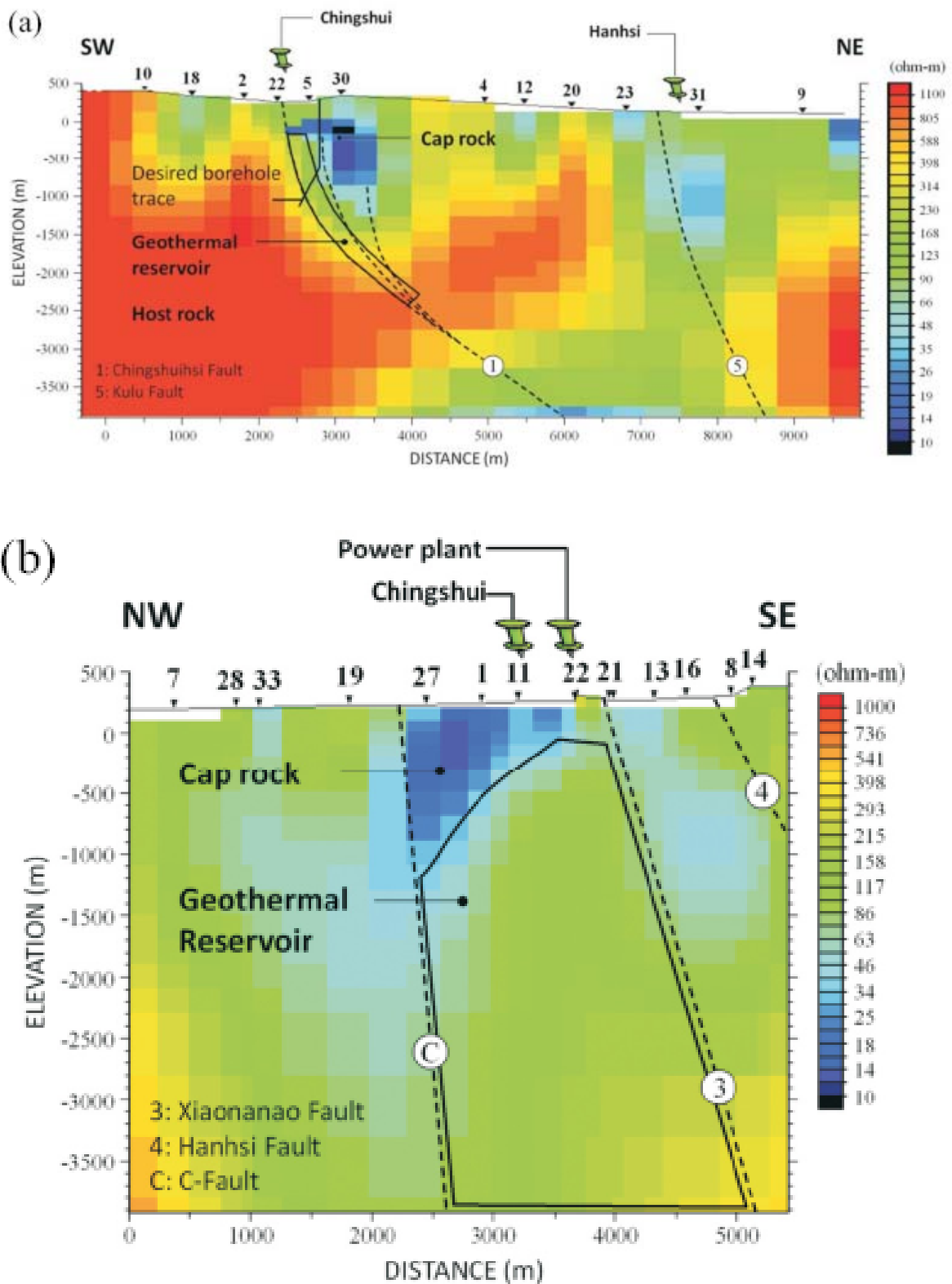
Fig. 2.60: The conceptual model of the Chingshui Ilan geothermal deposit in Taiwan (Lung-tao Tong et al., 2008).
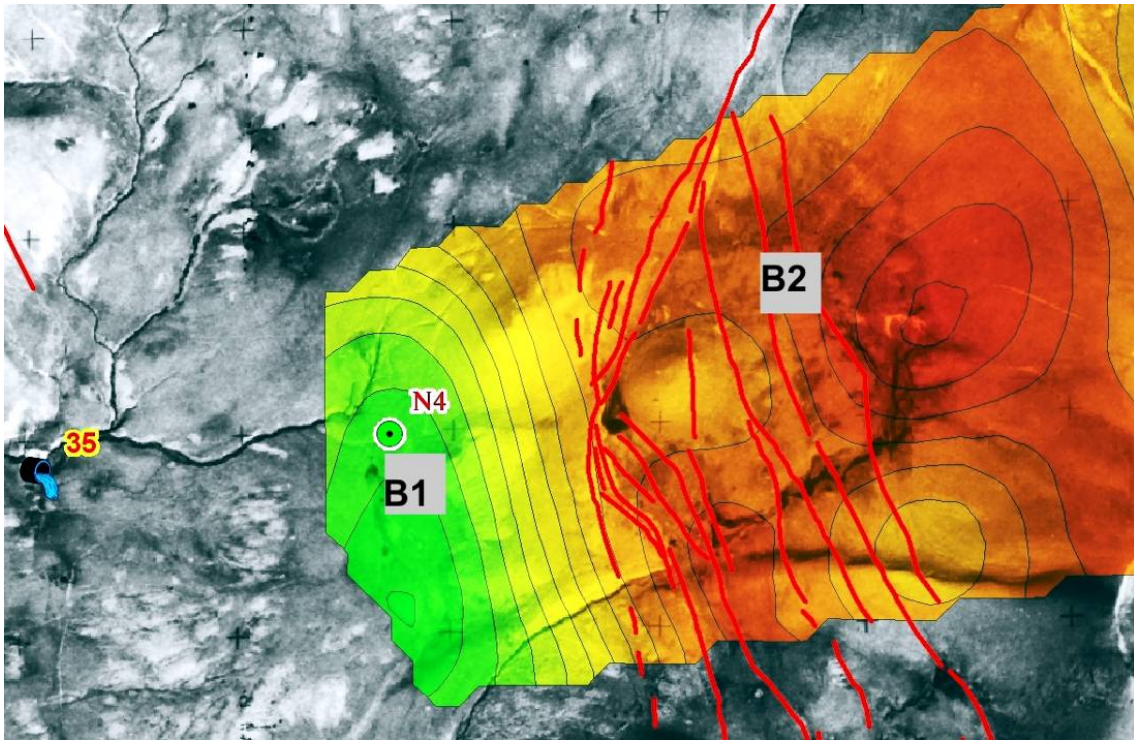
Fig. 2.61: The proposed locations of exploratory drilling. B1 – Exploratory Well 1; B2 – Exploratory Well 2; N4 – Borehole 4.
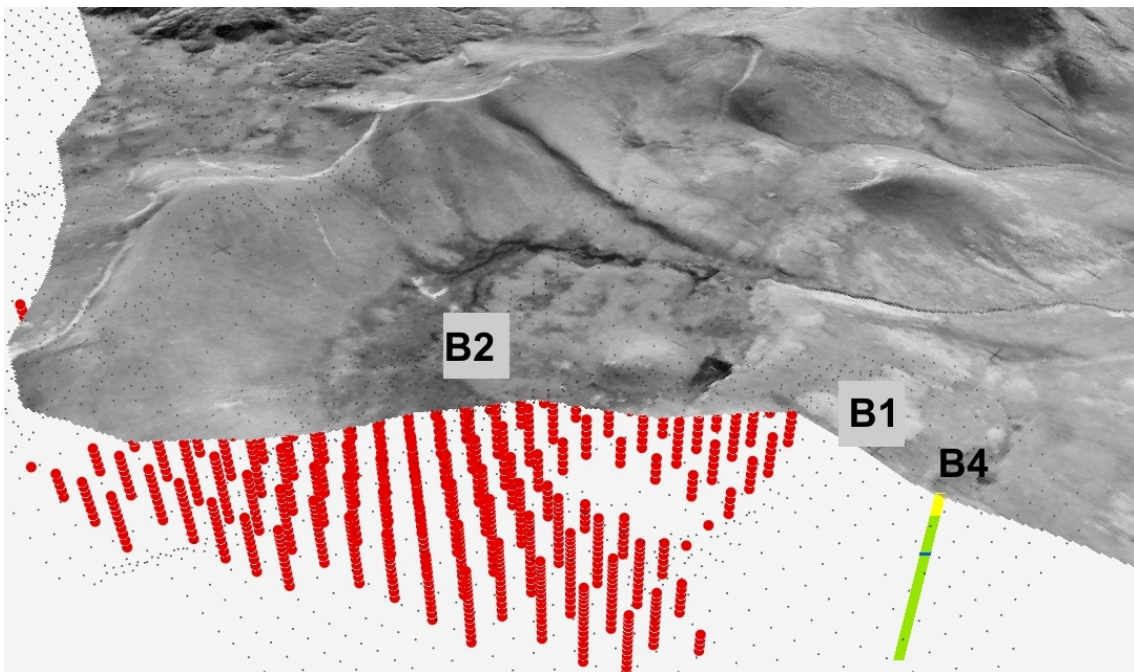
Fig. 2.62: The proposed locations of exploratory drilling. B1 – Exploratory Well 1; B2 – Exploratory Well 2; N4 – Borehole 4.
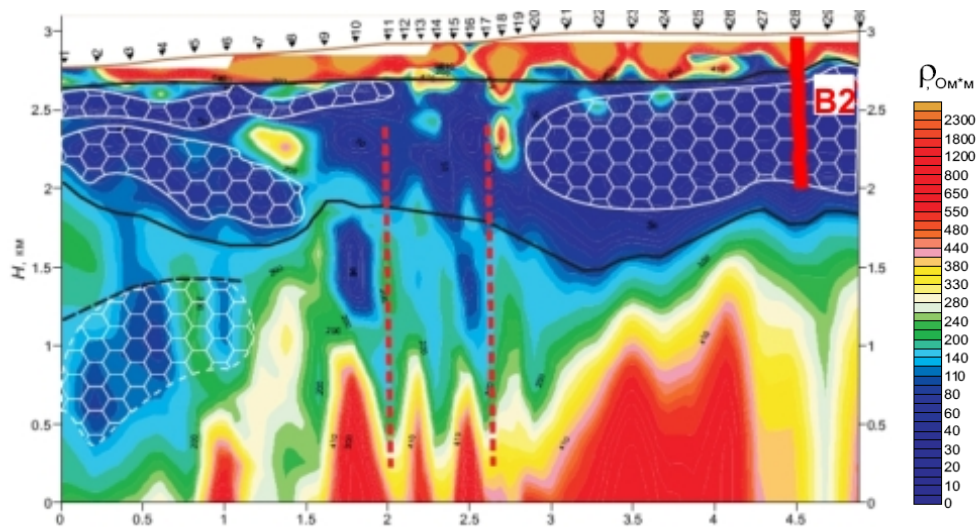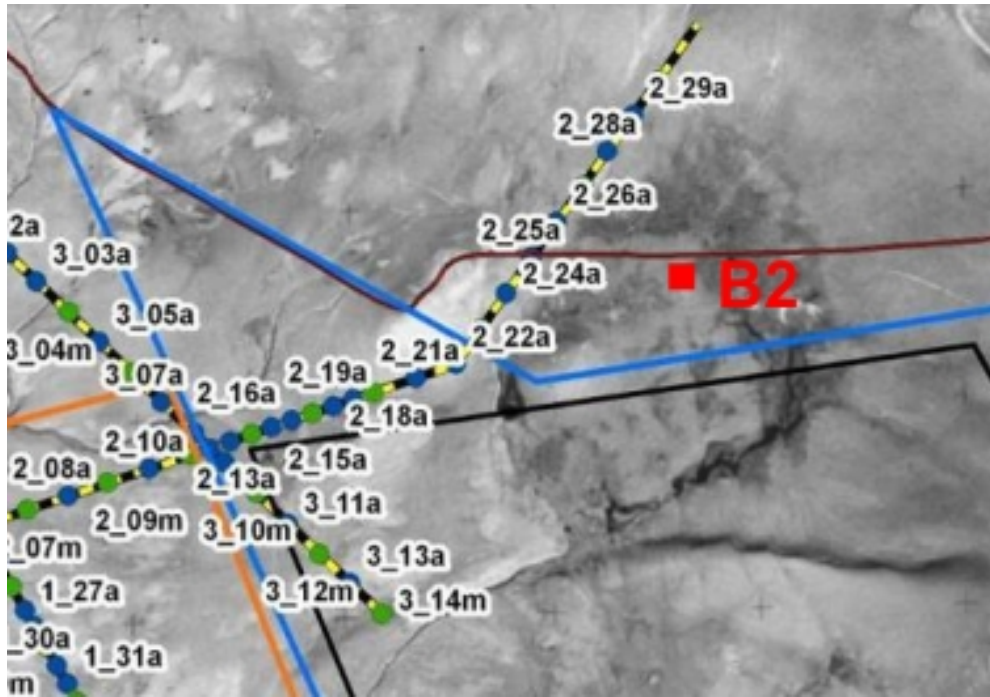
Fig. 2.63: Correlation of the 2D MT inversion data of 2004, conducted by the «Nord-West» company (RF), with indication of proposed exploratory well B2, located in Layer 2.

Fig. 2.64: Correlation of the 2D MT inversion data of 2009, conducted by the South Florida University (USA) with indication of exploratory well B2, located in Layer 2.
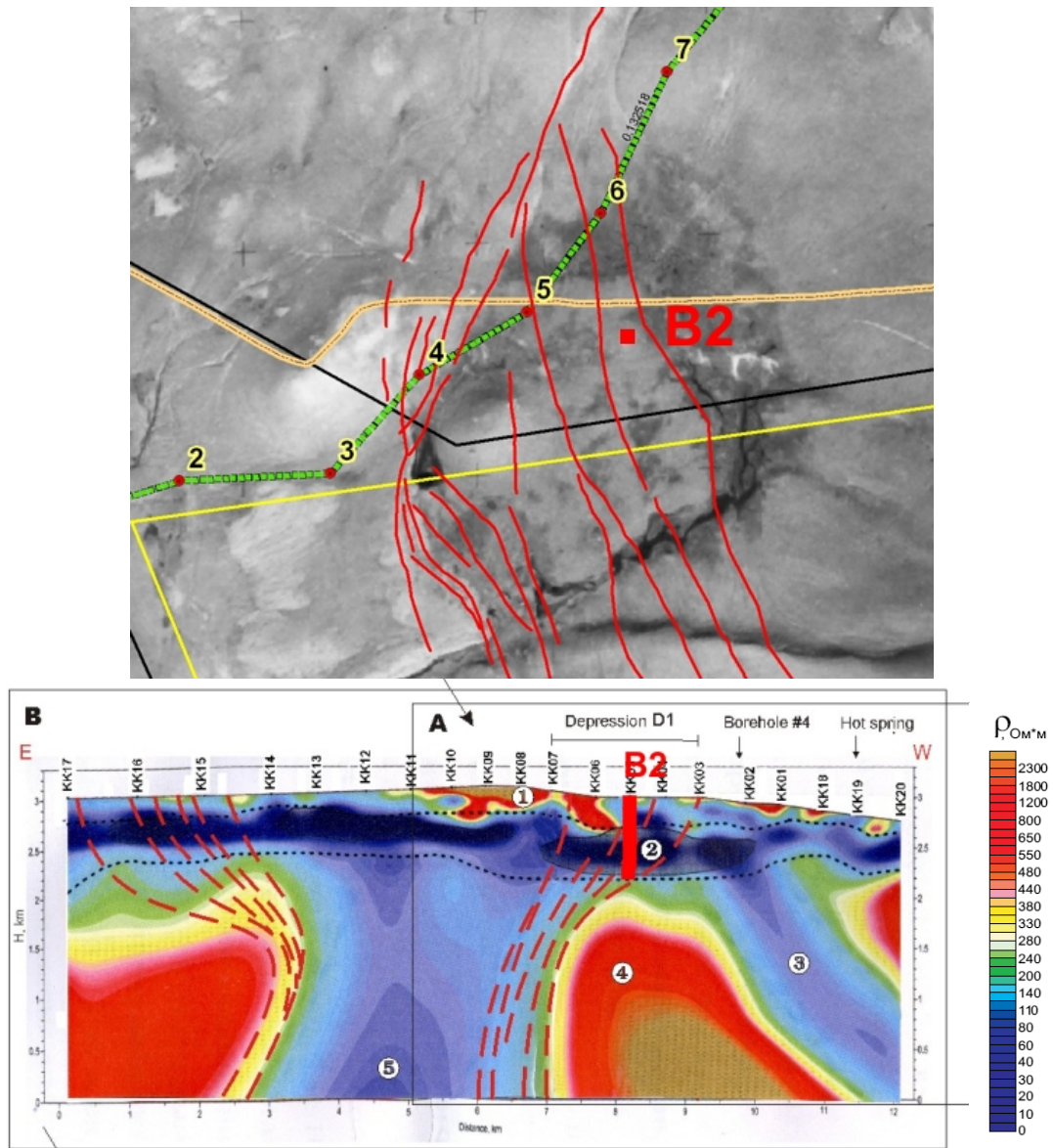
Fig. 2.65: Correlation of the 2D MT inversion data of 2009, conducted by the «Nord-West» company (RF), with indication of proposed exploratory well B2, located in Layer 2.
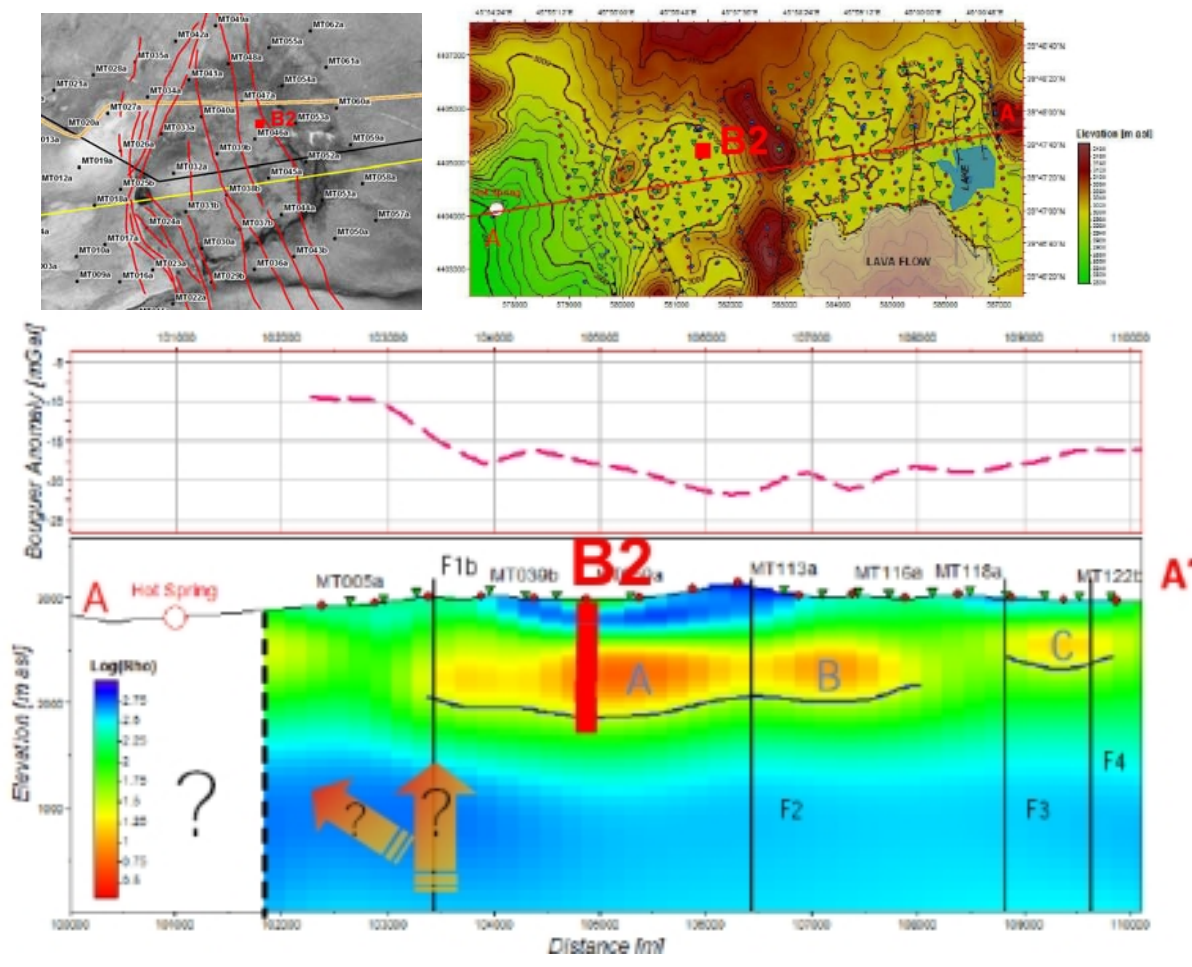
Fig. 2.66: Correlation of the 3D MT inversion data of 2011, conducted by the «Western Geco» company, with indication of proposed exploratory well B2, located within Anomaly A in Layer 2.
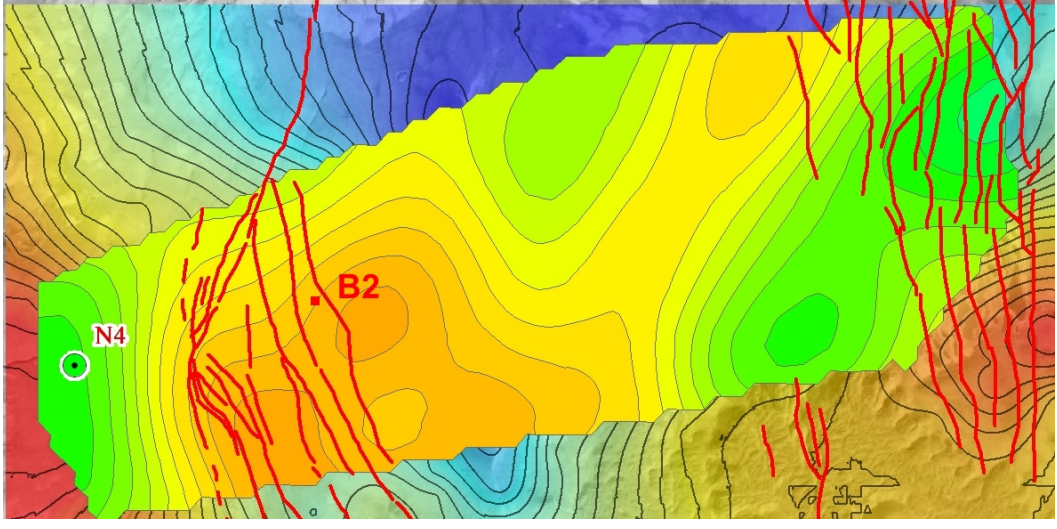
Fig. 2.67. Correlation of the gravity model of 2011 with the faults from the structural model of 2009 and the findings of the 3D MT survey: section at the depth of 1 km, with indication of proposed location of exploratory well B2.
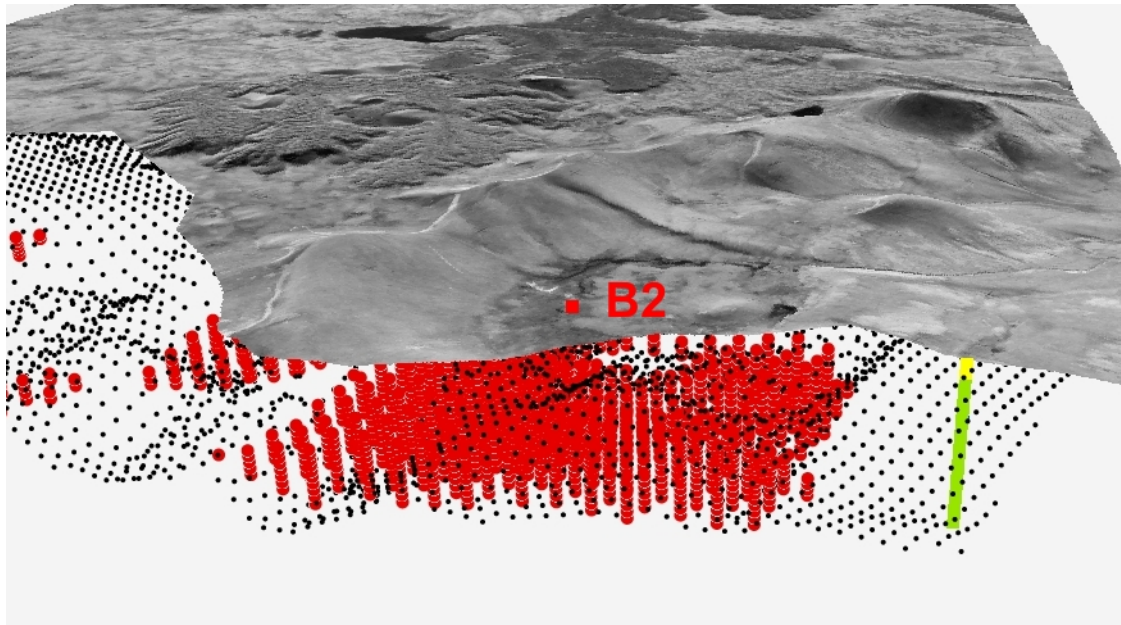
Fig. 2.68.: Correlation of the gravity model of 2011 (black dots) with the findings of the 3D MT survey (red dots) and with indication of proposed location of exploratory well B2.

REFERENCES

Blais, J. A. R. and Ferland, R. (1984). Optimization in gravimetric terrain corrections. Canadian Journal of Earth Sciences, 21:505-570

Campbell, D. L. (1980). Gravity terrain corrections for stations on a uniform slope – a power law approximation. Geophysics, 45:109-112.

Daly, R. (1935). Densities of rocks calculated from their chemical analyses. Proceedings of the National Academy of Sciences, 21:657-663.

Kane, M. F. (1962). A comprehensive system of terrain corrections using a digital computer. Geophysics, 27:455-462.

LaFehr, T. R. (1991). Standardization in gravity reduction. Geophysics, 56:1170-1178.

Langevin, C., Thorne, D.T., J., Dausman, A., Sukop, M., and Guo, W. (2008). SEAWAT version 4: A computer program for simulation of multi-species solute and heat transport: U.S. Geological Survey techniques and methods book 6, chapter a22. In U.S. Geological Survey Techniques and Methods Book 6, Chapter A22. U.S. Geological Survey.

Moore, J. G. (2001). Density of basalt core from Hilo drill hole, Hawaii. Journal of Volcanology and Geothermal Research, 112:221-230.

Nowell, D. A. G. (1999). Gravity terrain corrections - an overview. Journal of Applied Geophysics, 42:117-134.

Абовян, С. Б., и Малхасян, Э. Г., 1961. О редком случае прорыва граносиенитового интрузива четвертичным вулканом в Армянской ССР. Доклады Академии Наук Армянской ССР, стр. 231-234 [Abovyan, S. B., and Malkhasyan, E. G., 1961. About a rare case of a Quaternary volcano cutting through granosyenite intrusion, Armenian SSR. Contributions of the Academy of Sciences of the Armenian SSR, pp. 231-234]

Azizbekyan, O. G. Study and generalization of data on the geological structure, recent volcanism and tectonics in the Vorotan River basin

Азизбекян О.Г. и др., 1987. Региональные геолого-геофизические исследования в районах интенсивного развития неоген-четвертичных вулканических процессов (общие поиски геотермальных месторождений). Ереван. [Azizbekyan, O. G., et al., 1987. Regional geological and geophysical studies in the regions of intense development of Neogene-Quaternary volcanic processes (common exploration of geothermal deposits, Yerevan)]

Al-Lazki, A., Seber, D., Sandvol, E., Turkelli, N., Mohamad, R., and Barazangi, M., 2003. Tomographic Pn velocity and anisotropy structure beneath the Anatolian plateau (eastern Turkey) and the surrounding regions, *Geophys. Res. Lett.,* 30(24)

Бабурян Г.М. и др., 1984. Сейсморазведочные работы, проведенные Южной геофизической партией в Сисианском, Горисском, Кафанском и Мегринском районах Армянской ССР за 1981-84 гг. Ереван, 1984. [Babouryan, G. M., et al., 1984. Seismic prospecting activities conducted by the Southern Geophysical Party in the Sissian, Goris, Kafan and Meghri regions of the Armenian SSR during 1981-84, Yerevan]

Габриелян А.А., Саркисян О.А., Симонян Г.П., 1981. Сейсмотектоника Армении. ЕрГу, стр. 270. [Gabriyelyan, A.A., Sargsyan, O.A., Simonyan, G.P., 1981. The Seismotectonics of Armenia, Yerevan State University, p. 270.]

Kompani-Zare, M. and Moore, F., 2001. Chemical thermometry and origin of the Dalaki mineral springs, Bushehr Province, Iran. Journal of Hydrology (NZ), 40 (2), 189-204

Lun-Tao Tong, Shoung Ouyang, Tai-Rong Guo, Ching-Ray Lee, Kou-Hsin Hu, Chun-Li Lee and Chun-Jao Wang, 2008. Insight into the Geothermal Structure in Chingshui, Ilan, Taiwan, *Terr.Atmos. Ocean. Sci.,* vol. 19, pp. 413-424

Мусаев, Ш. Дж, 1983. Механизм формирования магматических комплексов Далидагского рудного тела. В сборнике: Вопросы магматизма Азербайджана, Издание Азербайджанского Государственного университета, Баку, 134-137 [Mousayev, Sh. J., 1983. Mechanism of formation of the magmatic complexes of the Dalidagh ore body. In: vol. Issues of Magmatism in Azerbaijan, published by the Azerbaijan State University, Baku, 134-137]

Меликсетян, Б. М., Архипов, Б. К., Капралов, Г. П., и Мещерякова, В. Б., 1975. Особенности тектоно-магматического развития и закономерности размещения магматизма и оруденения в южной части Малого Кавказа. Известия АН Армянской ССР, Науки о Земле, 6, 52-69 [Meliksetyan, B. M., Arkhipov, B. K., Kapralov, G. P., and Mescheryakova, V. B., 1975. Features of tectonic and magmatic development, and magmatism and mineralization distribution regularities over the southern part of the Lesser Caucasus. Izvestiya AN Armyanskoi SSR, Nauki o Zemle, 6, 52-69]

Nafi Toksoz, M., Van der Hilst, R., Benoit, M. H., Gulen, L., Kalafat, D., Kuleli, S. H., Chang Li and Youshun Sun, 2007. Seismic Tomography of the Arabian-Eurasian Collision Zone and Surrounding Areas. 29th Monitoring Research Review: Ground-Based Nuclear Explosion Monitoring Technologies

Оганисян С.М., Гаспарян Р.К., Яковлев А.Г. и др. Комплексные геофизические исследования зоны сейсмической неоднородности на участке Джермахпюрского геотермального поля. Отчет по договору N 403/792, Гюмри 2004. [Ohanissyan, S. M., Gasparyan, R. K., Yakovlev, A. G., et al., 2004. Complex geophysical investigations of the zone of seismic inhomogeneity at the site of Jermaghbyur geothermal field, Report on Contract N 403/792, Gyumri]

Оровецкий, Ю. П., и Егоркина, Г. Ж., 1983. Глубинный магматический диапиризм Центральной Армении. Известия АН Армянской ССР, Науки о Земле, XXXVI, 5, 41-45 [Orovetsky, Yu. P., and Yegorkina, G. Zh., 1983. Deep-seated magmatic diapirism in Central Armenia. Izvestia AN Armyanskoi SSR, Nauki o Zemle, XXXVI, 5, 41-45]

Ozacar, A. A., Gilbert, H., and Zandt, G., 2008. Upper mantle discontinuity beneath East Abatolian Plateau (Turkey) from receiver functions. *Earth and Planetary Science Letters*

Р**езультаты электроразведочных исследований** Мутновского месторождения Парогидротерм, **Вебсайт компании Северо-Запад** [Results of electrical prospecting investigations of the Moutnovsky Deposit. PAROHYDROTHERM, "Nord-West" Company website]

Tatar, O., Yurtmen, S., Temiz, H., Gursoy, H., Kocbulut, F., Mesci, B. L., and Guezou, J.-C., 2007. Intracontinental Quaternary Volcanism in the Niksar Pull-Apart Basin, North Anatolian Fault Zone, Turkey. Turkish Journal of Earth Sciences, vol. 16, pp. 417-440.

Туманян Г. А., 1983. Глубинная структура земной коры на космических изображениях. Исследование Земли из космоса, N5, стр. 32-39 [Toumanyan, G. A., 1983. Deep structure of the Earth crust on satellite images. "EARTH STUDY FROM THE SPACE", N5, pp. 32-39]

Zor, E., 2008. Tomographic evidence of slab detachment beneath eastern Turkey and the Caucasus. *Geophys. J. Int.*, 175, 1273-1282

Faulds, J., F., Coolbaugh, M, E., Vice, G. S., and Edwards, M. I., 2006. Characterizing Structural Controls of Geothermal Field in the Northwestern Great Basin: A progress Report. *GRC Transactions*, vol. 30.

Yanikyan, V. O. Prospecting activities to identify geothermal deposits in the northwestern part of the Sissian region for 1987-1990

Яникян В.О., Оксузян Л.Н., 1994. Отчет гравиметрической партии «О гравиразведочных работах в Вайкском, Ехегнадзорском районах РА и составление сводной гравиметрической карты Капанского и Зангезурского рудных районов м-ба 1 :50000, проведенных в 1989-1994гг.", Фонды "Армгеология", Ереван [Yanikyan, V. O., Oxouzyan, L. N., 1994. Gravimetry Party Report "About the gravimetric exploration activities in the Vaik, Yeghegnadzor regions of the RA, and preparation of a summary gravimetric map of the Kapan and Zanghezour ore districts at the scale of 1:50,000, conducted in 1989-1994". ARMGEOLOGIYA Archives, Yerevan]

Annex 1.

Sample Kar-2

Alunitized rhyolite (from the extrusion)

This sample represents a hydrothermally altered rock (alunitized rhyolite) of fully crystalline structure with rare porphyry impregnations of resorbed quartz. Apart of these, there are single grains of altered minerals: prismatic plagioclase, amphibole, and biotite, which develop pelitic, alunitic and chlorite-magnetite aggregates.

The matrix is composed of fully devitrified grains of quartz, potassium feldspar, and flakes of hydromica. Its structure is hypidiomorphic-grainy, of fine crystals, xenomorphic-grainy; typical veinlets and lithophyses of devitrified quartz are observed.

The chemical analysis of this sample is shown in the table below:

Kar-2	Weight, %
SiO_2	79.43
TiO_2	0.32
Al_2O_3	7.2
Fe_2O_3	0.19
FeO	0.14
MnO	-
MgO	0.09
CaO	0.62
Na_2O	1.20
K_2O	1.90
P_2O_5	0.18
H_2O	0.11
CO_2	0.56
S	5.89
П.п.п	2.18
Total	100.017

The high content of sulfur (up to 6%) is related to the presence of alunite mineral in the rock. The presence of alunite in this sample was confirmed by X-ray structural analysis. Hydrothermal alteration of the rocks is manifested in the accompanying process of silicification and alunitization, related with post-volcanic effects such as impacts of solfatara solutions and fumaroles.

Gravity inversion results using a Bouguer density of 2700 kg m^{-3} for different Pareto points
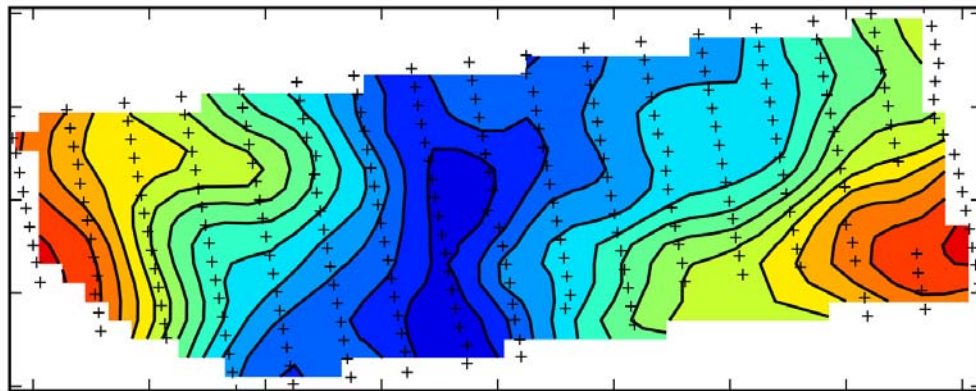
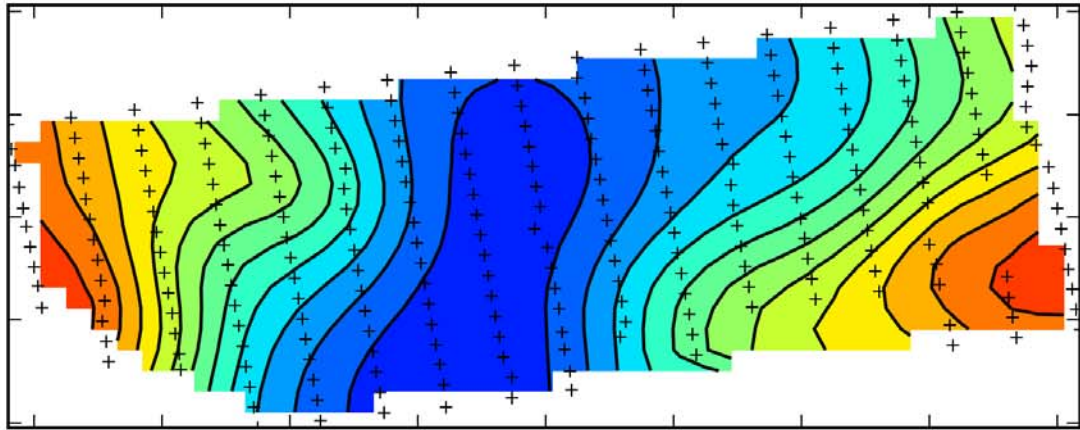(a) simulated gravity response

depth (meters)
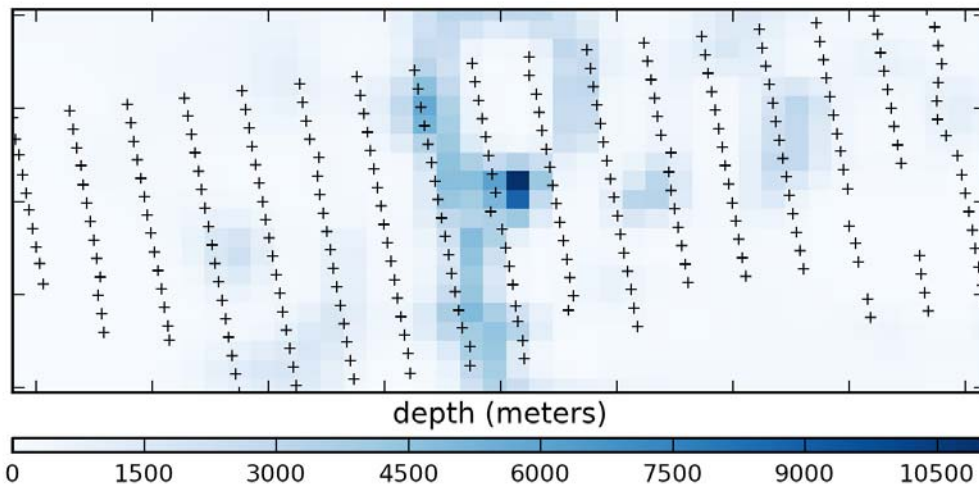
(b) inverted depth distribution
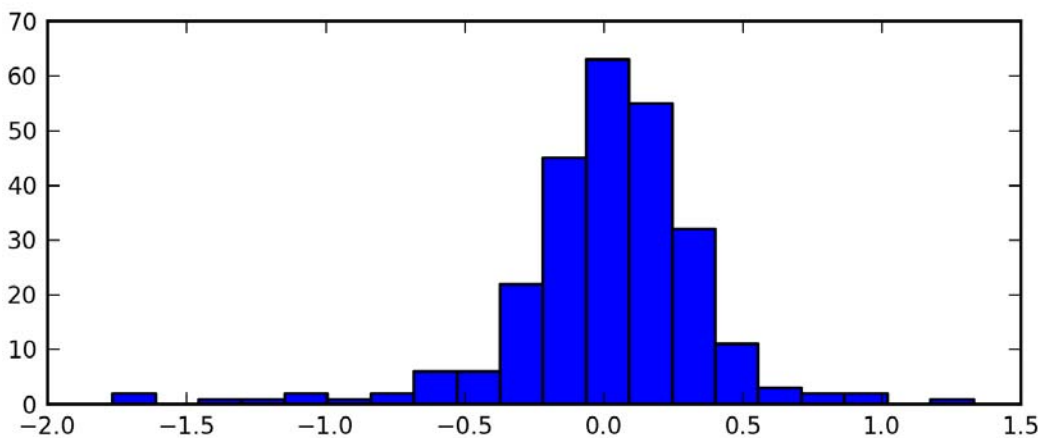
(c) histogram of residuals
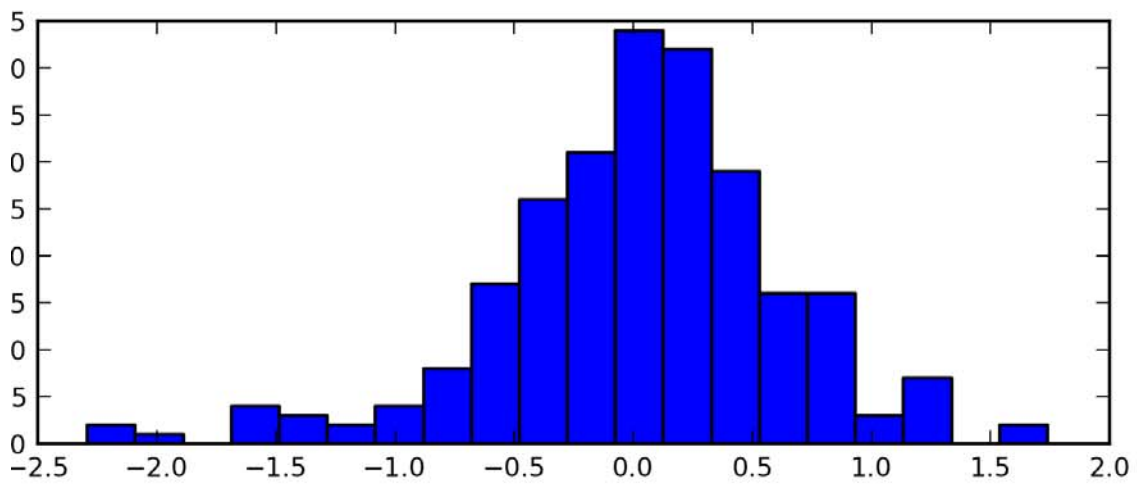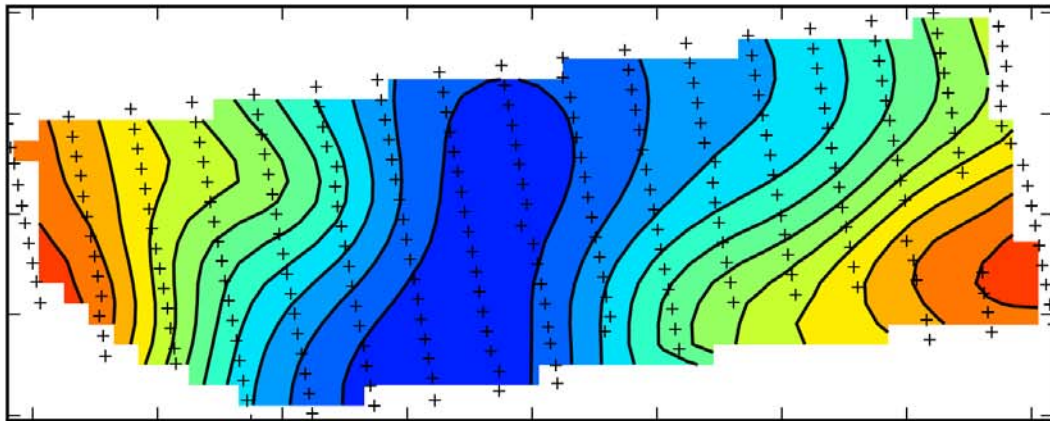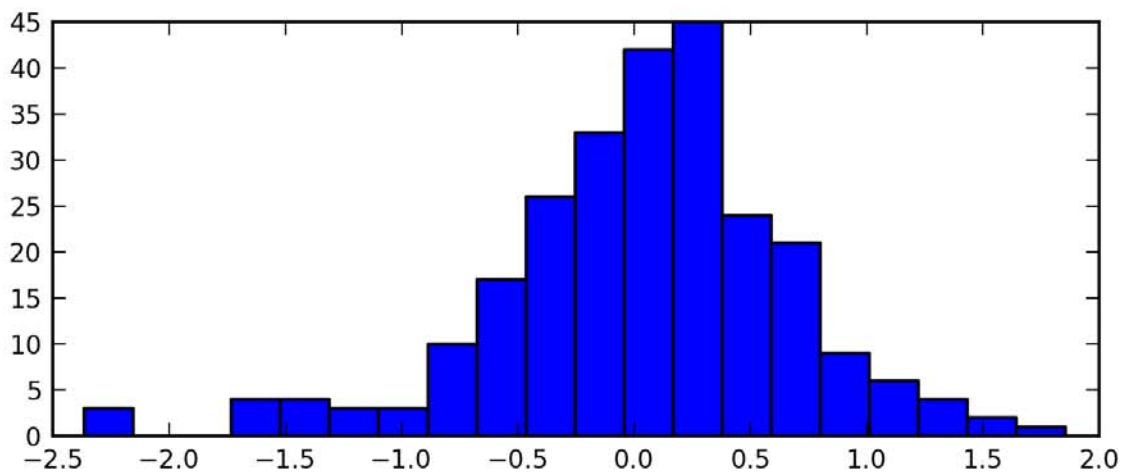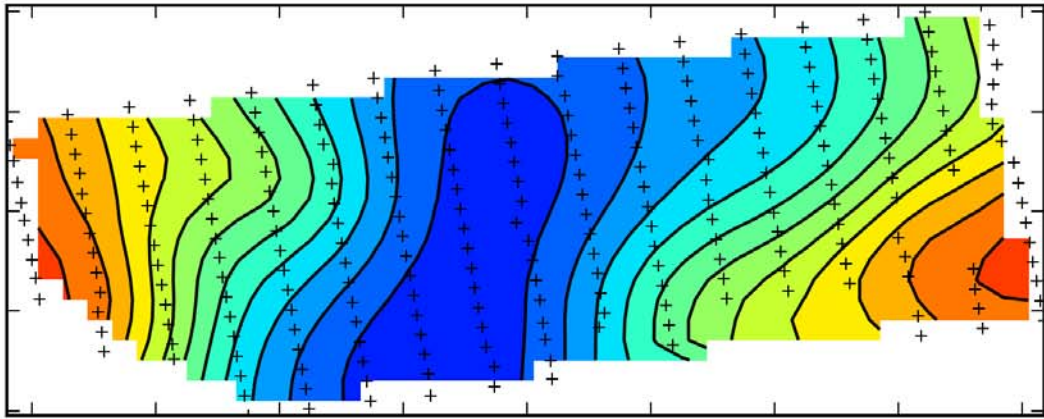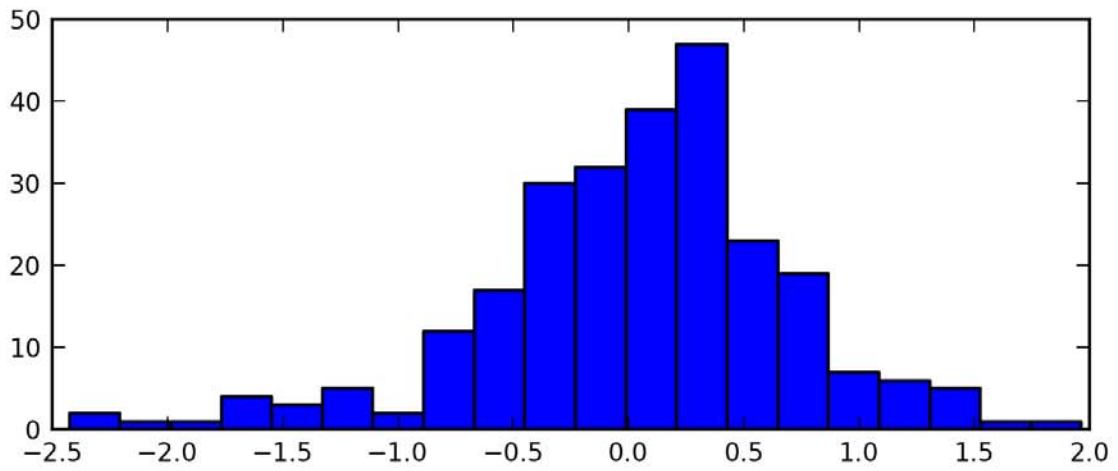
Fig. 1. Summary of Pareto point 1

(a) simulated gravity response

depth (meters)
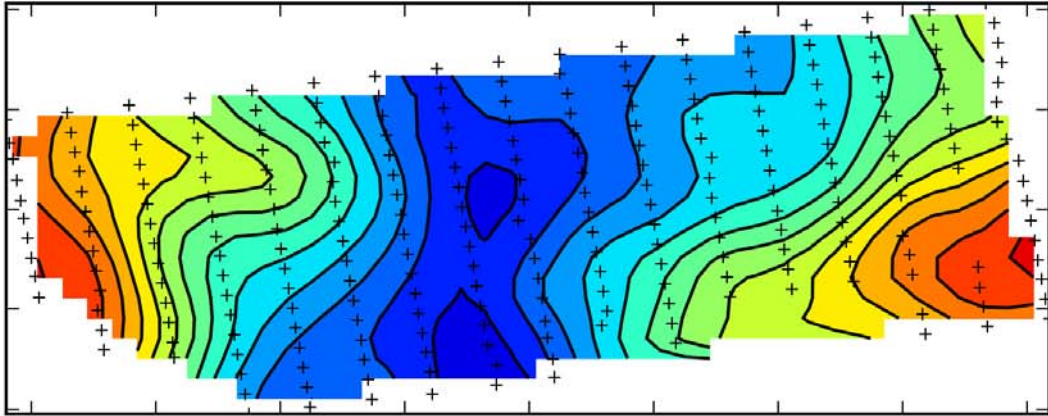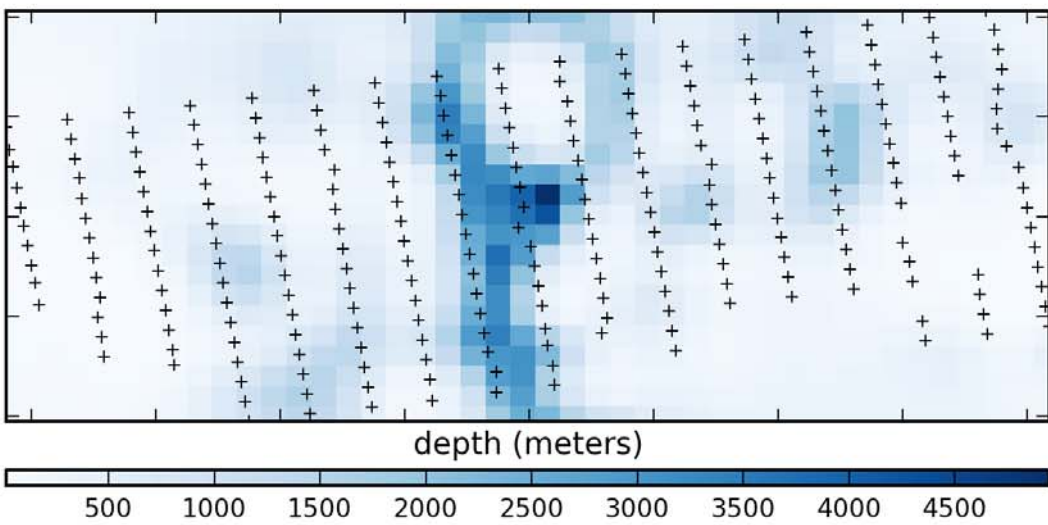
(b) inverted depth distribution
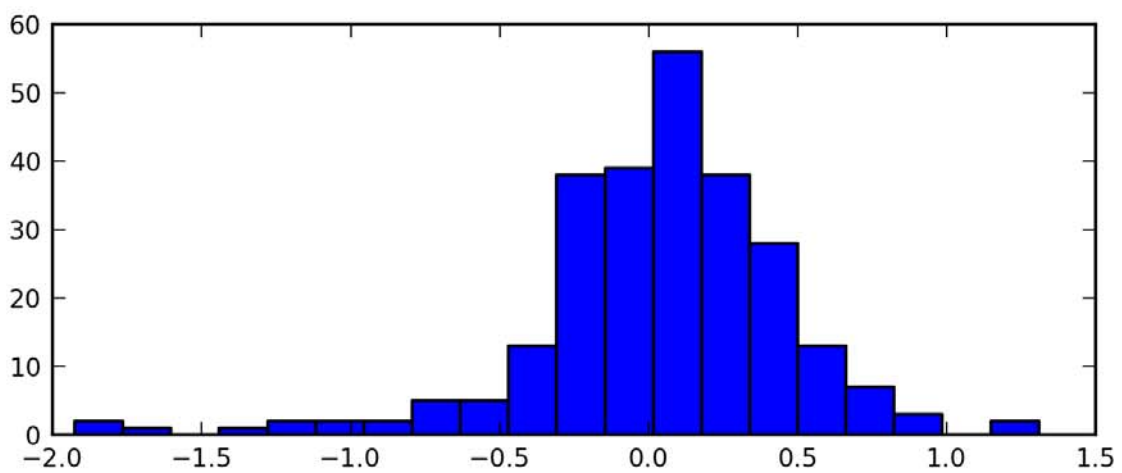
(c) histogram of residuals

Fig. 2. Summary of Pareto point 2

157

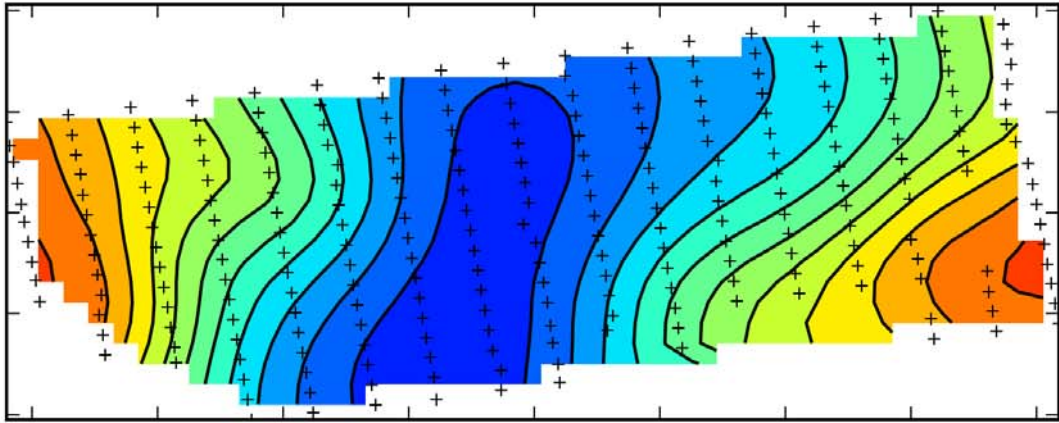(a) simulated gravity response

depth (meters)
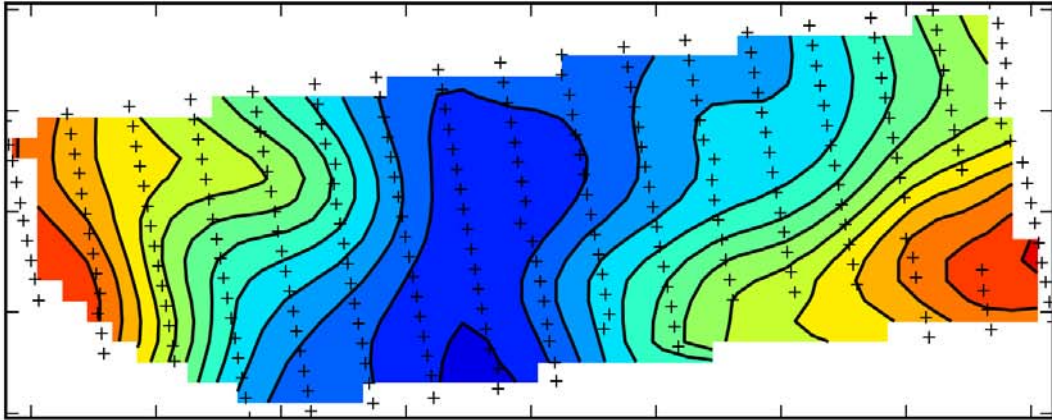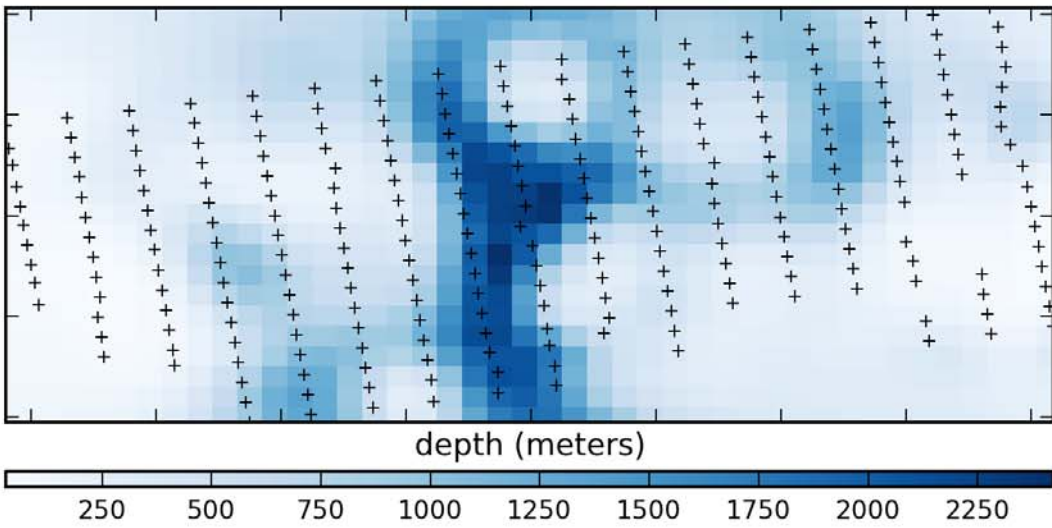
(b) inverted depth distribution
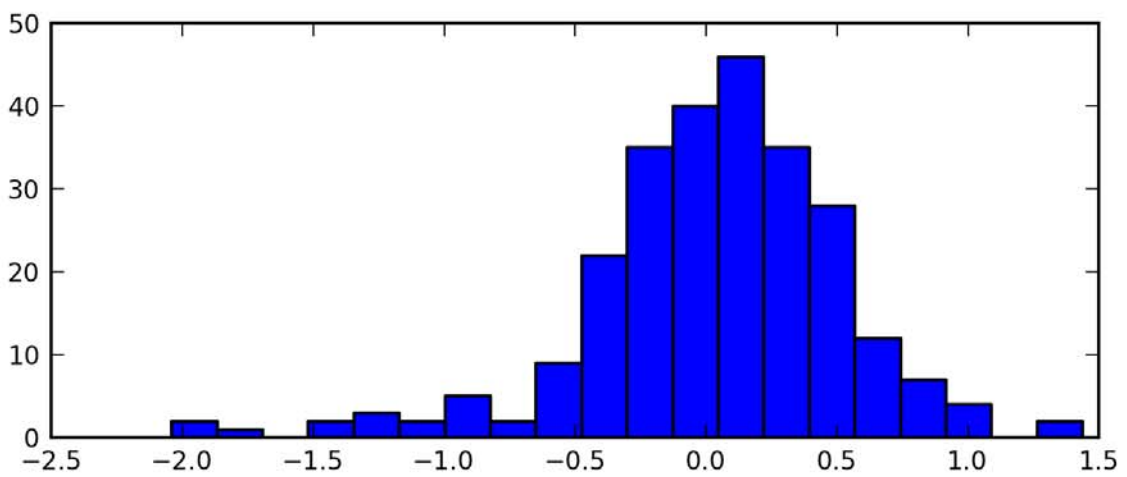
(c) histogram of residuals

Fig. 3. Summary of Pareto point 3

158

(a) simulated gravity response

depth (meters)
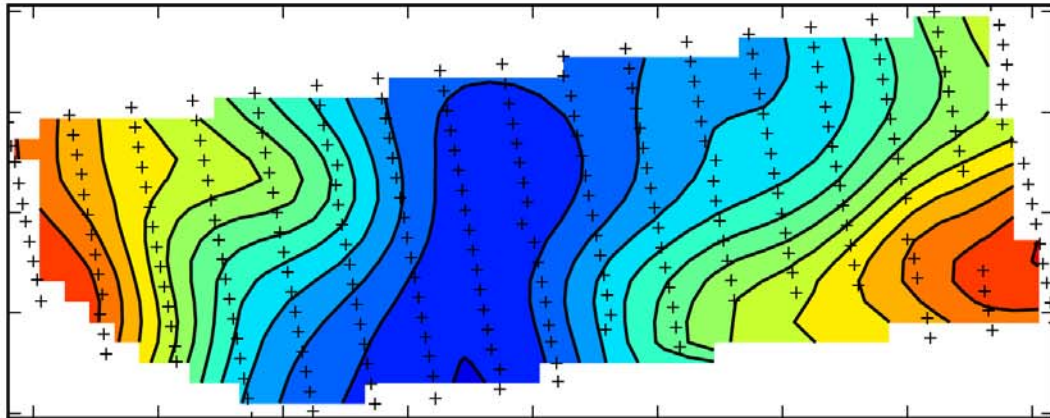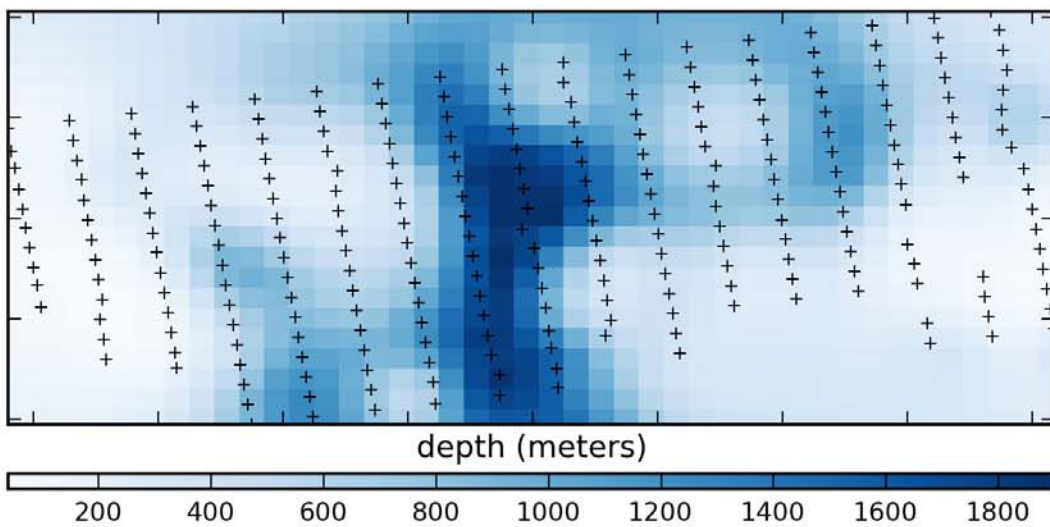
(b) inverted depth distribution
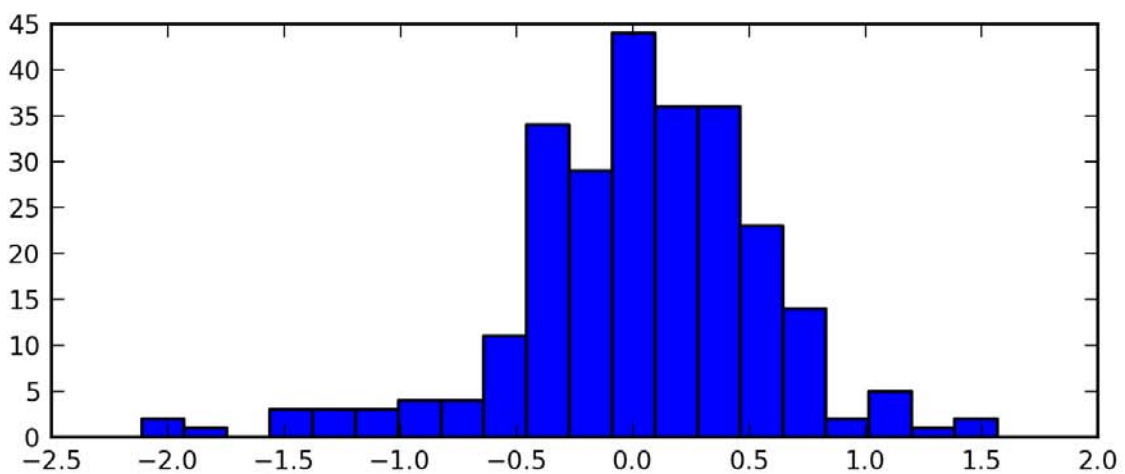
(c) histogram of residuals

Fig. 4. Summary of Pareto point 4

159

(a) simulated gravity response

depth (meters)
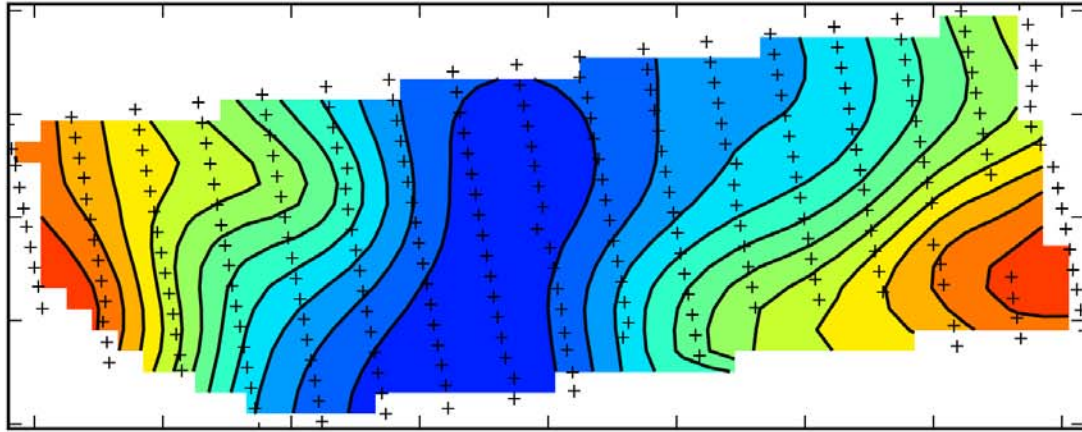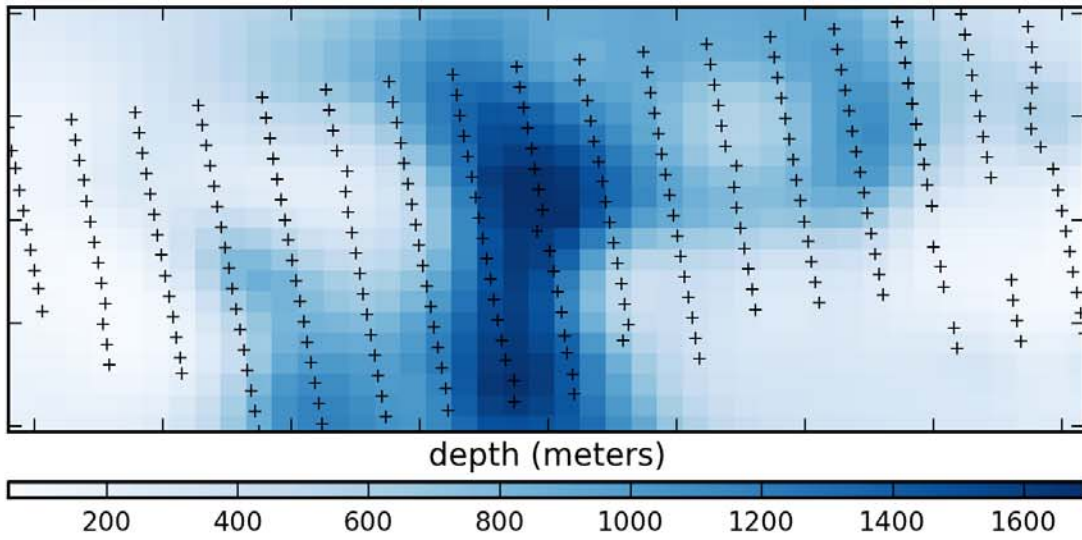
(b) inverted depth distribution
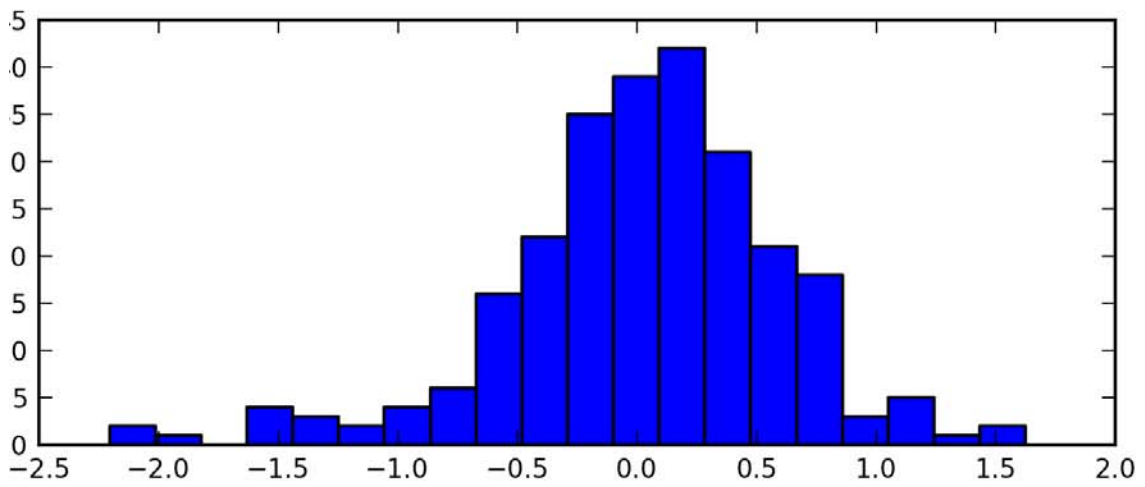
(c) histogram of residuals

Fig. 5. Summary of Pareto point 5

160

(a) simulated gravity response

depth (meters)

| 200 | 400 | 600 | 800 | 1000 | 1200 | 1400 | 1600 |
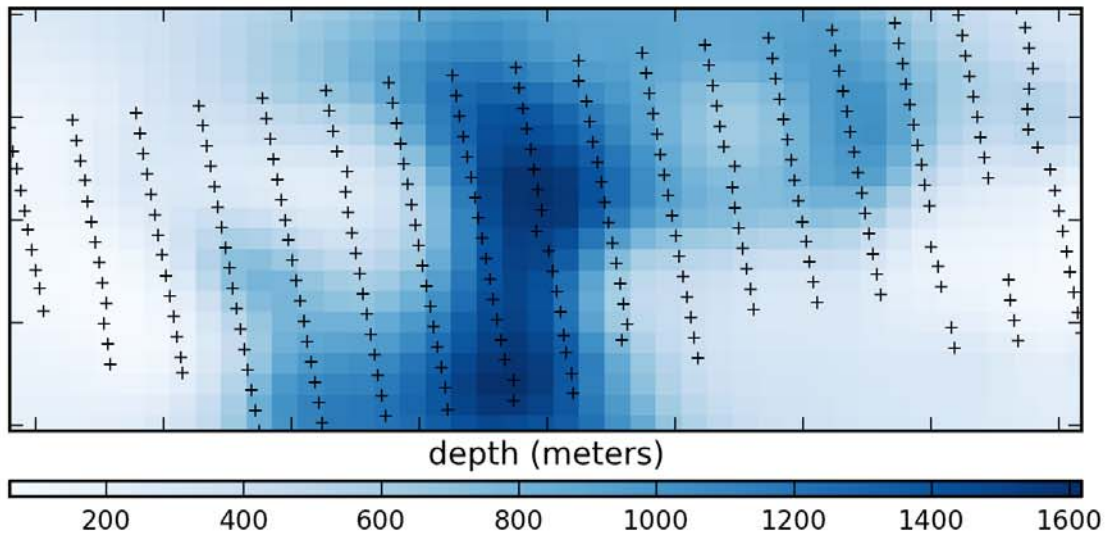
(b) inverted depth distribution

(c) histogram of residuals

Fig. 6. Summary of Pareto point 6

161

(a) simulated gravity response

depth (meters)
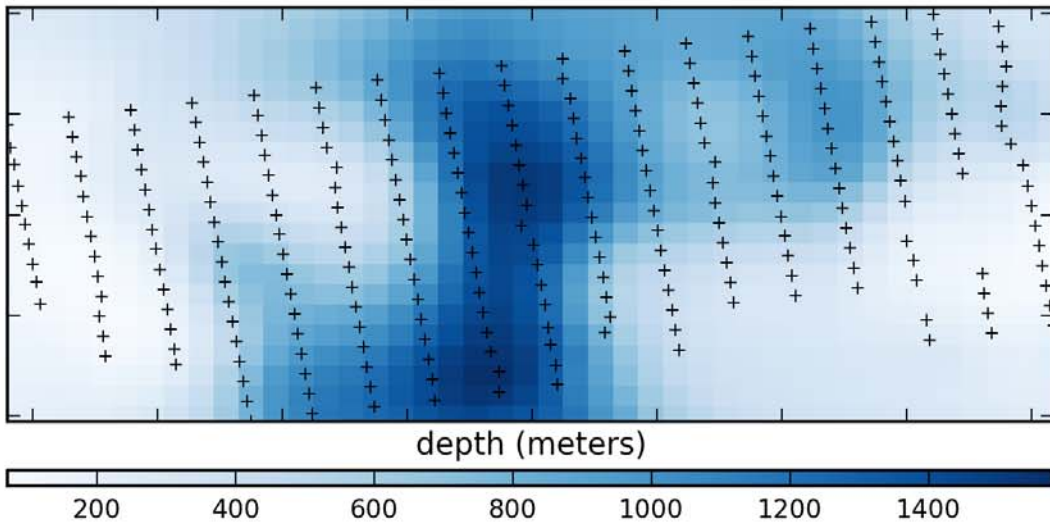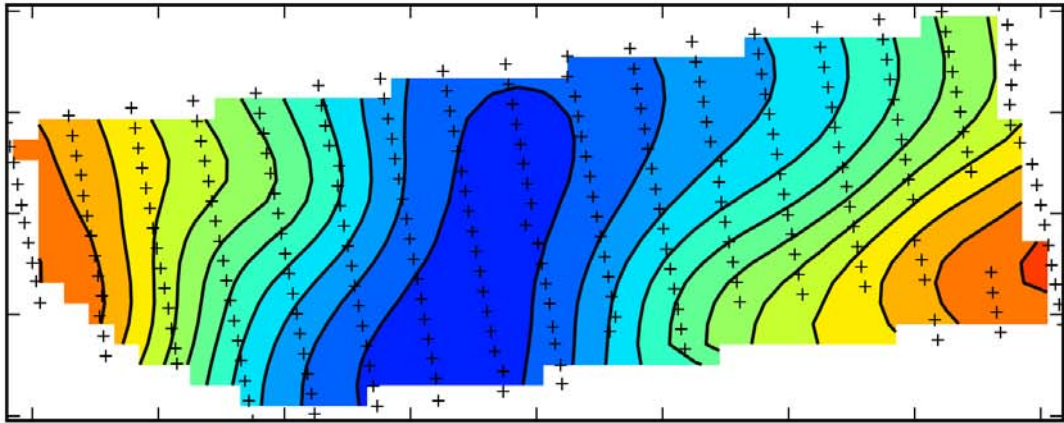
(b) inverted depth distribution

(c) histogram of residuals

Fig. 7. Summary of Pareto point 7

162

(a) simulated gravity response

depth (meters)
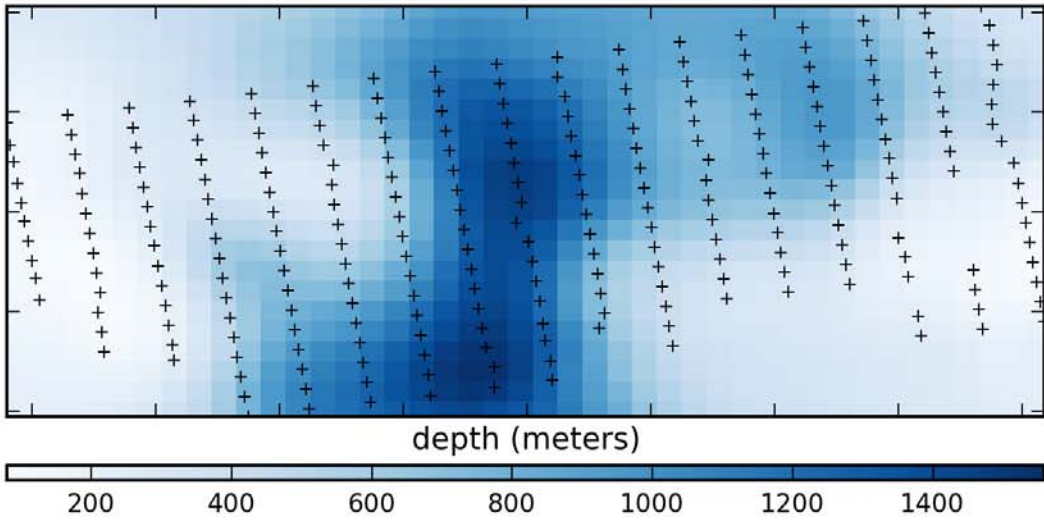
(b) inverted depth distribution

(c) histogram of residuals

Fig. 8. Summary of Pareto point 8

163

(a) simulated gravity response

depth (meters)
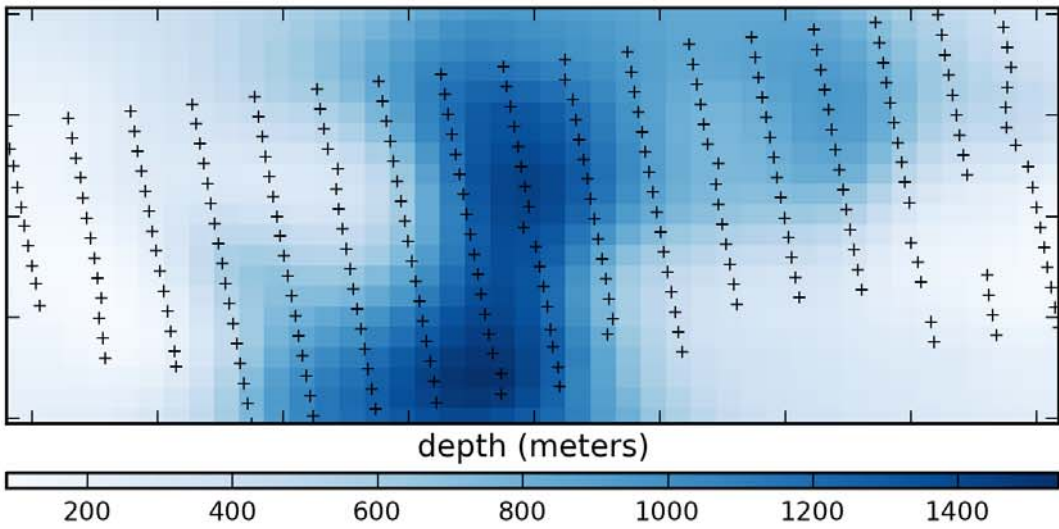
(b) inverted depth distribution
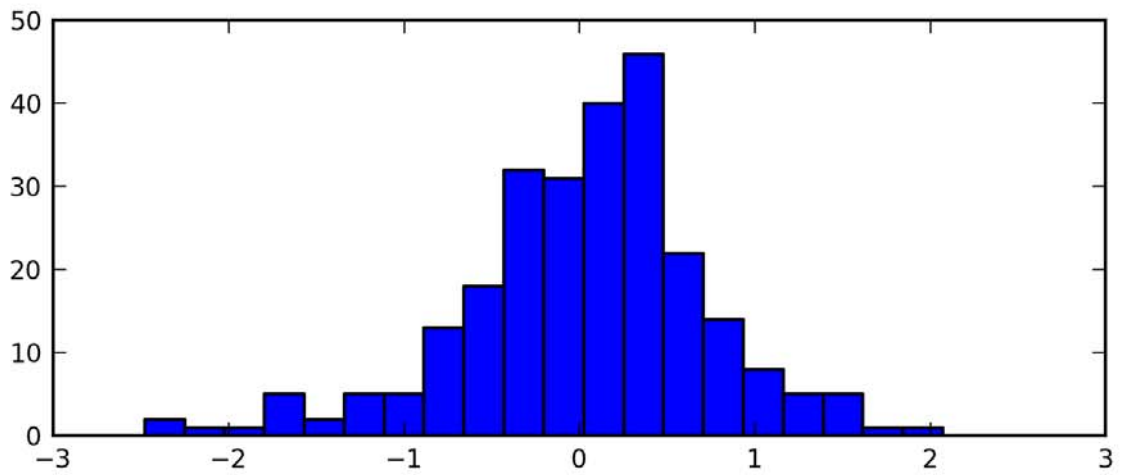
(c) histogram of residuals

Fig. 9. Summary of Pareto point 9

164

(a) simulated gravity response

depth (meters)
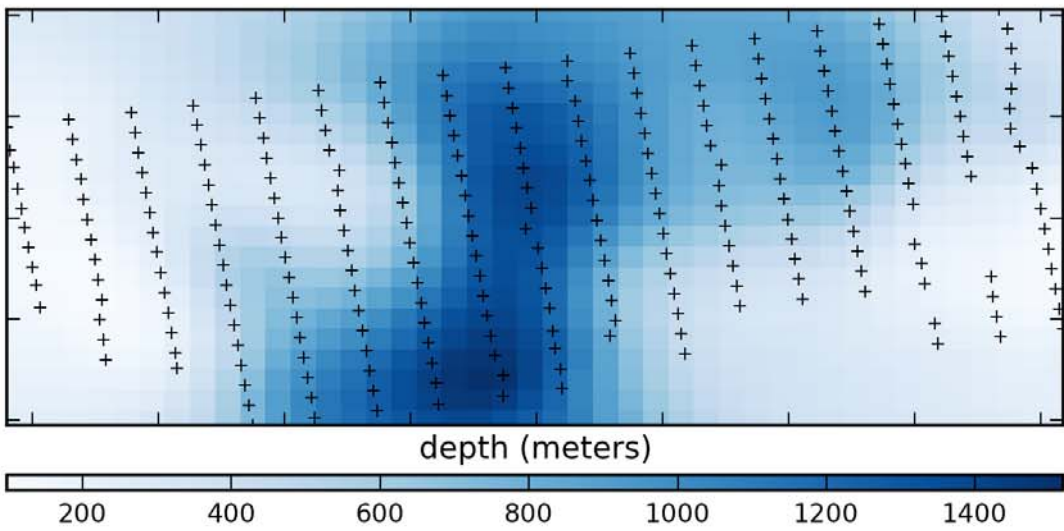
(b) inverted depth distribution
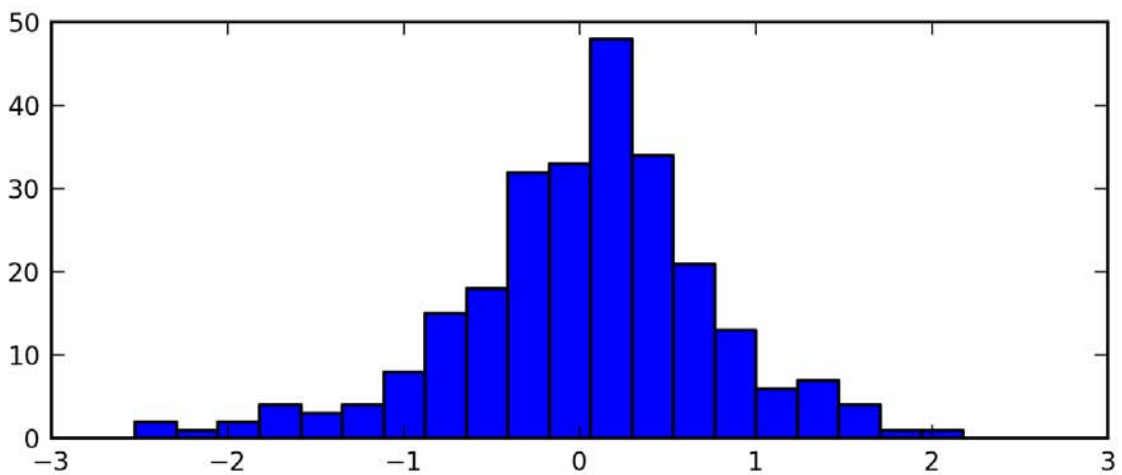
(c) histogram of residuals

Fig. 10. Summary of Pareto point 10

165

Analysis of the results of CO_2 and other soil gas surveys completed in 2009 and 2011

Initial Data

In 2009, GEORISK Scientific Research CJS conducted surveys to analyze soil gases along a profile cutting through Depression D1. Subsoil air contents of the following gases were measured in field: methane and accompanying hydrocarbon gases, hydrogen, helium, carbon oxide and carbon dioxide, and hydrogen sulfide. Fig. 1 shows location of the profile, along which the soil gases were measured.
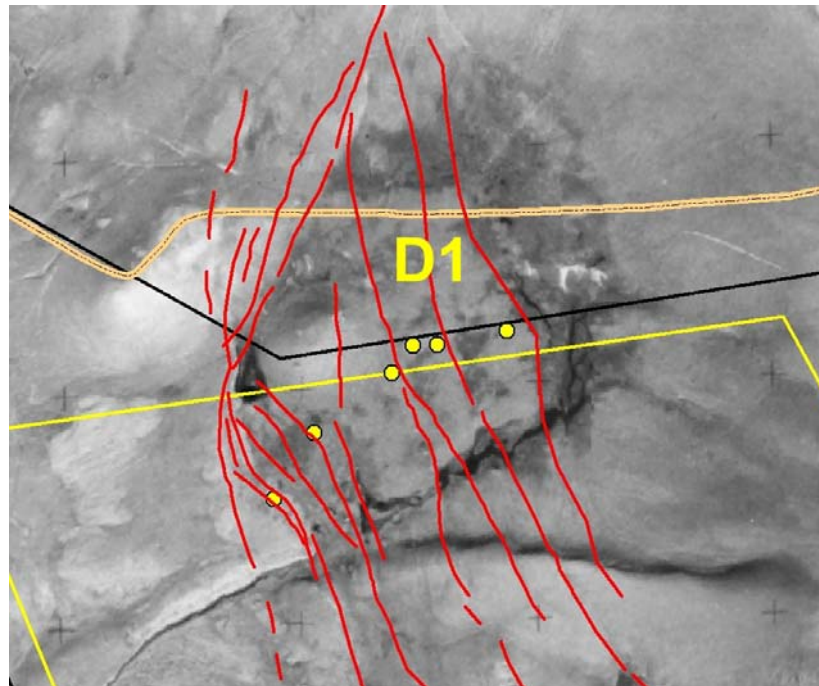

Fig. 1: Location of the profile, along which soil gases were measured in 2009.

No noticeable anomalies were discovered.

In 2011, "Western Geco" conducted an areal survey of CO_2 gas. The area covered by that survey, and the locations of measurement points, are demonstrated in Fig. 2. The survey established increased rates of CO_2 emission at Points 38, 79, 201, 202a, 206, 207, 216, and 217, and the highest rate was measured at Point 208. However, those increased values were related to Jermaghbyur thermal spring, hence they do not represent true anomaly (Fig. 2).

According to the data of "Western Geco", Points 38 and 79, located three kilometers apart, were the only potential anomaly points not associated with the thermal spring (Fig. 2). At both points, "Western Geco" company repeated the measurements along short profiles.
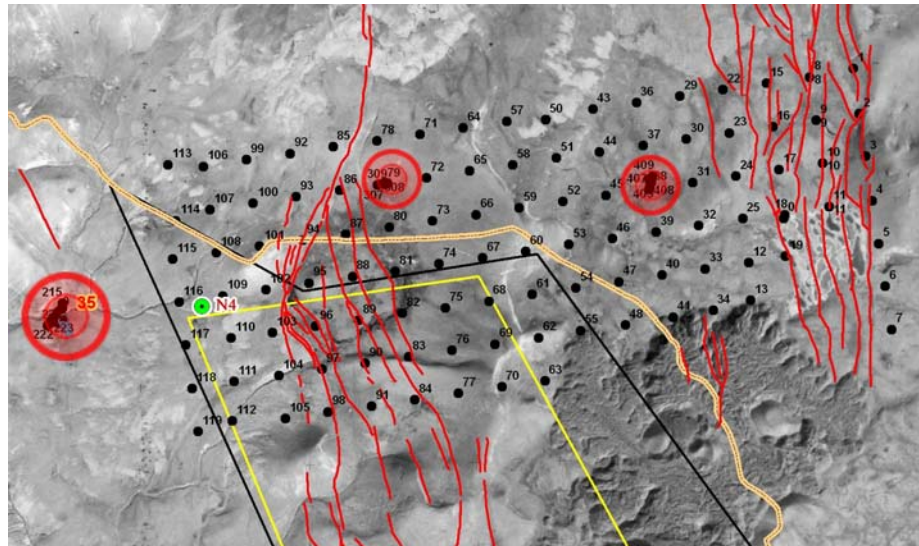
Fig. 2: Locations of CO$_2$ survey points in 2011 and the recorded anomalies

These profiles included Points 301-309 (measured over Point 79) and Points 401- 409 (measured above Point 38). The results obtained along both profiles did not allow detection of any anomalous flows. This suggests that the higher values of CO$_2$ flows for Points 38 and 79 merely reflect the extreme high limit of background values for the considered area (Fig. 3).

According to the data of "Western Geco", the histogram of CH$_4$ flows displays normal distribution that suggests deficit of anomaly data. Additionally, all flows of CH$_4$ have very low values, many of which correspond to, or are below detection limit of the sensor. The CH$_4$ data were collected primarily to make it certain that the CO$_2$ anomaly data did not reflect microbial activity related to plant matter decomposition in soil, and that the CO$_2$ was rather transported from the depth (Fig. 4). The lack of any CH$_4$ flow anomaly values suggests that this is not the case for the studied area.
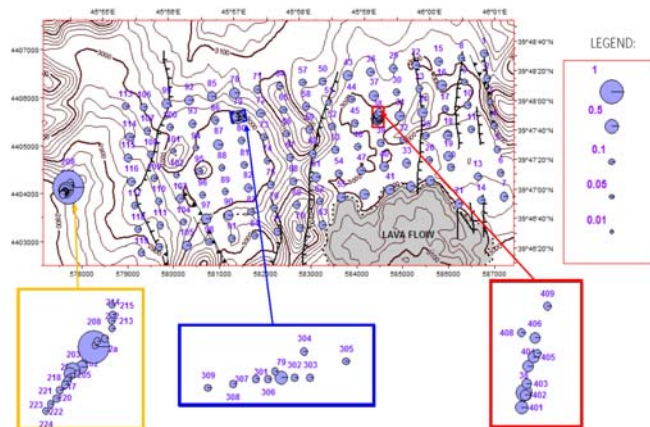

Fig. 3: Measured values of the C0$_2$ flow. Dot sizes reflect CO$_2$ flow values. The three colored boxes contour areas of dense spacing of points, which were measured in relation to the hot spring (yellow) and anomaly points 38 and 79 (red and blue colors, respectively).

167

Fig. 4: Measured values of the CH$_4$ flow. Dot sizes reflect CH$_4$ flow values. The three colored boxes contour areas of dense spacing of points, which were measured in relation to the hot spring (yellow) and anomaly points 38 and 79 (red and blue colors, respectively).
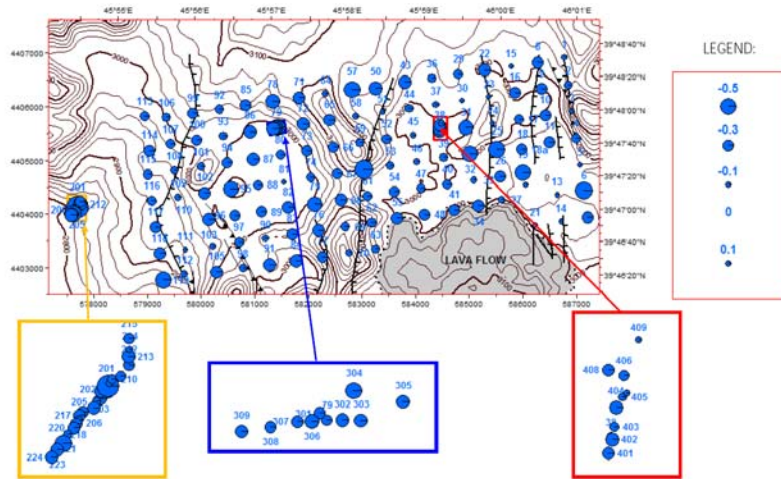
Analysis of the obtained results.

The studies of soil gases conducted in 2009 and 2011 did not reveal any considerable anomalies.

A few interpretations could be proposed for the results:

1. Any high-temperature reservoir is not present at the site; hence gas emanations from soil do not occur. This suggestion agrees with the **conceptual and hydrothermal model A**, providing for a diffuse source of heat.

2. Below the layer of basalts, there is a stratum isolating the surface from any gas emanations from the depth. This suggestion agrees with the **conceptual and hydrothermal model B**, providing for presence of a sealed high-temperature reservoir at the depth. The suggestion is supported by the location of both recorded anomalies in the limits of the anomalous sites, identified by the 2D and 3D MT surveys (Fig. 5), also within Depression D1.

3. Both in 2009, and in 2011, measurements of surface gases were conducted under unfavorable climate conditions. June 2009 was very rainy and cold. Daily air temperature was not higher than 9°C, while a considerable part of Depression D1 was covered with snow melt water. Probably, that had determined absence of gas emanations from humid and marshy soil. In 2011, measurements were made late in September- early in October and the weather was even colder: it snowed heavily in the end of the measurement period. Therefore, the climate factor could have influenced the collected results.

In any case, soil gas measurements do not have any decisive value for geothermal potential assessment, but play an auxiliary, secondary role. The presence of anomalous CO$_2$ emission values allows positive assessment of the geothermal potential of the site. However, considering the lack of soil gas anomalies, this is by no means evidence in favor of a negative assessment of its geothermal potential.
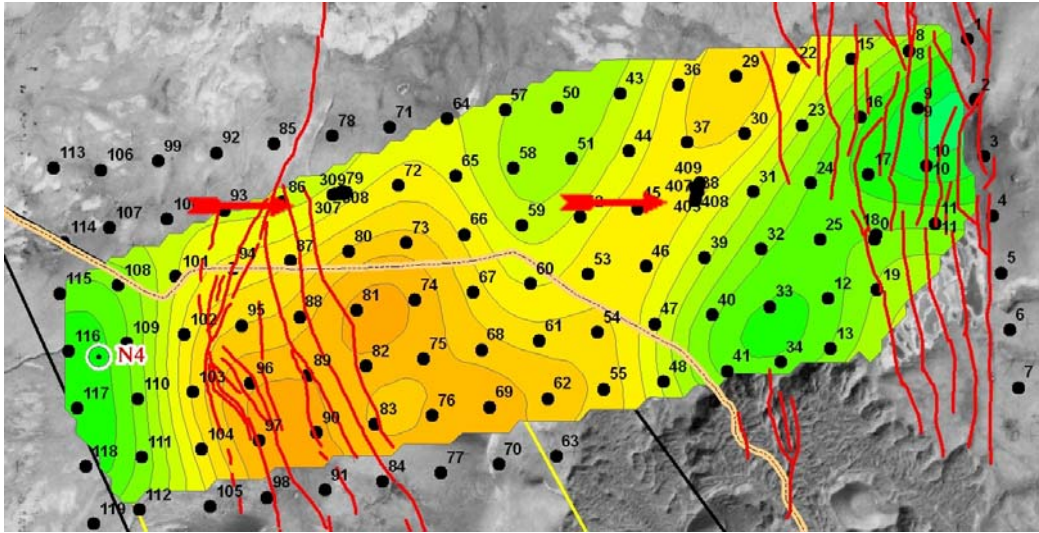
Fig. 5: Superposition of the 3D MT survey data of 2011 (Layer 2 at the depth of 1000 m, displaying low resistance) and CO_2 emission anomalies at Points 38 and 79.